Study of the Seismic Response of Unanchored Equipment and Contents in Fixed-Base and Base-Isolated Buildings

STUDY OF THE SEISMIC RESPONSE OF UNANCHORED EQUIPMENT AND CONTENTS IN FIXED-BASE AND BASE-ISOLATED BUILDINGS

By

FARZAD NIKFAR, BSC, MSC

Faculty of Engineering

Department of Civil Engineering

A Thesis Submitted to the School of Graduate Studies in Partial Fulfilment of the Requirements for the Degree of Doctor of Philosophy

McMaster University

Doctor of Philosophy (2016) McMaster University
(Civil Engineering) Hamilton, Ontario, Canada

TITLE:	Study of the Seismic Response of Unanchored Equipment and Contents in Fixed-Base and Base-Isolated Buildings
AUTHOR:	Farzad Nikfar
SUPERVISOR:	Dr. Dimitrios Konstantinidis
NUMBER OF PAGES:	277 pages (xxiv, 252)

To my lovely parents who were my main supporters

Abstract

Immediate occupancy and functionality of critical facilities including hospitals, emergency operations centers, communications centers, and police and fire stations is of utmost importance immediately after a damaging earthquake, as they must continue to provide fundamental health, emergency, and security services in the aftermath of an extreme event. Although recent earthquakes have proven the acceptable performance of the structural system in such buildings, when designed according to recent seismic design codes, in many cases damage to the nonstructural components and systems was the main cause of disruption in their functionality.

Seismic isolation is proven to be an effective technique to protect building structures from damaging earthquakes. It has been the method of choice for critical facilities, including hospitals in Japan and the United States in recent years. Seismic isolation appears to be an ideal solution for protecting the nonstructural components as well. While this claim was made three decades ago, the supporting research for freestanding (unanchored) equipment and contents (EC) is fairly new.

With the focus on freestanding EC, this study investigates the seismic performance of sliding and wheel/caster-supported EC in fixed-base and base-isolated buildings. The study adopts a comparative approach to provide a better understanding of the advantages and disadvantages of using each structural system. The seismic response of sliding EC is investigated analytically in the first part of the thesis, while the response of EC supported on wheels/casters is examined through shake table experiments on two pieces of hospital equipment.

The study finds base isolation to be generally effective in reducing seismic demands on freestanding EC, but it also exposes certain situations where isolation in fact increases demands on EC. Increasing the frictional resistance for sliding EC or locking the wheel/casters in the case of wheel/caster-supported EC is highly recommended for EC in base-isolated buildings to prevent excessive displacement demands. Furthermore, the study suggests several design probability functions that can be used by practicing engineers to estimate the peak seismic demands on sliding and wheel/caster-supported EC in fixed-base and base-isolated buildings.

Acknowledgements

I would like to express my sincere gratitude to my supervisor, Dr. Dimitrios Konstantinidis, for his support, advice, encouragement, and guidance during the course of this research. I am also extremely grateful to the members of my supervisory committee, Dr. Michael Tail and Dr. John Vlachopoulos, for their valuable comments and suggestions throughout the course of this research work.

I want to thank Hamilton Health Sciences for providing hospital equipment for this research, and Mr. Saman Rastgoo Moghadam for assisting in conducting the shake table experiments.

Finally and most importantly, this work would not have been possible without the love and support of my parents to whom this thesis is dedicated.

Table of Contents

List of Tables

List of Figures

Co-Authorship

This thesis has been prepared in accordance with the regulations for a "sandwich" thesis format as stipulated by the School of Graduate Studies at McMaster University. The thesis has been co-authored as:

Chapter 2: Seismic Response of Sliding Equipment in Base Isolated Buildings Subjected to Broad-Band Ground Motions

Authors: D. Konstantinidis and F. Nikfar

The analytical model and analysis were carried out by Farzad Nikfar under the supervision of D. Konstantinidis. The formulations regarding the appropriate Intensity Measure and Engineering Demand Parameter for sliding equipment and contents in base-isolated buildings as well as the formulations to develop the fragility functions were derived by D. Konstantinidis. The manuscript was prepared by F. Nikfar under the supervision of D. Konstantinidis. This chapter has been published in the Journal of Earthquake Engineering and Structural Dynamics.

Chapter 3: Peak Sliding Demands on Unanchored Equipment and Contents in Base-Isolated Buildings under Pulse Excitation

Authors: F. Nikfar and D. Konstantinidis

The analytical model was developed by F. Nikfar under the supervision of D. Konstantinidis. The dimensional analysis formulations and analyses were carried out by F. Nikfar under the supervision of D. Konstantinidis. The manuscript was prepared by F. Nikfar under the supervision of D. Konstantinidis. This chapter will be submitted for publication as a peer-reviewed journal paper.

Chapter 4: Effect of the Stick-Slip Phenomenon on the Sliding Response of Objects Subjected to Pulse Excitations

Authors: F. Nikfar and D. Konstantinidis

The mathematical formulation of the stick-slip sliding model, dimensional analysis formulation, and analysis were carried out by F. Nikfar under the supervision of D. Konstantinidis. The manuscript was prepared by F. Nikfar under the supervision of D. Konstantinidis. This chapter has been submitted to the Journal of Engineering Mechanics (ASCE).

Chapter 5: Shake Table Investigation on the Seismic Performance of Hospital Equipment Supported on Wheels/Casters

Authors: F. Nikfar and D. Konstantinidis

Design of the experimental program, construction of the test set-up, instrumentation, running the shake table, analytical modeling, and analysis were performed by F. Nikfar under the supervision of D. Konstantinidis. The manuscript was prepared by F. Nikfar under the supervision of D. Konstantinidis. This chapter has been submitted to the Journal of Earthquake Engineering and Structural Dynamics.

Chapter 6: Experimental Study on the Seismic Response of Equipment on Wheels/Casters in Base-Isolated Hospitals

Authors: F. Nikfar and D. Konstantinidis

The experimental program, analytical modeling and analysis were carried out by F. Nikfar under the supervision of D. Konstantinidis. The manuscript was prepared by F. Nikfar under the supervision of D. Konstantinidis. This chapter will be submitted for publication as a peer-reviewed journal paper.

Chapter 7: Evaluation of Vision-Based Measurements for Shake Table Testing of Nonstructural Components

Authors: F. Nikfar and D. Konstantinidis

The image processing and motion capture codes in MATLAB were developed by F. Nikfar under the supervision of D. Konstantinidis. The experimental program was designed and carried out by F. Nikfar under the supervision of D. Konstantinidis. The manuscript was prepared by F. Nikfar under the supervision of D. Konstantinidis. This chapter has been submitted to the Journal of Computing in Civil Engineering (ASCE).

Chapter 1: Introduction

1.1 Importance of nonstructural components

The efforts of the earthquake engineering community over the years have been overwhelmingly focused on the design of earthquake-resistant structural systems, while substantially less attention has been paid to ensuring the adequate seismic performance of nonstructural components. Structural integrity during a seismic event is paramount to ensure life safety, but this level of performance is often insufficient from the point of view of resilience. To minimize downtime and large economic losses, it is generally necessary to target an immediate occupancy or operational performance level. This is hardly achievable unless the performance of nonstructural components is taken into consideration. Damage to critical facilities such as hospitals, emergency response centers, power plants, key governmental facilities, and also special buildings containing expensive research laboratories and high-technology fabrication facilities may bring about severe human, environmental and economic losses [1]. From the economic point of view, neglecting to provide for the satisfactory seismic performance of nonstructural components is imprudent [2]. The value of nonstructural components in a typical commercial building dwarfs the cost of the structure itself, often accounting for 80 to 90% of the total value of a building [3]. In view of this and the fact that nonstructural damage typically initiates at lower levels of shaking intensity than structural damage, it is expected that a significant portion of the total economic losses resulting from a major seismic event will be attributed to nonstructural damage [4]. For example, the 1994 Northridge earthquake resulted in major economic losses upwards of $3.4 billion in hospitals, and nonstructural damage accounted for most of this figure [5]. For critical facilities, such as hospitals, emergency operations centers, and police and fire stations, continued functionality during and after the seismic event is of utmost importance. In the 2001 El Salvador Earthquake, the loss of functionality of the healthcare system was mostly due to the damage to nonstructural elements, medical equipment, and supplies;

only limited damage to engineered structural elements was reported [6]. A similar scenario led to nonstructural damage requiring repair to 62% of the hospitals located in the areas affected by 2010 Maule, Chile Earthquake; 83% of these hospitals suffered impaired functionality mainly due to nonstructural damage, while the structure suffered no damage [7].

1.2 Performance of nonstructural components in past earthquakes

Although recent earthquakes have proven the acceptable performance of the structural systems in critical buildings designed according to recent structural design codes, in many cases damage to nonstructural components was the main cause of disruption to their functionality [8,9,10,11,5,7]. Recent examples of poor seismic performance of nonstructural components in structurally code-compliant hospitals include hospitals during the 2010 Chile Earthquake [12]. The hospital buildings were designed based on Chilean seismic design codes, which are very similar to recent United States codes. Nevertheless, there were several cases of damage to unsecured equipment and contents that fell or broke during the earthquake, hindering the emergency response function of the hospitals [12]. In many cases, large, unanchored equipment, such as incubators and computers, was reported damaged after falling to the floor [12]. Similarly, in the 2011 Christchurch earthquakes, poor performance of utility networks and damage to nonstructural components were reportedly the major problems affecting the operation of the Canterbury hospital system [13]. Severe nonstructural damage and loss of functionality in medical facilities during the 1994 Northridge, 1995 Kobe, and 1999 Chi-Chi earthquakes resulted in impaired emergency response operations, demonstrating that the resilience of critical facilities, such as hospitals, is highly correlated to the seismic performance of their nonstructural components [14,15].

1.3 Nonstructural components types and associated hazards

The list of nonstructural components in a building is vast. Both the FEMA E-74 [16] and the CAN/CSA S832 [17] documents divide nonstructural components into three broad categories: architectural components, equipment (electrical, mechanical and plumbing), and contents. The present study focuses on *Unanchored* (freestanding) items under the *equipment* and *contents* (EC) categories. Figure 1-1 shows examples of freestanding EC. During earthquake shaking, EC located at various floor levels of buildings can vibrate, break loose of their restrainers, slide, rock, jump, twist, impact neighbouring EC, walls, and occupants, or overturn. Shenton [18] presented criteria for determining the mode of response of freestanding objects. In this study, we focus on EC for which sliding and rolling (in case of wheel/caster-supported EC) are the only modes of response. Rocking as a mode of response of the EC is not considered in this study. Slender EC with relatively high frictional resistance tend to rock and possibly overturn when subjected to base excitation.

Sliding is very common for freestanding (i.e., unanchored) EC, particularly those that are stocky and have a relatively low friction coefficient (examples are shown in Figure 1-1 (right) and Figure 1-2). The concern for sliding EC is excessive displacements, which can lead to different problems depending on the type of EC. For example, for a small or light EC item resting on top of a benchtop/shelf (e.g., see Figure 1-2), excessive sliding may result in the EC falling off the edge or impacting adjacent objects [19]. Sliding can also result in impact with people working in the vicinity of the EC, putting their safety at risk. Furthermore, excessive sliding displacements of very heavy EC may block an evacuation path or doorway. Large displacements of sensitive/heavy EC that can result in impact with walls or neighbouring EC should be avoided, since the resulting acceleration spikes can damage the EC and impair functionality [20]. Moreover, there are other hazards that might initiate due to EC displacement. Fires can be initiated from EC (an example of this was a fire initiated in the building of the School of Chemical Sciences in the University of Concepción in the 2010 Chile earthquake [7]); (b) loss of valuable lab samples (e.g., stem cells [24, 20]); (c) spill of hazardous materials (chemical, biohazardous, radioactive materials, etc.)

In this study, rolling EC is refers to EC supported on wheels/casters that roll during seismic shaking, causing the EC to move. They are very common in hospitals (Figure 1-1 (left) and Figure 1-3), power plants, and nuclear facilities (Figure 1-4) due to their mobility requirements. About one-third of hospital equipment and appliances are on wheels and casters [21]. The concern with equipment and appliances on wheels and casters during earthquakes is that they might exhibit large movements. Excessive movements could tear off or disconnect the electric plugs and impair the functionality of the equipment. For instance, large movements of an Anesthesia Machine (shown in Figure 1-1 (left)) may not only tear off its electric plug, but also disconnect its connections to piped hospital oxygen, medical air, and nitrous oxide. This would lead to malfunction of the equipment and possible loss of life. Large motion of EC in the operating room is also a big concern for doctors during operations. Moreover, large displacement increases the possibility of collision with other furniture, equipment and surrounding partitions. Impact as a result of collision introduces high accelerations that can lead to damage to acceleration-sensitive equipment and components. In the case of heavy equipment on wheels, a collision with people in vicinity of the equipment may result in injury.

The hazard associated with rolling EC can stem from one or combination of: (a) excessive displacement that can increase the potential of impact with adjacent EC as well as other nonstructural components, including partition walls; (b) large relative velocity, which, if coincident with large relative displacement, may result in damaging impact that can put the safety of the people working in the vicinity of the equipment or the functionality of the equipment at risk; (c) large accelerations, particularly in the high frequency range, that can cause resonance and damage to the electronic parts and attached components of equipment.

1.4 Seismic mitigation strategies

Although seismic restraints are typically recommended to prevent sliding of EC, such restraints can be costly. For example, a study by Comerio and Stallmeyer [22] estimated the cost of restraining the EC in five typical University of California, Berkeley, laboratories at US$25 per square foot (US$270 per square meter). For UC Berkeley buildings where the dominant use is laboratories, the cost of seismically restraining the EC could range from US$8 to $12 million [23]. Besides cost, there are also practical limitations associated with restraining EC. Some EC items need to remain mobile. Even though some light benchtop items can be restrained by detachable devices, most heavy items and items on carts or wheels require a permanent wall or counter anchor to which the removable anchor can be attached. If such a fixity point is not available, successful restraint is not possible [23]. Another problem associated with restraining EC is the transmitted accelerations to the EC through its anchorage. A shake table test study [24] on chain-anchored laboratory equipment showed the peak accelerations of anchored equipment to be significantly (as much as 7 times) larger than those of freestanding equipment. Such excessive accelerations can damage internal parts of acceleration-sensitive equipment and result in loss of functionality [22].

As mentioned earlier, excessive relative displacement, relative velocity, absolute acceleration, and vibration frequency that EC experience are the main causes of hazard in earthquakes. Thus, the desirable characteristics of earthquake protection systems for building EC include the ability to decrease floor acceleration, relative displacement, and relative velocity together with shifting the floor vibration frequency to frequencies lower than the equipment resonance frequency. Seismic isolation appears to be an ideal solution for protecting building EC since it aims to control all of the aforementioned demand parameters. While this claim has been made three decades ago [25], the supporting research for unanchored EC is fairly new.

It is worth mentioning that component-level base isolation that isolates individual EC from floor excitations is another alternative [26] that has been implemented for seismically upgrading facilities, particularly, electrical equipment in data centers. However, the study of this type of isolation system is beyond the scope of this thesis.

1.5 Recent studies on the performance of nonstructural components in base-isolated buildings

To date, there has been only one comprehensive experimental program that examined the performance of freestanding EC and particularly hospital equipment on wheels/casters in a base-isolated hospital [21,27,28]. It included full-scale shake table experiments of a four-story RC building at E-Defense facility, Japan, to evaluate the performance of fixed-base and base-isolated medical facilities. Various rooms at different floor levels of the building were outfitted with hospital equipment and appliances to replicate realistic hospital rooms [21,27,28]. The experimental program was aimed at studying various aspects of the facility. Shi et al. [28] focused specifically on the performance of items on casters. It was observed that the equipment with unlocked casters may experience movements as large as three meters [28]. Multiple collisions with other equipment, furniture, and partitions were observed that resulted in accelerations up to 10 g [28]. The experimental results of the base-isolated building showed that most equipment and appliances (including the ones with locked casters) experienced negligible movement except for those with unlocked casters that exhibited very large motions, leading to collisions with other equipment and surrounding partition walls [28]. For equipment with locked casters, the response was very small when the building was tested as base-isolated, but when the building was tested as fixed-base, especially under near-fault ground motion, the equipment experienced the largest response and damage [28]. Although the study provides valuable information about the performance of this class of EC, it does not provide a tool to estimate the EC demands in an earthquake event.

Notable full-scale shake table test studies which included the performance of nonstructural components were undertaken. Ryan et al. [29] carried out a shake table study of a five-story, steel moment-frame building, in both fixed-base and base-isolated configurations. The building featured an array of nonstructural components, including interior walls, ceiling systems, sprinkler piping systems, and loose contents [30]. Pantoli et al. [31] conducted shake table tests of a five-story reinforced-concrete building (both fixed base and base isolated) that featured a variety of nonstructural components and systems. Di Sarno et al. [32] and Cosenza et al. [33] investigated the dynamic response of nonstructural components (freestanding cabinets and desks) in typical hospital rooms through shake table tests and fragility analysis.

The intent of the brief literature review that was presented in this introductory chapter was to provide an overview of previous work on the seismic response of nonstructural components in a general context, with some specifics about equipment and contents that are prone to sliding or rolling. An in-depth literature review on the specific topic covered in each chapter of this sandwich thesis is presented in the Introduction section of that chapter.

1.6 Impetus and research objectives

Although the concept of base isolation is well established and it has been the method of choice for critical facilities particularly hospitals in Japan and the United States, the supporting research on its effectiveness to protect freestanding EC is limited. Experimental and analytical/numerical research studies to evaluate the seismic performance of important nonstructural components, including medical equipment, seem to be urgent to fill in current knowledge gaps and improve seismic provisions for nonstructural components that have been for the most part based on empirical approaches.

The objective of this thesis is to develop a greater understanding and quantitative characterization of the seismic behaviour of freestanding equipment and contents that tend to slide or roll. The study investigates the seismic response of EC in fixed-base buildings and assesses the effectiveness of base isolation in reducing the seismic demands on these types of EC. An analytical approach was adopted to study the behaviour of sliding EC in fixed-base and base-isolated buildings. Advanced analytical models were developed to better estimate the sliding response of rigid and flexible EC in buildings. The seismic behaviour of EC supported on wheels/casters was studied through an extensive experimental program, which included shake table tests.

1.7 Structure of thesis

This thesis was prepared in accordance with the regulations of a "sandwich" thesis format containing previously published and prepared materials. Since Chapter 2 to Chapter 7 were prepared to become stand-alone documents, each chapter has its own introduction, conclusion and bibliography. Overlap is likely to occur between chapters, mainly in the introduction part of each.

PART I of this thesis, consisting of Chapters 2, 3, and 4, include analytical investigations on the seismic response of sliding EC.

Chapter 2 investigates the seismic behaviour of sliding EC inside base-isolated buildings subjected to broadband ground motions. The effect of isolation system properties on the response of rigid sliding EC with various friction coefficients is examined. Two widely used isolation models are considered: viscously damped linear elastic, and bilinear. The study identifies physically motivated dimensionless intensity measure and engineering demand parameter for sliding equipment in base-isolated buildings. Finally, design fragility curves are presented for EC in base-isolated buildings.

In Chapter 3, pulse-like ground motions are approximated by analytical pulses that facilitate performing dimensional analysis. Dimensional analysis is performed to explore the existence of physical similarities in the sliding response of EC in buildings isolated using viscoelastic and bilinear isolation systems. An advanced friction model with capability of capturing velocity-dependent friction in low and high velocities is utilized. The effect of various parameters, including isolation nominal period and damping, static friction and its transition to kinetic friction, interaction between the sliding object and the seismically isolated building, and vertical flexibility of the isolation and super-structure are investigated.

Chapter 4 investigates the effect of EC flexibility and velocity dependence of friction that may lead to stick-slip during sliding of the EC. The mathematical formulation of a sliding system that can capture the stick-slip phenomenon is developed. A dimensional analysis approach is taken to expose the underlying physical similarities in the sliding problem and to compare the results of the stick-slip model with conventional sliding models, such as Newmark's rigid block and coupled sliding models that are not capable of capturing the stick-slip phenomenon.

PART II of this thesis, consisting of Chapters 5, 6, and 7, investigate the seismic response of EC supported on wheels/casters through shake table experiments.

Chapter 5 contains the results of the experiments to evaluate the frictional resistance of the wheels and casters of two pieces of hospital equipment. It also presents the results of the shake table experiments for evaluating the seismic response of the equipment in a fixed-base steel special-braced-frame hospital. The experimental data is presented for the equipment in locked and unlocked conditions. Finally, probability functions that can be used to predict the peak seismic demands on EC supported on wheels/casters in fixed-base buildings are proposed.

Chapter 6 investigates the seismic response of wheel/caster-supported EC in base-isolated buildings through shake table tests of two pieces of hospital equipment. This chapter adopts a comparative approach to examine the performance of bilinear (LRB) and triple-friction-pendulum (TFP) isolation systems against a conventional fixed-base hospital. It provides probability functions that can be used by practicing engineers to estimate the peak relative displacement and relative velocity of EC on wheels/casters in base-isolated buildings.

Chapter 7 discusses the application of camera for measuring the complex motion of medical equipment during the shake table experiments. It presents the results of controlled shake table tests performed to evaluate the accuracy of a low-cost consumer-grade camera for this purpose. The chapter provides contour plots that can be used to determine the maximum displacement, velocity, and acceleration errors for a wide combination of camera resolution and frame rate values. Furthermore, the chapter introduces a useful method to synchronize the output of conventional sensors and camera recordings based on a wavelet approach. Such synchronization is necessary, and is often a challenge, in experimental setups where a combination of camera and conventional sensors are used to collect data.

Chapter 8 concludes the thesis. It summarizes the important findings from each chapter and provides recommendations for future studies.

1.8 References

[1] I. Politopoulos and C. Feau, "Some aspects of floor spectra of 1DOF nonlinear primary structures," *Earthquake Engineering and Structural Dynamics*, vol. 36, pp. 975–993., 2007.

[2] C.A. Kircher, "It makes dollars and sense to improve nonstructural system performance," in *Proceedings of Seminar on Seismic Design, Performance and Retrofit of Nonstructural Components in Critical Facilities, Applied Technology Council, ATC 29-2*, Newport Beach, CA, Oct 23-24, 2003.

[3] S. Taghavi and E. Miranda, "Response assessment of nonstructural building elements," University of California, Berkeley, CA, Report No. 2003/05, 2003.

[4] M.C. Comerio, "PEER testbed study on a laboratory building: exercising seismic performance assessment," University of California, Berkeley, CA, Report No. 2005/12, 2005.

[5] E.A. Fierro, E. Miranda, C.L. Perry, A.C. Lynn, and R. Reitherman, "Behavior of nonstructural components in recent earthquakes," in *Proc. 2011 Architectural Engineering National Conference*, Oakland, CA, 2011.

[6] R.L. Boroschek, "Seismic vulnerability of the healthcare system in El Salvador and recovery after the 2001 earthquakes," *Special Papers-Geological Society of America*, vol. 375, 2004, Special Paper 375.

[7] E. Miranda, G. Mosqueda, R. Retamales, and G. Pekcan, "Performance of nonstructural components during the 27 February 2010 Chile earthquake," *Earthquake Spectra*, vol. 28, no. S1, pp. S453-S471, 2012.

[8] A. Filiatrault, C-M Uang, B. Folz, C Christopulos, and K. Gatto, "Reconnaissance report of the February 28, 2001 Nisqually (Seattle-Olympia) Earthquake," Department of Structural Engineering, University California, San Diego, La Jolla, CA, Structural Systems Research Project Report N SSRP-2000/15, 2001.

[9] ASCE/SEI 7-05, *Minimum design loads for buildings and other structures*. Reston, Virginia, USA: American Society of Civil Engineers, 2006.

[10] R. Myrtle, S. Masri, R. Nigbor, and J. Caffrey, "Classification and prioritization of essential systems in hospitals under extreme events," *Earthquake Spectra*, vol. 21, no. 3, pp. 779–802, 2005.

[11] G. Mosqueda, R. Retamales, A. Filiatrault, and A. Reinhorn, "Testing facility for

experimental evaluation of non-structural components under full-scale floor motions," *The Structural Design of Tall and Special Buildings*, vol. 18, no. 4, pp. 387–404, 2008.

[12] J. Mitrani-Reiser et al., "A functional loss assessment of a hospital system in the Bío-Bío province," *Earthquake Spectra*, vol. 28, no. S1, pp. 473-502, 2012.

[13] C.C. Jacques et al., "Resilience of the canterbury hospital system to the 2011 Christchurch earthquake," *Earthquake Spectra*, vol. 30, no. 1, pp. 533-554, 2014.

[14] G.P. Cimellaro, A.M. Reinhorn, and M. Bruneau, "Seismic resilience of a hospital system," *Structure and Infrastructure Engineering*, vol. 6, no. 1-2, pp. 127-144, 2010.

[15] A. Filiatrault and T. Sullivan, "Performance-based seismic design of nonstructural building components: The next frontier of earthquake engineering," *Earthquake Engineering and Engineering Vibration*, vol. 13, no. 1, pp. 17-46, 2014.

[16] FEMA E-74, "Reducing the risks of nonstructural earthquake damage – a practical guide," Washington, DC, 2011.

[17] CSA, "CSA S832-06 (R2011): Seismic risk reduction of operational and functional components (OFCs) of buildings," Mississauga, ON, 2011.

[18] H.W. Shenton III, "Criteria for initiation of slide, rock, and slide-rock rigid-body modes," *Journal of Engineering Mechanics(ASCE)*, vol. 122, no. 7, pp. 690–693, 1996.

[19] S.R. Chaudhuri and T.C. Hutchinson, "Fragility of bench-mounted equipment considering uncertain parameters," *Journal of Structural Engineering*, vol. 132, no. 6, pp. 884–898, 2006.

[20] D. Konstantinidis and N. Makris, "Experimental and analytical studies on the response of freestanding laboratory equipment to earthquake shaking," *Earthquake Engineering and Structural Dynamics*, vol. 38, no. 6, pp. 827–848, 2009.

[21] E. Sato, S. Furukawa, A. Kakehi, and M. Nakashima , "Full-scale shaking table test for examination of safety and functionality of base-isolated medical facilities,"

Earthquake Engineering and Structural Dynamics, vol. 40, no. 13, pp. 1435–1453, 2011.

[22] M.C. Comerio and J.C. Stallmeyer, "Laboratory equipment: estimating losses and mitigation costs," *Earthquake Spectra*, vol. 19, no. 4, pp. 779–797, 2003.

[23] M.C. Comerio and J.C. Stallmeyer, "Nonstructural loss estimation:the UC Berkeley case study," College of Engineering, University of California, Berkeley, CA, Report No. 2002/01, 2002.

[24] D. Konstantinidis and N. Makris, "Experimental and analytical studies on the seismic response of freestanding and anchored laboratory equipment," University of California, Berkeley, CA, Report No. 2005/07, 2005.

[25] J.M. Kelly and H.C. Tsai, "Seismic response of light internal equipment in base-isolated structures," *Earthquake Engineering and Structural Dynamics*, vol. 13, no. 6, pp. 711–732, 1985.

[26] P.S. Harvey and H.P. Gavin, "Assessment of a rolling isolation system using reduced order structural models," *Engineering Structures*, vol. 99, pp. 708–725, 2015.

[27] S. Furukawa, E. Sato, Y. Shi, T. Becker, and M. Nakashima, "Full-scale shaking table test of a base-isolated medical facility subjected to vertical motions," *Earthquake Engineering and Structural Dynamics*, vol. 42, no. 13, pp. 1931–1949, 2013.

[28] Y. Shi, M. Kurata, and M. Nakashima, "Disorder and damage of base-isolated medical facilities when subjected to near-fault and long-period ground motions," *Earthquake Engineering and Structural Dynamics*, vol. 43, no. 11, pp. 1683–1701, 2014.

[29] K. Ryan et al., "Seismic simulation of an integrated ceiling-partition wall-piping system at E-Defense. I: Three-dimensional structural response and base isolation," *Journal of Structural Engineering (ASCE)*, vol. 142, no. 2, 2016.

[30] S. Soroushian et al., "Seismic Simulation of an Integrated Ceiling-Partition Wall-Piping System at E-Defense. II: Evaluation of Nonstructural Damage and

Fragilities," *Journal of Structural Engineering (ASCE)*, vol. 142, no. 2, 2016.

[31] E. Pantoli et al., "Landmark Dataset from the Building Nonstructural Components and Systems (BNCS) Project," *Earthquake Spectra*, vol. (In-Press), 2015.

[32] L. Di Sarno, C. Petrone, G. Magliulo, and G. Manfredi, "Dynamic properties of typical consultation room medical components," *Engineering Structures*, vol. 100, pp. 442-454, 2015.

[33] E. Cosenza et al., "Shake table tests for the seismic fragility evaluation of hospital rooms," *Earthquake Engineering and Structural Dynamics*, vol. 44, no. 1, pp. 23-40, 2015.

Rolling Equipment
(equipment on wheels/casters)

Rocking Equipment
(slender objects / high friction)

Sliding Equipment
(stocky objects / low friction)

Anesthesia Machine
(Hamilton Cancer Hospital)

Electrical Equipment
(FEMA E-74 [16])

Kelvinator Refrigerator
(PEER Report [24])

Figure 1-1: Examples of wheel/caster supported, rocking, and sliding equipment and contents

Figure 1-2: Sliding hospital EC on shelves

Figure 1-3: Example of a typical hospital operating room[1]

Figure 1-4: Examples of EC on wheels/casters at a nuclear facility (McMaster University Nuclear Reactor facility)

[1] Online Source (Feb. 17, 2016): http://www.vancouversun.com/cms/binary/11490373.jpg

PART I

ANALYTICAL INVESTIGATIONS ON THE SEISMIC RESPONSE OF SLIDING EQUIPMENT AND CONTENTS

Chapter 2: Seismic Response of Sliding Equipment in Base Isolated Buildings Subjected to Broad-Band Ground Motions

Konstantinidis D., Nikfar F. 2015, Seismic Response of Sliding Equipment in Base Isolated Buildings Subjected to Broad-Band Ground Motions, *Earthquake Engineering and Structural Dynamics*, 44(6): 865-887.

Abstract

Base isolation has been established as the seismic design approach of choice when it comes to protecting nonstructural contents. However, while this protection technology has been widely shown to reduce seismic demands on *attached* oscillatory equipment and contents (EC), its effectiveness in controlling the response of *freestanding* EC that are prone to sliding has not been investigated. This study examines the seismic behavior of sliding EC inside base-isolated buildings subjected to broadband ground motions. The effect of isolation system properties on the response of sliding EC with various friction coefficients is examined. Two widely used isolation models are considered: viscously damped linear elastic, and bilinear. The study finds isolation to be generally effective in reducing seismic demands on sliding EC, but it also exposes certain situations where isolation in fact increases demands on EC, most notably for low friction coefficients and high earthquake intensities. Damping at the isolation level is effective in controlling the EC sliding displacements, although damping over about 20% is found to be superfluous. The study identifies a physically motivated dimensionless intensity measure and engineering demand parameter for sliding equipment in base-isolated buildings subjected to broadband ground motions. Finally, the paper presents easy-to-use design fragility curves and an example that illustrates how to use them.

2.1 Introduction

The effort of the earthquake engineering community over the years has been overwhelmingly focused on the design of earthquake-resistant structural systems, while substantially less attention has been paid to ensuring the adequate seismic performance of nonstructural components. Structural integrity during a seismic event is paramount to ensure life safety, but this level of performance is often insufficient from the point of view of resilience. To minimize downtime and large economic losses, it is generally necessary to target an immediate occupancy or operational performance level. This is hardly achievable unless the performance of nonstructural components is taken into consideration. From the economic point of view, neglecting nonstructural components is imprudent [1]. The value of nonstructural components in a typical commercial building dwarfs the cost of the structure itself, often accounting for 80 to 90% of the total value of a building [2]. In view of this and the fact that nonstructural damage typically occurs at lower levels of shaking intensity than structural damage, it is expected that a significant portion of economic losses resulting from a major seismic event will be attributed to nonstructural damage [3]. For example, the 1994 Northridge earthquake resulted in major economic losses upwards of $3.4 billion in hospitals, and nonstructural damage accounted for most of this figure [4]. For critical facilities, such as hospitals, emergency operations centers, and police and fire stations, continued functionality during and after the seismic event is of utmost importance. In the 2001 El Salvador Earthquake, the loss of functionality of the healthcare system was mostly due to the damage to nonstructural elements, medical equipment, and supplies; only limited damage to engineered structural elements was reported [5].

The list of nonstructural components in a building is vast. Both the United States Federal Emergency Management Agency (FEMA) E-74 [6] and the Canadian Standards Association (CSA) S832 [7] documents divide nonstructural components into three broad categories: architectural components, equipment (electrical, mechanical and plumbing), and contents. This study focuses on nonstructural components that belong predominantly in the equipment and contents categories, abbreviated herein as EC. During earthquake shaking, EC located at various floor levels of buildings can vibrate, break loose of their restrainers, slide, rock, jump, twist, impact neighboring EC or walls, or overturn. Shenton [8] presented criteria for determining the mode of response of freestanding objects. The rocking response of freestanding objects has been studied in great length elsewhere, e.g. [9–13]. In this study, we focus on objects for which sliding is the only mode of response. Sliding is very common for freestanding (i.e., unrestrained) EC, particularly those that are stocky and have a relatively low friction coefficient. The problem of sliding objects has been studied at various levels by Shao and Tung [14], Choi and Tung [15], Lopez Garcia and Soong [16,17], Chaudhuri and Hutchinson [18], Hutchinson and Chaudhuri [19], Konstantinidis and Makris [20,21], and references reported therein. The concern for sliding EC is excessive displacements, which can lead to different problems depending on the type of EC. For example, for a small or light EC item resting on top of a benchtop/shelf, excessive sliding may result in the EC falling off the edge or impacting adjacent objects [22]. In the case of relatively heavy EC, sliding can result in impact with people working in the vicinity of the EC, putting their safety at risk. Furthermore, excessive sliding displacements of very heavy EC may block an evacuation path or doorway. Large displacements of sensitive/heavy EC that can result in impact with walls or neighboring EC should be avoided, since the resulting acceleration spikes can damage the EC and impair functionality [20].

Although seismic restraints are typically recommended to prevent sliding of EC, such restraints can be costly. For example, a study by Comerio and Stallmeyer [23] estimated the cost of restraining the EC in five typical University of California, Berkeley, laboratories at US$25 per square foot (US$270 per square meter). For UC Berkeley buildings where the dominant use is laboratories, the cost of seismic restraining the EC could range from US$8 to $12 million [24]. Besides cost, there are also practical limitations associated with restraining EC. Some EC items need to remain mobile. Even though some light benchtop items can be restrained by detachable devices, most heavy items and items on carts or wheels require a permanent wall or counter anchor to which the removable anchor can be attached. If such a fixity point is not available, successful restraint is not possible [24]. Another problem associated with restraining EC is the transmitted accelerations to the EC through its anchorage. A shake table test study [25] on chain-anchored laboratory equipment showed the peak accelerations of anchored equipment to be significantly (as much as 7 times) larger than those of freestanding equipment. Such excessive accelerations can damage internal parts of acceleration-sensitive equipment and result in loss of functionality [23].

Seismic isolation is a proven design approach for mitigating earthquake damage. Unlike traditional earthquake-resistant design approaches which aim at increasing the structure's capacity, seismic isolation aims at reducing seismic demand, protecting both the structural system and the nonstructural components [26]. This is achieved by decoupling the building from the ground motion by placing horizontally flexible bearings between the building and its foundation. The fundamental period of the system is increased, and interstory drifts and story accelerations in the building are substantially reduced. The effect of different seismic isolation systems on the performance of attached equipment that behave like viscously damped linear oscillators has been studied at various levels in [27–33].

Recently, large-scale experimental studies have investigated the response of nonstructural components in base-isolated (BI) buildings. A shake-table test study of a full-scale, four-story, BI reinforced-concrete specimen representing a medical facility was conducted at E-Defense [34–36]. The structural specimen housed a wide variety of furniture and medical appliances. The study used near-fault and long-period, long-duration ground motions as input. An overview of the study and its findings is offered in Sato et al. [34], while Furukawa et al. [35] focused on the effects of vertical motion on the structure and its contents, and Shi et al. [36] focused on the response of the contents. A large portion of the nonstructural components investigated in this study consisted of objects that were supported on casters, both locked and unlocked. Objects on locked casters had a friction coefficient of 0.63 and experienced no motion, while objects on unlocked casters rolled to very large distances (as much as 3.6 m) under excitations with spectral peaks near the isolation period. More recently, Ryan et al. [37] undertook a shake-table test study of a five-story, BI steel moment-frame building at E-Defense. The building featured an array of nonstructural components, including interior walls, ceiling systems, sprinkler piping systems, and loose contents [38]. Hutchinson et al. [27] conducted shake-table tests of a five-story, BI reinforced-concrete building that featured a variety of nonstructural components. Detailed findings from the last two test programs are expected in forthcoming publications.

Except for some preliminary efforts [40,36,41], the performance of sliding EC in isolated buildings has not been previously studied in depth. This paper presents the results of an extensive study aiming to quantify the performance of sliding EC in isolated buildings subjected to broadband ground motions. An EC item is modeled as a rigid mass, and the contact interface between the mass and its base is modeled using Coulomb friction. Discussion on the validity of these assumptions is offered in [25,20,21]. While isolation is generally beneficial in reducing the seismic demands on EC, the study exposes circumstances where isolating a building may in fact result in increased demands on EC. The paper introduces a physically motivated Intensity Measure (IM) and its associated Engineering Demand Parameter (EDP) for the sliding response of EC in BI buildings. The functional dependence between the EDP and the IM is established using results of numerical simulations. Finally, the EDP is treated as a lognormally distributed random variable, and practical fragility curves corresponding to different sliding limit states are developed.

2.2 Description of the model

The discussion in this paper is limited to planar analysis. Under this assumption, a freestanding rigid object subjected to base excitation has three modes of response (assuming that the object does not lift off): pure rocking, pure sliding, and rocking-sliding. The study presented herein focuses entirely on the response of rigid EC that are stocky enough and/or for which the friction coefficient is low enough that the rocking mode is not engaged; thus pure sliding is the only mode of response. Figure 2-1 shows a schematic of the model used in this study. The model consists of three parts: the sliding EC, the superstructure, and the base isolation system. The horizontal displacement of the ground is u_g, and the vertical displacement is v_g. The horizontal displacements of the base floor and the story, both relative to the ground, are u_1 and u_2. The displacement of the EC relative to the floor (i.e., the sliding displacement) is u. The elements of the model are assumed rigid in the vertical direction; therefore, the EC experiences the same vertical acceleration as the ground. A detailed description of each part of the model follows.

2.2.1 Sliding EC

A rigid block (i.e., the EC item) of mass m_{EC} at the story level is considered, as shown in Figure 2-1. The block is subjected to horizontal and vertical base excitations, $\ddot{u}_2 + \ddot{u}_g$ and $\ddot{v}_g$ respectively, as shown in Figure 2-2. It is assumed that the mechanical behavior of the contact interface can be described by a classical Coulomb friction model with coefficient of static friction μ_s and kinetic friction μ. Typically the value of μ_s tends to be slightly higher than that of μ; however, based on previous studies [22,20], for all practical purposes, the variation of the static friction coefficient μ_s has little influence on the maximum sliding displacement. A Coulomb model with $\mu_s = \mu$ in essence describes rigid-perfectly-plastic behavior. Heavy EC are commonly supported on legs, whose elasticity in conjunction with the Coulomb friction on the contact interface results in an elastic-perfectly-plastic behavior. Validation of this model with shaking table test results was presented in [25,20]. The model was found to capture well the mean response of light EC under a set of ground excitations [22]. An improved prediction of shake table test results can be achieved by taking into account the pressure- and velocity-dependence of μ; however, a sophisticated friction model of that kind is beyond the scope of this study.

The equation of motion of the block in Figure 2-2 is

$$\ddot{u} + \mu\left(\ddot{v}_g + g\right)\ \mathrm{sgn}\left(\dot{u}\right) = -\left(\ddot{u}_g + \ddot{u}_2\right) \tag{2.1}$$

where g is the acceleration of gravity, and $\mathrm{sgn}(\cdot)$ is the *signum* function, which describes the rigid-perfectly-plastic nature of the Coulomb force when $\mu_s = \mu$. If $\dot{u}$ becomes zero, then the block sticks to the floor. The singularity presented by the *signum* function is not amenable to numerical solutions; therefore, the contact interface can be instead described by a rate-independent perfect plasticity model where the yield displacement is set to a very small value.

The earthquake engineering simulation software framework OpenSees [42] is employed to simulate the dynamic system shown in Figure 2-1. The friction mechanism at the interface between the sliding EC and the floor is simulated using the *Flat Slider Bearing Element* (FSBE), developed by Schellenberg [43]. This element is defined by two nodes: one representing the sliding EC and the other the floor. The elastoplastic behavior modeled by the element is depicted in Figure 2-3 (bottom-right), where u_y is the yield displacement, μ is the normalized strength (i.e., friction coefficient), F_f is the friction force, and *N* is the normal force. This model permits any elasticity in the legs to be taken into account by adjusting the value of u_y. While for the same value of μ, the maximum displacement tends to increase with increasing yield displacement [44], it is mainly the value of μ itself that dominates the peak response. Hence, in the current study the yield displacement is taken to be very small ($u_y = 10^{-7}$m), essentially representing a nearly rigid mounting system. To validate the FSBE, results of dynamic simulations in OpenSees using the FSBE were compared with results obtained by directly integrating Equation (2.1) in MATLAB [45], using the available ODE45 solver that utilizes the procedure presented in [46], and also results obtained by implementing Newmark's method in MATLAB with Newton-Raphson iterations. The routine implemented in MATLAB was able to vary the analysis time step to achieve accuracy similar to what is considered in OpenSees. Figure 2-3 shows the sliding response of an EC with $\mu = 0.1$ subjected to the Takatori record of the 1995 Kobe, Japan, earthquake for these three approaches. As it is evident in this example, results obtained using the FSBE in OpenSees are in excellent agreement with results obtained using Newmark's method in MATLAB. Moreover, both methods give a very good estimation compared with the MATLAB

ODE45 solver, which here is considered to be an “exact” solution. The slight discrepancy between the results obtained with the ODE45 solver and other two methods is attributed to the order of the solvers. OpenSees utilizes Newmark’s 2nd-order method to solve the equation, while the ODE45 solver uses fourth and fifth order Runge-Kutta formulas known as the Dormand-Prince pair [45].

The dynamic response of the EC shown in Figure 2-1 is coupled with the dynamic response of the structural model; however, if the mass of the EC is very small compared to the mass of the floor, this interaction is negligible. As investigation of the dynamic interaction between the structure and the EC is beyond the scope of this study, all dynamic simulation results presented herein were obtained with $m_{EC} = m/10^5$. This value was chosen to be small enough to ensure no dynamic interaction, but large enough to avoid any numerical problems in the numerical simulations.

In passing, we note that even though for small values of m_{EC}/m, the analysis could be carried out in a de-coupled manner, in this study a coupled analysis was used for two practical reasons: (i) The OpenSees model was originally created so that we would also be able to investigate the dynamic interaction of structure and EC (not addressed in this paper), and (ii) It was found that the computational effort to conduct the coupled analyses was very comparable to first carrying out an analysis of the BI building and then using the floor motions as input for the EC.

2.2.2 Superstructure

The superstructure above the base isolation system (Figure 2-1) is modeled as a one-story viscously damped linear elastic shear structure. The superstructure has mass m, stiffness k_{fb}, and viscous damping coefficient c_{fb}. In all the analyses presented in this study the period of the superstructure is $T_{fb} = 2\pi\sqrt{m/k_{fb}} = 0.2$ s, and the viscous damping ratio is $\xi_{fb} = c_{fb}/2\sqrt{mk_{fb}} = 0.02$.

2.2.3 Base isolation system

The base isolation system consists of a base floor of mass m_b, which in this study is assumed to be equal to the story mass m, and the seismic isolators. Two idealized types of seismic isolators are considered: (a) viscously damped linear elastic isolators, and (b) bilinear isolators.

2.2.3.1 Viscously damped linear elastic isolation system

This model was used early on to introduce the linear theory of seismic isolation [47] and continues to be used widely, primarily due to its simplicity. The numerical efficiency of this linear model lends itself to large parametric investigations. The model consists of a linear spring of stiffness k_i in parallel with a linear viscous damper of damping coefficient c_i. Utilizing this model, the nominal period T_i and damping ratio ξ_i of the isolated system are given by [47]

$$T_i = 2\pi\sqrt{\frac{m+m_b}{k_i}} \quad , \quad \xi_i = \frac{c_i}{2\sqrt{k_i(m+m_b)}} \tag{2.2}$$

The definition for the nominal fundamental period and damping ratio of the isolated structure, given by Equation (2.2), are based on the premise that in a seismically isolated building, the superstructure moves as a nearly rigid body on a very flexible base. In reality, the fundamental period of the system is slightly larger than the nominal period.

2.2.3.2 Bilinear isolation system

A bilinear model is very commonly used to represent the behavior of a lead plug system (LPS) or a friction pendulum system (FPS), two widely used types of isolation systems. A bilinear model requires three parameters to fully describe it. In this study, the following triad is used: the characteristic strength where the hysteresis loop crosses the *y*-axis, *Q*, the second stiffness, k_2, and the ratio of the second to the initial stiffness, $\beta = k_2/k_1$. In the case of LPS, this ratio is of the order of around 0.1 [48], while for the FPS it is about 0.01.

For the design of a bilinear isolation system, the most common procedure begins with the designer choosing an effective isolation period and viscous damping ratio. These are design parameters that relate the bilinear system to an equivalent viscously damped linear system. Customarily, the effective period is computed from the peak-to-peak stiffness of the bilinear isolation system, which means that it depends on the isolation displacement. An alternative, and convenient, choice is the use of a nominal period for the isolation system, given by

$$T_i = 2\pi\sqrt{\frac{m + m_b}{k_2}} \tag{2.3}$$

which does not depend on the maximum displacement of the isolation system. In this case, the second stiffness of the bearing is considered dominant in determining the period of the isolation system. Makris and Black [44] have demonstrated that the yield displacement (or initial stiffness) has little effect on the response of bilinear oscillators that exhibit large values of ductility. This conclusion is especially applicable to a bilinear isolation system with relatively low characteristic strength, which is expected to experience very large inelastic displacements.

The most common definition of equivalent viscous damping ratio ξ_i comes from equating the energy dissipated in a vibration cycle of the bilinear system and the viscously damped linear system that is forced at a frequency equal to its natural frequency. Unlike the nominal period, the equivalent damping ratio ξ_i cannot be liberated from its dependence on the expected maximum isolation displacement D_{max}. In this study, the mean of the maximum displacements resulting from twenty time-history analyses on the equivalent linear model is assumed to be the target D_{max}. The characteristic strength of the bilinear isolation system can be computed from

$$Q = \frac{1-\beta}{\beta}\frac{2\pi^2}{T_i^2}\left(m + m_b\right)D_{max}\left[1 - \sqrt{1 - 2\pi\xi_i\frac{\beta}{1-\beta}}\right] \tag{2.4}$$

2.3 Selection of ground motions

The focus of this study is the seismic response of sliding EC in BI buildings subjected to broadband earthquake motions. A suite of twenty ground motions was selected randomly from the standardized sets of ground motions provided in Baker et al.

[49]. The standardized ground motion sets in Baker et al. [49] were developed by matching the mean and variance of the logarithmic response spectra of the ground motions to the predicted spectrum for a generic earthquake in California, representative of high seismicity sites in California [49]. The ground motions used in this study, together with selected characteristics, are listed in Table 2-1. More details on these motions can be found in [49]. In this study, the original records from [49] are used without scaling, and the mean of the maximum responses is calculated for comparison purposes. In order to get an idea of the intensity associated with the chosen ground motion set, a comparison between the mean of the acceleration response spectra and design response spectra is made. For this purpose, design response spectra corresponding to a site located in San Francisco, California, are determined based on the seismic maps in ASCE 7 [50]. The 0.2 s and 1.0 s spectral values are $S_s = 1.0$ and $S_1 = 0.5$. It is also assumed that the geotechnical characteristics of the site are compatible with Soil Type C. ASCE 7 code spectra are determined for four seismic hazard levels: (1) Maximum Considered Earthquake (MCE), representing very rare earthquakes with a return period of 2475 years; (2) Design Basis Earthquake (DBE), corresponded to rare earthquakes with a return period of 475 years; (3) Service Level Earthquake (SLE), which represents moderate earthquake events with a return period of 225 years; and (4) weak earthquake with return period of 75 years. These code spectra are shown in Figure 2-4 together with the mean spectrum of the ground motions used in this study. It can be seen that in the period range of interest for BI structures, i.e., 1.5 s to 4.0 s, the mean of the unscaled response spectra is very close to the DBE code spectrum.

2.4 Dynamic analysis procedure

To examine the performance of sliding EC in BI buildings, a series of nonlinear time history analyses were carried out using the model discussed earlier. For simplicity, only the horizontal component of the ground motion is considered at first. The effect of incorporating the vertical component of the ground motion on the sliding response of the EC is presented later in this paper. The engineering demand parameters (EDPs) of interest for the sliding EC in this study are the peak EC sliding displacement and the peak EC absolute acceleration in the horizontal direction.

Firstly, time history analyses were conducted in OpenSees for the FB model with $T_{fb} = 0.2$ s and $\xi_{fb} = 0.02$ subjected to the twenty ground motions listed in Table 2-1. To simulate a wide range of EC-floor frictional resistance, the analyses were conducted for a friction coefficient varying from $\mu = 0.05$, e.g., for portable EC items on casters [34], to $\mu = 0.8$, which can be thought of as an upper limit for sliding EC for all practical purposes; EC with such large values of μ are more prone to rocking and possible overturning, depending also on their width-to-height aspect ratio. For a FB model with a given set of T_{fb}, ξ_{fb} and μ values, the mean of the peak displacements of the EC, $\bar{U}_{fb}$, and the mean of the peak absolute accelerations of the EC, $\bar{A}_{fb}$, over the twenty motions were computed. Secondly, time history analyses were conducted for the BI model with $T_{fb} = 0.2$ s, $\xi_{fb} = 0.02$, and a wide range of T_i and ξ_i values. The analyses were conducted for μ varying from 0.05 to 0.8, as with the FB model. For a BI model with a given set of T_{fb}, ξ_{fb}, T_i, ξ_i, and μ, the mean of the peak displacements of the EC, $\bar{U}_i$, and the mean of the peak absolute accelerations of the EC, $\bar{A}_i$, were computed. The effectiveness of seismic isolation on the performance of the EC was investigated by comparing the response of the EC in a BI building to the response of the same EC in a fixed-base (FB) building.

To investigate the effect of earthquake intensity on the response of the EC, time history analyses were conducted for ground motions that were scaled by an intensity factor α. In addition, as one of the purposes of this study was to compare the seismic performance of EC in buildings isolated with different base isolation system types, the analyses were carried out for viscously damped linear elastic and bilinear base isolation models.

2.5 Effect of seismic isolation on the performance of sliding equipment and contents

The effectiveness of base isolation on reducing the seismic demand on sliding EC is examined. A parametric study is conducted using the two previously defined seismic isolation systems. The FB structure (which is identical to the superstructure in the BI model) is assumed to have a natural period of 0.2 s and a viscous damping ratio of 2%. A discussion on the effects of various isolation system parameters on the EDPs for the sliding EC follows. In this section, the FB building is assumed elastic; while Section 7 investigates the effect of yielding in the FB building.

2.5.1 Viscously damped linear elastic isolation system

2.5.1.1 Peak sliding displacement demand

The effectiveness of base isolation in reducing the sliding displacements of EC is evaluated by means of the ratio of the mean peak displacement of the EC in the BI structure, $\bar{U}_i$, to the mean peak displacement of the EC in the FB structure, $\bar{U}_{fb}$,

$$\frac{\bar{U}_i}{\bar{U}_{fb}} = \frac{\frac{1}{N}\sum_{j=1}^{N} \text{peak displacement of EC in BI building due to ground motion } j}{\frac{1}{N}\sum_{j=1}^{N} \text{peak displacement of EC in FB building due to ground motion } j} \tag{2.5}$$

where $N = 20$ is the number of ground motions used in this study. Figure 2-5 shows the sliding displacement ratio as a function of nominal isolation period T_i of a viscously damped linear elastic isolation system. Curves for various values of the friction coefficient μ are shown. The graph on the left corresponds to unscaled motions, while the graph on the right corresponds to analysis results obtained for ground motions that were scaled by a factor of $\alpha = 2$.

The dashed line at $\bar{U}_i / \bar{U}_{fb} = 1$ denotes the case when the sliding EC in the seismically isolated and the fixed-base structures experience the same peak sliding displacement. The points above this line indicate that seismically isolating the building results in amplification of EC displacement demand. The figure shows that there are a number of combinations for which seismic isolation results in amplification in sliding displacement. Figure 2-5 (left), which plots the sliding displacement ratio for buildings subjected to unscaled ground motions, shows that EC with friction coefficient less than 0.15 experience larger sliding displacements if the building is isolated than if the building is fixed-base. Under intensified ground motions, $\alpha = 2$, the friction coefficient limit where this occurs is about 0.3, as shown in Figure 2-5 (right). Therefore, in general, amplification in EC sliding displacement response in BI buildings is more likely to occur for either lower friction coefficients or higher intensities.

The amplification of EC sliding displacement response in BI buildings can be explained by examining the solution to the maximum displacement of a sliding mass subjected to pulse ground acceleration. Motivated by Newmark's early solution [51] for the case of rectangular ground acceleration pulse, and using dimensional analysis, Makris and Black [44] and Konstantinidis and Makris [25] exposed that the sliding problem exhibits self-similarity under various pulse excitations. For these pulse excitations, the maximum sliding displacement U_{max} of the mass, expressed as a dimensionless parameter, is a function of the dimensionless strength of the pulse

$$\frac{U_{max}}{a_p T_p^2} = \Phi\left(\frac{a_p}{\mu g}\right) \tag{2.6}$$

where a_p is the pulse acceleration amplitude, and T_p is the duration of the pulse. The function Φ depends on the type of pulse, and it can be obtained either analytically or numerically. Rearranging the closed-form solution presented by Newmark [51] for square acceleration pulse with amplitude a_p and duration T_p, we obtain

$$\frac{U_{max}}{a_p T_p^2} = 2\pi^2\left(\frac{a_p}{\mu g} - 1\right) \tag{2.7}$$

Equation (2.7) shows that the maximum sliding displacement U_{max} scales with the so-called *characteristic length* of the excitation, $L_p = a_p T_p^2$. For an EC item in a BI building, a_p can be thought of as the floor acceleration amplitude (where the floor acceleration is the strongest and induces most of the sliding), while T_p can be thought of as the fundamental period of the BI building (since the building acts as a filter, and the participation of the first mode dominates). Although isolation results in lower values of a_p above the isolation level, compared to the FB building, the vibration period T_p is considerably larger, and since U_{max} scales with the square of T_p, it is possible that U_{max} will be amplified if the building is isolated. In reality, an *a priori* conclusion on which system has larger U_{max} cannot be drawn because the form of the function Φ is not known; any attempt to draw general conclusions is further complicated by the fact that for a random excitation the idea of self-similarity vanishes.

In passing, we note that Figure 2-5 shows that increasing the isolation period does not necessarily lead to an increase in the sliding displacement response of the EC in the BI building. Lastly, the figure confirms the more obvious conclusion that sliding displacements tend to decrease with increasing friction coefficient. Comparing the curves for the two input intensities demonstrates that seismic isolation becomes more efficient for higher friction coefficients.

EC sliding displacements can be controlled through the addition of damping in the isolation system. Figure 2-6 presents the effect of the nominal isolation damping ratio on the sliding displacement ratio. It can be seen that an increase in damping results in a decrease in sliding displacement, although little additional benefit is gained by using very large amounts of damping, i.e., more than, say, 20%. However, as this figure shows, providing a minimum damping can be very effective in this respect.

2.5.1.2 Peak absolute acceleration demand

Absolute EC acceleration in the horizontal direction is the other engineering demand parameter of interest in this study. Figure 2-7 (left) plots the mean of the maximum absolute acceleration response for different T_i and μ. The figure clearly shows that utilizing seismic isolation dramatically decreases the absolute acceleration response of the EC, especially for large μ. Figure 2-7 (right) illustrates the effect of isolation damping on the EC absolute acceleration. Increasing the isolation damping clearly results in decreased EC acceleration response. However, as for sliding displacement, the addition of very large amounts of damping has little extra benefit in controlling the EC accelerations. As can be seen in Figure 7 (right), the EC maximum acceleration response saturates for damping ratios greater than 25%. Lastly, the figure shows that the effectiveness of damping in controlling EC accelerations depends on μ .

2.5.2 Bilinear isolation system

This section compares the response of EC in FB and BI buildings, when the isolation system is described by a bilinear model. For designing the system, the target displacement of the bilinear isolation system, D_{max} , is taken to be the mean of the peak isolation displacements resulting from the selected ground motions (Table 2-1) using an equivalent viscous linear model. Given D_{max} , the characteristic strength of the isolation system corresponding to equivalent isolation damping ratio ξ_i is calculated using Equation (2.4). A stiffness ratio $\beta = 0.1$ is assumed.

2.5.2.1 Peak sliding displacement demand

Figure 2-8 plots the sliding displacement ratio as a function of T_i for unscaled motions (left) and scaled motions with $\alpha = 2$ (right). As in the case of a linear elastic isolation system, amplification of the EC sliding displacement response is evident in many combinations of the bilinear isolation system parameters. The figure suggests that there is a minimum amount of μ (≈0.2) necessary to render isolation effective in reducing the EC sliding displacement demands, compared to the FB structure. Figure 2-8 shows no discernible trend in sliding displacement response with isolation period. The graph on the right indicates that under stronger excitation, greater value of friction coefficient ($\mu > 0.4$) is required to render isolation effective.

The effect of isolation equivalent damping ratio ξ_i on the sliding displacement ratio is presented in Figure 2-9. Similar to the case of linear elastic isolation system described in the previous section, increasing isolation damping in the bilinear isolation system results in a decrease in sliding displacement ratio, but very large amounts of damping offer little extra benefit. Furthermore, the figure shows that damping in the isolation system is more effective for larger values of μ.

2.5.2.2 Peak absolute acceleration demand

Figure 2-10 (left) plots the mean of the computed maximum absolute horizontal accelerations of the EC for different T_i and μ. It is obvious from the graph that the absolute acceleration response of EC is dramatically reduced in the BI structure, compared to the FB one, especially for large μ. Figure 2-10 (right) presents the effect of isolation damping on the absolute EC acceleration. Contrary to the case of the viscously damped linear elastic system, for the bilinear isolation system, an increase in ξ_i leads to an increase in absolute acceleration response. According to Equation (2.4), equivalent damping increases by increasing the characteristic strength of the isolation system, *Q*. The greater *Q*, the higher the transmitted inertia force and consequently absolute acceleration response. However, as can be seen in the figure, curves corresponding to different damping ratios are relatively close to each other and varying ξ_i has no pronounced effect on the absolute acceleration response, especially when μ is small. The adverse effects of *Q* on the response of attached vibrating equipment in BI structures have been discussed in [31].

2.5.3 Effect of the isolation system type on the performance of sliding EC

The previous two sections presented results of the parametric study using a viscously damped linear elastic isolation system and a bilinear isolation system. In this section, the seismic response of the two systems is compared. This comparison is facilitated through the use of an *Equivalent* viscously damped linear isolation system. The bilinear isolation system is referred to as *Hysteretic*. Figure 2-11 presents the computed EDPs of interest for EC inside BI buildings with Equivalent and Hysteretic isolation types. The results are presented for unscaled ground motions. Figure 2-11 (left) shows the maximum sliding displacement of the EC as a function of μ for different T_i values. It can be seen that in all cases the EC inside the hysteretic BI building exhibit greater sliding displacements compared to the EC inside the equivalent linear BI building. In terms of maximum absolute accelerations, Figure 2-11 (right) shows that demands on EC inside the hysteretic system are substantially higher. This suggests that the sliding displacement and absolute acceleration demands on EC in a BI building that features bilinear isolators (e.g., LPS or FPS) are higher than in a building that features equivalent linear isolators with viscous damping (e.g., bearings made with carbon-black filled natural rubber).

2.6 Effect of vertical component of base excitation

The analyses results presented up to this point considered only the horizontal component of the ground motions. This section discusses the effect of including the vertical component of the earthquake excitation on the response of EC. For this purpose, the EDPs of interest are re-computed under simultaneous horizontal and vertical excitation. The flexibilities of the isolators, the columns, and the slabs in the vertical direction are neglected in this analysis. In reality these components are not rigid (although they are quite stiff), and although most previous experimental studies [52–54] have found that the effect of vertical excitation on the response of base isolated buildings is negligible, some recent experimental studies [35,55] have reported that in certain cases there is response amplification that is not negligible. Dao and Ryan [56] noted a vertical-horizontal mode coupling, whereby the vertical component of the ground excitation affects the horizontal response of the structure. A sophisticated structural model that takes into account the vertical flexibility of the structure (such as in [56]) is beyond the scope of the present study. Under the assumption of a vertically rigid structure, the EC at the floor level experiences the same vertical acceleration as the ground.

Figure 2-12 plots the mean of the maximum absolute horizontal EC acceleration, with and without the vertical component of the excitation considered. The graph on the left, which corresponds to unscaled motions, shows that the response is larger when the vertical component of the excitation is included. This effect is more pronounced for lower values of μ. With reference to Equation (2.1), the vertical excitation $\ddot{v}_g$ affects the magnitude of the normal force (and thus the friction force) at the contact interface between the EC and the floor, and thus the maximum absolute horizontal acceleration of the EC. The effect of the vertical component becomes more pronounced for the scaled-up ground motions shown in Figure 2-12 (right).

The mean of the maximum horizontal EC sliding displacements is shown in Figure 2-13. The graphs show that the effect of the vertical excitation component on the sliding displacement response is negligible. This observation is also made in Shao and Tung [14]. This is contrary to the findings in [16], which investigated the sliding response of equipment in FB buildings. It is suspected that the amplified response observed in [16] was due to the assumption that the vertical excitation had the same form as the horizontal one, scaled down by a coefficient *k*, i.e., $\ddot{v}_g = k\ddot{u}_g$. Given that vertical ground motions tend to have a lot more high-frequency content than horizontal ones, this assumption might have been unrealistic. The present study finds that the vertical component has little effect on the absolute acceleration and practically no effect on sliding displacement of the EC.

2.7 Effect of structural yielding

While the code permits for some inelastic behavior to occur in the superstructure of a BI building (force-reduction factor *R* up to 2), it is generally accepted that in a well-designed BI building, the superstructure should remain "essentially elastic." Vassiliou et al. [57] examined the effect of superstructure yielding in BI buildings and recommended against permitting any inelastic behavior in the superstructure since that can result in large ductility demands. Modern FB structures, on the other hand, are expected to yield and deform well into the inelastic range. For these structures, depending on the type of lateral force resisting system, the code currently allows a force-reduction factor up to 8.

This section compares the response of EC in FB buildings that are allowed to yield and deform inelastically and BI buildings in which the superstructure is designed to remain elastic. Only the horizontal component of the ground excitation is considered in this comparison. The isolation system is modeled as viscously damped linear elastic. The FB structure is assumed to behave as an elastic-perfectly-plastic system with strength $f_y = \bar{f}_e / \sqrt{2\bar{\mu}_d - 1}$, where $\bar{f}_e$ is the average peak elastic force value over the 20 ground motions, and $\bar{\mu}_d$ is the target displacement ductility ($= 2, 4, 6, \text{and } 8$). As $T_{fb} = 0.2$ s, the design is based on the simple R–μ_d relationship for equal-energy rule, proposed by Veletsos and Newmark [58].

Figure 2-14 (top-left) compares the mean peak displacement of the EC with various values of friction coefficient μ in the BI structures with $\xi_i = 0.1$ and different values of T_i and in FB structures with different $\bar{\mu}_d$. It can be seen that for FB structures, as $\bar{\mu}_d$ increases, the combination of decreased strength and elongated effective period results in reduced sliding displacement demands on EC. Also, it can be seen that EC with $\mu = 0.1$ experience larger displacements in BI structures, for any T_i, than in FB structures, regardless of $\bar{\mu}_d$. As μ is increased to 0.2, EC in the elastic FB structure experience larger displacements than in any of the BI structures, but as $\bar{\mu}_d$ of the inelastic FB systems is increased, the EC sliding displacements become smaller than in the BI structures. The graph confirms the earlier observation that EC with small values of μ can exhibit larger sliding displacement demands in BI buildings than in FB buildings. For larger values of μ the sliding displacement is negligible in both the BI and inelastic FB buildings. Figure 2-14 (top-right) shows the same response quantities but for $\xi_i = 0.2$. The demands on EC in the BI structures is decreased compared to the graph on the left, and for the case of $\mu = 0.1$, EC in the inelastic FB buildings may experience larger or smaller displacements than in the BI buildings, depending on T_i. For $\mu \geq 0.2$, the displacement demands on EC are either lower in the BI buildings, or negligible in both BI and FB buildings.

Figure 2-14 (bottom) shows the average peak absolute acceleration of EC in the elastic and inelastic FB buildings and in BI buildings with $\xi_i = 0.1$ (left) and $\xi_i = 0.2$ (right). The EC acceleration demand in FB buildings is not affected by $\bar{\mu}_d$ for lower values of friction coefficient ($\mu \leq 0.2$), whereas for larger values of μ the demand decreases with increasing $\bar{\mu}_d$. In all cases, the EC accelerations in the BI buildings are lower than those in the FB buildings.

2.8 Incremental dynamic analysis

As noted earlier, there are situations where EC experience amplified displacement response when placed inside BI buildings, compared to FB buildings. Amplification in sliding displacement was observed for lower values of the friction coefficient μ and for scale intensity α=2. This section investigates in more detail the effect of earthquake intensity on the sliding response of the EC through incremental dynamic analysis (IDA) [59]. Although multiplication of a real ground motion by a scale factor α does not necessarily result in a physically realizable earthquake motion, it facilitates a better understanding of the behavior of non-linear dynamical systems over a range of intensities. The analyses are carried out using a viscously damped linear elastic isolation system. The only source of nonlinearity in the response originates from the frictional behavior of the EC-floor interface.

Figure 2-15 (left) shows the mean of the maximum sliding displacements, $\bar{U}_i$, as a function of the intensity scale factor α. In order to demonstrate the correlation of α to μ, the relation between these two parameters is presented for maximum sliding displacement contours in Figure 2-15 (right). It can be seen that for a given maximum sliding displacement, μ varies almost linearly with α. This means that each of these parameters does not represent the severity of the sliding response independently. Thus, introducing a ratio that includes components of both earthquake intensity and friction coefficient is a better measure of intensity for sliding EC.

2.9 Regression and fragility analysis

An EC item inside a structure is subjected to absolute floor acceleration. For a BI building like the one shown in Figure 2-1, with $m = m_b$, $T_{fb} = 0.2$ s, and $T_i = 2$ s, the effective modal mass of the fundamental mode [47,60] is 1.00, and since the fundamental mode is $\phi_1 = [1, 0.01]^{\mathrm{T}}$, it is reasonable to treat the superstructure as a rigid structure supported on a very flexible base, thus reducing the BI structure to a single degree of freedom system. The peak absolute floor acceleration can be approximated by the pseudo-acceleration $S_a(T_i,\xi_i)$. Based on the previous discussion on dimensional analysis and Newmark's solution for a square pulse [51], i.e., Equation (2.7), together with the conclusions of the IDA section, the IM should be a ratio that contains parameters of both shaking intensity, $S_a(T_i,\xi_i)$, and friction coefficient μ. Motivated by the form of the IM presented in [25], in conjunction with the above observations, and after several considerations for a possible IM, the following dimensionless IM is found to be appropriate for sliding EC in seismically isolated buildings

$$IM_i = \frac{S_a\left(T_i,\xi_i\right)}{\mu g} - 1 \tag{2.8}$$

The condition for sliding to occur is $S_a(T_i,\xi_i)/\mu_s g > 1$, and since generally $\mu_s > \mu$, it is possible for sliding to occur even for negative values of the IM. However, as mentioned earlier, the maximum sliding displacement is much more sensitive to the kinetic friction coefficient μ than the static friction coefficient μ_s. Therefore, Equation (2.8) for the IM features μ, not μ_s. The chosen dimensionless EDP for displacement, also motivated by the form of Equation (2.6) and [25], is

$$\Delta_i = 4\pi^2 \frac{U_i}{S_a\left(T_i,\xi_i\right)T_i^2} = \frac{U_i\omega_i^2}{S_a\left(\omega_i,\xi_i\right)} \tag{2.9}$$

where $\omega_i = 2\pi / T_i$.

2.9.1 The EDP as a lognormally distributed random variable; regression analysis

Figure 2-16 (left) plots Δ_i as a function of IM_i for the assumed ground motion set and various combinations of μ (from 0.05 to 0.8), T_i (from 1.5 to 4.0 s), and ξ_i (from 0.05 to 0.2). It is obvious that the data exhibits considerable scatter, which suggests that Δ_i should be treated as a random variable. When a random variable, Δ_i, expresses a quantity that is only positive ($\delta > 0$), it is common to assume that the variable is lognormally distributed. A lognormal distribution has been found to be compatible with a variety of structural as well as nonstructural component failure data [61]. In this study, we hypothesize that the EDP is lognormally distributed, and we test this hypothesis against the results of the numerical simulations. The reason behind the name lognormal is that the lognormally distributed variable Δ_i is related to a normally distributed variable X by $X = \ln\Delta_i$. Note that Δ_i attains only positive values, $\delta > 0$, while the corresponding X variable is unrestricted, $-\infty < x < \infty$. Figure 2-16 (left) shows that the scatter increases with increasing IM_i (*funneling effect*), i.e., the variance is non-constant. However, Figure 2-16 (right) shows that the logarithmic transformation of the data stabilizes the variance, and therefore ordinary least squares can be used to compute the variance. Figure 2-16 (right) shows that $X = \ln\Delta_i$ exhibits a quadratic trend as a function of $\ln(IM_i)$. Therefore, Δ_i can be expressed as a function of the independent variable IM_i through

$$\ln\left(\Delta_i\right) = a\left(\ln IM_i\right)^2 + b\left(\ln IM_i\right) + c + \ln Z \tag{2.10}$$

where *a*, *b*, and *c*, are regression parameters and *Z* is a lognormally distributed random variable (thus $\ln Z$ is normally distributed) which represents the dispersion of the data about the mean. Equation (2.10) without the $\ln Z$ term represents the mean of $X = \ln\Delta_i$ as a function of IM_i. In statistics, there are several measures for the central tendency of a probability distribution besides the arithmetic mean. A commonly used one is the trimmed-mean, especially for determining the central tendency of Cauchy and normal distributions. The trimmed-mean provides an estimate of the central tendency of a distribution by neglecting a percentage of the uppermost and lowermost data as outliers [62–64]. Ignoring the tails of such symmetric bell-shape distributions results in a better estimate of their central tendency. In this respect, one may find alternative methods, such as Robust-Regression, which considers lower weight for outliers, to determine the regression parameters. In this study, a 1.5% trimmed-mean is used to determine the regression parameters of the model. The resulting values are shown in Figure 2-16 (right).

In order to test the hypothesis that Δ_i is lognormally distributed (or, that $\ln\Delta_i$ is normally distributed), the Kolmogorov-Smirnov (K-S) goodness-of-fit test [65] was performed. This test compares the largest difference between the empirical cumulative distribution function (ECDF), obtained from numerical simulation results, and the cumulative distribution function (CDF) of the hypothesized distribution to a critical value which depends on the sample size. Figure 2-17 (left) compares the ECDF and CDF. Using the K-S test, the null hypothesis that the transformed data has a normal distribution could not be rejected at the 5% significance level. Therefore, fragility functions derived from this model can be considered reliable for design purposes [61].

2.9.2 Fragility curves

Fragility is broadly defined as a conditional probability of failure. For the problem at hand, where we want to characterize the sliding response of EC in probabilistic terms, we define fragility as the probability P_{f} that the EDP, Δ_i, for an EC item will exceed a certain threshold (capacity) limit, *c*, given the IM_i. Therefore,

$$P_{\mathrm{f}} \equiv P\left(\Delta_i > c \mid IM_i\right) = 1 - P\left(\Delta_i < c \mid IM_i\right) = 1 - F_{\Delta_i}\left(\delta = c\right) \tag{2.11}$$

where F_{Δ_i} is the CDF of lognormally distributed random variable Δ_i. Using the substitution $\eta = (\ln\delta' - m_X)/\sigma_X$, in the definition of the CDF for Δ_i gives

$$F_{\Delta_i}\left(\delta\right) = \int_0^{\delta} \frac{1}{\sqrt{2\pi}\sigma_X \delta'} e^{-\frac{1}{2}\left(\frac{\ln\delta' - m_X}{\sigma_X}\right)^2} \mathrm{d}\delta' = \int_{-\infty}^{(\ln\delta - m_X)/\sigma_X} \frac{1}{\sqrt{2\pi}} e^{-\frac{\eta^2}{2}} \mathrm{d}\eta = \Phi\left(\frac{\ln\delta - m_X}{\sigma_X}\right) \tag{2.12}$$

where the two defining parameters m_X and σ_X of the distribution are in fact the mean and standard deviation of the corresponding normally distributed variable *X*, and Φ is the CDF of a standard normal variable (i.e., mean zero and standard deviation of 1). Note that m_X is the fitted curve in Figure 2-16 (right), represented as a quadratic function of $\ln IM_i$. The standard deviation of *X*, σ_X, can be obtained from

$$\sigma_X = \sigma_{\ln\Delta_i} = \sqrt{\frac{1}{n}\sum_{j=1}^{n}\left[\ln\delta_j - m_X(\ln IM_{i_j})\right]^2} \tag{2.13}$$

where n is the sample size, here $n = 1367$. Evaluation of Equation (2.13) gives $\sigma_X = 0.46$, and with $m_X = m_X(\ln IM_i)$ as shown in Figure 2-16 (right), the fragility curves can be generated using Equations (2.11) and (2.13) for different capacities *c*. Figure 2-17 (right) shows fragility curves for five values of *c* (0.25, 0.5, 1.0, 2.0, and 3.0).

Given a family of such fragility curves, a practicing engineer who wants to evaluate the probability that an EC item in a BI building will not exceed a threshold displacement could proceed as follows.

2.9.3 Example: how to use the fragility curves

Suppose that a practicing engineer is concerned that stocky table-top equipment in a base-isolated research facility may fall off a table edge, which would occur if $U_i = 20\,\text{cm}$. It is assumed that the kinetic friction coefficient of the contact surface is $\mu = 0.15$. The table is assumed to be fairly rigid and fixed to the floor. If the table is not rigid, and it is in a FB building, the dynamic interaction between table and equipment can affect the sliding response of the table-top equipment because the natural frequency of a regular laboratory table, e.g., 10 Hz~15 Hz [22], is comparable to the natural frequency of the FB building. However, for the target laboratory, which is assumed to be a low-rise building isolated with a viscously damped linear isolation system, the period is $T_i = 2.5\,\text{s}$, i.e., far away from the table's natural frequency. It should be noted that for the case of a bilinear isolation system, one should be cautious about resonance effects under weaker ground shaking since the isolation system oscillates primarily in the pre-yield regime where the initial stiffness is high [31]. The equivalent viscous damping in the isolation is assumed to be $\xi_i = 0.2$. The MCE response spectrum for $\xi = 0.05$ is given. Let us assume that $S_a\left(T_i = 2.5\,\text{s},\ \xi = 0.05\right) = 0.375g$. Then using reduction factors to take into account the isolation damping being different than 5% (e.g., from Table 17.5.1 in ASCE 7 [50]), $S_a\left(T_i = 2.5\,\text{s},\ \xi_i = 0.2\right) = S_a\left(T_i = 2.5\,\text{s},\ \xi = 0.05\right) / B_M = 0.375g / 1.5 = 0.25g$. The intensity measure is estimated as $IM_i = 0.25g/0.15g - 1 = 0.67$, and the dimensionless capacity is $c = 4\pi^2 U_i / S_a\left(T_i, \xi_i\right) T_i^2 = 4\pi^2 \times 0.2\text{m}/(0.25 \times 9.8\text{m/s}^2 \times 2.5^2) = 0.5$. Referring to the generated fragility curve for $c = 0.5$ in Figure 2-17 (right), the probability of exceeding 20 cm sliding displacement, given the IM_i, is $P_\text{f} = P\left(\Delta_i > c = 0.5 \mid IM_i = 0.67\right) = 0.6$. Note that in lieu of fragility curves, this estimate could be obtained from Equation (2.11). If the calculated probability is deemed unsatisfactory, appropriate measures, such as implementation of friction pads or other mitigation strategies, need to be adopted.

2.10 Conclusion

This study investigated the seismic response of sliding equipment and contents (EC) in seismically isolated buildings. The effect of isolation period and damping on the sliding displacement and absolute acceleration of EC with various friction coefficients was investigated using a suite of twenty broad-band ground motions. The effectiveness of seismic isolation on reducing the seismic demand on sliding EC was assessed by comparing the response of the EC inside base-isolated (BI) buildings to the response of the same EC inside corresponding fixed-base (FB) buildings. Two types of BI systems were considered: viscously damped linear elastic, and bilinear. The nonlinear time history analyses were conducted with OpenSees [42] after it was validated by comparing its numerical simulation results to the results obtained from direct integration of the equations of motion in MATLAB [45]. The effect of the vertical component of the ground motion on the response of the EC was examined for a vertically rigid isolation system and superstructure, and it was found that the vertical component has little effect on the maximum absolute acceleration and practically no effect on the maximum sliding displacement of the EC. The effect of structural yielding of the FB structure on the response of EC was also evaluated.

The results of the parametric investigation suggest that seismic isolation is in general an excellent earthquake protection technology for reducing seismic demands on sliding equipment and contents in buildings. However, there are certain situations in which seismic isolation may in fact increase seismic demands on sliding EC, and due caution must be exercised. The most important observations of this study are summarized as follows:

1. Seismic isolation is very effective in reducing the peak sliding displacement of EC, especially for high friction coefficient values. There are, however, cases for which

seismic isolation results in amplification of sliding response, more notably for low friction coefficients and high earthquake intensities.

2. Providing a minimum amount of damping at the isolation level works effectively to decrease the sliding displacements of EC. However, the use of very large amounts of damping in the isolation is not warranted, since it was observed that damping ratios larger than about 20% did not provide any additional benefit.
3. Seismic isolation is very effective in controlling absolute accelerations of sliding EC, in all cases, but especially for EC with large friction coefficients.
4. For a viscously damped linear elastic isolation system, larger isolation damping results in lower EC absolute accelerations, while for a bilinear isolation system, hysteretic damping has an adverse effect on absolute accelerations.
5. The response of EC in yielding FB buildings is affected by the structure's strength. The sliding displacement demands on EC decrease with increasing structural ductility. EC with small friction coefficients (≤0.1) experience larger displacements in BI structures than in FB structures. For larger values of μ the sliding displacement is negligible in both building types. For intermediate values of the friction coefficient, the response of EC in BI buildings may be larger or smaller than in FB buildings, depending on the ductility level of the FB building. In terms of EC acceleration demands, the acceleration demands on EC in FB buildings is not affected by structural ductility for lower values of the friction coefficient (≤0.2), whereas for larger values of the friction coefficient, the demand decreases with increasing ductility. In all cases, the EC accelerations in the BI buildings are lower than those in the FB buildings.

In an effort to estimate sliding displacements of EC in BI buildings subjected to broadband ground motions, the study identified a new, physically motivated, dimensionless intensity measure, and corresponding engineering demand parameter. The EDP was treated as a lognormally distributed random variable, and its distribution parameters were estimated from nonlinear regression analysis. Design fragility curves were generated for different capacity threshold values. Finally, an example was presented to illustrate how the fragility curves could be used in practice.

In this study, the behavior of the EC was assumed to be rigid-perfectly-plastic. There remains a need to investigate the response of EC models that exhibit more complex behavior, including elasticity of the EC and the stick-slip phenomenon along the contact interface. Furthermore, while the present study focused on broadband ground motions, preliminary investigations by the authors [40] have shown that the kinematic characteristics of the ground motion can have a significant effect on the response of EC in BI buildings. The authors are currently investigating the response of EC in BI buildings subjected to pulse-like ground motions, and their findings will be presented in a future publication.

2.11 References

1. Kircher CA. It makes dollars and sense to improve nonstructural system performance. Proc. *ATC 29-2 Seminar on Seismic Design, Performance and Retrofit of Nonstructural Components in Critical Facilities, Applied Technology Council,* Newport Beach, CA, 2003.
2. Taghavi S, Miranda E. Response assessment of nonstructural building elements. *Report No. PEER-2003/05*, Pacific Earthquake Engineering Research Center, University of California, Berkeley, 2003.
3. Comerio MC. PEER testbed study on a laboratory building: exercising seismic performance assessment. *Report No. PEER-2005/12*, Pacific Earthquake Engineering Research Center, University of California, Berkeley, 2005.
4. Fierro EA, Miranda E, Perry CL, Lynn AC, Reitherman R. Behavior of nonstructural components in recent earthquakes. Proc. *2011 Architectural Engineering National Conference*, Oakland, CA, 2011.
5. Boroschek RL. Seismic vulnerability of the healthcare system in El Salvador and recovery after the 2001 earthquakes. *Special Papers-Geological Society of America* 2004; 375.

6. FEMA E-74. *Reducing the risks of nonstructural earthquake damage – a practical guide*. United States Federal Emergency Management Agency: Washington, DC, 2011.
7. *CSA S832-06 (R2011): Seismic risk reduction of operational and functional components (OFCs) of buildings*. Canadian Standards Association: Mississauga, ON, 2011.
8. Shenton III HW. Criteria for initiation of slide, rock, and slide-rock rigid-body modes. *Journal of Engineering Mechanics (ASCE)* 1996; 122(7):690–693.
9. Housner GW. The behavior of inverted pendulum structures during earthquakes. *Bulletin of the Seismological Society of America* 1963; 53(2):404–417.
10. Yim CK, Chopra AK, Penzien J. Rocking response of rigid blocks to earthquakes. *Earthquake Engineering and Structural Dynamics* 1980; 8(6):565–587.
11. Makris N, Konstantinidis D. The rocking spectrum and the limitations of practical design methodologies. *Earthquake Engineering and Structural Dynamics* 2003; 32(2):265–289.
12. Konstantinidis D, Makris N. Seismic response analysis of multidrum classical columns. *Earthquake Engineering Structural Dynamics* 2005; 34(10):1243–1270.
13. Konstantinidis D, Makris N. The dynamics of a rocking block in three dimensions. Proc. *8th HSTAM (Hellenic Society for Theoretical and Applied Mechanics) International Congress on Mechanics*, Patras, Greece, 2007.
14. Shao Y, Tung C. Seismic response of unanchored bodies. *Earthquake Spectra* 1999; 15(3):523–536.
15. Choi B, Tung CCD. Estimating sliding displacement of an unanchrored body subjected to earthquake. *Earthquake Spectra* 2002; 18(4):601–613.
16. Lopez Garcia D, Soong TT. Sliding fragility of block-type non-structural components. Part 1: unrestrained components. *Earthquake Engineering and Structural Dynamics* 2003; 32(1):111–129.
17. Lopez Garcia D, Soong TT. Sliding fragility of block-type non-structural

components. Part 2: restrained components. *Earthquake Engineering and Structural Dynamics* 2003; 32(1):131–149.

18. Chaudhuri SR, Hutchinson TC. Characterizing frictional behavior for use in predicting the seismic response of unattached equipment. *Soil Dynamics and Earthquake Engineering* 2005; 25:591–604.
19. Hutchinson TC, Chaudhuri SR. Bench-shelf system dynamic characteristics and their effects on equipment and contents. *Earthquake Engineering and Structural Dynamics* 2006; 35(13):1631–1651.
20. Konstantinidis D, Makris N. Experimental and analytical studies on the response of freestanding laboratory equipment to earthquake shaking. *Earthquake Engineering and Structural Dynamics* 2009; 38(6):827–848.
21. Konstantinidis D, Makris N. Experimental and analytical studies on the response of 1/4-scale models of freestanding laboratory equipment subjected to strong earthquake shaking. *Bulletin of Earthquake Engineering* 2010; 8(6):1457–1477.
22. Chaudhuri SR, Hutchinson TC. Fragility of bench-mounted equipment considering uncertain parameters. *Journal of Structural Engineering* 2006; 132(6):884–898.
23. Comerio MC, Stallmeyer JC. Laboratory equipment: estimating losses and mitigation costs. *Earthquake Spectra* 2003; 19(4):779–797.
24. Comerio MC, Stallmeyer JC. Nonstructural loss estimation:the UC Berkeley case study. *Report No. PEER-2002/01*, Pacific Earthquake Engineering Research Center, University of California, Berkeley, 2002.
25. Konstantinidis D, Makris N. Experimental and analytical studies on the seismic response of freestanding and anchored laboratory equipment. *Report No. PEER-2005/07*, Pacific Earthquake Engineering Research Center, University of California, Berkeley, 2005.
26. Kelly JM, Konstantinidis D. *Mechanics of rubber bearings for seismic and vibration isolation*. Wiley: Chichester, 2011.
27. Kelly JM, Hsiang-Chuan T. Seismic response of light internal equipment in base-

isolated structures. *Earthquake Engineering and Structural Dynamics* 1985; 13(6):711–732.

28. Juhn G, Manolis GD, Constantinou MC, Reinhorn AM. Experimental study of secondary systems in base-isolated structure. *Journal of Structural Engineering (ASCE)* 1992; 118(8):2204–2221.
29. Kelly JM. The role of damping in seismic isolation. *Earthquake Engineering and Structural Dynamics* 1999; 28(1):3–20.
30. Politopoulos I. A review of adverse effects of damping in seismic isolation. *Earthquake Engineering and Structural Dynamics* 2008; 37(3):447–465.
31. Yang TY, Konstantinidis D, Kelly JM. The influence of isolator hysteresis on equipment performance in seismic isolated buildings. *Earthquake Spectra* 2010; 26(1):275–293.
32. Isakovic T, Zevnik J, Fischinge M. Floor response spectra in isolated structures subjected to earthquakes weaker than the design earthquake—Part I: Isolation with high-damping rubber bearings. *Structural Control and Health Monitoring* 2011; 18(6):635–659.
33. Becker TC, Mahin SA. Approximating peak responses in seismically isolated buildings using generalized modal analysis. *Earthquake Engineering and Structural Dynamics* 2013; 42(12):1807–1825.
34. Sato E, Furukawa S, Kakehi A, Nakashima M. Full-scale shaking table test for examination of safety and functionality of base-isolated medical facilities. *Earthquake Engineering and Structural Dynamics* 2011; 40(13):1435–1453.
35. Furukawa S, Sato E, Shi Y, Becker T, Nakashima M. Full-scale shaking table test of a base-isolated medical facility subjected to vertical motions. *Earthquake Engineering and Structural Dynamics* 2013; 42(13):1931–1949.
36. Shi Y, Kurata M, Nakashima M. Disorder and damage of base-isolated medical facilities when subjected to near-fault and long-period ground motions. *Earthquake Engineering and Structural Dynamics* 2014; 43(11):1683–1701.

37. Ryan KL, Dao ND, Sato E, Sasaki T, Okazaki T. Aspects of isolation device behavior observed from full-scale testing of an isolated building at E-Defense. Proc. *Structures Congress*, Chicago, IL, 2012.
38. Soroushian S, Ryan KL, Maragakis M, Wieser J, Sasaki T, Sato E, Okazki T, Tedesco L, Zaghi AE, Mosqueda G, Alarez D. NEES/E-Defense tests: Seismic performance of ceiling/sprinkler piping nonstructural systems in base isolated and fixed base building. Proc. *15th World Conference on Earthquake Engineering*, Lisbon, 2012.
39. Hutchinson TC, Restrepo JI, Conte JP, and Meacham, B. Overview of the building nonstructural components and systems (BNCS) project. Proc. *Structures Congress*, Pittsburgh, PA. 2013.
40. Nikfar F, Konstantinidis D. Sliding response analysis of operational and functional components (OFC) in seismically isolated buildings. Proc. *3rd Specialty Conference on Disaster Prevention and Mitigation, Canadian Society of Civil Engineering (CSCE)*, Montreal, QC, 2013.
41. Konstantinidis D, Nikfar F. Seismic performance of sliding contents in base-isolated buildings. Proc. *10th National Conference in Earthquake Engineering,* Anchorage, AK, 2014.
42. McKenna F, Fenves GL, Scott MH. Open system for earthquake engineering simulation (OpenSees) [Internet]. 2000. http://opensees.berkeley.edu.
43. Schellenberg A, Maffei J, Telleen K, Ward R. Structural analysis and application of wind loads to solar arrays. *Journal of Wind Engineering and Industrial Aerodynamics* 2013; 123(A):261–272.
44. Makris N, Black CJ. Dimensional analysis of rigid-plastic and elastoplastic structures under pulse-type excitations. *Journal of Engineering Mechanics (ASCE)* 2004; 130(9):1006–1018.
45. MATLAB. *High-performance language software for technical computing*. The MathWorks: Natick, MA, 2002.

46. Nikfar F, Konstantinidis D. Solving dynamical systems with path-dependent nonlinearities using MATLAB ODE solvers. Proc. *10th National Conference in Earthquake Engineering, Earthquake Engineering Research Institute*, Anchorage, AK, 2014.
47. Kelly JM. *Earthquake-resistant design with rubber*. 2nd ed. Springer: London, 1997.
48. Skinner RI, Robinson WH, McVerry GH. *An introduction to seismic isolation*. Wiley: Chichester, 1993.
49. Baker JW, Lin T, Shahi SK, Nirmal J. New ground motion selection procedures and selected motions for the PEER transportation research program. *Report No. PEER-2011/03*, Pacific Earthquake Engineering Research Center, University of California, Berkeley, 2011.
50. ASCE/SEI 7-05. *Minimum design loads for buildings and other structures*. American Society of Civil Engineers: Reston , Virginia, 2006.
51. Newmark NM. Effects of earthquakes on dams and embankments. *Géotechnique* 1965; 15:139–160.
52. Clark PW, Kelly JM. Experimental testing of the resilient-friction base isolation system. *Report No. UCB/EERC-90/10*, Earthquake Engineering Research Center, University of California, Berkeley, 1990.
53. Fenz DM, Constantinou MC. Development, implementation and verification of dynamic analysis models for multi-spherical sliding bearings. *Report No. MCEER-08-0018*, Multidisciplinary Center for Earthquake Engineering Research, University at Buffalo, State University of New York, 2008.
54. Morgan TA, Mahin SA. The use of base isolation systems to achieve complex seismic performance objectives. *Report No. PEER 2011-06*, Pacific Earthquake Engineering Research Center, University of California, Berkeley, 2011.
55. Ryan KL, Dao ND, Sato E, Sasaki T, Okazaki T. NEES/E-Defense base-isolation tests: Interaction of horizontal and vertical response. Proc. *15th World Conference on Earthquake Engineering*, Lisbon, 2012.

56. Dao ND, Ryan KL. Computational simulation of a full-scale, fixed-base, and isolated-base steel moment frame building tested at E-Defense. *Journal of Structural Engineering (ASCE)* 2014; 140(8):A4014005.
57. Vassiliou MF, Anastasios T, Stojadinović B. Dynamics of inelastic base-isolated structures subjected to analytical pulse ground motions. *Earthquake Engineering and Structural Dynamics* 2013; 42(14):2043–2060.
58. Veletsos AS, Newmark NM. Effect of inelastic behavior on the response of simple systems to earthquake motions. Proc. *2nd World Conference on Earthquake Engineering*, Tokyo and Kyoto, Japan, 1960.
59. Vamvatsikos D, Cornell CA. Incremental dynamic analysis. *Earthquake Engineering and Structural Dynamics* 2002; 31(3):491–514.
60. Chopra AK. *Dynamics of structures, theory and applications to earthquake engineering*. 4th ed. Prentice Hall: Upper Saddle River, NJ, 2007.
61. Porter K, Kennedy R, Bachman R. Creating fragility functions for performance-based earthquake engineering. *Earthquake Spectra* 2007; 23(2):471–489.
62. Rothenberg T, Fisher FM, Tilanus CB. A note on estimation from a Cauchy sample. *Journal of the American Statistical Association* 1964; 59(306):460–463.
63. Bloch D. A note on the estimation of thelocation parameter of the Cauchy distribution. *Journal of the American Statistical Association* 1966; 61(315):852–855.
64. Prescott P. Selection of trimming proportions for robust adaptive trimmed means. *Journal of the American Statistical Association* 1978; 73(361):133–140.
65. Scheaffer RL, McClave JT. *Probability and statistics for engineers*. Duxbury Press: Belmont, CA, 1995.

Table 2-1: Broadband ground motions used in this study

Record	Earthquake	Station	Magnitude	Distance (km)	Soil Shear Velocity (m/s)
FN-1	Mammoth Lakes, California - 01/1980	Long Valley Dam (Upr L Abut)	6.1	15.5	345
FN-3	Cape Mendocino, California - 1992	Rio Dell Overpass - FF	7.0	14.3	312
FP-5	Kocaeli, Turkey - 1999	Yarimca	7.5	4.8	297
FP-8	Chi-Chi, Taiwan - 1999	NST	7.6	38.4	375
FP-9	Kocaeli, Turkey - 1999	Duzce	7.5	15.4	276
FN-12	Loma Prieta, California - 1989	Gilroy Array #4	6.9	14.3	222
FP-15	Loma Prieta, California - 1989	Fremont - Emerson Court	6.9	39.9	285
FP-16	Chalfant Valley, California - 02/1986	Zack Brothers Ranch	6.2	7.6	271
FN-19	Imperial Valley, California - 06/1979	El Centro Array #4	6.5	7.1	209
FP-21	Landers, California - 1992	Yermo Fire Station	7.3	23.6	354
FN-23	San Fernando, California - 1971	LA - Hollywood Stor FF	6.6	22.8	317
FP-24	N. Palm Springs, California - 1986	Morongo Valley	6.1	12.1	345
FN-25	Loma Prieta, California - 1989	Hollister - South & Pine	6.9	27.9	371
FN-27	Chi-Chi, Taiwan - 1999	CHY025	7.6	19.1	278
FN-28	Imperial Valley, California - 06/1979	Brawley Airport	6.5	10.4	209
FN-30	Duzce, Turkey - 1999	Duzce	7.1	6.6	276
FP-31	Chi-Chi, Taiwan - 1999	TCU061	7.6	17.2	273
FN-32	Loma Prieta, California - 1989	Saratoga - Aloha Ave	6.9	8.5	371
FN-33	Imperial Valley, California - 02/1940	El Centro Array #9	7.0	6.1	213
FP-38	Loma Prieta, California - 1989	Coyote Lake Dam (Downst)	6.9	20.8	295

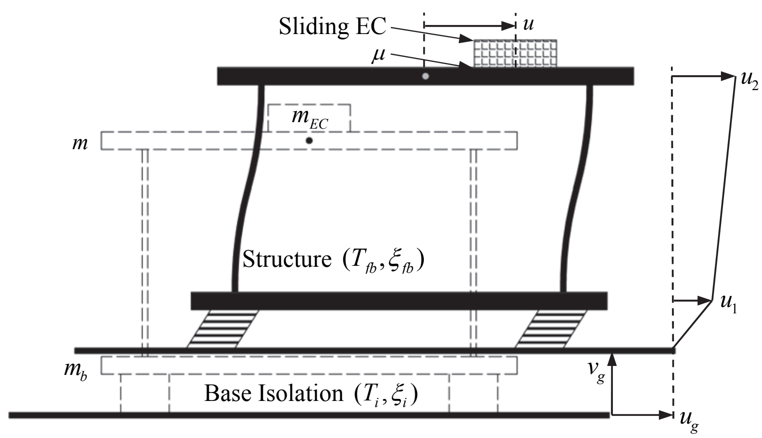

Figure 2-1: Schematic of the model used in this study

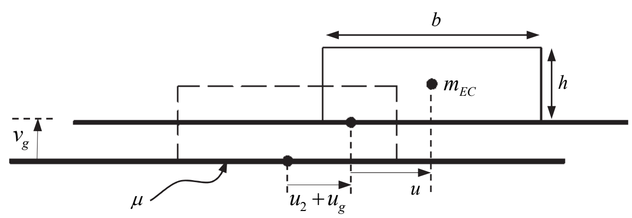

Figure 2-2: Schematic of the sliding EC

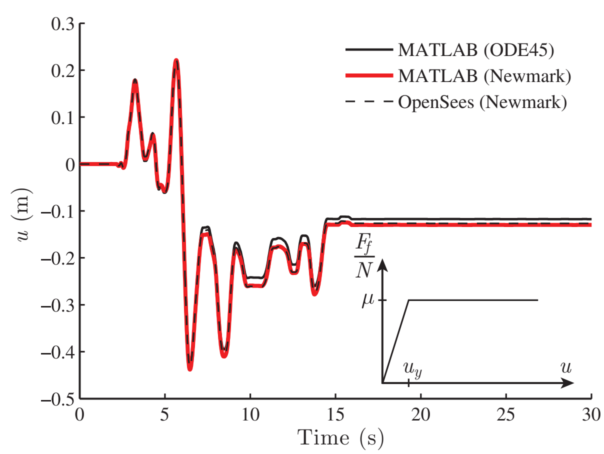

Figure 2-3: Numerical verification of the OpenSees Flat Slider Bearing Element (FSBE) for a sliding object with $\mu = 0.1$ and $u_y = 10^{-7}$ m subjected to the Takatori record of the 1995 Kobe, Japan, earthquake

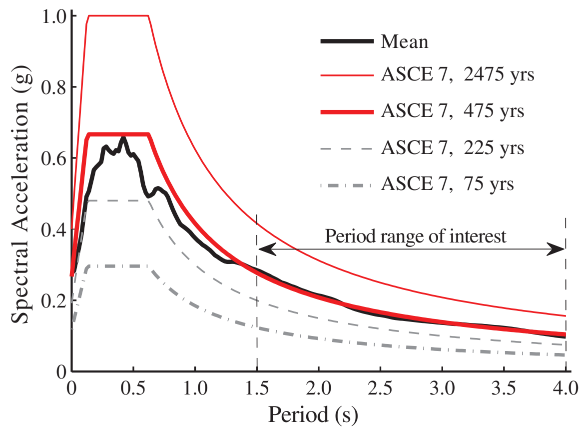

Figure 2-4: Mean acceleration response spectrum (5% damping) of the selected ground motion set together with the ASCE 7 [50] code spectra corresponding to a Soil Type C site in San Francisco

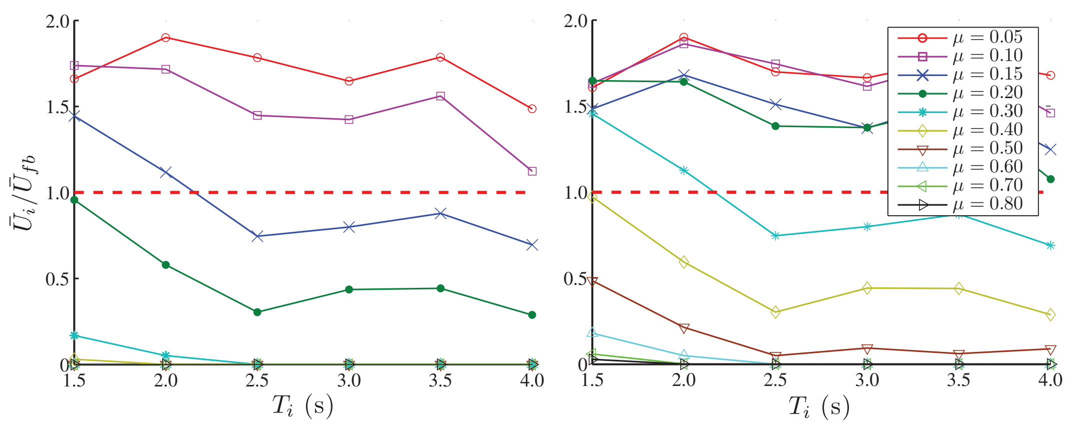

Figure 2-5: Sliding displacement ratio as a function of nominal isolation period for a viscously damped linear elastic isolation system with $\xi_i = 0.1$. *Left*: unscaled records. *Right*: scaled records, $\alpha = 2$

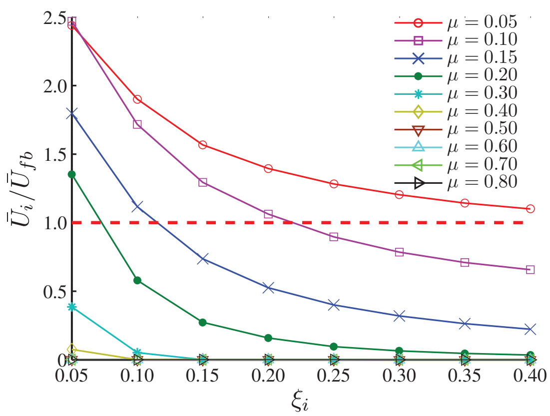

Figure 2-6: Sliding displacement ratio as a function of isolation damping ratio for viscously damped linear elastic isolation system with $T_i = 2\,\text{s}$

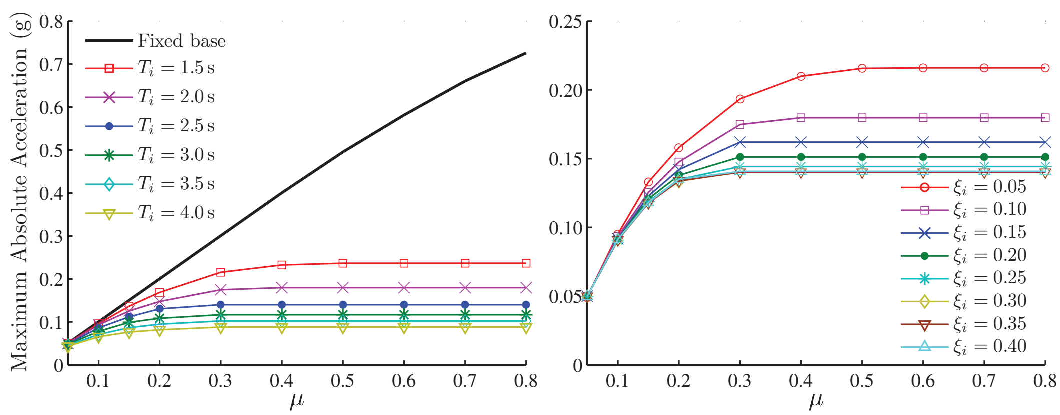

Figure 2-7: Mean of the maximum absolute EC accelerations as a function of friction coefficient for a viscously damped linear elastic isolation system. *Left*: $\xi_i = 0.1$. *Right*: $T_i = 2\,\text{s}$

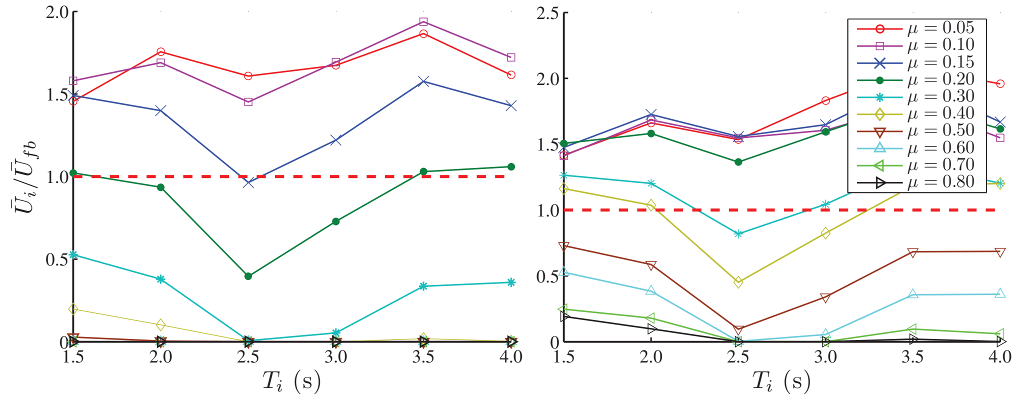

Figure 2-8: Sliding displacement ratio as a function of nominal isolation period for a bilinear isolation system with $\xi_i = 0.1$. *Left*: unscaled records. *Right*: scaled records, $\alpha = 2$

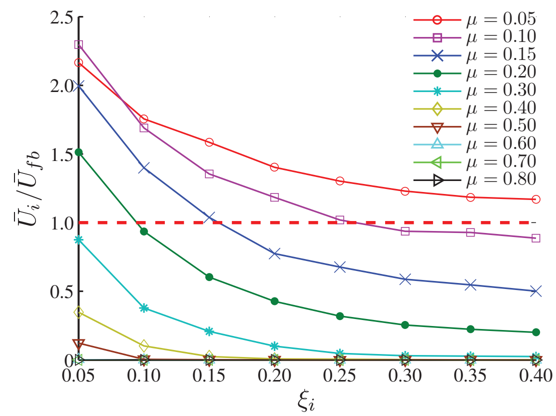

Figure 2-9: Sliding displacement ratio as a function of isolation damping ratio for a bilinear isolation system with $T_i = 2$ s

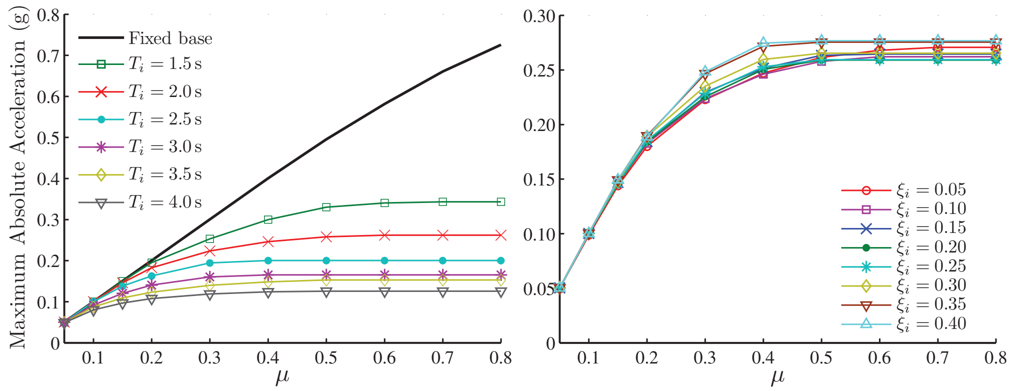

Figure 2-10: Mean of the maximum absolute EC accelerations as a function of friction coefficient for a bilinear isolation system. *Left:* $\xi_i = 0.1$. *Right:* $T_i = 2$ s

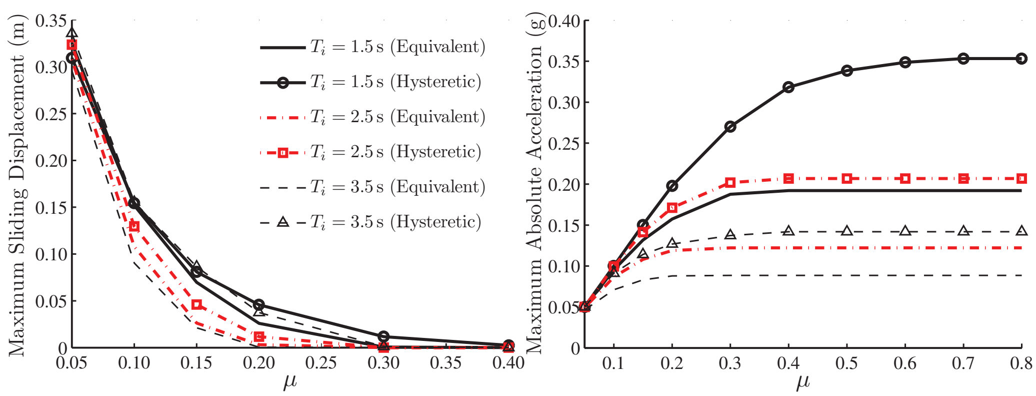

Figure 2-11: Comparison of the EC mean responses in BI buildings equipped with hysteretic and equivalent isolation systems ($\xi_i = 0.2$)

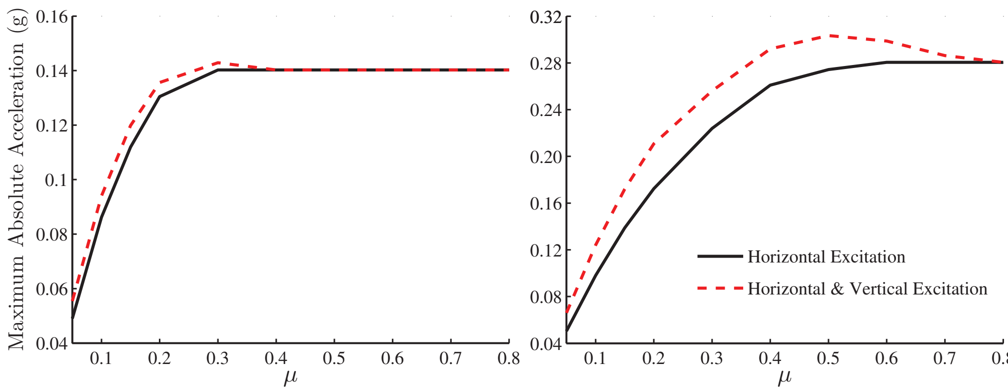

Figure 2-12: Effect of the vertical component of ground motion on the horizontal absolute acceleration of EC in a BI building with $\xi_i = 0.1$ and $T_i = 2.5$s. *Left*: unscaled records. *Right*: scaled records, $\alpha = 2$

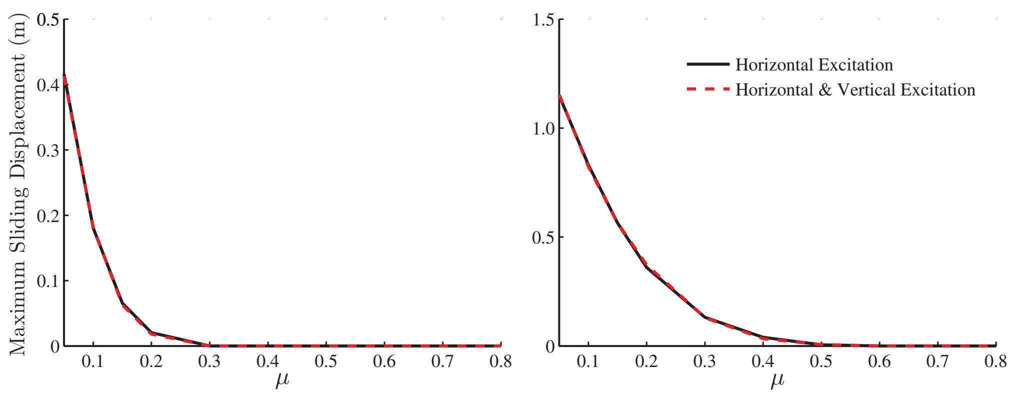

Figure 2-13: Effect of the vertical component of ground motion on the sliding displacement of EC in a BI building with $\xi_i = 0.1$ and $T_i = 2.5$s. *Left*: unscaled records. *Right*: scaled records, $\alpha = 2$

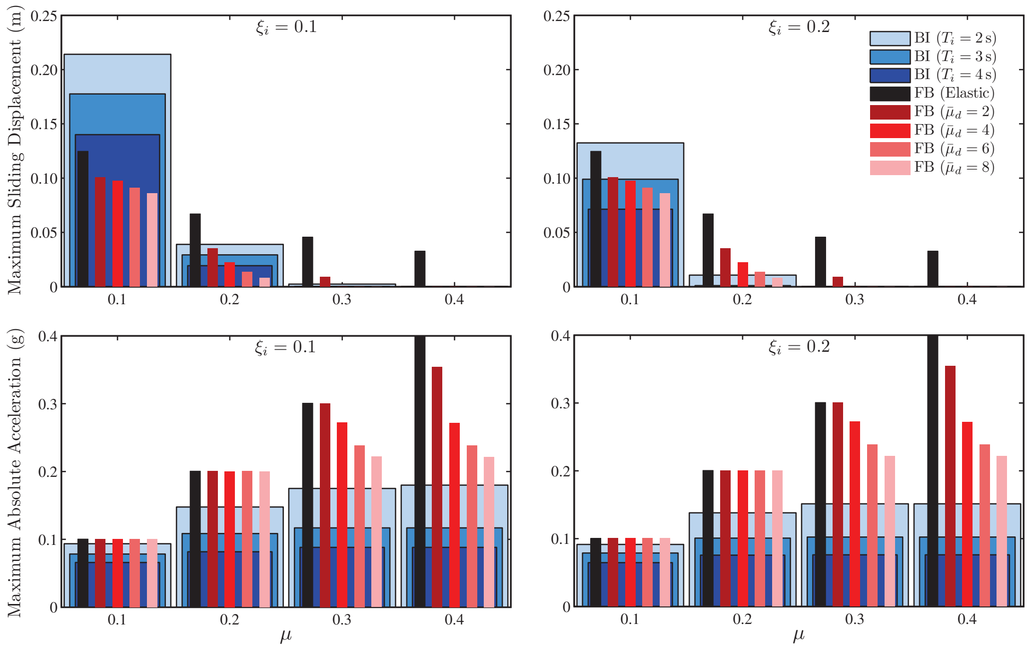

Figure 2-14: Response quantities for EC in BI buildings and in inelastic FB buildings

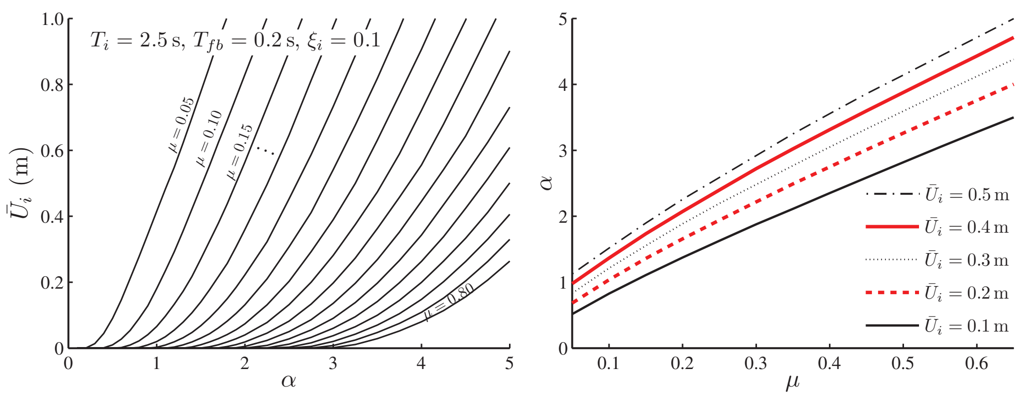

Figure 2-15: IDA curves for different friction coefficient values. Left: Mean of the maximum sliding displacement response as a function of intensity factor. Right: Intensity factor versus friction coefficient

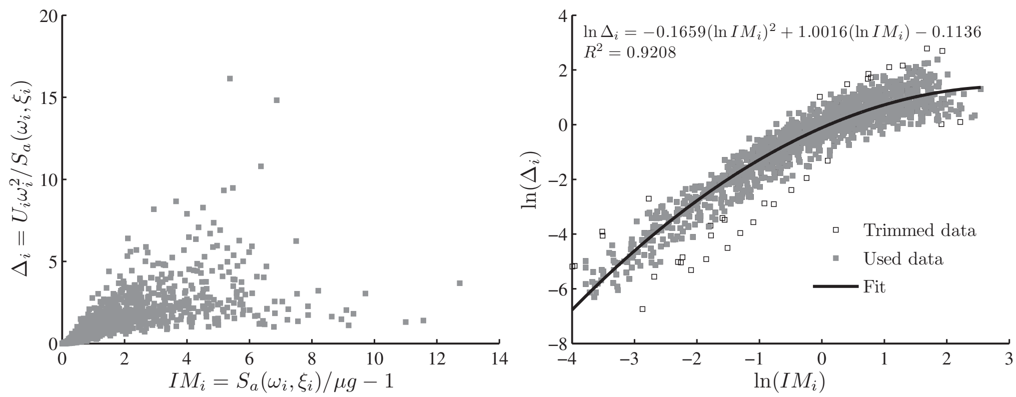

Figure 2-16: *Left*: the EDP as a function of IM. *Right*: the log-log transformation of the EDP and IM together with the regression model that gives the mean of $\ln(\Delta_i)$.

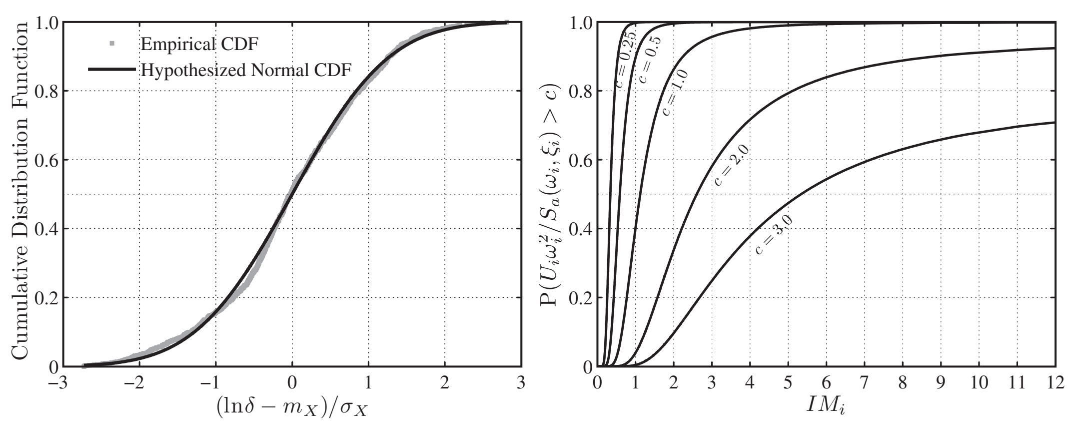

Figure 2-17: *Left*: Comparison of the empirical cumulative distribution function and the cumulative distribution function of the hypothesized normally distributed variable $\ln\Delta_i$. *Right*: Fragility curves for different objective thresholds c

Chapter 3: Peak Sliding Demands on Unanchored Equipment and Contents in Base-Isolated Buildings under Pulse Excitation

F. Nikfar, D. Konstantinidis, Peak Sliding Demands on Unanchored Equipment and Contents in Seismically Isolated Buildings under Pulse Excitation, submitted to *Earthquake Engineering and Structural Dynamics*.

Abstract

Sliding equipment and contents (EC) in buildings is of primary concern during an earthquake because not only can they contribute to substantial nonstructural losses, but also pose a serious safety risk to building occupants. Base isolation is widely considered to be an effective mitigation technique for nonstructural components, but recent research has noted situations, under broadband ground motions, where isolation can in fact amplify the sliding response of EC. This study investigates the sliding response of unanchored EC in base-isolated buildings subjected to analytical pulse excitation representing pulse-like ground motions. The analytical pulse excitation allowed treatment of the problem through dimensional analysis, giving insight into how different parameters affect the response. The EC are idealized as freestanding rigid bodies, and the contact surface between the EC and the floors is described by a Stribeck friction model taking into account the transition from static to kinetic friction. The isolation system is treated as either viscoelastic or bilinear. The study shows that the peak sliding response of rigid objects exhibits complete similarity in the ratio of kinetic-to-static friction coefficient. Therefore, a simple Coulomb model with a single friction coefficient value is adequate for estimating the peak sliding displacement. Moreover, it is observed that as the isolation damping increases, the sliding response exhibits complete similarity in the ratio of isolation-to-pulse period. The study concludes that certain combinations of the isolation design parameters can result in amplification in the peak sliding response of contents, compared to the fixed-base building.

3.1 Introduction

The 1994 Northridge, 2001 Nisqually-Seattle, and many other earthquakes that have struck developed countries in recent years have shown that repair costs and business downtime as a result of damage to nonstructural components and systems (NCS) far exceed those due to structural damage [1]. Losses associated with nonstructural damage are substantially larger primarily for two reasons: the total value of NCS in a typical building dwarfs that of the structure itself (e.g., 4~6 times for a typical commercial building); and damage to NCS initiates at lower seismic intensities than structural damage [2]. The 1994 Northridge, 2010 Chile, and 2011 Christchurch earthquakes confirmed that earthquake damage to NCS can limit or completely disable the functionality of critical facilities even when the structural system performs satisfactorily. The disparity between the performance of structural and nonstructural systems is largely due to the fact that the earthquake engineering community overwhelmingly focused on the design of earthquake-resistant structural systems, while significantly less attention has been given to ensuring the adequate seismic performance of NCS.

A typical building houses a very wide collection of NCS. This study focuses on unanchored building Equipment and Contents (EC) for which sliding is the only mode of response. Sliding is very common for freestanding (i.e., unrestrained) EC, particularly those that are stocky and have a relatively low friction coefficient. Although seismic restraints are typically recommended to prevent sliding of EC, such restraints can be costly. For example, in UC Berkeley buildings that serve primarily as laboratories, the cost of seismic restraining of the EC could range from US$8 to $12 million (US$270 per m^2) [3]. Besides cost, there are also practical limitations associated with restraining EC. Some EC items need to remain mobile [4]. Another problem associated with restrained EC is that they can exhibit significantly larger accelerations compared to freestanding EC [5].

The hazard associated with freestanding sliding EC can stem from any, or a combination, of: (a) excessive sliding displacement, regardless of velocity and acceleration, that can result in the EC falling off the edge of its support surface (if, for example, it is placed on a benchtop), or, in the case of large heavy EC, blocking an egress path or doorway; (b) impact due to large sliding displacement and velocity that can put the safety of the people working in the vicinity of the EC or the functionality of the EC at risk; and (c) large accelerations, particularly in the high frequency range, that can cause resonance and damage to the electronic parts of EC. Therefore, desirable characteristics of earthquake mitigation strategies for EC include reduction in floor acceleration, sliding velocity, and sliding displacement, as well as shifting the floor vibration frequency to frequencies lower than the content resonance frequency. Seismic isolation is widely considered to be the solution of choice for protecting a building's EC. However, while significant research has been conducted on the seismic performance of attached EC in base-isolated buildings, very little research has been conducted on the behaviour of unattached EC in isolated buildings. Nikfar and Konstantinidis [6] carried out a preliminary parametric evaluation of the response of sliding EC in isolated buildings under broad-band and pulse-like ground motions, concluding that the sliding response of EC is considerably different under pulse-like ground motions compared to under broad-band ground motions. Sliding fragility curves for EC in isolated buildings subjected to broad-band ground motions are presented in [7], where it was concluded that there are cases for which isolation resulted in amplification of sliding response, more notably for low friction coefficients and high earthquake intensities.

Past earthquakes have demonstrated that near-fault ground motions are often more destructive than far-field motions. The destructive trait of near-fault ground motions is attributed to a powerful pulse contained in the ground motion [8-10]. In some near-fault records, a coherent pulse is distinguishable not only in the velocity, but also in the acceleration time history. In other cases, the acceleration time history contains random spikes, resembling the ground motions recorded far from the source, but a long-period coherent pulse is evident in their displacement and velocity time histories [11,12]. The presence of low-amplitude, long-period pulses in such ground motions has cast doubts on the effectiveness of seismic isolation technology when the structure is subjected to pulse-like ground motions due to the possible proximity of the pulse frequency to the isolation frequency [10,13,14].

The destructive potential of near-fault ground motions containing coherent pulses has motivated the development of a number of closed-form analytical pulses approximating their leading kinematic characteristics [15]. Vast amount of research is devoted on investigating the characteristics of the pulse including the shape, number of cycles, period, and domain, i.e., velocity or acceleration domain [16,10,13,17,18,19,15,20], among others. Pulse representations of pulse-like ground motions have been very attractive to researchers because they enable the reduction of a complex ground motion to a simple waveform characterized by a handful of parameters for the shape, period, and amplitude of the pulse. This simplification facilitates parametric studies through dimensional analysis of complicated nonlinear structural systems to reveal the physical similarities underlying their response [21-24].

This paper investigates the sliding response of EC in base-isolated buildings under pulse excitations. Closed-form analytical representations of pulse-like ground motions are used together with formal dimensional analysis to explore the existence of physical similarities in the sliding response of EC in base-isolated buildings. Buckingham's Π-theorem is used to introduce dimensionless Π-terms and the corresponding governing dimensionless equation. An advanced friction model (*Stribeck* model) that takes into account the velocity dependence of friction is assumed to describe the contact interface between the EC and their base. The effect of various parameters on the sliding response of the EC is investigated, including the ratio of the isolation period to pulse period, the isolation damping ratio, the ratio of static friction coefficient to kinetic friction coefficient for the EC, parameters associated with velocity-dependent friction, the interaction between the sliding object and the isolated building, and the vertical flexibility of the isolation and superstructure.

3.2 Model of the structure and building equipment/content

3.2.1 Structural model

A seismically isolated building and its sliding EC can be mathematically described by the 3 degree-of-freedom (DOF) system shown in Figure 3-1. In this model, u_s is the displacement of the EC relative to the floor (i.e., the sliding displacement), u_1 is the horizontal displacement of the base slab relative to the ground (i.e., the deformation of the isolators), and u_2 is the horizontal displacement of the story slab relative to the ground. The horizontal and vertical displacements of the ground are represented by u_g and v_g. m_b and m_{st} represent the mass of the base slab and the mass of the story slab, respectively. The base isolation system is modeled as either viscously damped linear elastic or bilinear.

The viscoelastic isolation system was used early on to introduce the linear theory of seismic isolation [25] and continues to be used widely, primarily due to its simplicity. The numerical efficiency of this linear model lends itself to large parametric investigations [26]. The model consists of a linear spring of stiffness k_b in parallel with a linear viscous damper of damping coefficient c_b. The nominal period T_b and damping ratio ξ_b of the isolated system are given by

$$T_b = 2\pi\sqrt{\frac{M_b}{k_b}} \quad , \quad \xi_b = \frac{c_b}{2\sqrt{k_b M_b}} \tag{3.1}$$

where $M_b = m_{st} + m_b$. The nominal fundamental period and damping ratio of the isolated structure, given by Equation (3.1), are based on the premise that in a seismically isolated building, the superstructure moves as a nearly rigid body on a very flexible base. This simplifies the parametric investigations, as the base-isolated building can be approximated by a single-degree-of-freedom system [6]. In the early part of this paper, which focuses primarily on studying the effects of various friction and nominal isolation parameters, the superstructure is assumed to be rigid. Later, the paper also investigates the effect of the superstructure's horizontal flexibility, as well as the flexibilities of the isolation layer and the superstructure in the vertical direction.

The response of sliding EC is also examined under the assumption of a bilinear isolation system, which is commonly used to represent the behavior of a lead plug system (LPS) or a friction pendulum system (FPS). A bilinear model requires three parameters to fully describe it. In this study, the following triad is used: the characteristic strength, where the hysteresis loop crosses the *y*-axis, *Q*, the yielding displacement, u_y, the second stiffness, k_2. Customarily, the effective period of bilinear systems is computed from the peak-to-peak stiffness of the bilinear isolation system, which means that it depends on the isolation displacement. An alternative, and convenient, choice is the use of a nominal period for the isolation system, given by

$$T_b = 2\pi\sqrt{\frac{M_b}{k_2}} \tag{3.2}$$

which does not depend on the maximum displacement of the isolation system. In this case, the second stiffness of the bearing is considered dominant in determining the period of the isolation system. Makris and Black [21] have demonstrated that the yield displacement (or initial stiffness) has little effect on the response of bilinear oscillators that exhibit large values of ductility. This conclusion is especially applicable to a bilinear isolation system with relatively low characteristic strength, which is expected to experience very large inelastic displacements.

3.2.2 Sliding content model

A rigid block of mass m_{EC} is considered to represent the EC, as shown in Figure 3-1. The contact friction is defined using a *Stribeck* friction model that takes into account the rate dependence of friction, as illustrated in Figure 3-2. A Stribeck friction model that takes into account both static, μ_s, and kinetic, μ_k, friction coefficients and the transition between the two expressed by a hyperbolic secant function, as suggested in [27], as well as viscosity at the contact, can be expressed by

$$\mu(\dot{u}_s) = \mu_s \operatorname{sech}(\beta \dot{u}_s) + \mu_k \left[1 - \operatorname{sech}(\beta \dot{u}_s)\right] + \gamma_n \left|\dot{u}_s\right|^n \tag{3.3}$$

where $\dot{u}_s$ represents sliding velocity; constant β defines the transition sharpness from static to kinetic friction; and γ represents viscous characteristics of the contact.

The first two terms of Equation (3.3) account for the smooth transition from static to kinetic friction. The larger β, the sharper the transition, as shown in Figure 3-2. Kinetic friction itself is defined as a velocity-dependent parameter. The last term of Equation (3.3), $\gamma_n |\dot{u}_s|^n$, captures any nonlinear viscous velocity dependence of friction, known as *viscous contact*. This definition is well explained in mechanical engineering literature, specifically for friction between lubricated surfaces. However, the velocity dependence of kinetic friction is not limited to lubricated surfaces and has been observed in dry friction experiments as well. In structural engineering, for example, the velocity dependence of the kinetic friction in sliding bearings has been observed experimentally in several studies [28-35]. These studies usually included cyclic tests at different frequencies, and the value of the kinetic friction coefficient for each experiment was related to the *peak* (amplitude) velocity of that harmonic excitation. Even though this approach does illustrate the velocity dependence of kinetic friction, it does not provide information about the friction coefficient as a function of instantaneous sliding velocity. Depending on the surface characteristics, the actual behaviour may be approximated by a linear or nonlinear function, $\gamma_n \dot{u}_s^n$. In this study, for the sake of simplicity, n is assumed to be equal to unity in Equation (3.3), representing linear viscous damping for the contact. The friction force for the sliding block under horizontal and vertical excitation is defined by

$$F_f = \mu(\dot{u}_s)\mathrm{sgn}(\dot{u}_s) m_{EC}(g + \ddot{y}_2) \quad , \quad \ddot{y}_2 \geq -g \tag{3.4}$$

in which $\mathrm{sgn}(\cdot)$ represents *signum* function and $\ddot{y}_2$ is the absolute floor acceleration in the vertical direction. Equation (3.4) assumes that the block never loses contact with the surface, which is satisfied as long as $\ddot{y}_2 \geq -g$. The equation of motion of the system including the sliding EC, superstructure, and isolation system is constructed in state-space form and solved using MATLAB ODE solvers. A bilinear model with very large initial stiffness is assumed to approximate the signum function in Equation (3.4). The procedure to solve such dynamic systems with path-dependent nonlinearities, i.e., bilinear hysteresis restoring forces, is explained in detail by the authors in [36].

3.3 Dimensional analysis

Dimensional analysis is employed in this section to examine the underlying physics in the sliding of EC in seismically isolated buildings under analytical pulse excitations, as well as to demonstrate the complete- and self-similarities in the sliding response of the EC. The dimensional analysis requires a *length scale* of the ground excitation, which represents the persistence of the excitation in displacing the object [15]. In particular, the length scale, L_p, of the excitation is needed to normalize the peak sliding demand parameter. Voyagaki [37] and Voyagaki et al. [38] showed, in a systematic manner, that there are six possible L_p that can be obtained from the peak acceleration a_p, peak velocity v_p, peak displacement d_p, and period T_p of the pulse, i.e., $L_p = \left(v_p^2 / a_p , a_p T_p^2 , v_p T_p , d_p , v_p d_p / a_p T_p , a_p d_p T_p / v_p \right)$. The first parameter, $L_p = v_p^2 / a_p$, was used in the early studies by Newmark [39] and Newmark and Rosenblueth [40]. The second parameter, $L_p = a_p T_p^2$, was employed by several researchers [41,21,42]. Makris and Black [12] compared the adequacy of a parameter equivalent to $L_p = v_p T_p$, i.e., $L_p = v_p / \omega_p = v_p T_p / 2\pi$, against $L_p = a_p T_p^2$ to represent length scale of pulse-like ground motions. They demonstrated that both linear and nonlinear responses of structural systems scale better with the peak pulse acceleration than the peak pulse velocity, concluding that peak pulse acceleration is a better representative measure of intensity of a pulse [12]. To the best knowledge of the authors, the last three parameters in [37] have not been investigated within the context of nonlinear structural systems. Based on the findings of Makris and Black [12], and since this study deals with the sliding problem, wherein sliding initiation depends merely on the condition that base acceleration overcomes the frictional resistance, $L_p = a_p T_p^2$ is considered as the length scale of the ground pulse excitation. To demonstrate the concept of the length scale of a pulse excitation, assume a sliding rigid block on the ground that is subjected to a rectangular horizontal acceleration pulse, as shown in Figure 3-3(a). Provided that a Coulomb friction force resists the sliding of the block, the early solution presented by Newmark [39] describes the maximum sliding displacement of the block as

$$u_{\max} = \frac{a_p T_p^2}{2}\left(\frac{a_p}{\mu g} - 1\right) \quad , \quad (a_p > \mu g) \tag{3.5}$$

Equation (3.5) shows that $u_{\max}$ is proportional to the length scale $L_p = a_p T_p^2$ and the *intensity* of the pulse, which is represented by the term in parentheses. As shown in Figure 3(c), after expiration of this pulse, the ground moves with constant velocity, eventually resulting in infinite ground displacement. Such a pulse is not physically realizable. In order for a pulse to generate finite ground displacement, the area under the acceleration time history must be zero (i.e., zero mean acceleration); in other words, the final velocity must be zero. In addition, the energy released by earthquake shaking is always finite. Because of these conditions, wavelets are commonly utilized to characterize ground motions with coherent pulses. A wavelet is a waveform (signal), $\varphi(t)$, in time domain that satisfies the finite energy and zero mean conditions, respectively:

$$E = \int_{-\infty}^{\infty} \left|\varphi(t)\right|^2 dt < \infty \tag{3.6}$$

$$\int_{-\infty}^{\infty} \varphi(t) dt = 0 \tag{3.7}$$

In Figure 3-4, the long-period pulse of the RSS228 motion recorded during 1994 Northridge earthquake is approximated using the symmetric Ricker wavelet with effective period of $T_p = 1.0$ s. The symmetric Ricker wavelet is basically the second derivative of the Gaussian distribution, $e^{-t^2/2}$, described by [43]

$$\varphi(t) = a_p\left(1 - \frac{2\pi^2 t^2}{T_p^2}\right) e^{-\frac{1}{2}\frac{2\pi^2 t^2}{T_p^2}} \tag{3.8}$$

where $T_p = 2\pi/\omega_p$ is the effective period corresponding to the peak Fourier spectrum of the wavelet. Analytical pulse excitations such as the Ricker wavelet, if consistent to the coherent pulse, can approximately simulate the kinematics of pulse-like ground motions. The capability of the closed-form analytical pulses to simulate real ground motions for studying structural response has been investigated in [16,10,13,18,21], among others. Various analytical two- and four- parameter pulses have been proposed. In this study, the Ricker wavelet is used in the demonstrations of the dimensionless master curves.

3.3.1 Dimensional analysis for viscoelastic isolation system

Using the model shown in Figure 3-1, under an excitation with coherent pulse acceleration amplitude a_p and period T_p and the assumption of rigid superstructure (i.e. $k_{st} \to \infty$) and a viscoelastic isolation system, and based on Equations (3.3) and (3.5), the maximum sliding displacement of EC, as a dependent variable $u_{\max}$, is expected to be a function of ten independent variables (for each pulse type),

$$u_{\max} = f(a_p, T_p, M_b, T_b, \xi_b, m_{EC}, \mu_s, \mu_k, \beta, \gamma, \text{shape of pulse}) \tag{3.9}$$

In Equation (4.8), the eleven variables, having dimensions $u_{\max} \doteq [L]$, $a_p \doteq [L][T]^{-2}$, $T_p \doteq [T]$, $T_b \doteq [T]$, $M_b \doteq [M]$, $m_{EC} \doteq [M]$, $\xi_b \doteq [\cdot]$, $\mu_s \doteq [\cdot]$, $\mu_k \doteq [\cdot]$, $\beta \doteq [L]^{-1}[T]$ and $\gamma \doteq [L]^{-1}[T]$, involve all three reference dimensions: that of mass $[M]$, length $[L]$ and time $[T]$. Again, at this initial stage, the superstructure is assumed to be rigid relative to the isolation layer. This helps to reduce the number of parameters by two. Also, only the horizontal component of excitation is considered. Based on Buckingham's Π-theorem, the number of independent dimensionless Π-terms is equal to the number of variables in Equation (4.8) (eleven variables) minus the number of reference dimensions (three); leading to eight dimensionless Π-products. Repeated variables should contain the parameters representing the pulse characteristics, i.e., a_p and T_p, together with M_b. Consequently, the dimensionless Π-products considered are

$$\Pi_1 = \frac{u_{\max}}{a_p T_p^2},\ \Pi_2 = \frac{\mu_k g}{a_p},\ \Pi_3 = \frac{T_b}{T_P},\ \Pi_4 = \xi_b$$
$$\Pi_5 = \frac{\mu_k}{\mu_s},\ \Pi_6 = \beta a_p T_p,\ \Pi_7 = \gamma a_p T_p,\ \Pi_8 = \frac{m_{EC}}{M_b} \tag{3.10}$$

Therefore, the resultant dimensionless equation takes the form

$$\frac{u_{\max}}{a_p T_p^2} = \Phi\left(\frac{\mu_k g}{a_p}, \frac{T_b}{T_P}, \xi_b, \frac{\mu_k}{\mu_s}, \beta a_p T, \gamma a_p T_p, \frac{m_{EC}}{M_b}\right) \tag{3.11}$$

where Φ is the function that can be obtained either analytically, if a closed-form solution exists, or numerically, for each pulse type. Reduction in the number of variables by three results in self-similar solutions for Equation (3.11) with respect to the repeated variables chosen. In other words, the dimensionless solutions will be the same for all the values of a_p, T_p and M_b. By expressing the behaviour in terms of dimensionless products, the effects of different parameters on the response can be examined.

3.3.1.1 Effect of the isolation-to-pulse period ratio ($\Pi_3 = T_b/T_P$*)*

$\Pi_3 = T_b/T_P$ is the measure of the relative stiffness of the isolation system. Small values of T_b/T_P (e.g., $T_b/T_P < 0.01$) represent no isolation, while large values represent a large degree of isolation. Figure 3-5 (left) plots the so-called dimensionless master curves for various T_b/T_P values, while other Π -terms are fixed. These curves are presented for 10% isolation damping ($\xi_b = 0.1$). The term master curve refers to the self-similar curves with respect to the repeating variables that in this study are a_p, T_p and M_b. The presented curves are the same for all possible combinations of values of these three parameters. One interesting characteristic of these master curves is that they are independent of the pulse amplitude, a_p [22]. In this context, the vertical axis, $u_{\max}/a_p T_p^2$, represents the dimensionless displacement, and the horizontal axis, $\mu_k g/a_p$, represents the dimensionless frictional resistance. Either $\mu_k/\mu_s = 1$ or $\beta a_p T_p = 0.0$ in these plots eliminates the static phase of friction and therefore denotes the case with Coulomb friction model. Note that 1000 s/m is the maximum value of β used in this study, representing a sudden drop from static to kinetic friction coefficient. Dynamic interaction between the sliding object and the isolation system is avoided by considering a mass ratio as small as $m_{EC}/M_b = 10^{-5}$. Considering the $T_b/T_P = 0.01$ curve to represent a very stiff isolation system, or effectively a fixed-base system, we note that seismic isolation does not necessarily decrease the maximum sliding demand on the EC for all the values of isolation period and EC frictional resistance. Amplification occurs specifically for low friction coefficient values; whereas, as the friction coefficient increases, the sliding demand becomes lower in systems with a higher degree of isolation. The highest amplification is associated with the resonance condition, $T_b = T_p$.

3.3.1.2 Effect of the isolation damping ratio ($\Pi_4 = \xi_b$)

Figure 3-5 (right) demonstrates the effect of isolation damping under the resonance condition, $T_b/T_P = 1.0$, on the sliding of EC. Providing a minimum amount of damping, i.e., 10%, considerably reduces the sliding response. However, the efficiency drops rapidly for damping values grater that 15%. Moreover, the effect of isolation damping in displacement reduction is evident in the resonance condition ($T_b/T_P = 1.0$), shown in Figure 3-5 (right), while it has marginal effect for non-resonance cases.

3.3.1.3 Effect of the kinetic-to-static friction coefficient ratio ($\Pi_5 = \mu_k/\mu_s$)

Π_5 represents the ratio of kinetic to static friction coefficient. $\Pi_5 = 1$ indicates Coulomb friction model (where $\mu_s = \mu_k$), while values lower than unity describe Stribeck friction that itself subsumes the Static+Coulomb friction model when $\beta \to \infty$, leading to a sudden drop from static to kinetic friction. The practical range of μ_k/μ_s changes based on the properties of the problem being investigated. For instance, experimental tests on light science laboratory equipment items [44] showed μ_k/μ_s to range between 0.73 and 1.0, while tests on heavy laboratory equipment [5,45] measured μ_k/μ_s to range between 0.72 and 0.77. Based on those observations, a lower bound value of $\mu_k/\mu_s = 0.5$ is assumed in this study. The dimensionless curves (master curves) demonstrating the effect of μ_k/μ_s ratio on the maximum sliding response are presented in Figure 3-6 for three different isolation-to-pulse period ratios and 10% isolation damping. The dimensionless curves are obtained for $\beta = 1000$ s/m (i.e., $\Pi_6 = 1000 a_p T_p$). Presence of static friction reduces the maximum sliding response for large values of $\mu_k g/a_p$, while it results in amplification for low values of $\mu_k g/a_p$. Therefore, neglecting the static phase of friction, as is done when using the Coulomb friction model, is unconservative when estimating the maximum sliding displacement of contents with low friction coefficient.

This finding may be one of the reasons explaining why the Coulomb friction model underestimated the actual sliding displacements of the heavy laboratory equipment in experimental tests [5,45]. Observations like this highlight the profound advantage of dimensional analysis, which can be used to study the behaviour of a complicated problem by condensing a number of curves in only one master curve. Otherwise, a comprehensive parametric study would be necessary to arrive at such a conclusion. The amplification under the symmetric Ricker wavelet excitation is attributed to the resistance of the system with high static friction to the first pulse of the Ricker wavelet which results in one directional sliding under the major pulse of the excitation (See Figure 3-4-left). In other words, for $\mu_k/\mu_s = 1$, sliding of the EC under the first minor pulse of the Ricker excitation in the negative direction cancels out a portion of the sliding in positive direction under the major pulse of the Ricker wavelet, resulting in smaller maximum sliding displacement. Therefore, even though presence of a static friction increases the overall strength (resistance) of the system, it may result in amplification effects due to the presence of preceding or succeeding pulses close to the major pulse in real earthquake excitations. Such sensitivity in sliding response calls for more accurate estimations of the kinematics of pulse-like ground motions, when analytical pulses are to be used. Moreover, as can be seen in Figure 3-6, there is a similarity in maximum sliding response in the range of sliding equipment tested previously ($0.7 \le \mu_k/\mu_s \le 1.0$). Thus, one may assume that $u_{\max}/a_pT_p^2$ is almost independent of μ_k/μ_s (and consequently $\Pi_6 = \beta a_pT_p$) in that range and simplify the dimensionless sliding equation to:

$$\begin{cases} \dfrac{u_{\max}}{a_pT_p^2} \approx f\left(\dfrac{\mu_k g}{a_p}, \dfrac{T_b}{T_P}, \xi_b, \gamma a_pT_p, \dfrac{m_{EC}}{M_b}\right) & \text{for} \quad 0.7 \le \dfrac{\mu_k}{\mu_s} \le 1.0 \\ \dfrac{u_{\max}}{a_pT_p^2} \approx f\left(\dfrac{\mu_k g}{a_p}, \dfrac{T_b}{T_P}, \xi_b, \dfrac{\mu_k}{\mu_s}, \beta a_pT_p, \gamma a_pT_p, \dfrac{m_{EC}}{M_b}\right) & \text{for} \quad \dfrac{\mu_k}{\mu_s} \le 0.7 \end{cases} \tag{3.12}$$

3.3.1.4 Effect of transition sharpness ($\Pi_6 = \beta a_pT_p$) and viscous contact parameter ($\Pi_7 = \gamma a_pT_p$)

The effect of the transition parameter βa_pT_p on the sliding response is examined by computing the dimensionless curves for $10a_pT_p \le \beta a_pT_p \le 1000a_pT_p$. The master curves are presented in Figure 3-7 (left). The curves are close to each other in the range of interest for this parameter. Consequently, since changing βa_pT_p by two orders of magnitude results in relatively comparable master curves, it can be said that the dimensionless sliding response, $u_{\max}/a_pT_p^2$, exhibits *complete-similarity* in βa_pT_p. Hence, the simplified dimensionless maximum sliding equation described by Equation (3.12) becomes

$$\begin{cases} \dfrac{u_{\max}}{a_pT_p^2} \approx f\left(\dfrac{\mu_k g}{a_p}, \dfrac{T_b}{T_P}, \xi_b, \gamma a_pT_p, \dfrac{m_{EC}}{M_b}\right) & \text{for} \quad 0.7 \le \dfrac{\mu_k}{\mu_s} \le 1.0 \\ \dfrac{u_{\max}}{a_pT_p^2} \approx f\left(\dfrac{\mu_k g}{a_p}, \dfrac{T_b}{T_P}, \xi_b, \dfrac{\mu_k}{\mu_s}, \gamma a_pT_p, \dfrac{m_{EC}}{M_b}\right) & \text{for} \quad \dfrac{\mu_k}{\mu_s} \le 0.7 \end{cases} \tag{3.13}$$

If assuming no viscous damping at the contact, i.e. $\gamma a_pT_p \to 0$, and neglecting the dynamic interaction between the content and isolation system by assuming a very small mass for the EC, i.e. $m_{EC}/M_b \to 0$, the dimensionless sliding displacement, $u_{\max}/a_pT_p^2$, for a massless rigid sliding block is approximately a function of only $\mu_k g/a_p$ in the range observed for sliding EC, i.e., $0.7 \le \mu_k/\mu_s \le 1.0$. Here, the dimensional analysis proved the dominant role of kinetic friction on the maximum sliding response in its general form, which has been observed in previous investigations [39,5,44,46,45,47].

Only a handful of experiments are available for evaluating the velocity dependence of friction in earthquake engineering. One such study [48] included cyclic testing of sliding bridge bearings, which on average exhibited a maximum γ value of about 0.05. In the dimensional analysis of the current study, the upper bound for $\gamma a_p T_p$ is determined by assuming $\gamma_{\max} = 0.1\,\mathrm{s/m}$, $a_{p(\max)} = 2g$, and $T_{\mathrm{p(max)}} = 5\,\mathrm{s}$, resulting in $\Pi_{5(\max)} \approx 10$. Figure 3-7(right) illustrates how $\gamma a_p T_p$ affects the sliding response of EC; the higher the contact damping, the lower the sliding response.

3.3.1.5 Effect of the dynamic interaction between the structure and the EC ($\Pi_8 = m_{EC}/M_b$)

Depending on their friction coefficient and mass, building EC may influence the dynamic response of the building. Heavy EC with high friction coefficient move rigidly with their base, resulting in a longer isolation period. EC with low friction coefficient, which are more prone to sliding, may increase the damping of the system by dissipating energy through friction.

Figure 3-8 shows the effect of the mass ratio on the normalized peak sliding displacement for isolation period ratios of 0.1, 1.0, 3.0, and 4.0. According to this figure, the maximum sliding displacement is not affected by the mass of the EC for $T_b/T_P = 0.1$ which represents either stiff systems or base-isolated buildings under very long-period pulse excitations. At resonance condition, $T_b/T_P = 1.0$, a mass ratio even as high as 20% results in less than 10% increase in the normalized sliding response in the $0.05 < \mu_k g/a_p < 0.45$ range, while the sliding response is completely unaffected for other values of $\mu_k g/a_p$. Considering the plots for $T_b/T_P = 3.0$ and 4.0 representing effective isolation systems, the dynamic interactions appear to have considerable effect on the sliding response of EC. This suggests that dynamic interaction would be a concern for base-isolated buildings subjected to short-period pulses or broad-band ground motions having high frequency excitations. This highlights the possible contribution of short-period acceleration pulses overriding the coherent long-period pulses existing in certain pulse-like ground motions. Recent studies by Vassiliou and Makris [15] and Lu and Panagiotou [20], have characterized these short-period acceleration pulses (i.e., with $0.5 \le T_P \le 1.5$) that Makris and Black [12] earlier claimed to have far more contribution to the response of both elastic and inelastic systems than the coherent long-period pulses distinguishable in the velocity time-history.

3.3.2 Dimensional analysis for bilinear isolation system

The procedure to determine the dimensionless equation in the case of a bilinear isolation system is similar to that of viscoelastic isolation, with the difference that bilinear systems are defined by three parameters (Q, u_y, and k_2), while viscoelastic systems are defined by only two (k_b and c_b). For this system, the maximum sliding displacement of the EC will be a function of eleven independent variables and the shape of the pulse (under the assumption of rigid superstructure),

$$u_{\max} = f(a_p, T_p, M_b, T_b, Q, u_y, m_{EC}, \mu_s, \mu_k, \beta, \gamma, \text{shape of pulse}) \tag{3.14}$$

where the dimensions of the new variables are $u_y \doteq [L]$ and $Q \doteq [M][L][T]^{-2}$. Note that in this case the isolation nominal period is described by Equation (3.2). Again, the Equation (3.14) has all three reference variables involved resulting in nine dimensionless selected Π-terms, selected as follows:

$$\begin{gathered}\Pi_1 = \frac{u_{\max}}{a_p T_p^2}, \Pi_2 = \frac{\mu_k g}{a_p}, \ \Pi_3 = \frac{T_b}{T_P}, \ \Pi_4 = \frac{Q}{M_b a_p}, \ \Pi_5 = \frac{\mu_k}{\mu_s} \\ \Pi_6 = \beta a_p T_p, \ \Pi_7 = \gamma a_p T_p, \ \Pi_8 = \frac{m_{EC}}{M_b}, \ \Pi_9 = \frac{u_y}{a_p T_p^2}\end{gathered} \tag{3.15}$$

and similarly the dimensionless equation becomes

$$\frac{u_{\max}}{a_p T_p^2} = \Phi\left(\frac{\mu_k g}{a_p}, \frac{T_b}{T_P}, \frac{Q}{M_b a_p}, \frac{\mu_k}{\mu_s}, \beta a_p T_p, \gamma a_p T_p, \frac{m_{EC}}{M_b}, \frac{u_y}{a_p T_p^2}\right) \tag{3.16}$$

Assuming a friction pendulum bearing (FPB) system with very small yield displacement $u_y = 0.25$ mm and friction coefficient $\mu_{FPB} = 0.05$, the effect of the isolation period ratio is shown in Figure 3-9. It can be seen that the peak response occurs at the resonance condition where $T_b/T_P = 1.0$. In this plot, the curves were produced for a dimensionless isolation strength of $Q/M_b a_p = \mu_{FPB} g / a_p =$ 0.2. Figure 3-10 shows the effect of $Q/M_b a_p$ on the peak sliding displacement response for the resonance condition (left plot), and when the period ratio is 3.0. As it is evident from the figure, increase in $Q/M_b a_p$ (i.e., hysteretic isolation damping) is very effective in reducing the peak sliding response under the resonance condition, but it leads to an increase in peak sliding displacement demands for EC with higher frictional resistance ($\mu_k g/a_p > 0.1$) for short-period pulses (see the plot for $T_b/T_P = 3.0$). This is due to the fact that increasing the hysteretic damping (through an increase in the isolation system's characteristic strength) allows the isolation layer to transfer larger accelerations to the superstructure. On the contrary, increase in hysteretic damping results in a reduction in isolation peak displacement, leading to a reduction in peak sliding response of EC with low friction coefficient.

Previous works [14,21,24] suggest that the peak displacement response of yielding systems, including buildings with bilinear isolation systems, exhibits complete-similarity with respect to the yielding displacement, i.e., $u_y/a_p T_p^2$. In other words, the peak displacement of the system is insensitive to the exact value of u_y. This is because in base isolation systems, which exhibit large displacement demands ($u_m \gg u_y$), the dissipated energy associated with the yield displacement is negligible compared to total energy dissipated [24]. Similarly, it is expected that this complete similarity extends to the peak sliding response of EC within such buildings.

Figure 3-11 indeed confirms that the dimensionless peak sliding displacement exhibits complete similarity when the dimensionless yield displacement, $u_y/a_p T_p^2$, is varied from 0.0001 to 0.001 for resonance (left) and non-resonance (right) conditions.

The figure shows that there is only a very slight increase in $u_{\max}/a_pT_p^2$ for the entire range of $\mu_k g/a_p$ as $u_y/a_pT_p^2$ increases. However, concerns remain over the effect of the isolation system's u_y when considering the flexibility of the superstructure, which up to this point has been neglected. The effect of the superstructure's lateral flexibility on the sliding response of the EC is investigated in the next section.

3.3.3 Effect of the lateral flexibility of superstructure

When considering the lateral flexibility of the superstructure, proximity of the period associated with the isolation system's initial stiffness with the period of the superstructure, $T_{fb} = 2\pi\sqrt{m_{st} / k_{st}}$, may trigger the participation of the second mode, resulting in increased first-story accelerations [26]. In this case, the complete similarity observed in Figure 3-11 may vanish. To investigate this, dimensionless curves similar to those in Figure 3-11 were produced, but this time including the lateral flexibility of the superstructure. Figure 3-12 shows dimensionless sliding displacement curves for $T_{fb} / T_b = 0.1$ and 0.3 for resonance (top) and non-resonance (bottom) conditions. It can be seen that the sliding response exhibits complete similarity with respect to the isolation's dimensionless yield displacement, $u_y/a_pT_p^2$, even for these representative cases of flexible superstructure. Figure 3-13 presents dimensionless curves for three isolation-to-pulse period ratios, T_b/T_P, and different superstructure-to-isolation period ratios, T_{fb} / T_b. It can be concluded from this figure that the peak sliding displacement is insensitive to the flexibility of the superstructure when T_{fb} / T_b is less than 0.3.

3.3.4 Effect of the vertical component of excitation

The effect of the vertical component of the ground excitation on the performance of building EC is a common concern. As this paper follows a dimensional analysis approach, and since it focuses primarily on the sliding under the coherent pulse of pulse-like ground motions, a pulse identical to the horizontal ground acceleration pulse is assumed as the vertical excitation. Such an assumption, i.e., the coincidence of vertical and horizontal pulses with identical shape, period, and amplitude, may not seem very realistic since the vertical component of pulse-like ground motions may be expected to have a high frequency content. According to Gazetas et al. [23], however, such a coincidence is not so unrealistic due to the inherent characteristics of *P* and *S* waves dominating the ground motion in the vertical and horizontal directions, although exceptions to this rule are not uncommon. Figure 3-14 shows the coincidence of coherent horizontal and vertical pulses contained in the horizontal and vertical components of the Pacoima Dam-Downstream record of the 1994 Northridge earthquake and the TCU-068 and TCU-052 records of the 1999 Chi-Chi earthquake. Considering the Northridge earthquake, the vertical component exhibits a pulse with almost similar shape and duration, but with lower amplitude. Even though high frequency components exist in the record, they are not present during the occurrence of the main pulse. In the case of Chi-Chi TCU068, both the shapes and amplitudes of the horizontal and vertical pulses are comparable. Unlike the Northridge Pacoima Dam record, the presence of high frequency excitation is evident throughout the vertical component of Chi-Chi TCU052, including during the main pulse. In this example, the shape and duration of the vertical pulse is comparable to the horizontal pulse while having lower amplitude.

The vibration of the structure due to the vertical excitation input, $\ddot{v}_g$, affects the vertical floor acceleration and, consequently, the normal force on the EC, $m_{EC}(g+\ddot{y}_2)$, which in turn affects the frictional resistance of the sliding objects, as described by Equation (3.4). Note that the flexibility of the structure in the vertical direction, due to the flexibility of isolation bearings, columns, beams, and slabs, can result in amplification in the vertical floor accelerations compared to the vertical ground acceleration. Moreover, the vertical excitation can indirectly affect the horizontal floor response due to a horizontal-vertical coupling that exists in some isolation systems. For instance, a study by Ryan and Dao [49] pointed out that in the case of friction bearings, the vertical ground excitation introduces high-frequency fluctuations in the horizontal force because the frictional force of the isolators is proportional to the normal force which is directly affected by the vertical ground acceleration, which tends to be richer in the higher frequency range for most ground motions. It is likely that this coupling results in transferring the high-frequency vibrations to the superstructure and exciting higher modes [49]. The transfer of high-frequency content vibrations is of concern for attached acceleration-sensitive nonstructural components.

To simplify the parametric study, horizontal-vertical coupling effects of base isolation system are not considered in this study. Annular rubber isolators with a shape factor of S=25 are assumed as the isolation system. Note that typical shape factor for seismic isolation applications is ranging between 20 to 40 [50]. Figure 3-15 shows an annular bearing and provides definitions for various pertinent quantities.

The *pressure solution* predicts the vertical [51,50] and horizontal [50] stiffness of rubber isolators. The horizontal (K_H) and vertical stiffness (K_V) of the bearings can be computed using the following equations [50], where in Equation 3.18 it is assumed that all rubber layers have the same thickness,

$$K_H = \frac{GA}{t_r} \tag{3.17}$$

$$K_V = \frac{E_c A}{t_r} \tag{3.18}$$

where G is shear modulus of rubber, and E_c is the compression modulus of a single rubber layer which, assuming incompressible rubber, is given by

$$E_c = 6GS^2\lambda \tag{3.19}$$

in which

$$\lambda = \frac{b^2 + a^2 - \dfrac{b^2 - a^2}{\ln(\mathrm{b/a})}}{(\mathrm{b-a})^2} \tag{3.20}$$

The presence of even a very small hole causes the value of λ to drop rapidly from unity (for a solid circular bearing) to 2/3. Hence, in most cases for rubber bearings with central holes, the value of E_c should be taken as $4GS^2$ [50]. Therefore, the ratio of vertical to horizontal stiffness is

$$K_V / K_H = 4S^2 \tag{3.21}$$

Thus, the vertical stiffness of the rubber isolators assumed in this study is 2500 times the horizontal stiffness. For instance, an isolation system with nominal horizontal isolation period of 2.5 s exhibits a nominal vertical isolation period of $T_b^{vert} = 0.05$ s.

In addition to the flexibility of the isolation system, it is assumed that the superstructure itself has a vertical vibration period of $T_{fb}^{vert} = 0.1$ s. To investigate the possible effect of the vertical excitation on the peak sliding displacement demands on EC, the vertical pulse is applied in both the positive and negative directions. As shown in Figure 3-1, the positive direction is upward. Thus, the negative vertical pulse most likely reduces the normal force and, depending on the pulse amplitude and vertical flexibility of the system, can lead to jumping of the EC. The full-scale experimental study conducted at E-Defence [52] reported vertical floor accelerations higher than 1.0 g due to vertical acceleration amplification as a result of the proximity of the natural frequency of the isolated building with the dominant ground frequency in the vertical direction; as a result of which, jumping of EC within the building was observed. However, this special case is beyond the scope of the present study, which focuses on the sliding response and, in this section, how this is affected by vertical excitation. To prevent the occurrence of jumping, the amplitude of the pulse is adjusted. It should be noted that use of a pulse with small amplitude does not alter the dimensionless master curves since they are inherently self-similar.

Figure 3-16 compares the peak sliding response of EC under only horizontal pulse and under horizontal pulses with coincident identical vertical pulse acting in the positive or negative direction, for isolation-to-pulse period ratio values of $T_b/T_p = 0.5,\ 1.0,\ 2.0, \text{and } 3.0$. These curves are generated for a $T_{fb}/T_b = 0.1 \text{ and } 0.3$. According to this figure, the direction of vertical ground pulse excitation does not necessarily increase or decrease the peak sliding response. For $T_b/T_p = 0.5$ the vertical pulse acting in the negative direction results in a decrease in the peak sliding response, while for $T_b/T_p = 2.0$ and 3.0 it results in an increase. For $T_b/T_p = 1.0$ it results in an increase for smaller values of $\mu_k g/a_p$, but an increase for larger $\mu_k g/a_p$. Comparing the top row plots ($T_{fb}/T_b = 0.1$) with the bottom row plots ($T_{fb}/T_b = 0.3$) shows that the flexibility of superstructure in the range of typical base-isolated buildings (i.e., low- to mid-rise buildings) has no noticeable effect on the peak sliding demands on EC when identical vertical pulse is present. From the plots, it can be seen that the vertical ground pulse excitation can affect the peak sliding response appreciably for $T_b/T_p = 0.5$. However, its contribution becomes small for larger isolation-to-pulse period ratios, meaning that the vertical pulse has minor contribution in the case of short-period pulses. This finding is in good agreement with the results of previous studies denoting the minor effect of high-frequency vertical component of actual earthquakes on the peak sliding response of rigid objects [23,7].

3.4 Conclusion

This study presented the results of a comprehensive parametric investigation on the sliding response of equipment and contents (EC) in seismically isolated buildings subjected to pulse-type excitations through the use of dimensional analysis. The isolation system was modelled as either viscoelastic or bilinear. The EC was assumed to be rigid, and the frictional resistance between the EC and the floors was characterized using an advanced Stribeck friction model. At first, the flexibility of the superstructure and the vertical component of the ground excitation were neglected. Subsequently, the effect of the superstructure's flexibility on the sliding response was examined. Finally, the study investigated the effect of the vertical excitation (represented by pulse motions) when the flexibilities of the superstructure and isolation system in the vertical direction were considered. The main findings of this research can be summarized as follows:

- Under pulse excitations, amplification occurs in the peak sliding displacement of EC with increasing isolation-to-pulse period ratio, T_b/T_P, specifically for low $\mu_k g / a_p$ (i.e., low friction coefficient values or large acceleration pulse amplitudes). The highest amplification is associated with the resonance condition, where the isolation period is very close to the pulse period. For $T_b/T_P > 1$, the dimensionless sliding displacement parameter decreases with increasing T_b/T_P, demonstrating the decoupling effect associated with isolation.
- Even a relatively small amount of isolation damping, say 10%, is very effective in reducing the peak sliding displacement demand under the resonance condition ($T_b/T_P = 1.0$), while large damping ratios, say over 20%, provided little additional benefit in controlling the maximum sliding displacement for non-resonance cases.
- The presence of static friction reduces the maximum sliding response for large $\mu_k g / a_p$, while it results in some amplification in the response for low $\mu_k g / a_p$. Therefore, neglecting the static phase of friction is not always conservative when estimating the maximum sliding displacement of EC with low friction or for pulses with high acceleration amplitude. However, in the range of kinetic-to-static friction ratio of sliding equipment tested previously ($0.7 \le \mu_k/\mu_s \le 1.0$), the maximum sliding response exhibits similarity. Master curves also show that the dimensionless displacement exhibits *complete similarity* with respect to the dimensionless product associated with the static-kinetic transition parameter β.
- The dynamic interaction between the EC and the base-isolated building is negligible when the building is subjected to very long-period pulses (i.e., pulses with periods longer than isolation nominal period). Even under the resonance condition, the interaction between EC with $m_{EC} / M_b < 0.2$ and base-isolated building results in less than 10% increase in the peak normalized sliding response. However, the interaction becomes considerable under pulses with periods shorter than the isolation period,

indicating the importance of considering the short-period acceleration pulses overriding the coherent long-period pulse in certain pulse-like ground motions.

- Dimensional analysis indicates the existence of complete similarity in the sliding response of EC with respect to the dimensionless yield displacement of the isolation system. In other words, the peak sliding displacement is insensitive to the exact value of the isolation yield displacement.
- The peak sliding displacement of EC is not affected appreciably by the lateral flexibility of superstructure when the superstructure to isolation period ratio is less than 0.3.
- Depending on the isolation to pulse period, addition of an identical pulse in vertical direction can affect the peak sliding response. However, its contribution becomes small for larger isolation to pulse period ratios, meaning that the vertical pulse has minor contribution in the case of short-period pulses.

3.5 References

1. Filiatrault A, Sullivan T. Performance-based seismic design of nonstructural building components: The next frontier of earthquake engineering. *Earthquake Engineering and Engineering Vibration*. 2014;13(1):17-46.
2. Taghavi S, Miranda E. Response assessment of nonstructural building elements. CA: Pacific Earthquake Engineering Research Center (PEER); 2003 University of California, Berkeley. Report No. 2003/05.
3. Comerio MC, Stallmeyer JC. Nonstructural loss estimation:the UC Berkeley case study. CA: Pacific Earthquake Engineering Research Center (PEER); 2002 University of California, Berkeley. Report No. 2002/01.
4. Dar A, Konstantinidis D, El-Dakhakhni W. Evaluation of ASCE 43-05 seismic design criteria for rocking objects in nuclear facilities. *Journal of Structural Engineering (ASCE)* (under review). 2016.
5. Konstantinidis D, Makris N. Experimental and analytical studies on the seismic

response of freestanding and anchored laboratory equipment. CA: Pacific Earthquake Engineering Research Center(PEER); 2005 University of California, Berkeley. Report No. 2005/07.

6. Nikfar F, Konstantinidis D. Sliding response analysis of operational and functional components (OFC) in seismically isolated buildings. In: *3rd Specialty Conference on Disaster Prevention and Mitigation, Canadian Society of Civil Engineering (CSCE)*; 2013; Montreal.
7. Konstantinidis D, Nikfar F. Seismic response of equipment and contents in base-isolated buildings subjected to broad-band ground motions. *Earthquake Engineering and Structural Dynamics*. 2015;44(6):865–887.
8. Bertero VV, Mahin SA, Herrera RA. Aseismic design implications of near-fault San Fernando earthquake records. *Earthquake Engineering and Structural Dynamics*. 1978;6(1):31–42.
9. Somerville P, Graves R. Conditions that give rise to unusually large long period ground motions. *The Structural Design of Tall Buildings*. 1993;2(3):211–232.
10. Hall JF, Heaton TH, Halling MW, Wald DJ. Nearsource ground motion and its effects on flexible buildings. *Earthquake Spectra*. 1995;11(4):569–605.
11. Anderson JG, Bodin P, Brune JN, Prince J, Singh SK, Quaas R, Onate M. Strong ground motion from the Michoagan, Mexico, Earthquake. *Science*. 1986;233(4768):1043-1049.
12. Makris N, Black C. Evaluation of peak ground velocity as a ’Good’ intensity measure for near-source ground motions. *Journal of Engineering Mechanics (ASCE)*. 2004;130(9):1032-1044.
13. Makris N. Rigidity–plasticity–viscosity: can electrorheological dampers protect base-isolated structures from nearsource ground motions? *Earthquake Engineering and Structural Dynamics*. 1997;26(5):571–591.
14. Makris N, Chang SP. Effect of viscous, viscoplastic and friction damping on the response of seismic isolated structures. *Earthquake Engineering and Structural*

Dynamics. 2000;29(1):85–107.

15. Vassiliou MF, Makris N. Estimating time scales and length scales in pulse-like earthquake acceleration records with wavelet analysis. *Bulletin of the Seismological Society of America*. 2011;101(2):596–618.
16. Veletsos AS, Newmark NM, Chelepati CV. Deformation spectra for elastic and elastoplastic systems subjected to ground shock and earthquake motions. In: *Proceedings of the 3rd World Conference on Earthquake Engineering*; 1965; Wellington, New Zealand. p. 663–682.
17. Alavi B, Krawinkler H. Effects of near-fault ground motions on frame structures. John A. Blume Earthquake Engineering Center; 2001. Report No. 138.
18. Mavroeidis GP, Papageorgiou AS. A mathematical representation of near-fault ground motions. *Bulletin of the Seismological Society of America*. 2003;93(3):1099–1131.
19. Baker WJ. Quantitative classification of near fault ground motions using wavelet analysis. *Bulletin of the Seismological Society of America*. 2007;97(5):1486–1501.
20. Lu Y, Panagiotou M. Characterization and representation of near-fault ground motions using cumulative pulse extraction with wavelet analysis. *Bulletin of the Seismological Society of America*. 2014;104(1):410–426.
21. Makris N, Black CJ. Dimensional analysis of rigid-plastic and elastoplastic structures under pulse-type excitations. *Journal of Engineering Mechanics (ASCE)*. 2004;130(9):1006–1018.
22. Makris N, Black CJ. Dimensional analysis of bilinear oscillators under pulse-type excitations. *Journal of Engineering Mechanics (ASCE)*. 2004;130(9):1019-1031.
23. Gazetas G, Garini E, Anastasopoulos I, Georgarakos T. Effects of Near-Fault Ground Shaking on Sliding Systems. *Journal of Geotechnical and Geoenvironmental Engineering*. 2009;135(12):1906–1921.
24. Makris N, Vassiliou MF. The existence of “complete similarities” in the response of seismic isolated structures subjected to pulse-like ground motions and their implications in analysis. *Earthquake Engineering and Structural Dynamics*.

2011;40(10):1103–1121.

25. Kelly JM. *Earthquake-resistant design with rubber*. 2nd ed. London: Springer; 1997.
26. Yang T, Konstantinidis D, Kelly J. The influence of isolator hysteresis on equipment performance in seismic isolated buildings. *Earthquake Spectra*. 2010;26(1):275–293.
27. Xia F. Modelling of a two-dimensional Coulomb friction oscillator. *Journal of Sound and Vibration*. 2003;265(5):1063-1074.
28. Mokha A, Constantinou M, Reinhorn A. Teflon Bearings in Base Isolation I: Testing. *Journal of Structural Engineering (ASCE)*. 1990;116(2):438–454.
29. Mokha A, Constantinou M, Reinhorn A. Further Results on Frictional Properties of Teflon Bearings. *Journal of Structural Engineering (ASCE)*. 1991;117(2):622–626.
30. Tsopelas P, Constantinou M, Kim YS, Okamoto S. Experimental study of FPS sytem in bridge sesimic isolation. *Earthquake Engineering and Structural Dynamics*. 1996;25(1):65–78.
31. Wolff E, Constantiniou M. Experimental study of seismic isolation systems with emphasis on secondary system response and verification of accuracy of dynamic response history analysis methods. Technical Report. NY: Multidisciplinary Center for Earthquake Engineering Research; 2004 University at Buffalo. MCEER-04-0001.
32. Konstantinidis D, Kelly JM, Makris N. Seismic response of bridge bearings. Earthquake Engineering Research Center, University of California, Berkeley; 2008. Report No. UCB/EERC-2008/02.
33. Fenz DM, Constantinou MC. Spherical sliding isolation bearings with adaptive behavior: Experimental verification. *Earthquake Engineering and Structural Dynamics*. 2008;37(2):185–205.
34. Dao ND, Ryan KL, Sato E, Sasaki T. Predicting the displacement of triple pendulum™ bearings in a full-scale shaking experiment using a three-dimensional element. *Earthquake Engineering and Structural Dynamics*. 2013;42(11):1677–1695.
35. Steelman J, Fahnestock L, Hajjar J, LaFave J. Performance of nonseismic PTFE

sliding bearings when subjected to seismic demands. *Journal of Bridge Engineering (ASCE)*. 2015;(in press).

36. Nikfar F, Konstantinidis D. Solving dynamical systems with path-dependent nonlinearities using MATLAB ODE solvers. In: *10th National Conference in Earthquake Engineering*, Earthquake Engineering Research Institute; 2014; Anchorage, AK.
37. Voyagaki E. Contributions to dynamic response of yielding systems to near-fault earthquake motions. School of Civil Engineering, National Technical University, Athens, Greece; 2012.
38. Voyagaki E, Mylonakis G, Psycharis I. Rigid block sliding to idealized acceleration pulses. *Journal of Engineering Mechanics (ASCE)*. 2012;138(9):1071-1083.
39. Newmark NM. Effects of earthquakes on dams and embankments. *Géotechnique*. 1965;15:139–160.
40. Newmark NM, Rosenblueth E. *Fundamentals of earthquake engineering*. Englewood Cliffs, NJ.: Prentice Hall; 1971.
41. Sarma SK. Seismic stability of earth dams and embankments. *Géotechnique*. 1975;25(4):743–761.
42. Konstantinidis D, Makris N. Seismic response analysis of multidrum classical columns. *Earthquake Engineering and Structural Dynamics*. 2005;34(10):1243–1270.
43. Vassiliou MF, Makris N. Analysis of the rocking response of rigid blocks standing free on a seismically isolated base. *Earthquake Engineering and Structural Dynamics*. 2012;41(2):177–196.
44. Chaudhuri SR, Hutchinson TC. Characterizing frictional behavior for use in predicting the seismic response of unattached equipment. *Soil Dynamics and Earthquake Engineering*. 2005;25:591–604.
45. Konstantinidis D, Makris N. Experimental and analytical studies on the response of freestanding laboratory equipment to earthquake shaking. *Earthquake Engineering and Structural Dynamics*. 2009;38(6):827–848.

46. Hutchinson TC, Chaudhuri SR. Bench-shelf system dynamic characteristics and their effects on equipment and contents. *Earthquake Engineering and Structural Dynamics*. 2006;35(13):1631–1651.

47. Konstantinidis D, Makris N. Experimental and analytical studies on the response of 1/4-scale models of freestanding laboratory equipment subjected to strong earthquake shaking. *Bulletin of Earthquake Engineering*. 2010;8(6):1457–1477.

48. Konstantinidis D, Kelly JM, Makris N. Experimental investigation on the seismic response of bridge bearings. Earthquake Engineering Research Center, University of California, Berkeley; 2008. Report No. UCB/EERC-2008/02.

49. Ryan K, Dao N. Influence of vertical ground shaking on horizontal response of seismically isolated buildings with friction bearings. *Journal of Structural Engineering (ASCE)*. 2015.

50. Kelly J, Konstantinidis D. *Mechanics of rubber bearings for seismic and vibration isolation*. Chichester: John Wiley & Sons; 2011.

51. Konstantinidis D, Rastgoo Moghadam S. Compression of unbonded rubber layers taking into account bulk compressibility and contact slip at the supports. *International Journal of Solids and Structures*. 2016;87:206–221.

52. Furukawa S, Sato E, Shi Y, Becker T, Nakashima M. Full-scale shaking table test of a base-isolated medical facility subjected to vertical motions. *Earthquake Engineering and Structural Dynamics*. 2013;42(13):1931–1949.

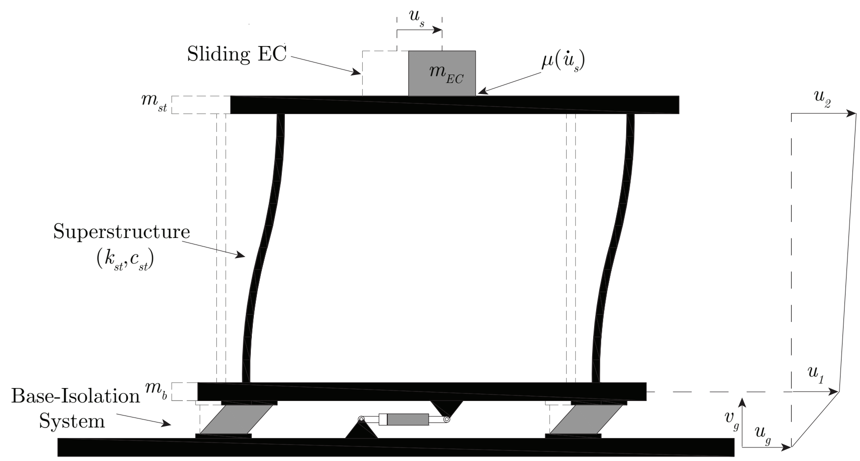

Figure 3-1. Model of the base isolated structure containing a sliding rigid EC on the first story.

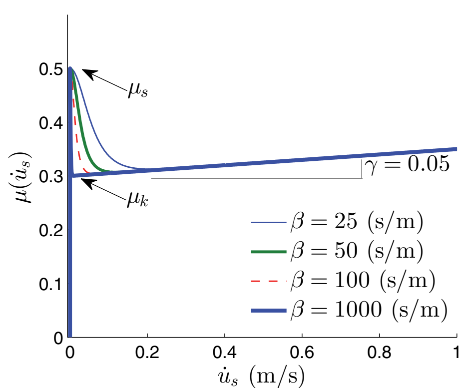

Figure 3-2. Stribeck friction model

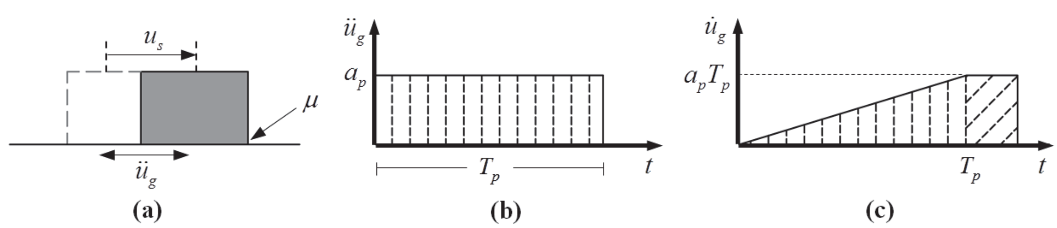

Figure 3-3. (a) sliding rigid block subjected to a horizontal ground excitation. (b) Rectangular ground acceleration pulse with amplitude a_p and duration T_p. (c) Ground velocity.

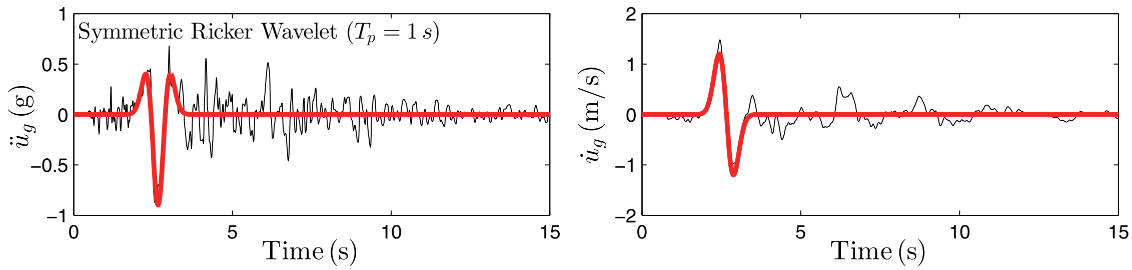

Figure 3-4. Ground acceleration and velocity time histories of the Rinaldi motion (RRS228) recorded during the 1994 Northridge earthquake, together with the symmetric Ricker wavelet with effective period of 1.0 s matched to the long-period pulse.

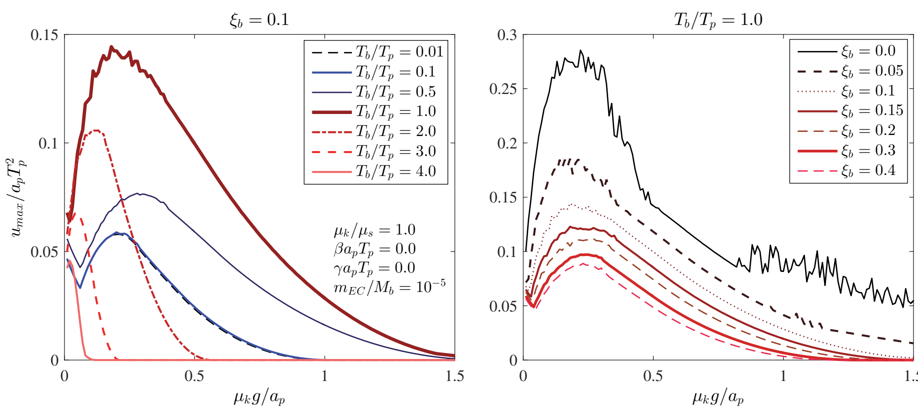

Figure 3-5. Dimensionless solutions to demonstrate the effect of isolation period ratio T_b/T_P (left) and isolation damping ξ_b (right) for rigid superstructure.

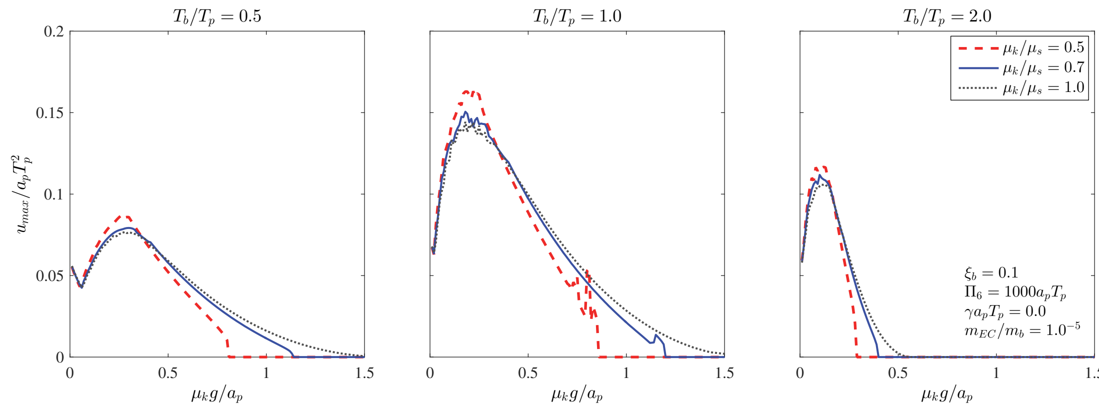

Figure 3-6. Effect of kinetic-to-static friction coefficient ratio μ_k/μ_s (rigid superstructure).

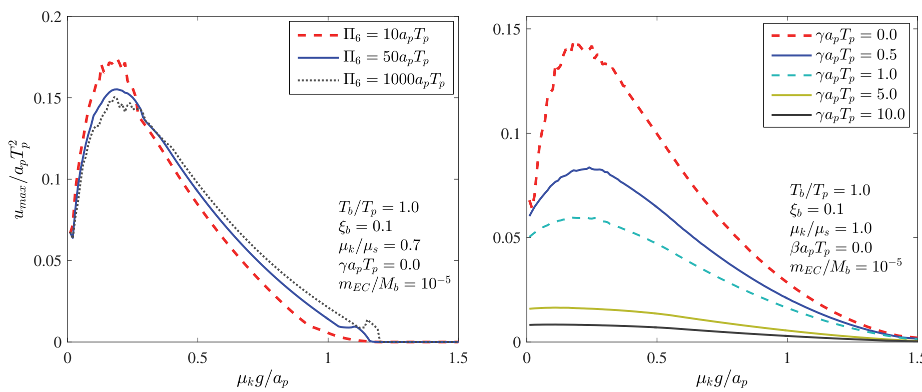

Figure 3-7. Left: Effect of the transition between static and kinetic friction, $\beta a_p T_p$. Right: Effect of viscous property of the contact, $\gamma a_p T_p$ (rigid superstructure).

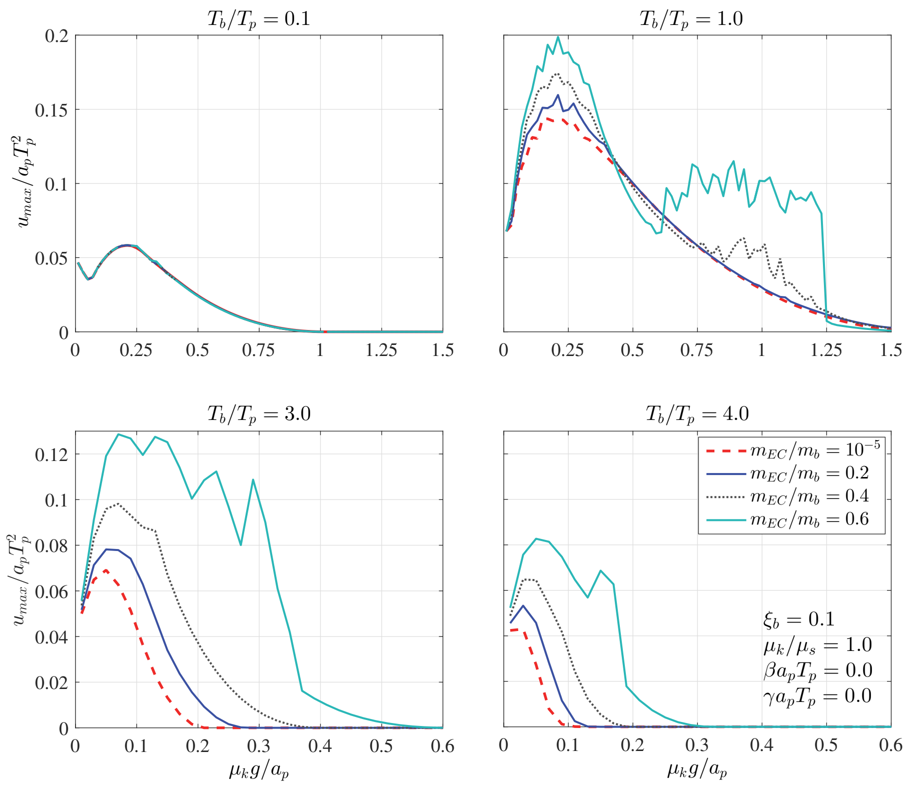

Figure 3-8. Effect of the mass ratio m_{EC}/M_b on the maximum sliding response (rigid superstructure).

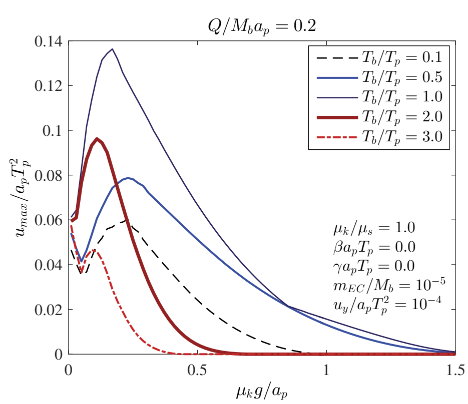

Figure 3-9. Dimensionless curves to demonstrate the effect of isolation period for bilinear systems (rigid superstructure).

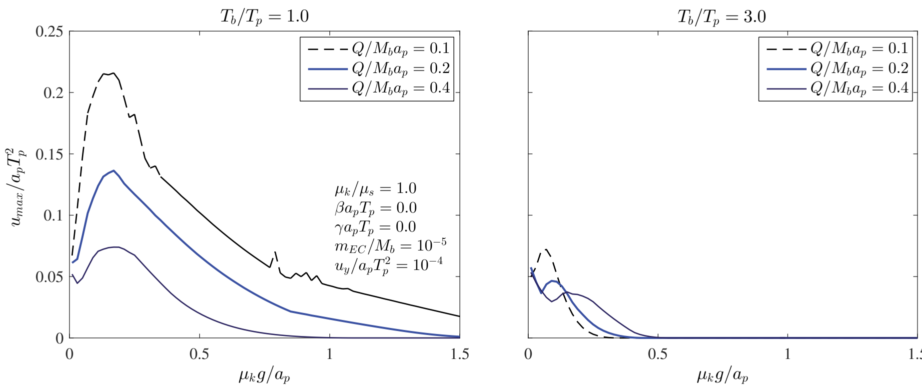

Figure 3-10. Effect of dimensionless characteristic strength on peak sliding displacement (rigid superstructure).

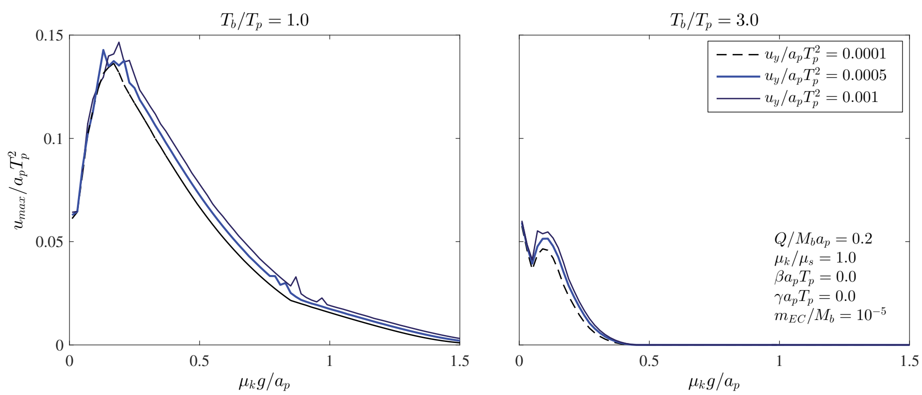

Figure 3-11. Effect of the isolation system's dimensionless yield displacement, $u_y / a_p T_p^2$, on the peak sliding displacement (assuming rigid superstructure).

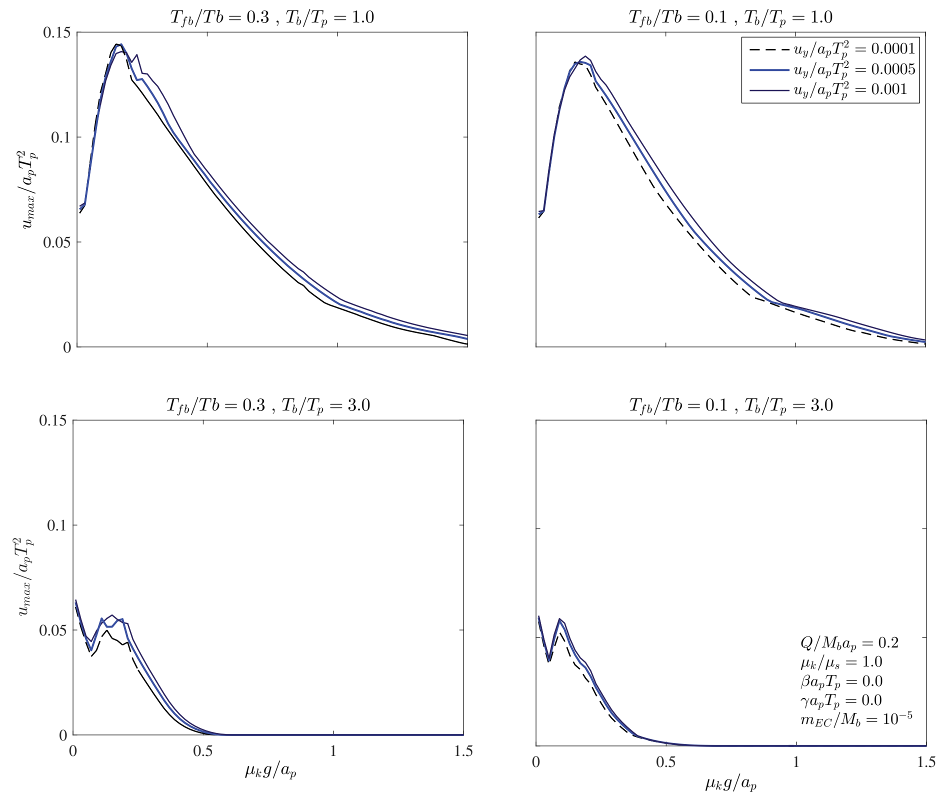

Figure 3-12. Effect of the isolation system's dimensionless yield displacement, $u_y/a_pT_p^2$, on the peak sliding displacement, considering the lateral flexibility of the superstructure.

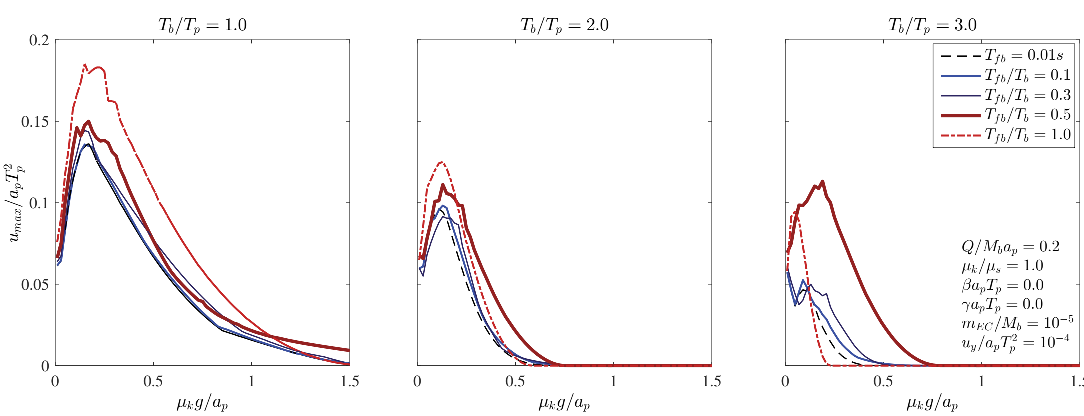

Figure 3-13. Effect of the superstructure-to-isolation period ratio, T_{fb}/T_b, on the peak sliding response.

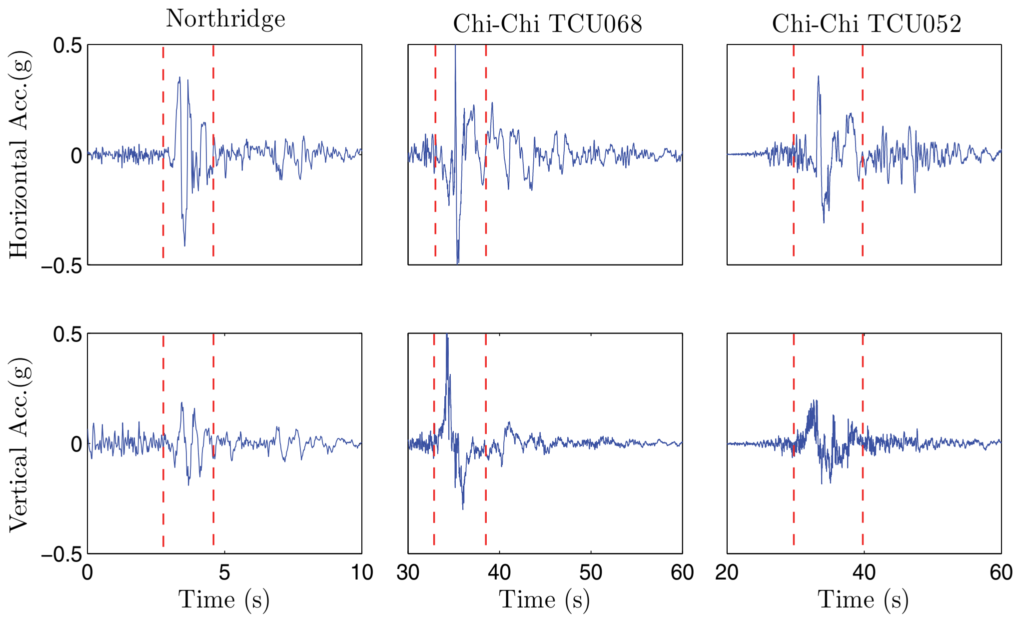

Figure 3-14. Coincidence of coherent horizontal and vertical pulses with similar characteristics. Left: 1994 Northridge earthquake recorded at Pacoima Dam-Downstream. Middle: 1999 Chi-Chi earthquake recorded at TCU-068 station. Right: 1999 Chi-Chi earthquake recorded at TCU-052 station.

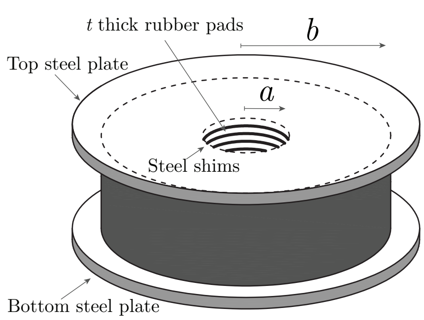

$S = (b-a)/2t$

$A = \pi(b^2 - a^2)$

t = tickness of individual rubber layer

t_r = total tickness of rubber

Figure 3-15. Schematic of an annular rubber isolator and its shape factor.

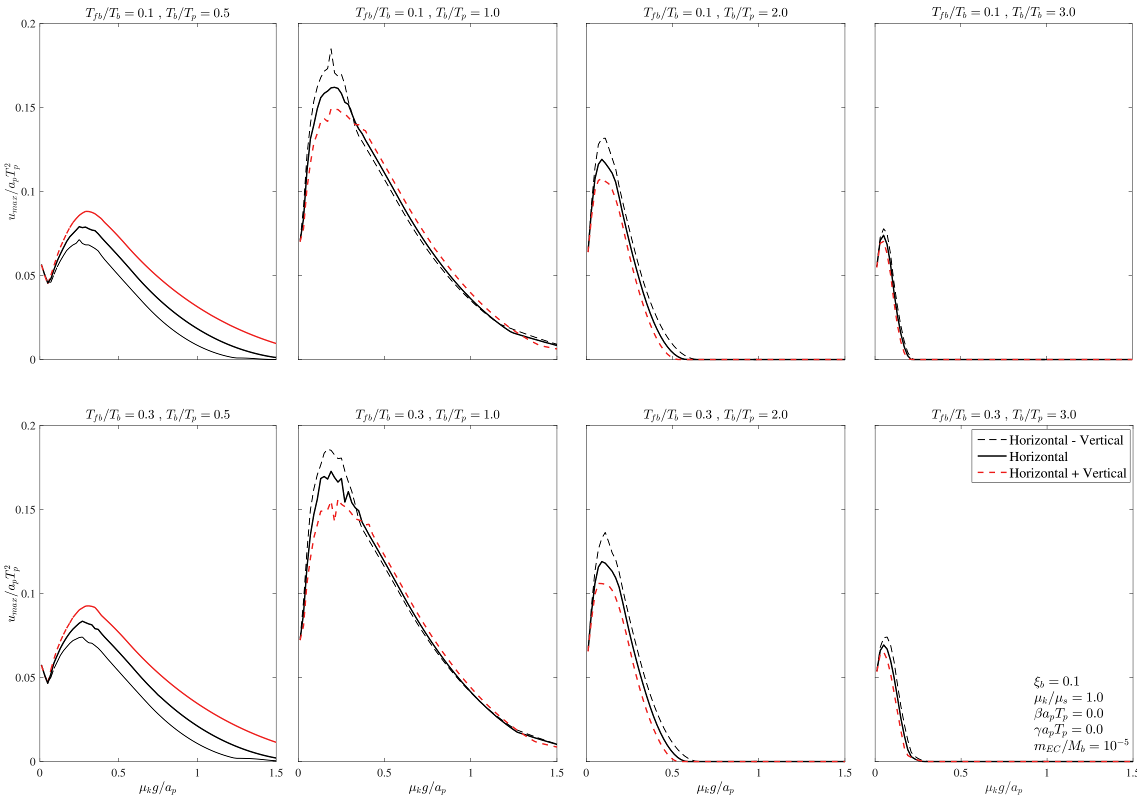

Figure 3-16. Effect of the vertical excitation on the dimensionless sliding response of EC, including the flexibilities of the isolation system and the superstructure in both the horizontal and vertical directions.

Chapter 4: Effect of the Stick-Slip Phenomenon on the Sliding Response of Objects Subjected to Pulse Excitations

Nikfar F., Konstantinidis D., 2016, Effect of the Stick-Slip Phenomenon on the Sliding Response of Objects Subjected to Pulse Excitations, submitted to the *Journal of Engineering Mechanics (ASCE)*.

Abstract

The response analysis of sliding objects and structures subjected to ground excitation is most often performed using Newmark's rigid sliding block with Coulomb friction. This simplified sliding model has been shown to sometimes result in poor predictions of sliding displacement. In an effort to improve sliding response predictions, this paper introduces a model that relaxes the rigidity constraint of the Newmark model and takes into account velocity-dependence of the friction force using a Stribeck friction model. It is shown that the flexibility of the support system in conjunction with velocity-dependent friction at low velocities can result in intermittent stick-slip phases during sliding. A dimensional analysis approach is taken to expose the underlying physical similarities in the sliding problem and to compare the results of the stick-slip model with conventional sliding models, including Newmark's rigid block and coupled sliding models that are not capable of capturing the stick-slip phenomenon. It is demonstrated that implementation of simplified sliding models may result in underestimating the sliding response.

4.1 Introduction

One of the earliest systematic investigations on friction between solid surfaces was conducted by Coulomb (Coulomb 1785). The analytical model for the friction coefficient (i.e., the ratio of friction to normal force) proposed by Coulomb assumes rigid-perfectly-plastic behavior, as shown in Figure 3-2(a). This model served as a foundation for further studies that proposed more intricate models, such as Static+Coulomb (Figure 3-2-b), to better describe the breakaway friction observed in experiments (Armstrong-Helouvry et al. 1994). Even though this model is adequate for estimating the friction force in many engineering problems, it has limitations when it comes to simulating the widely observed phenomenon of *intermittent stick-slip* during sliding. *Stick-slip* in this study refers to spasmodic sliding motion, i.e., jerking motion, characterized by successive rapid bursts of sticking and slipping, caused by a combination of mechanical (flexibility of the sliding system) and tribological (unstable friction force due to change from static to kinetic friction) properties of the system (Van De Velde & De Baets 1996). The non-smooth sliding motion occurring under this relaxation-oscillation type of motion is in contrast to what is often described in the earthquake engineering literature as stick-slip: the distinct 'stick' and 'slip' phases experienced by a rigid block under time-varying excitation; e.g., during an earthquake when the block initially at rest (stick) may start sliding (slip), then come to a stop relative to the base (stick), then continue moving with the base (stick) until the excitation is strong enough to overcome the interface strength and cause sliding again (slip), either in the same or opposite direction from before, depending on the direction of the base excitation, and so on. In this context, once the rigid block begins to slide, the sliding motion is smooth. On the contrary, what is referred to as stick-slip sliding motion in this paper is non-smooth (jerky). The dynamic model presented later in this paper is general in the sense that it is capable of capturing jerky sliding motion when the conditions (described later) are such that the stick-slip phenomenon arises, but also smooth sliding motion when those conditions are not present. The stick-slip phenomenon can explain complicated physical phenomena; for instance, stick-slip instability is known as the main source of earthquakes (Dieterich 1991; Armstrong-Helouvry et al. 1994;

Scholz 2002).

The conventional Static+Coulomb friction model is not capable of capturing the occurrence of stick-slip because it does not take into account the so-called *Stribeck* effect (Stribeck 1902; Armstrong-Helouvry et al. 1994; Armstrong-Helouvry 1990), which is the main source of instability in the friction force during sliding. The Static+Coulomb model assumes an instantaneous drop in friction force from the static to the kinetic state, and a constant friction thereafter (Figure 3-2-b). However, friction experiments (Armstrong-Helouvry 1990) have shown that the transition from the static to the kinetic state is smooth, as illustrated in Figure 3-2(c), i.e., the friction is velocity-dependent at low sliding velocities. Characteristics of this transition depend on several parameters, such as the surface material, surface roughness, lubrication, and dwell time.

As part of a study investigating the sliding response of heavy equipment, such as incubators, freezers, etc., housed in a science laboratory facility subjected to earthquake shaking, Konstantinidis and Makris conducted quasi-static pull tests of heavy equipment items resting on unwaxed (Konstantinidis & Makris 2005; Konstantinidis & Makris 2009) and waxed floor surfaces. During sliding on waxed floor surfaces, jerky motion as a result of stick-slip was observed. Fig. 4-3 shows the lateral load-displacement response of an incubator tested on a waxed floor. Cycles of stick and slip are evident during sliding. Stick-slip vibration was also observed in pull tests of lightweight benchtop equipment, conducted by Hutchinson and Chaudhuri (Chaudhuri & Hutchinson 2005; Hutchinson & Chaudhuri 2006). Stick-slip is evident from the fluctuations in the friction-velocity curves of the equipment supported on rubber pads, presented in the paper. Similar stick-slip oscillations were observed in shaking table tests of a desk on common flooring materials (Yeow et al. 2014). Stick-slip was also present in slow cyclic tests performed to characterize friction pendulum isolators (Paolacci et al. 2014).

Although stick-slip in the response of equipment has been experimentally observed, studies examining the sliding response of equipment have hitherto used either Coulomb or Static+Coulomb models to characterize the frictional characteristics of the contact interface in numerical simulations (Chaudhuri & Hutchinson 2005; Konstantinidis

& Makris 2005; Hutchinson & Chaudhuri 2006; Konstantinidis & Makris 2009; Konstantinidis & Makris 2010). As mentioned earlier, these simple models are not able to capture the stick-slip phenomenon during sliding. Newmark's sliding block (Newmark 1965), which is widely used to determine the sliding response of earth/waste structures, e.g., earth dams and landfills, under earthquake excitations, cannot capture the stick-slip phenomenon either. Newmark's sliding block consists of a rigid block, as shown in Fig. 4-2(a), resting on a moving base. The friction between the block and the base in Newmark's original work was described by a Coulomb model, as shown in Figure 3-2(a). In more recent adaptations of the model, the friction may also be described by a Static+Coulomb model (Chaudhuri & Hutchinson 2005), i.e., Figure 3-2(b). Even though substantial effort has been concentrated on developing more advanced analytical methods to take into account the deformability of earth structures in sliding analyses, the frictional behavior along the sliding surface is still characterized by early friction models. Several simplified de-coupled (Makdisi & Seed 1978; Lin & Whitman 1983) and coupled (Chopra & Zhang 1991; Gazetas & Uddin 1994; Kramer & Smith 1997; Rathje & Bray 2000) analysis methods based on Coulomb friction have been developed to incorporate this flexibility in the sliding analysis. The flexibility of the soil column and its dynamic effects introduce a type of strain relaxation in the sliding of these structures, similar to what is called *pre-elasticity* in the context of friction dynamics, i.e., the elasticity between the mass and the sliding surface which is requisite for the stick-slip phenomenon to arise. Despite their level of sophistication in characterizing elasticity, these models are not able to capture the intermittent stick-slip during sliding. This is because the other necessary condition for stick-slip, i.e., the Stribeck effect, or unstable friction force, is not considered. Stribeck friction can be present in the sliding of such structures. Shear failure of soil profiles also follows a transition from maximum shear strength (that can be thought of as static friction) to complete failure and sliding of the soil layer along the sliding surface, leading to a drop in shear resistance until the residual strength of the soil is reached (that can be thought of as kinetic friction). Experimental studies have noted the rate dependency of shear strength in soils and geosynthetic interfaces (Biscontin &

Pestana 2001; Kim et al. 2005; Wartman et al. 2005). Moreover, the smooth transition from static to kinetic friction, representing Stribeck friction, has been observed in experimental investigations on the friction of granular layers (Nasuno et al. 1997). Such rate dependency and consequent transitions from maximum strength to residual strength together with the deformability (elasticity) of the structure may result in stick-slip in the sliding of earth structures.

Based on the discussion above, both flexibility in the sliding body or its support system (in contrast with the rigid sliding block) *and* velocity-dependent friction are simultaneously necessary for the intermittent stick-slip phenomenon to arise. However, while necessary, the mere presence of conditions is not sufficient for stick-slip to occur. Stick-slip usually occurs in sliding velocities below a specific limit in conjunction with a minimum amount of flexibility at the contact interface (Singh 1960; Armstrong-Helouvry et al. 1994; Persson & Popov 2000). This paper introduces a 2-degree-of-freedom (DOF) sliding model that incorporates both elasticity in the support system and Stribeck friction along the contact interface and is able to capture stick-slip oscillations during the sliding process under ground excitation. The effect of the stick-slip phenomenon on the sliding response of objects subjected to unidirectional, horizontal pulse-like ground motions is investigated using the proposed model. A dimensional analysis approach is employed to explore the physical similarity of the solutions. Using this method, results of conventional sliding models are compared with the stick-slip model under various wavelet excitations. It is shown that the presence of elasticity and velocity-dependent friction has dominant effects on the sliding response and alter the nature of problem considerably. It is concluded that simplified sliding models, which cannot capture stick-slip effects, may underestimate the sliding response.

4.2 Problem presentation

The sliding model introduced in this paper (the mathematical formulation of which is presented later) is capable of capturing stick-slip and is applicable to a wide range of dynamic systems with friction, including sliding of freestanding equipment or building contents, buildings and bridges isolated with friction devices, earth and geotechnical structures, retaining walls, masonry walls, etc. (Fig. 4-4). As the flexibility in the system is described entirely by a single DOF (see Fig. 4-4 –'Idealization'), the accuracy of the model increases for flexible superstructures with first-mode dominant response.

The velocity-dependent friction (i.e., Stribeck friction) used in this model follows a hyperbolic secant functions for transition from static to kinetic friction. As suggested in (Xia 2003), a general friction model that can account for both static, μ_s, and kinetic, μ_k, friction, their transition, as well as the presence of viscosity at the contact interface can be expressed as

$$\mu(\dot{u}_s) = \mu_s \mathrm{sech}(\dot{u}_s\beta) + \mu_k \left[1 - \mathrm{sech}(\dot{u}_s\beta)\right] + \gamma_n \left|\dot{u}_s\right|^n \tag{4.1}$$

Equation (4.1) introduces the rate dependence of the friction coefficient. In this equation, $\dot{u}_s$ represents sliding velocity (i.e., the relative velocity between the sliding surfaces); constant β controls the transition sharpness from static to kinetic friction (the larger β, the sharper the transition, as shown in Figure 3-2(c)); and γ_n represents viscous characteristics of the contact.

In addition to the transition property from static to kinetic friction as a function of sliding velocity, kinetic friction itself is defined as a velocity-dependent parameter. The last term of Equation (4.1), $\gamma_n \left|\dot{u}_s\right|^n$, captures any nonlinear viscous velocity dependence of friction. This kind of force arising from viscous properties between the surfaces is called *viscous contact*. This definition is well explained in mechanical engineering literature, specifically for friction between lubricated surfaces. However, velocity dependence of kinetic friction is not limited to lubricated surfaces and has been observed in dry friction experiments as well. In structural engineering, for example, the velocity dependence of the kinetic friction in sliding bearings has been observed experimentally in several studies (Mokha et al. 1990; Mokha et al. 1991; Tsopelas et al. 1996; Wolff & Constantiniou 2004; Konstantinidis et al. 2008; Fenz & Constantinou 2008; Dao et al. 2013; Steelman et al. 2015). These studies usually included cyclic tests at different frequencies, and the value of the kinetic friction coefficient for each experiment was related to the *peak* (amplitude) velocity of that harmonic excitation. Even though this approach does illustrate the velocity dependence of kinetic friction, it does not provide information about the friction coefficient as a function of *instantaneous* sliding velocity. Aside from the inherent viscous behavior in dry and lubricated contacts, viscosity can also be introduced by supplemental damping devices. Examples of such systems include structures isolated by sliding bearings together with viscous dampers (Wolff & Constantinou 2004; Wolff et al. 2015). Hence, the application of viscous friction goes beyond the limits of the in-contact surfaces and includes a wide range of problems. Analytical solutions for oscillators with combination of viscous damping and linear/velocity-dependent Coulomb friction have been presented in (Makris & Constantinou 1991a,b). Depending on the surface characteristics, the actual behavior may be approximated by a linear or nonlinear function, $\gamma_n \dot{u}_s^n$. In this study, n is assumed to be equal to unity, representing linear viscous damping for the contact. Thus, the friction coefficient can be expressed as

$$\mu(\dot{u}_s) = \mu_s \operatorname{sech}(\dot{u}_s \beta) + \mu_k \left(1 - \operatorname{sech}(\dot{u}_s \beta)\right) + \gamma \dot{u}_s \tag{4.2}$$

The friction force for the sliding problem (Fig. 4-4) under horizontal excitation is given by

$$F_f = \mu(\dot{u}_s)(m + m_e) g \operatorname{sgn}(\dot{u}_s) \tag{4.3}$$

where sgn($\cdot$) is the *signum* function, m is mass of the block, m_e represents mass of the legs or support, and g is the acceleration due to gravity. Note that in the case where supplementary damping device connects the non-rigid superstructure to the base, the damping force should be computed based on the relative velocity of the connecting point and base; not merely the sliding velocity. For this case, one may discern the supplementary damping from the damping of the contact mechanism by considering it directly in the equation of motion. The general form of Equation (4.2) subsumes more elementary friction models and, depending on the presence or absence of elasticity at the contact, different dynamical sliding models can be obtained.

The intermittent stick-slip in the process of sliding is illustrated in Fig. 4-5. A mass supported by an elastic leg is subjected to a gradually increasing horizontal force, P. The mass is free to translate, but restricted to rotate in its plane. Stribeck friction is assumed at the contact between the tip of the support and the base. As the driving force increases, the leg deforms until P reaches the static friction force, $P = F_s$, when sliding initiates. At the very moment when sliding initiates, the friction force on the surface drops rapidly from F_s to F_k introducing an unbalanced force between the mass and the base. This unbalanced force results in a sudden increase in sliding velocity of the tip of the leg leading to a strain relaxation in the leg. Strain relaxation means reduction of the elastic force of the leg to F_k. Even though it happens very fast, during the transition of the force from F_s to F_k, the sliding velocity of the tip drops, and since the drop in velocity contributes to an increase in friction force, it leads to sticking of the tip to the base. Sticking of the tip results in an increase in friction force to F_s. These stick-slip cycles continue provided that the system slides with a velocity lower than a critical value. Once the velocity exceeds the critical value, stick-slip vanishes, and sliding proceeds steadily. As shown in Fig. 4-5, after some cycles of stick-slip, and by increasing the velocity, the steady sliding phase initiates. In case that the mass decelerates, the velocity decreases and consequently there will be the possibility that stick-slip occurs before the permanent sticking of the tip to the base. At the end of the process, since the mass and its supporting leg form a dynamic system, the mass vibrates freely in its natural period of vibration.

4.3 Friction models

4.3.1 Coulomb friction model

In the Coulomb friction model, friction exhibits rigid-perfectly-plastic behavior, as shown in Figure 3-2(a). This model has been extensively used to estimate sliding response of building contents and equipment (Choi & Tung 2002; Lopez Garcia & Soong 2003; Konstantinidis & Makris 2005; Konstantinidis & Makris 2009; Nikfar & Konstantinidis 2013; Konstantinidis & Nikfar 2015) as well as in sliding response evaluation of earth and other structures (Newmark 1965; Makris & Black 2004; Wartman et al. 2005; Gazetas et al. 2009; Garini et al. 2011; Voyagaki et al. 2012). Substituting μ_s

$= \mu_k$, $\beta = 0$, and $\gamma = 0$ in Equation (4.2) leads to the Coulomb friction model, i.e., $\mu(\dot{u}) = \mu_k$.

4.3.2 Static+Coulomb friction model

A static friction that is greater than the kinetic friction is present in the majority of sliding problems (Figure 3-2(b)). Dry friction in flat slider bridge bearings (Konstantinidis et al. 2008) and shear strength of soil under shear displacement are some examples. However, in previous studies where the sliding of objects or earth structures was investigated, for simplicity, only kinetic friction (Coulomb friction) was considered in most of the analyses. However, in some studies, friction was treated as a state variable in order to engage the static friction into the dynamic equation of motion. In this approach, static friction is considered merely to determine initiation of sliding, but, during sliding Coulomb friction is still used (Chaudhuri & Hutchinson 2005; Konstantinidis & Makris 2005; Hutchinson & Chaudhuri 2006; Konstantinidis & Makris 2009). Treating friction as a state variable ignores the realistic transition from static to kinetic friction. Assuming vary large numbers for β (e.g., $\beta = 1000$ s/m) in Equation (4.2) results in very sharp transition from static to kinetic friction, thus representing the Static+Coulomb friction model, shown in Figure 3-2(b).

4.3.3 Stribeck friction model

Extensive research has been done in order to quantify the friction properties between various surfaces. It has been shown that there is a transition from static to kinetic friction which can be expressed as a function of sliding velocity (Stribeck 1902; Armstrong-Helouvry 1990; Armstrong-Helouvry et al. 1994), and references therein. *Stribeck Friction* represents the rate dependency of friction in low sliding velocities. It makes the friction problem complicated and introduces other phenomena such as *intermittent stick-slip* during the sliding phase (unsteady sliding). By introducing a continuous transition from static to kinetic friction, the mathematical model presented herein has the ability to implement steady-state Stribeck friction. The model assumes a symmetric accelerating and decelerating behavior for friction as a function of sliding velocity. However, according to previous studies, i.e., (Van De Velde & De Baets, 1998; and references therein), the friction force remains constant or increases slightly (compared to the breakaway or stick-to-slip phase) in the decelerating branch, i.e., in the slip-to-stick phase. In Equation (4.2), β controls this transition. The constant β is adjusted based on *Stribeck velocity* (i.e., the sliding velocity at which the transition from static friction to kinetic is completed, and friction force reaches to the kinetic friction value), which is obtained through testing. The Stribeck velocity can be identified for different surfaces by performing constant-velocity tests using velocity feedback controller (Lampaert et al. 2002). Since in these tests inertial forces are zero, the resulting force equals the friction force, and the Stribeck velocity can be obtained by drawing the instantaneous friction-velocity curves. The Stribeck velocity depends on various parameters such as surface material, roughness, etc.; however, based on experimental investigations on different surfaces, it is usually in the order of $0.5 \sim 30$ cm/s (Hess & Soom 1990; Nasuno et al. 1997; Van De Velde & De Baets 1998; Bengisu & Akay 1999).

4.4 Dynamic sliding models

Dynamic models of sliding vary depending on the presence of elasticity in the system. When there is no elasticity, Newmark's rigid block model (Fig. 4-2-a) describes the dynamics of sliding, where in the case that elasticity is present it introduces an oscillatory system over the sliding surface changing the dynamics of the sliding problem (Fig. 4-2-b).

4.4.1 Newmark's rigid-block model (no elasticity at contact)

Newmark's rigid block model is a single-DOF model describing the dynamics of sliding for a rigid block when no elasticity exists in the contact between the sliding mass and the base, as shown in Fig. 4-2(a).

4.4.2 Stick-slip model (elastic contact)

Stribeck friction introduces instability in the friction force at low velocities, yet it cannot by itself generate intermittent stick-slip during sliding. Unsteady friction force *and* elasticity in the contact are necessary conditions for the intermittent stick-slip phenomenon. The elasticity can be included in the model by considering a new coordinate, u_e, to account for the elastic deformation of contact surface asperities, or of flexible legs for equipment supported on legs, or of deformations in earth/waste structures—see Fig. 4-2(b).

4.5 Numerical procedure

The numerical procedure to solve stick-slip sliding model is presented in this section. First, a 2DOF system is assumed, as shown in Fig. 4-6. In this model, m_e represents the mass associated with the elastic region of the contact. For instance, in case of heavy equipment items with legs, it represents the mass of the legs. Dynamic equilibrium for the 2DOF system gives

$$\begin{cases} -c_e\dot{u}_e - k_e u_e = m(\ddot{u}_e + \ddot{u}_s + \ddot{u}_g) \\ c_e\dot{u}_e + k_e u_e - F_f = \lambda m(\ddot{u}_s + \ddot{u}_g) \end{cases} \tag{4.4}$$

where λ is the mass ratio, $\lambda = m_e/m$, F_f is the friction force as a function of sliding velocity, given by Equation (4.3), and $\ddot{u}_g$ is the horizontal ground acceleration. The *signum* function in Equation (4.3) introduces a singularity in friction force. There are a number of procedures in the literature to treat this singularity (Mostaghel & Davis 1997). In this study, an elastoplastic model, $z(u_s, F_y, u_y, u_p)$, with yield displacement u_y and velocity-dependent strength, F_y, is used to approximate the hysteretic response of the friction force as presented in Fig. 4-7. F_y in this model represents the friction force as a function of velocity, $F_y = \mu(\dot{u}_s)(1+\lambda)mg$. For a very small u_y (e.g., 10^{-5} m), the hysteresis becomes nearly rigid-plastic. u_p is a memory variable keeping track of the plastic displacement history. u_s consists of two components, $u_s = u_1 + u_p$, where u_1 is the elastic displacement of the elastoplastic hysteresis at the contact surface (not to be confused with u_e, which represents the deformation of the support, as shown in Fig. 4-6) and u_p is the actual sliding displacement. Therefore, obtaining u_s from Equation (4.4) the u_1 and u_p will be available from the elastoplastic hysteresis, *z*. In this condition, u_1 and the corresponding stiffness can be thought of as the elastic deformation and stiffness of the contact zone between the legs and support suface. Equation (4.4) is transformed into state-space form, to be solved using a MATLAB ODE solver:

$$\mathbf{y}=\begin{Bmatrix} u_e \\ \dot{u}_e \\ u_s \\ \dot{u}_s \end{Bmatrix}=\begin{Bmatrix} y_1 \\ y_2 \\ y_3 \\ y_4 \end{Bmatrix}, \quad \mathbf{M}\,\dot{\mathbf{y}}=\begin{bmatrix} 1 & 0 & 0 & 0 \\ 0 & 1 & 0 & 0 \\ 0 & 0 & 1 & 0 \\ 0 & 0 & 0 & 1 \end{bmatrix}\begin{Bmatrix} \dot{u}_e \\ \ddot{u}_e \\ \dot{u}_s \\ \ddot{u}_s \end{Bmatrix}=\begin{Bmatrix} y_2 \\ -\dfrac{\lambda+1}{\lambda m}\left(c_e y_2+k_e y_1\right)+\dfrac{F_f}{\lambda m} \\ y_4 \\ \dfrac{1}{\lambda m}\left(c_e y_2+k_e y_1-F_f\right)-\ddot{u}_g \end{Bmatrix} \tag{4.5}$$

$$F_f=z\left(y_3,F_y\left(y_4\right),u_y,u_p\right)=f\left(y_3,y_4,u_y,u_p\right)\ , \text{ Path-dependent restoring force}$$

Above equation describes a system of ordinary differential equation (ODE) with path-dependent nonlinear force, F_f. The procedure to solve a system of ODE with path-dependent nonlinear restoring force with MATLAB ODE solvers is presented by the authors in (Nikfar & Konstantinidis 2014). Certain forms of piecewise nonlinearities can be solved using *state event location* approach as discussed in (Wright and Pei 2012). Solving the system of equations described by Equation (4.5) becomes computationally expensive as λ gets very small. In some applications such as sliding of equipment supported by rubber pads the mass ratio $\lambda=m_e/m$ becomes as small as $\lambda=1/1000$. In such cases where $\lambda\to 0$, the system reduces to a SDOF system:

$$\begin{cases} -c_e\dot{u}_e-k_e u_e=m(\ddot{u}_e+\ddot{u}_s+\ddot{u}_g) \\ c_e\dot{u}_e+k_e u_e-F_f\approx 0 \end{cases} \to F_f+m(\ddot{U}+\ddot{u}_g)=0 \tag{4.6}$$

where $U=u_e+u_s=u_1+u_p$. Provided that F_f is described by a similar velocity-dependent elastoplastic behavior but this time with an initial stiffness equal to k_e (i.e.,

$u_1 = u_e$), both elastic deformation of the leg, u_e, and sliding displacement, u_s (i.e., $u_p = u_s$), can be obtained from the hysteresis force relation, $F_f = z\left(\dot{U}, F_y\left(\dot{u}_p\right), u_y, u_p\right)$.

Taking $\mu_s = \mu_k$ when defining F_f in the stick-slip model reduces it to the specific coupled sliding model. Furthermore, the stick-slip model can become even simpler by assuming a very large elastic stiffness, $k_e \to \infty$. In this case, $u_e \to 0$, and the equation of motion collapses to an ODE representing Newmark's rigid sliding block model:

$$\ddot{u}_s + \mu(\dot{u}_s) g \,\mathrm{sgn}(\dot{u}_s) = -\ddot{u}_g \tag{4.7}$$

Analytical solutions for the sliding of a rigid block under simple pulses were used for validating the numerical solutions of the proposed stick-slip model. Closed-form solutions for Newmark's rigid sliding block with Coulomb friction are available in the literature for simple half-cycle pulses, including square, sinusoidal, and triangular pulses (Newmark 1965; Newmark & Rosenblueth 1971; Conte & Dente 1989). However, in this study, the exponential family of pulses was used for validation of the stick-slip model because of its versatility to generate an infinite set of symmetric pulses. The closed-form solutions for the peak sliding displacement due to the half-cycle exponential pulse developed by Voyagaki et al. (2012) were used for this validation. The reader is referred to (Voyagaki et al. 2012) for details on the formulation of the exponential pulse as well as the closed-form solution. Fig. 4-8 compares the closed-form solutions for sliding of a rigid block with Coulomb friction against the numerical solution of the stick-slip model for a block with very stiff support ($T = 2\pi\sqrt{m/k_e} = 10^{-5}$ s) under four types of pulses from the exponential family. In the numerical analysis, pulses were discretized with resolution of $0.0001T_p$. As can be seen, the numerical solution is in excellent agreement with the analytical solution.

4.6 Sliding response under pulse excitation

In this section, the sliding problem is investigated under analytical pulse excitations. Analytical pulse excitations are chosen, firstly, because dimensional analysis of the seismic response of sliding objects, presented later in this paper, requires a time scale and a length scale of the ground excitation. Secondly, analytical pulse-excitations, if developed consistently, can approximately simulate the kinematics of near-source pulse-like ground motions, which are known to be one of the most destructive class of ground motions to most civil structures (Somerville & Graves 1993; Hall et al. 1995).

The capability of closed-form analytical pulses to simulate structural response under real ground motions has been investigated at various levels (Veletsos et al. 1965; Makris 1997; Makris & Roussos 2000; Makris & Black 2004; Mavroeidis & Papageorgiou 2003), among others. Various analytical two- and four-parameter pulses have been proposed. In an effort to determine time and length scales of 183 pulse-like ground motions, Vassiliou and Makris (2011) demonstrated that in a contest between five common two-parameter wavelets, the *One-Cosine* and *Type C1* (C1 Cycloidal) pulses are the two best-matching pulses for symmetric and antisymmetric acceleration pulses of the selected ground motions. In this study, One-Cosine and Type C1 pulses are used based on the findings in (Vassiliou & Makris 2011), together with the symmetric Ricker wavelet for consistency with some recent studies (Gazetas et al. 2009; Garini et al. 2011; Makris & Vassiliou 2011; Vassiliou & Makris 2012; Vassiliou et al. 2013). These three wavelet types are shown in Fig. 4-9. The reader is referred to (Vassiliou & Makris 2011) for the mathematical formulations of the selected wavelet types.

To demonstrate how stick-slip may occur during sliding, a freestanding piece of equipment is considered with mechanical properties similar to those of the Forma Incubator tested previously by Konstantinidis and Makris (Konstantinidis & Makris 2005; Konstantinidis & Makris 2009): $m = 385$ kg and $k_e = 24 \times 10^4$ N/m, representing a dynamical system with fundamental period of $T = 0.25$ s. For the purposes of this example, it is assumed that the equipment does not rock, only slides and/or vibrates. The static and kinetic friction coefficients are assumed close to the ones obtained by slow pull tests: $\mu_s = 0.3$ and $\mu_k = 0.2$. Since no information is available for the transition characteristics of the surface, β is assumed to be equal to 100 s/m representing a Stribeck velocity of about 5 cm/s. The response is computed for $\lambda = 1/100$ and $\lambda = 0$. The absolute acceleration, sliding velocity, and sliding displacement response histories under a symmetric Ricker wavelet with amplitude $a_p = 0.65g$ and period $T_p = 1.0\,\mathrm{s}$ are shown in Fig. 4-10. As can be seen, there are cycles of stick and slip in the process of sliding. As sliding initiates, the sliding velocity increases under the effect of the input acceleration, and, once it exceeds a critical value, the system slides steadily. The velocity is the controlling parameter for stick-slip. The lower the sliding velocity, the longer the duration of stick-slip cycles. Moreover, at the end of the process, when complete sticking occurs, the system continues to free-vibrate in its natural frequency. It is worth mentioning that in addition to the input excitation characteristics, the parameters β, k_e, μ_s and μ_k affect the occurrence, frequency, and cycles of the stick-slip in the process of sliding. Comparing the response histories plotted in the left column of Fig. 4-10, for $\lambda = 1/100$, to those in the right column, for $\lambda = 0$, shows changes in the absolute acceleration of the mass. It is interesting to note that even though the sliding displacement responses are very similar in the two cases, the sliding velocity exhibits very large peaks in the case of $\lambda = 0$ compared to $\lambda = 1/100$.

As shown in this example, the flexibility of the sliding system and the Stribeck friction change the problem of sliding by creating a dynamic system above the sliding surface. Fig. 4-11 demonstrates the effects of such changes on the sliding response of the system due to a Ricker wavelet excitation with period $T_p = 0.25\,\mathrm{s}$ and amplitude $a_p = 0.5g$. The plots in the left column correspond to sliding response of Newmark's rigid block model, while the plots in the right column are for the responses of a flexible system (stick-slip model) with dynamic properties similar to Forma Incubator equipment, $T = 0.25\,\mathrm{s}$. The responses are computed for two different kinetic friction coefficients, presented as dimensionless parameter $\mu_k g / a_p$. For Stribeck friction, the value of the static friction coefficient is assumed to be double that of the kinetic friction coefficient, $\mu_k / \mu_s = 0.5$.

Fig. 4-11 compares the absolute acceleration, sliding velocity and sliding displacement response histories for four different models, namely: (1) Newmark model with Coulomb friction (called conventional sliding model), (2) Newmark model with

Stribeck friction, (3) Stick-slip model with Coulomb friction (called coupled sliding model in a geotechnical earthquake engineering context), and (4) Stick-slip model with Stribeck friction. Comparing the response of Newmark's sliding model (left column) having Coulomb vs Stribeck friction with $\mu_k g / a_p = 0.2$, the maximum sliding displacement corresponding to Stribeck friction (occurring in the negative direction) is greater than the system with Coulomb friction. This is due to the presence of static friction in the Stribeck model, which does not allow the system to slide substantially in the positive direction under the first minor pulse of Ricker wavelet. This is contrary to the Coulomb friction that allows the system to slide in the positive direction, cancelling a portion of the sliding in negative direction. However, when the friction coefficient increases to $\mu_k g / a_p = 0.4$, neither model exhibits sliding under the first minor pulse of the Ricker wavelet. Therefore, when the direction of loading reverses, the system with Coulomb friction experiences larger sliding displacement than the one with Stribeck friction. This suggests that the sequence of pulses can affect the sliding response appreciably. The plots in the right column of Fig. 4-11 show that the stick-slip model with Stribeck friction experiences two cycles of stick-slip under the first pulse of the Ricker wavelet. This is evident from the two spikes that appear in the sliding velocity history and also the step-like sliding displacement history. In this case, since the system has vibrational characteristics, and can experience amplification effects, the resultant sliding response can be larger than when the system is rigid. It can be observed that the stick-slip model with Stribeck friction exhibits larger sliding displacement for both friction coefficient values ($\mu_k g / a_p = 0.2$ and 0.4). As shown in this figure, the sliding response of each of these models is complex and depends on the combination of the parameters that describe the system and the excitation. The effect of these parameters on the sliding response is investigated next through the use of dimensional analysis.

4.7 Dimensional analysis

Dimensional analysis is employed in this study to reveal the underlying physics of the sliding problem for different friction and sliding models, as well as to simplify the parametric investigation. To normalize the peak sliding displacement for Newmark's sliding block subjected to a pulse excitation, the *characteristic length scale* of the pulse, L_p, should be determined. Voyagaki (2012) and Voyagaki et al. (2012) showed in a systematic manner that there are six possible L_p that can be obtained from the peak acceleration a_p, peak velocity v_p, peak displacement d_p, and period T_p of the pulse, i.e., $L_p = (v_p^2/a_p, a_pT_p^2, v_pT_p, d_p, v_pd_p/a_pT_p, a_pd_pT_p/v_p)$. The first parameter, $L_p = v_p^2/a_p$, was used in the early studies by Newmark (1965) and Newmark and Rosenblueth (1971). The second parameter, $L_p = a_pT_p^2$, was employed by several researchers (Sarma 1975; Makris & Black 2004a,b; Konstantinidis & Makris 2005). Makris & Black (2004b) compared the adequacy of a parameter equivalent to $L_p = v_pT_p$, i.e., $L_p = v_p/\omega_p = v_pT_p/2\pi$, against $L_p = a_pT_p^2$ to represent length scale of pulse-like ground motions. They demonstrated that both linear and nonlinear responses of structural systems scale better with the peak pulse acceleration than the peak pulse velocity, concluding that peak pulse acceleration is a better representative measure of intensity of a pulse (Makris & Black 2004b). To the best knowledge of the authors, the last three parameters in (Voyagaki et al. 2012) have not been investigated within the context of nonlinear structural systems. Based on the findings of Makris & Black (2004b), and since this study deals with the sliding problem, wherein sliding initiation depends merely on the condition that base acceleration overcomes the frictional resistance, $L_p = a_pT_p^2$ is considered as the length scale of the pulse.

In this study, the stick-slip sliding model with Stribeck friction is assumed as the most general friction model. For this model, and based on Equations (4.2) and (4.4), the maximum sliding displacement, as a dependent variable, under an excitation with coherent pulse acceleration amplitude a_p and duration T_p is expected to be a function of seven independent variables (for each pulse type),

$$u_{\max} = f(a_p, T_p, \mu_s, \mu_k, \beta, \gamma, T, \text{shape of the pulse excitation}) \tag{4.8}$$

where $T = 2\pi\sqrt{m/k_e}$. In Equation (4.8), the eight variables, having dimensions $u_{\max} \doteq [L]$, $a_p \doteq [L][T]^{-2}$, $T_p \doteq [T]$, $\mu_s \doteq [\cdot]$, $\mu_k \doteq [\cdot]$, $\beta \doteq [L]^{-1}[T], \gamma \doteq [L]^{-1}[T]$, and $T \doteq [T]$ (where in this context, T within square brackets is the dimension of time), involve only two reference dimensions, that of length $[L]$ and time $[T]$. As shown before, for small mass ratios, λ, the contribution of m_e to the sliding displacement is minor; therefore a mass ratio of $\lambda = 0$ is assumed in the dimensional analysis to reduce the number of parameters. Based on Buckingham's Π-theorem, the number of independent dimensionless Π-terms is equal to the number of variables in Equation (4.8) (i.e., $p = 8$) minus the number of reference dimensions (i.e., $q = 2$), leading to six dimensionless Π-products (i.e., $N = p - q = 6$). Based on conventional Π-theorem approach, the $N = 6$ dimensionless terms should be normalized by the remaining list of $p - N = q = 2$ *repeated* variables that are free to appear in all groups of dimensionless terms with the conditions that repeated variables cannot (a) themselves form a dimensionless term, (b) be dimensionless (e.g., μ_s and μ_k), and (c) be variables with the same or different powers of identical reference dimension (e.g., length $[L]$ and second moment of area $[L^4]$) (Butterfield 1999). The choice of the pulse length scale, $L_p = a_p T_p^2$, can aid the selection of an appropriate group of repeated variables since its parameters, a_p and T_p, should be among the admissible groups of repeated variables satisfying the aforementioned conditions. The pair (a_p, T_p) satisfies the conditions of repeated variables and is used to normalize the parameters of Equation (4.8). It is worth mentioning that although the Buckingham theorem determines the number of dimensionless terms needed to describe the solution, it does not provide any direction on how to select them, nor does it offer information on how these factors influence the solution. Thus, depending on the different physical justifications for a problem at hand and specific goal of the parametric study, one may choose different combinations of parameters that produce the same number of dimensionless terms. A proper choice of repeated variables is, however, the one that results in the least scatter in the results.

Normalizing the peak sliding displacement, $u_{\max}$, by the length scale of the pulse, $L_p = a_p T_p^2$, results in the first dimensionless Π-term

$$\Pi_1 = \frac{u_{\max}}{a_p T_p^2} \tag{4.9}$$

The choice of some of the remaining dimensionless parameters presented in this section is motivated by the previous works by Makris & Black (2004a, 2004b) on dimensional analysis of rigid-plastic and elastoplastic oscillators. Though some of the dimensionless parameters are similar to the ones presented in those works, they are presented again in this paper, together with new parameters that are exclusive to the Stribeck friction and flexible slider model. The second Π-term is constructed using the kinetic friction coefficient, μ_k,

$$\Pi_2 = \frac{\mu_k g}{a_p} \tag{4.10}$$

However, in the case of the dimensionless term including μ_s, first we assume a dummy dimensionless parameter as $\Pi_* = \mu_s g / a_p$, similar to $\Pi_2 = \mu_k g / a_p$. Subsequently, to obtain a more meaningful Π-term, Π_3 is defined as

$$\Pi_3 = \frac{\Pi_2}{\Pi_*} = \frac{\mu_k}{\mu_s} \tag{4.11}$$

More Π-terms follow by selecting

$$\Pi_4 = \beta a_p T_p \tag{4.12}$$

$$\Pi_5 = \gamma a_p T_p \tag{4.13}$$

Note that the force associated with the viscous properties of the contact is

$$F_\gamma = \gamma \dot{u}_s m g \tag{4.14}$$

And the last Π-term is defined by

$$\Pi_6 = \frac{T}{T_P} \tag{4.15}$$

The resulting dimensionless equation for sliding takes the form

$$\frac{u_{\max}}{a_p T_p^2} = \Phi\left(\frac{\mu_k g}{a_p}, \frac{\mu_k}{\mu_s}, \beta a_p T_p, \gamma a_p T_p, \frac{T}{T_P}\right) \tag{4.16}$$

where Φ is a function that can be obtained either analytically, if a closed-form solution exists, or numerically, for each pulse type. Exclusively, μ_k / μ_s, $\beta a_p T_p$, and T / T_P, among other Π-terms, affect the nature of the sliding problem. In other words, extreme limits of these parameters result in special cases of the sliding problem as presented in Table 4-1. Describing the behavior using dimensionless terms, the effects of different parameters on the response can be examined. In the following subsections, the effects of dimensionless parameters are investigated. Based on the extraction of coherent long-period pulses from eight famous pulse-like ground motions, $a_p T_p = 5$ m/s is the maximum value considered in this study. $\beta = 1000$ s/m is assumed to be a numerical value considerably larger than what has been observed in friction experiments performed on various surfaces, simulating a very sudden drop from static to kinetic friction force, i.e., Static+Coulomb friction model. Therefore, $\Pi_4 = \beta a_p T_p = 5000$ is the higher bound considered in this study.

4.7.1 Effect of $\Pi_3 = \mu_k / \mu_s$: the ratio of kinetic to static friction

Table 4-1 illustrates the range of parameter μ_k / μ_s for the various sliding models discussed in this study. $\mu_k / \mu_s = 1$ indicates Coulomb friction, while values lower than unity describe Stribeck friction, which reduces to the special-case of Static+Coulomb friction model when $\Pi_4 = \beta a_p T_p \to \infty$. The practical range of the parameter μ_k / μ_s changes based on the properties of the problem being investigated. For instance, experimental investigations on light science laboratory equipment items have shown μ_k / μ_s to range between 0.73 and 1.0 (Chaudhuri & Hutchinson, 2005).

Values of static and kinetic friction coefficients extracted from experimental tests on three heavy laboratory equipment (Konstantinidis & Makris 2005; Konstantinidis & Makris 2009) yield $\mu_k / \mu_s =$ 0.72, 0.76, and 0.77. Based on those observations, a lower bound value of $\mu_k / \mu_s = 0.5$ is assumed in this study. The dimensionless curves (master curves) demonstrating the effect of μ_k / μ_s on the response of a rigid block ($T / T_P = 0$) under One-Cosine, Type C1, and symmetric Ricker wavelet excitations are presented in Fig. 4-12. The dimensionless curves are obtained for $\beta a_p T_p = 5000$, representing Static+Coulomb friction. Regardless of the type of wavelet excitation, the presence of static friction reduces the maximum sliding response for larger values of $\mu_k g / a_p$ (approximately greater than 0.4). However, under the symmetric Ricker wavelet, the presence of static friction results in amplification in the response in the $0.1 < \mu_k g / a_p < 0.3$ range. Therefore, in these cases, using a Coulomb friction model, which neglects the static phase of friction, would result in unconservative predictions of the maximum sliding displacement. This finding may be one of the reasons explaining why the Coulomb friction model used by Konstantinidis and Makris (Konstantinidis & Makris 2005; Konstantinidis & Makris 2009) underestimated the sliding displacements of the heavy laboratory equipment, compared to observations from shake table tests.

The amplification under the symmetric Ricker wavelet excitation is attributed to the resistance of the system with high static friction during the first minor pulse of the Ricker wavelet (see Fig. 4-9). Specifically, during the first minor pulse (negative ground acceleration) of the Ricker wavelet, a block with $\mu_k / \mu_s = 1$ (black line in Fig. 4-12) starts sliding to the right earlier than a block with $\mu_k / \mu_s < 1$; subsequently, during the major pulse of the Ricker wavelet (positive ground acceleration), the direction of sliding reverses for both blocks but because by this point the block with $\mu_k / \mu_s = 1$ has slide to the right more than the block with $\mu_k / \mu_s < 1$, when it slides to the left and eventually comes to a stop, its peak sliding displacement is less. This type of response is illustrated in Fig. 4-11 (bottom left) for $\mu_k g / a_p = 0.2$, $\mu_k / \mu_s = 0.5$ and $\beta a_p T_p = 122.5$.

Therefore, even though static friction increases the strength (resistance) of the system, it may result in amplification due to the presence of preceding or succeeding pulses close to the major pulse in real earthquake excitations. Comparison of the different curves in Fig. 4-12 shows that the maximum sliding response exhibits similarity in the range of μ_k / μ_s corresponding to previously tested sliding equipment (i.e., $0.7 \le \mu_k / \mu_s \le 1.0$). Therefore, in the case of a rigid sliding block, one may assume that $\Pi_1 = u_{\mathbf{max}} \big/ a_p T_p^2$ is almost independent of μ_k / μ_s in that range and thus simplify the dimensionless sliding equation

$$\begin{cases} \dfrac{u_{\max}}{a_p T_p^2} \approx f\left(\dfrac{\mu_k g}{a_p}, \beta a_p T_p, \gamma a_p T_p \right) & \text{for} \quad 0.7 \le \dfrac{\mu_k}{\mu_s} \le 1.0 \text{ and } \dfrac{T}{T_P} = 0 \\ \dfrac{u_{\max}}{a_p T_p^2} \approx f\left(\dfrac{\mu_k g}{a_p}, \dfrac{\mu_k}{\mu_s}, \beta a_p T_p, \gamma a_p T_p \right) & \text{for} \quad \dfrac{\mu_k}{\mu_s} \le 0.7 \text{ and } \dfrac{T}{T_P} = 0 \end{cases} \tag{4.17}$$

Fig. 4-13 presents the master curves for $T / T_P = 1$, representing a dynamic system sliding under a wavelet excitation with period, T_P, equal to its fundamental natural period, T. The amplifications are now more pronounced comparing to rigid systems (presented in Fig. 4-12). In contrast to rigid sliding block, the similarity of the response to μ_k / μ_s in the range of sliding equipment is no longer valid. The curve corresponding to $\mu_k / \mu_s = 1$ represents the coupled sliding model with Coulomb friction used in sliding simulations of geotechnical structures. As can be seen, presence of a static friction greater than kinetic friction ($\mu_k / \mu_s < 1$) may result in considerable amplifications, e.g., more than 50% for $\mu_k / \mu_s = 0.7$, in the response that has not been considered in conventional coupled sliding models. Moreover, comparing Fig. 4-12 and Fig. 4-13 demonstrates a fundamental difference in the responses of rigid and non-rigid sliding blocks. The non-rigid sliding block (see Fig. 4-13) exhibits its peak sliding response ($u_{\mathbf{max}} \big/ a_p T_p^2 \approx 0.09$ for $\mu_k / \mu_s = 0.7$) at a $\mu_k g / a_p$ ($\mu_k g / a_p = 0.66$) relatively where sliding of rigid block (see Fig. 4-12) approaches to zero.

4.7.2 Effect of $\Pi_4 = \beta a_p T_p$: the transition sharpness from static to kinetic friction

The effect of transition parameter β on the sliding response is examined by developing dimensionless curves for $50 \le \beta a_p T_p \le 5000$. It is worth mentioning that, while the dimensioned parameter β controls the aggressiveness of the transition from static to kinetic friction, it is the dimensionless parameter $\beta a_p T_p$ that demonstrates the dynamic effects of this transition. The master curves associated with the rigid sliding block are presented in Fig. 4-14. The curves are close to each other in the assumed range of this parameter. Consequently, since changing $\beta a_p T_p$ by two orders of magnitude, from 50 to 5000, results in relatively comparable master curves, it can be said that the dimensionless sliding response, $u_{\mathbf{max}} / a_p T_p^2$, exhibits *complete similarity* in $\beta a_p T_p$ when $T / T_P \approx 0$. Hence, the simplified sliding equation described by Equation (4.17) becomes

$$\begin{cases} \dfrac{u_{\max}}{a_p T_p^2} \approx f\left(\dfrac{\mu_k g}{a_p}, \gamma a_p T_p\right) & \text{for} \quad 0.7 \le \dfrac{\mu_k}{\mu_s} \le 1.0 \text{ and } \dfrac{T}{T_P} = 0 \\ \dfrac{u_{\max}}{a_p T_p^2} \approx f\left(\dfrac{\mu_k g}{a_p}, \dfrac{\mu_k}{\mu_s}, \gamma a_p T_p\right) & \text{for} \quad \dfrac{\mu_k}{\mu_s} \le 0.7 \text{ and } \dfrac{T}{T_P} = 0 \end{cases} \tag{4.18}$$

If assuming no damping at the contact surface, $\gamma a_p T_p = 0$, the dimensionless sliding displacement $u_{\mathbf{max}} / a_p T_p^2$ for rigid sliding blocks is approximately a function of only $\mu_k g / a_p$, i.e., practically only the kinetic friction coefficient for sliding equipment and contents with $0.7 \le \mu_k / \mu_s \le 1.0$. The dimensional analysis approach used in this study, therefore, formally shows that the kinetic friction coefficient plays a dominant role on the maximum sliding response of a rigid object—an observation made experimentally or numerically in previous investigations (Newmark 1965; Konstantinidis & Makris 2005; Chaudhuri & Hutchinson 2005; Hutchinson & Chaudhuri 2006; Konstantinidis & Makris 2009). Fig. 4-15 shows the effect of $\beta a_p T_p$ on the response of a coupled sliding system at resonance and $\mu_k / \mu_s = 0.7$. Contrary to the rigid block, the dimensionless response of non-rigid blocks is affected considerably by $\beta a_p T_p$. Low values of $\beta a_p T_p$ increase the potential of stick-slip occurrence in the process of sliding. Fig. 4-15 illustrates that low values of $\beta a_p T_p$ can result in amplification in the response compared to Static+Coulomb friction model (black line).

4.7.3 Effect of $\Pi_5 = \gamma a_p T_p$: viscous property of the contact

Only a handful of experiments are available for evaluating the velocity dependence of friction in structural engineering applications. One of them (Konstantinidis et al. 2008) involved cyclic testing of sliding bridge bearings, which on average exhibited a maximum γ of about 0.05 s/m. For the purposes of the present study, the upper bound of $\gamma a_p T_p$ is considered by assuming the maximum values of $\gamma = 0.1$ s/m, $a_p = 2g$, and $T_p = 5$ s; resulting in $\gamma a_p T_p \approx 10$. Fig. 4-16 illustrates that increasing $\gamma a_p T_p$ has a profound effect on reducing the sliding response, especially for lower values of $\mu_k g / a_p$. Similar dimensionless curves but for non-rigid block at the resonant condition are shown in Fig. 4-17. The presence of damping at the contact changes the response of non-rigid block. In this case, increase of damping does not necessarily decrease the sliding response of the system.

4.8 Conclusion

This paper investigated the effect of the stick-slip phenomenon in the sliding problem widely encountered in structural and earthquake engineering applications, e.g., the seismic response of unanchored nonstructural components, base isolated structures and bridges, and geotechnical/earth structures. A sliding model capable of capturing intermittent stick-slip is developed by considering elasticity at the contact (equivalently, the flexibility of the structure above the sliding surface) and Stribeck friction, which defines the velocity-dependence of friction at low velocities. The stick-slip model is general in the sense that existing simplified sliding models, such as Newmark's rigid sliding block and the coupled sliding model developed previously to estimate the sliding response of geostructures can be considered to be special cases.

The mathematical formulation of the stick-slip sliding is derived. It is shown that the presence of flexibility (or elasticity at contact) and velocity-dependent friction (Stribeck friction) changes the nature of problem considerably and may introduce stick-slip oscillations in the sliding process. The effects of the kinetic-to-static friction ratio, transition sharpness from static to kinetic friction, viscous damping at the contact surface, and elasticity of contact (or the flexibility of the structure above the slide surface) are investigated through dimensional analysis. Dimensionless curves corresponding to three common wavelets are generated for various combinations of dimensionless parameters in order to compare the results of conventional sliding models, such as Newmark's sliding model and coupled sliding model with Coulomb or Static+Coulomb friction, with the stick-slip model. It is demonstrated that simplified sliding models may underestimate the sliding response. It is also shown that the sliding response is influenced by the sequence of pulses in the input excitation; therefore, the study suggests that when analytical pulses are to be used to represent pulse-like ground motions, they should not only represent the kinematics of the ground motions accurately, but also consistently simulate the sequence of preceding and succeeding minor pulses in the input excitation.

The most important observations of the parametric study presented in this paper are summarized as follows:

- Depending on the shape and parameter values of the excitation pulse, inclusion of static friction may result in larger peak sliding displacement for a rigid block. However, as the dimensionless curves demonstrated, within the range of $0.7 \leq \mu_k / \mu_s \leq 1.0$ (which corresponds to observed values in previously tested sliding equipment), the peak sliding response is primarily controlled by the kinetic friction, not the static friction. Consequently, the peak sliding response does not depend on the transition parameter either.
- The sliding of non-rigid blocks is greatly influenced by the presence of static friction. At the lower bound value of previously tested building equipment and

contents, i.e., $\mu_k / \mu_s = 0.7$, the assumption of Coulomb friction, i.e., $\mu_k / \mu_s = 1.0$, can underestimate the peak sliding demands by 31%, 24%, and 23% under One-Cosine, Type-C1, and Symmetric Ricker pulses, respectively.

- An increase in the viscous damping of the contact greatly reduces the peak sliding response of rigid blocks, whereas, if the block is non-rigid, it does not necessarily decrease the sliding response.

In closing, it is noted that studying the effects of various factors that may play a role in the response of a sliding system were beyond the scope of the current study. Future studies may examine the effects of vertical excitation and pressure-dependent friction.

4.9 References

Armstrong-Helouvry, B., 1990. Stick-slip arising from Stribeck friction. In *Proceedings of International Conference on Robotics and Automation, IEEE*. Cincinnati, 1990.

Armstrong-Helouvry, B., Dupont, P. & Canudas De Wit, C., 1994. A Survey of Models, Analysis Tools and Compensation Methods for the Control of Machines with Friction. *Automatica*, 30(7), pp.1083-138.

Bengisu, M.T. & Akay, A., 1999. Stick–slip oscillations: dynamics of friction and surface. *Journal of Acoustical Society of America*, 105(1), pp.194-205.

Biscontin, G. & Pestana, J.M., 2001. Influence of peripheral velocity on vane shear strength of an artificial clay. *Geotechnical Testing Journal*, 24(4), p.423–429.

Butterfield, R., 1999. Dimensional analysis for geotechnical engineers. *Geotechnique*, 46(3), p.357–366.

Chaudhuri, S.R. & Hutchinson, T.C., 2005. Characterizing frictional behavior for use in predicting the seismic response of unattached equipment. *Soil Dynamics and Earthquake Engineering*, 25, p.591–604.

Choi, B. & Tung, C.C.D., 2002. Estimating sliding displacement of an unanchrored Body subjected to earthquake. *Earthquake Spectra*, 18(4), p.601–613.

Chopra, A. & Zhang, L., 1991. Earthquake-induced base sliding of concrete gravity dams. *Journal of Structural Engineering, ASCE*, 117(12), p.3698–3719.

Conte, E. & Dente, G., 1989. An analytical solution for Newmark's sliding block. *Soils and Foundations*, 29(3), pp.152-56.

Coulomb, C.A., 1785. Theorie des machines simples, en ayant egard au frottement de leurs parties, et a la roideur dews cordages. *Memoirs on Differential equations and Mathematical Physics*, pp.161-342.

Dao, N.D., Ryan, K.L., Sato, E. & Sasaki, T., 2013. Predicting the displacement of triple pendulum™ bearings in a full-scale shaking experiment using a three-dimensional element. *Earthquake Engineering & Structural Dynamics*, 42(11), p.1677–1695.

Dieterich, J.H., 1991. Micro-mechanics of slip instabilities with rate- and state-dependent friction. *Eos, Transactions American Geophysical Union, Fall Meeting Abstract*, 324.

Fenz, D.M. & Constantinou, M.C., 2008. Spherical sliding isolation bearings with adaptive behavior: Experimental verification. *Earthquake Engineering & Structural Dynamics*, 37(2), p.185–205.

Garini, E., Gazetas, G. & Anastasopoulos, I., 2011. Asymmetric 'Newmark' sliding caused by motions containing severe 'directivity' and 'fling' pulses. *Géotechnique*, 61(9), p.733 –756.

Gazetas, G., Garini, E. & Anastasopoulos, I., 2009. Effect of near-fault ground shaking on sliding systems. *Journal of Geotechnical Engineering (ASCE)*, 135(12), p.1906–1921.

Gazetas, G. & Uddin, N., 1994. Permanent deformation on preexisting sliding surfaces in dams. *Journal of Geotechnical Engineering*, 120(11), p.2041–2061.

Hall, J.F., Heaton, T.H., Halling, M.W. & Wald, D.J., 1995. Nearsource ground motion and its effects on flexible buildings. *Earthquake Spectra*, 11(4), p.569–605.

Hess, D.P. & Soom, A., 1990. Friction at a lubricated line contact operating at oscillating sliding velocities. *Journal of Tribology*, 112(1), pp.147-52.

Hutchinson, T.C. & Chaudhuri, S.R., 2006. Bench-shelf system dynamic characteristics and their effects on equipment and contents. *Earthquake Engineering & Structural Dynamics*, 35(13), p.1631–1651.

Kim, J., Riemer, M. & Bray, J.D., 2005. Dynamic properties of geosynthetic interfaces. *Geotechnical Testing Journal*, 28(3), pp.288-96.

Konstantinidis, D., Kelly, J.M. & Makris, N., 2008. Report No. UCB/EERC-2008/02 *Seismic response of bridge bearings*. Earthquake Engineering Research Center, University of California, Berkeley.

Konstantinidis, D. & Makris, N., 2005. Seismic response analysis of multidrum classical columns. *Earthquake Engineering and Structural Dynamics*, 34(10), p.1243–1270.

Konstantinidis, D. & Makris, N., 2005. Report No. 2005/07 *Experimental and analytical studies on the seismic response of freestanding and anchored laboratory equipment*. CA: Pacific Earthquake Engineering Research Center(PEER) University of California, Berkeley. Report No. PEER 2005-07.

Konstantinidis, D. & Makris, N., 2009. Experimental and analytical studies on the response of freestanding laboratory equipment to earthquake shaking. *Earthquake Engineering & Structural Dynamics*, 38(6), p.827–848.

Konstantinidis, D. & Makris, N., 2010. Experimental and analytical studies on the response of 1/4-scale models of freestanding laboratory equipment subjected to strong earthquake shaking. *Bulletin of Earthquake Engineering*, 8, p.1457–1477.

Konstantinidis, D. & Nikfar, F., 2015. Seismic response of equipment and contents in base-isolated buildings subjected to broad-band ground motions. *Earthquake Engineering & Structural Dynamic*, 44(6), p.865–887.

Kramer, S. & Smith, M., 1997. Modified Newmark model for seismic displacements of compliant slopes. *Journal of Geotechnical and Geoenvironmental Engineering*, 123(7), p.635–644.

Lampaert, V., Swevers, J. & Al-bender, F., 2002. Experimental comparison of different friction models for accurate low-velocity tracking. In *Proceedings of the 10th Mediterranean Conference on Control and Automation*. Lisbon, Portugal, 2002.

Lin, J.-S. & Whitman, R.V., 1983. Decoupling approximation to the evaluation of earthquake-induced plastic slip in earth dams. *Earthquake Engineering & Structural Dynamics* , 11(5), p.667–678.

Lopez Garcia, D. & Soong, T.T., 2003. Sliding fragility of block-type non-structural components. Part 1: unrestrained components. *Earthquake Engineering & Structural Dynamics*, 32(1), p.111–129.

Makdisi, F.I. & Seed, H.B., 1978. Simplified procedure for estimating dam and embankment earthquake-induced deformations. *Journal of Geotechnical Engineering Division, ASCE*, 104(7), p.849–867.

Makris, N., 1997. Rigidity–plasticity–viscosity: can electrorheological dampers protect base-isolated structures from nearsource ground motions? *Earthquake Engineering & Structural Dynamics*, 26(5), p.571–591.

Makris, N. & Black, C.J., 2004. Dimensional analysis of rigid-plastic and elastoplastic structures under pulse-type excitations. *Journal of Engineering Mechanics(ASCE)*, 130(9), p.1006–1018.

Makris, N. & Black, C., 2004. Evaluation of peak ground velocity as a 'Good' intensity measure for near-source ground motions. *Journal of Engineering Mechanics (ASCE)*, 130(9), pp.1032-44.

Makris, N. & Constantinou, M.C., 1991. Analysis of motion resisted by friction. I. Constant Coulomb and Linear/Coulomb Friction. *Mechanics of Structures and Machines*, 19(4), pp.477-500.

Makris, N. & Constantinou, M.C., 1991. Analysis of motion resisted by friction. II. Velocity dependent friction. *Mechanics of Structures and Machines*, 19(4), pp.501-26.

Makris, N. & Roussos, Y.S., 2000. Rocking response of rigid blocks under near-source ground motions. *Géotechnique*, 50(3), p.243–262.

Makris, N. & Vassiliou, M.F., 2011. The existence of "complete similarities" in the response of seismic isolated structures subjected to pulse-like ground motions and their implications in analysis. *Earthquake Engineering & Structural Dynamics*, 40(10), p.1103–1121.

Mavroeidis, G.P. & Papageorgiou, A.S., 2003. A mathematical representation of near-fault ground motions. *Bulletin of the Seismological Society of America* , 93(3), p.1099–1131.

Mokha, A., Constantinou, M. & Reinhorn, A., 1990. Teflon Bearings in Base Isolation I: Testing. *Journal of Structural Engineering (ASCE)*, 116(2), p.438–454.

Mokha, A., Constantinou, M. & Reinhorn, A., 1991. Further Results on Frictional Properties of Teflon Bearings. *Journal of Structural Engineering (ASCE)*, 117(2), p.622–626.

Mostaghel, N. & Davis, T., 1997. Representation of coulomb friction for dynamic analysis. *Earthquake Engineering & Structural Dynamics*, 26(5), p.541–548.

Nasuno, S., Kudrolli, A. & Gollub, J.P., 1997. Friction in granular layers: hysteresis and precursors. *Physical Rivew Letter*, 79(5), p.949–952.

Newmark, N.M., 1965. Effects of earthquakes on dams and embankments. *Géotechnique*, 15, p.139–160.

Newmark, N.M. & Rosenblueth, E., 1971. *Fundamentals of earthquake engineering*. Englewood Cliffs, NJ.: Prentice Hall.

Nikfar, F. & Konstantinidis, D., 2013. Sliding response analysis of operational and functional components (OFC) in seismically isolated buildings. In *3rd Specialty Conference on Disaster Prevention and Mitigation, Canadian Society of Civil Engineering (CSCE)*. Montreal, 2013.

Nikfar, F. & Konstantinidis, D., 2014. Solving dynamical systems with path-dependent nonlinearities using MATLAB ODE solvers. In *10th National Conference in Earthquake Engineering, Earthquake Engineering Research Institute*. Anchorage, AK, 2014.

Paolacci, F. et al., 2014. JRC89069 *Assessment of the seismic vulnerability of an old RC viaduct with frame piers and study of the effectiveness of base isolation through PsD testing (RETRO)*. EUR - Scientific and Technical Research Reports. Ispra, Italy: Publications Office of the European Union JRC institute for the Protection and Security of the Citizen.

Persson, B.N.J. & Popov, V.L., 2000. On the origin of the transition from slip to stick. *Solid State Communications*, 114(5), p.261–266.

Rathje, E. & Bray, J., 2000. Nonlinear coupled seismic sliding analysis of earth structures. *Journal of Geotechnical and Geoenvironmental Engineering, ASCE*, 126(11), p.1002–1014.

Sarma, S.K., 1975. Seismic stability of earth dams and embankments. *Geotechnique*, 25(4), p.743–761.

Scholz, C.H., 2002. *The mechanics of earthquakes and faulting*. Cambridge University Press.

Singh, B.R., 1960. Study of critical velocity of stick-slip sliding. *Journal of Engineering for Industry*, 82(4), pp.393-98.

Somerville, P. & Graves, R., 1993. Conditions that give rise to unusually large long period ground motions. *The Structural Design of Tall Buildings* , 2(3), p.211–232.

Steelman, J., Fahnestock, L., Hajjar, J. & LaFave, J., 2015. Performance of nonseismic PTFE sliding bearings when subjected to seismic demands. *Journal of Bridge Engineering (ASCE)*, (in press).

Stribeck, R., 1902. Die Wesentlichen Eigenschaften der Gleit- und Rollenlager-the key qualities of sliding and roller bearings. *Zeitschrift des Vereines Seutscher Ingenieure*, 46(38), pp.1432-37.

Tsopelas, P., Constantinou, M., Kim, Y.S. & Okamoto, S., 1996. Experimental study of FPS sytem in bridge sesimic isolation. *Earthquake Engineering & Structural Dynamics*, 25(1), p.65–78.

Wright, J.P., ans Pei, J.S. (2012). “Solving dynamical systems involving piecewise restoring force using state event location.” *Journal of Engineering Mechanics (ASCE)*, 138(8), pp. 997-1020.

Van De Velde, F. & De Baets, P., 1996. Mathematical approach of the influencing factors on stick-slip induced by decelerative motion. *Wear*, 201(1-2), pp. 80-93.

Van De Velde, F. & De Baets, P., 1998. The relation between friction force and relative speed during the slip-phase of a stick-slip cycle. *Wear*, 219(2), p.220–226.

Vassiliou M.F. & Makris, N., 2012. Analysis of the rocking response of rigid blocks standing free on a seismically isolated base. *Earthquake Engineering & Structural Dynamics*, 41(2), p.177–196.

Vassiliou, M.F., Anastasios, T. & Stojadinović, B., 2013. Dynamics of inelastic base-isolated structures subjected to analytical pulse ground motions. *Earthquake Engineering & Structural Dynamics*, 42(14), p.2043–2060.

Vassiliou, M.F. & Makris, N., 2011. Estimating time scales and length scales in pulse-like earthquake acceleration records with wavelet analysis. *Bulletin of the Seismological Society of America*, 101(2), p.596–618.

Veletsos, A.S., Newmark, N.M. & Chelepati, C.V., 1965. Deformation spectra for elastic and elastoplastic systems subjected to ground shock and earthquake motions. In *Proceedings of the 3rd World Conference on Earthquake Engineering*. Wellington, New Zealand, 1965.

Voyagaki, E., 2012. *Contributions to dynamic response of yielding systems to near-fault earthquake motions*. PhD Thesis, School of Civil Engineering, National Technical University, Athens, Greece.

Voyagaki, E., Mylonakis, G. & Psycharis, I., 2012. Rigid block sliding to idealized acceleration pulses. *Journal of Engineering Mechanics (ASCE)*, 138(9), pp.1071-83.

Wartman, J., Seed, R.B. & Bray, J.D., 2005. Shaking table mdeling of seismically induced deformations in slopes. *Journal of Geotechnical and Geoenvironmental Engineering*, 131(5), pp.610-22.

Wolff, E. & Constantinou, M., 2004. MCEER-04-0001 *Experimental study of seismic isolation systems with emphasis on secondary system response and verification of accuracy of dynamic response history analysis methods*. Technical Report. NY: Multidisciplinary Center for Earthquake Engineering Research University at Buffalo.

Wolff, E., Ipek, C., Constantinou, M. & Tapan, M., 2015. Effect of viscous damping devices on the response of seismically isolated structures. *Earthquake Engineering & Structural Dynamics*, 44(2), p.185–198.

Xia, F., 2003. Modelling of a two-dimensional Coulomb friction oscillator. *Journal of Sound and Vibration*, 265(5), pp.1063-74.

Yeow, T.Z., MacRae, G.A., Dhakal, R.P. & Bradley, B.A., 2014. Preliminary experimental verification of current content sliding modelling techniques. In *2014 New Zealand Society for Earthquake Engineering Conference*. Auckland, New Zealand, 2014.

Table 4-1. Various rigid block sliding models and coupled sliding models with different friction descriptions, together with their associated ranges of dimensionless terms.

Rigid block sliding models			Coupled sliding models		
w/ Coulomb Friction (*Newmark's Block*)	w/ Static+Coulomb Friction	w/ Stribeck Friction	w/ Coulomb Friction	w/ Static+Coulomb Friction	w/ Stribeck Friction (*Stick-Slip Model*)
$\mu_k / \mu_s = 1$	$0 < \mu_k / \mu_s < 1$	$0 < \mu_k / \mu_s < 1$	$\mu_k / \mu_s = 1$	$0 < \mu_k / \mu_s < 1$	$0 < \mu_k / \mu_s < 1$
-	$\beta a_p T_p \to \infty$	$\beta a_p T_p = \text{finite}$	-	$\beta a_p T_p \to \infty$	$\beta a_p T_p = \text{finite}$
$T / T_P = 0$	$T / T_P = 0$	$T / T_P = 0$	$T / T_P \gg 0$	$T / T_P \gg 0$	$T / T_P \gg 0$

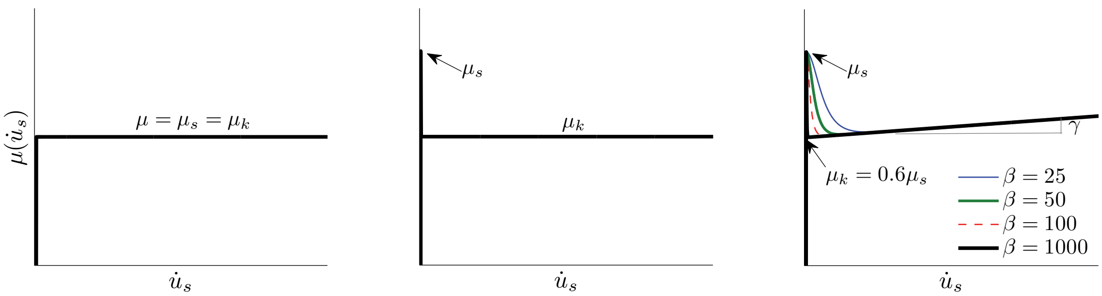

(a) Coulomb model (b) Static+Coulomb model (c) Stribeck model

Fig. 4-1. Friction coefficient μ as a function of sliding velocity $\dot{u}_s$ for various friction models.

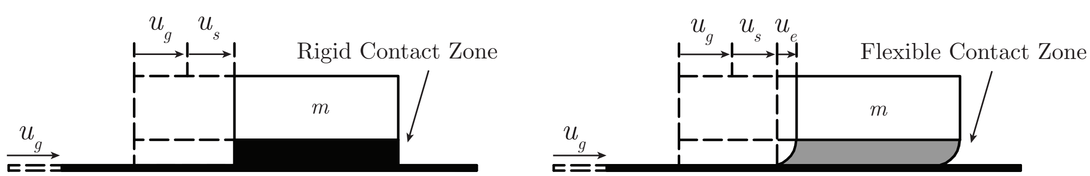

(a) Rigid block model (b) Block with flexible support

Fig. 4-2. (a) Rigid-block model, (b) Model of block with flexible support.

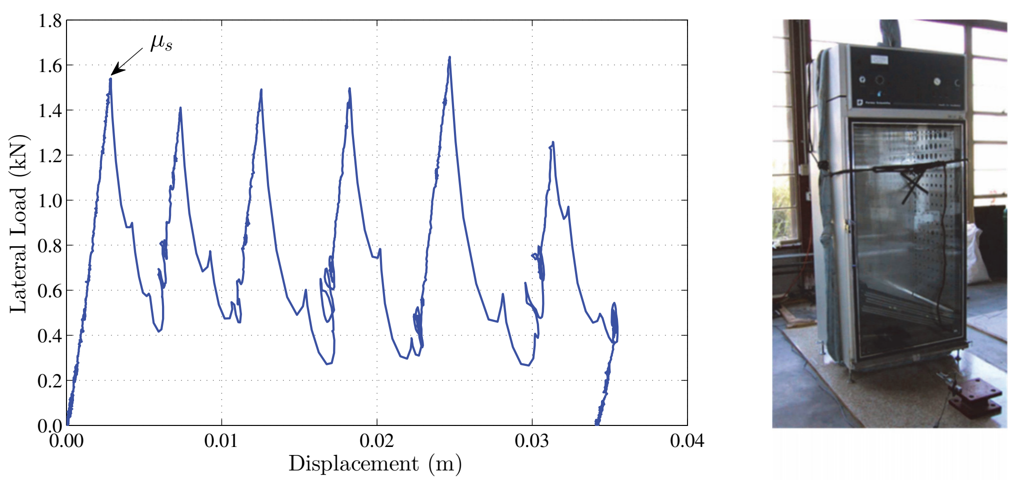

Fig. 4-3. Stick-slip sliding during slow pull test of a science laboratory incubator on a waxed floor surface.

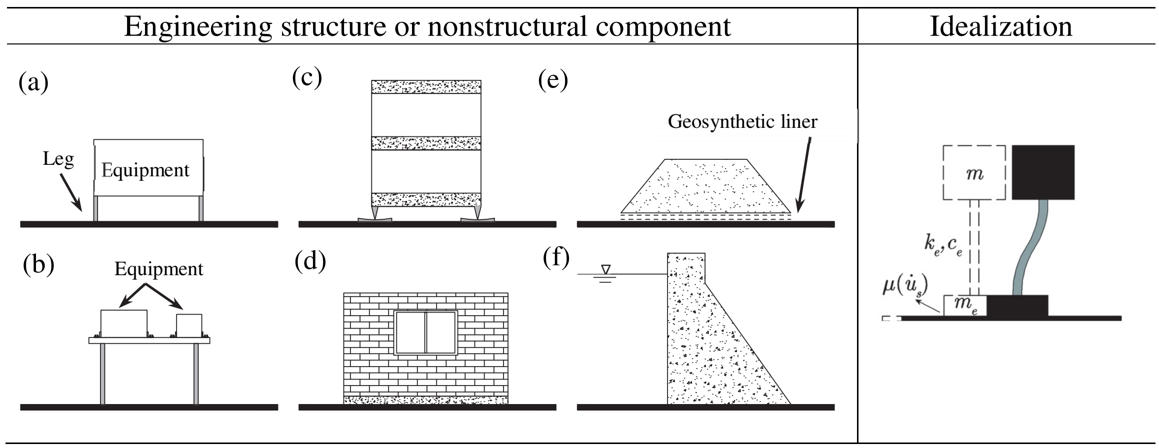

Fig. 4-4. Examples of structures and nonstructural components that can be mathematically modeled by the proposed model with flexibility and Stribeck friction: (a) Equipment on flexible legs, (b) Equipment attached on a freestanding table, (c) Building isolated on friction devices. (d) Masonry structures, (e) Geostructure on geosynthetic liner, (f) Gravity dam.

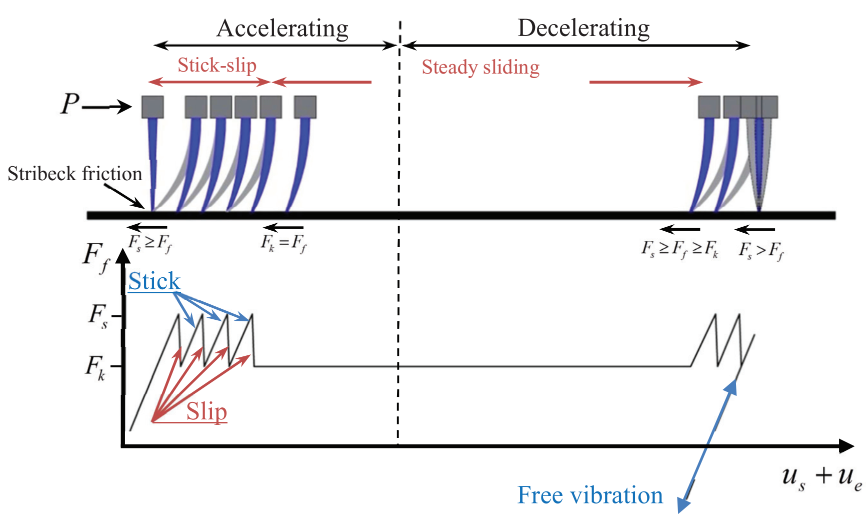

Fig. 4-5. Schematic illustration of the stick-slip phenomenon.

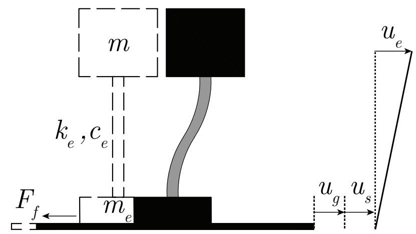

Fig. 4-6. 2DOF stick-slip model

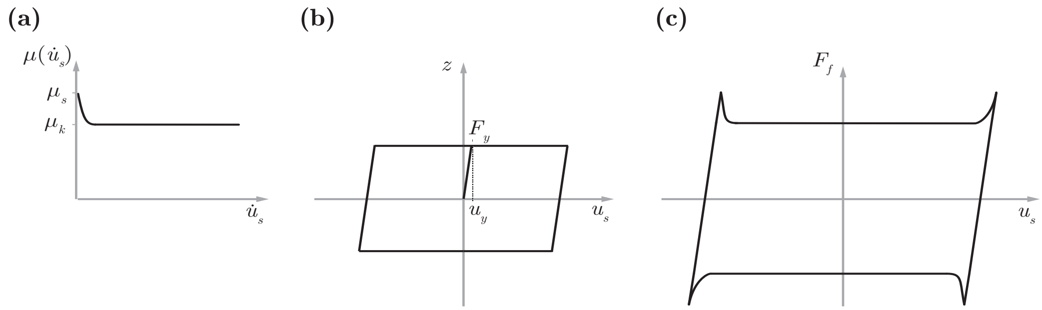

Fig. 4-7. Schematic of simulating friction hysteresis. (a) Velocity-dependent friction coefficient, (b) Elastoplastic hysteresis model, and (c) Resultant friction force hysteresis.

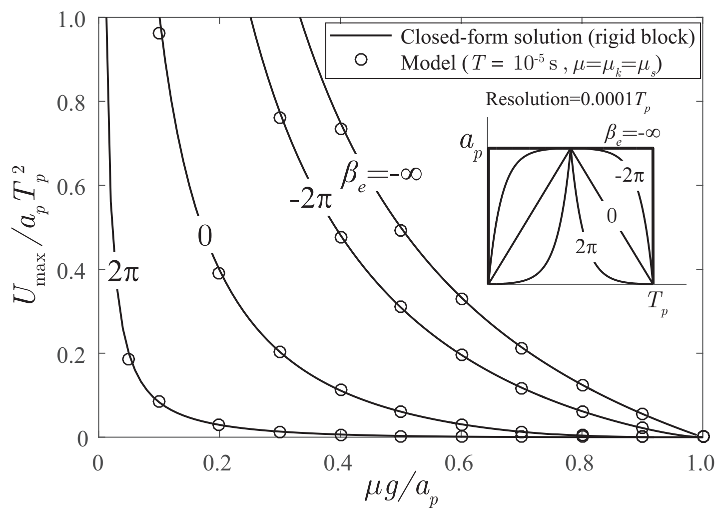

Fig. 4-8. Comparison between closed-form solutions for a rigid sliding block with Coulomb friction and numerical solutions of the stick-slip model ($m_e = 0$) under an exponential pulse excitation with acceleration amplitude a_p, duration T_p, and shape parameter β_e.

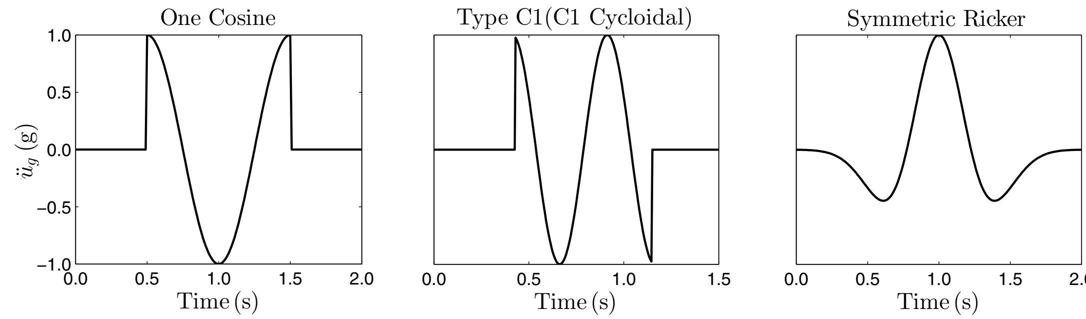

Fig. 4-9. Wavelet types used in this study (in these plots, $T_p = 1.0\,\text{s}$ and $a_p = g$).

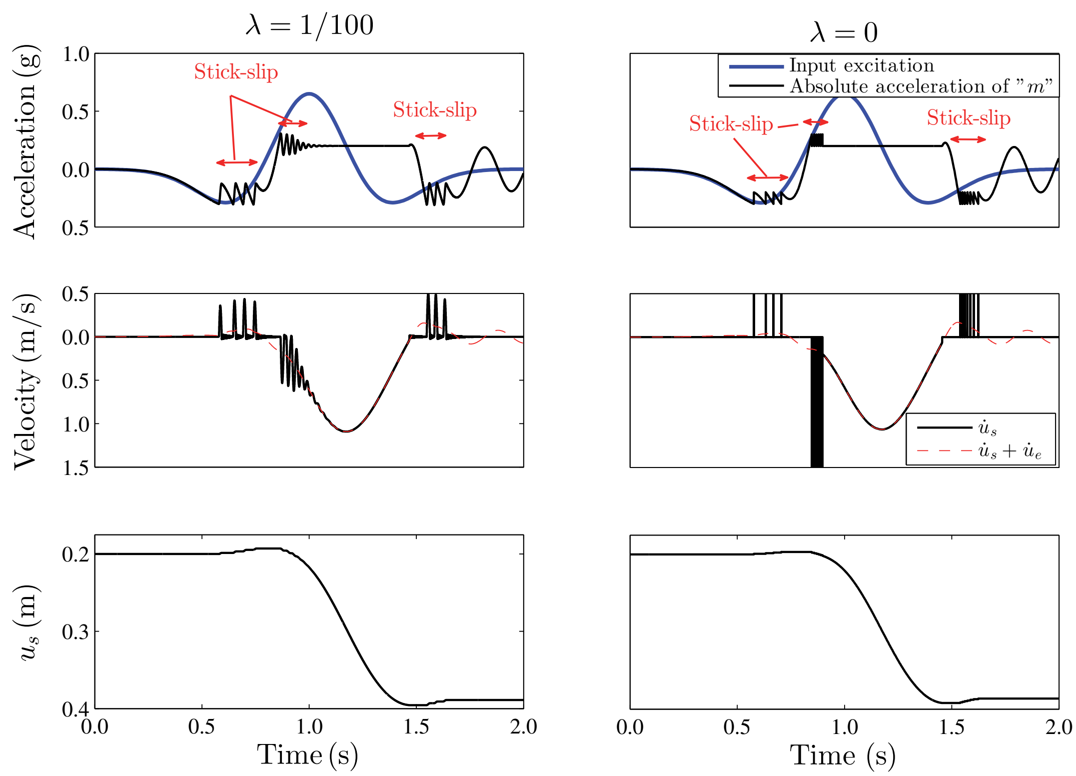

Fig. 4-10. Sliding response of a piece of equipment under a symmetric Ricker wavelet excitation for $\lambda = 1/100$ (left) and $\lambda = 0$ (right) ($k_e = 24.4 \times 10^4$ N/m, $m = 385\,\text{kg}$, 1% viscous damping, $\beta = 100$, $\gamma = 0.0$).

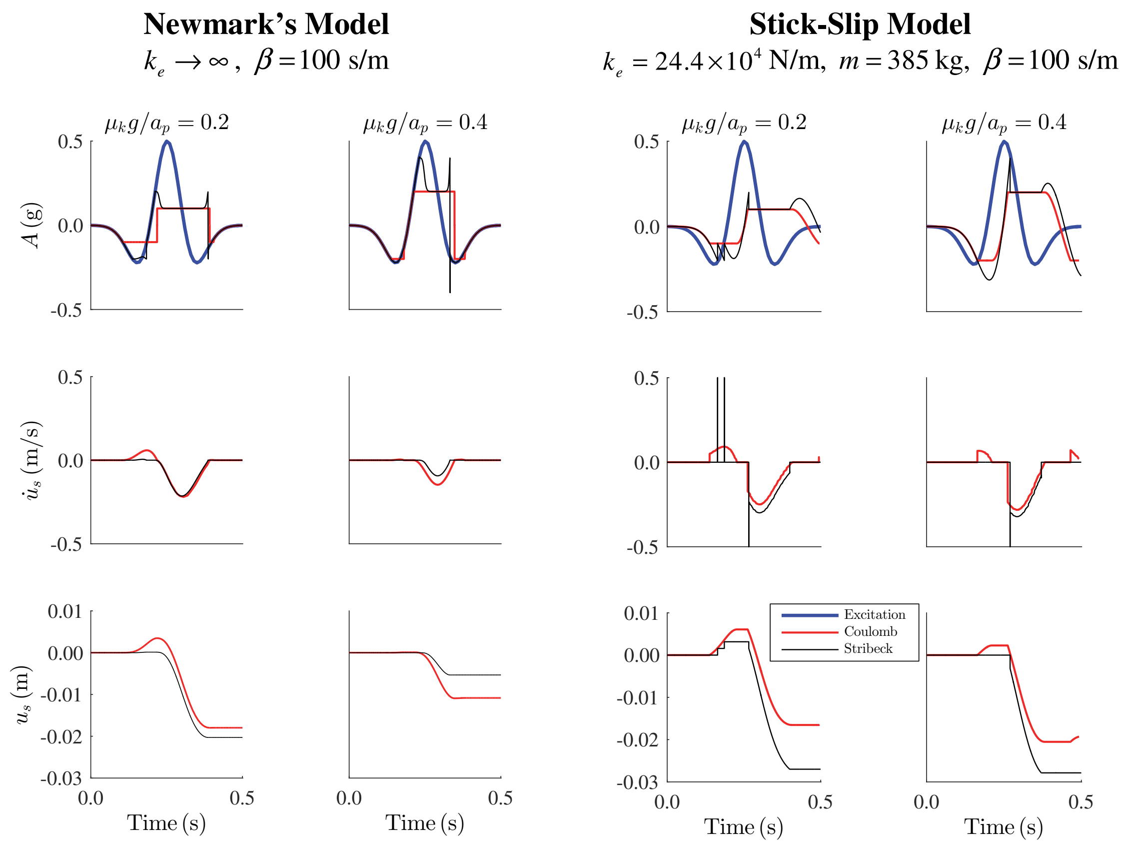

Fig. 4-11. Comparison of the response of Newmark (left) and Stick-slip (right) models ($\lambda = 0$) with Coulomb and Stribeck friction ($\mu_k/\mu_s = 0.5$), under symmetric Ricker wavelet excitation ($T_p = 0.25$ s and $a_p = 0.5g$)

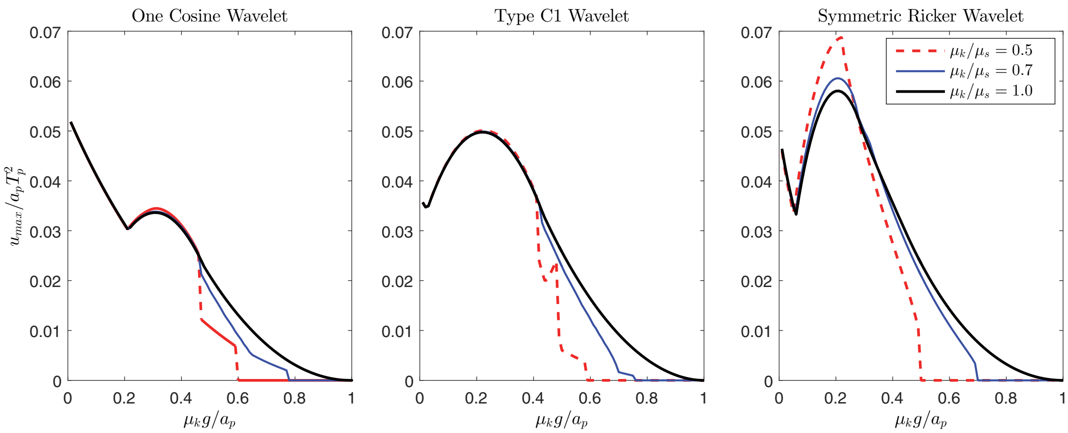

Fig. 4-12. Effect of μ_k / μ_s on the response of a rigid sliding system ($T / T_P = 0$) on a surface charactized by Static+Coulomb friction ($\beta a_p T_p = 5000$).

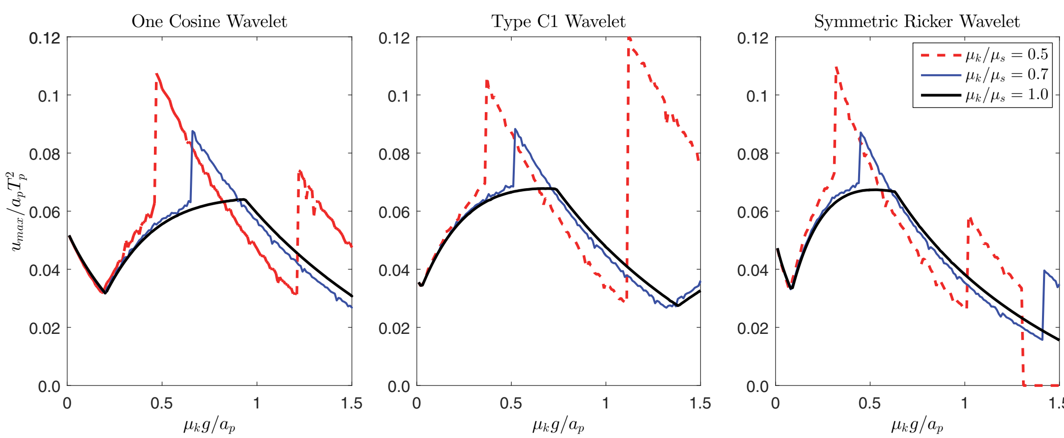

Fig. 4-13. Effect of μ_k / μ_s on the response of a coupled sliding system at resonance, i.e., $T / T_P = 1$. The support surface is characterized by Static+Coulomb friction ($\Pi_4 = \beta a_p T_p = 5000$).

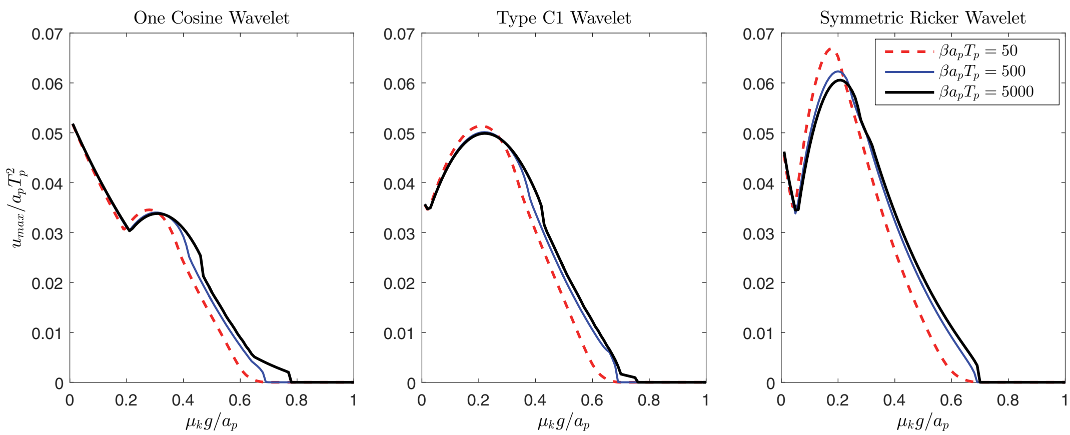

Fig. 4-14. Effect of $\beta a_p T_p$ on the response of a rigid sliding system ($T / T_P = 0$) on a surface with $\mu_k / \mu_s = 0.7$.

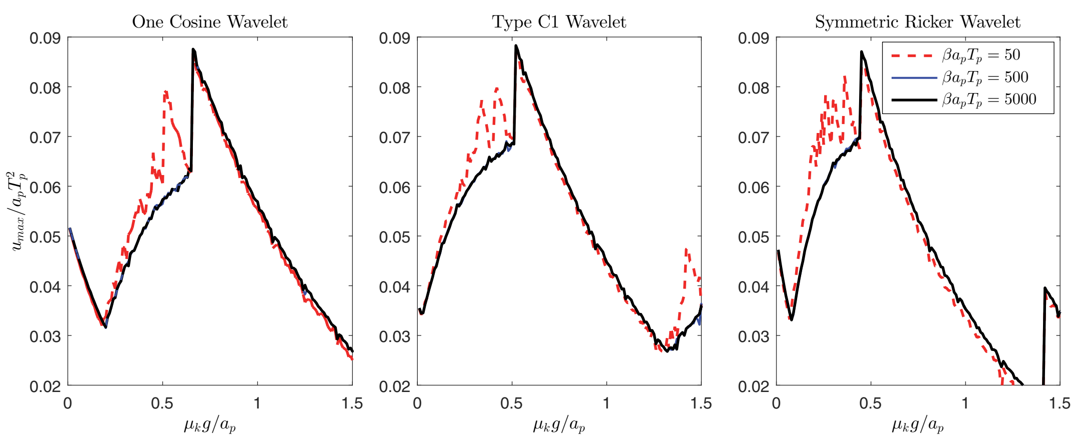

Fig. 4-15. Effect of $\beta a_p T_p$ on the response of a coupled sliding system at resonance ($T / T_P = 1$) on a surface with $\mu_k / \mu_s = 0.7$.

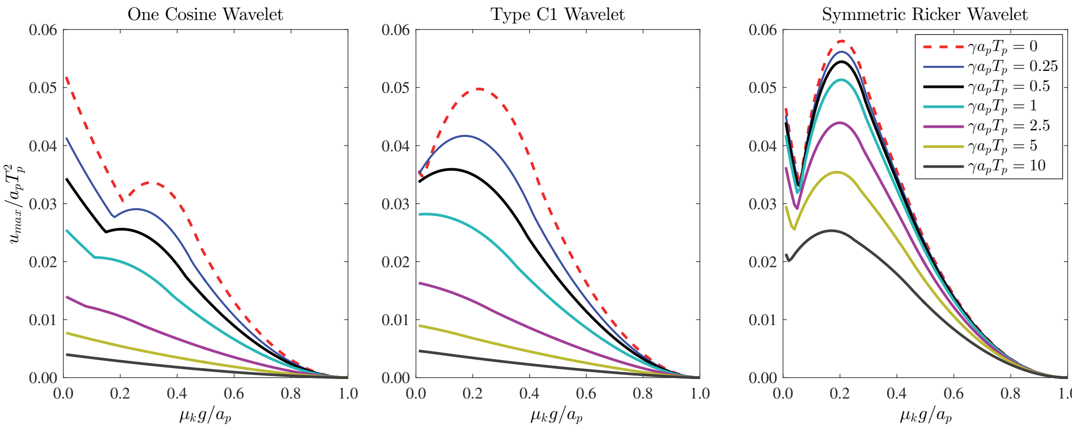

Fig. 4-16. Effect of $\gamma a_p T_p$ on the response of a rigid sliding system with Coulomb friction.

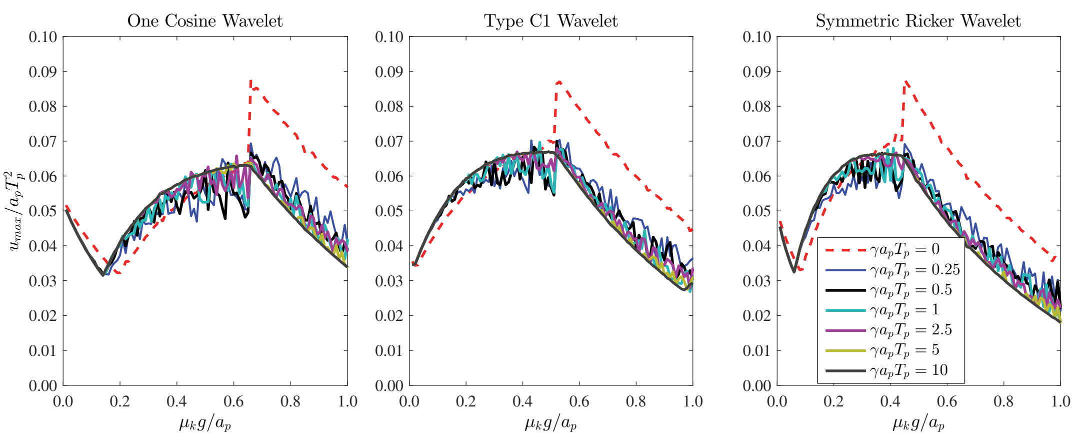

Fig. 4-17. Effect of $\gamma a_p T_p$ on the response of a coupled sliding system at resonance with $\mu_k / \mu_s = 0.7$, $\beta a_p T_p = 250$.

PART II

EXPERIMENTAL INVESTIGATIONS ON THE SEISMIC REPONSE OF EQUIPMENT AND CONTENTS ON WHEELS/CASTERS

Chapter 5: Shake Table Investigation on the Seismic Performance of Hospital Equipment Supported on Wheels/Casters

Nikfar F., Konstantinidis D., 2016, Shake Table Investigation on the Seismic Performance of Hospital Equipment Supported on Wheels/Casters, submitted to *Earthquake Engineering and Structural Dynamics*.

Abstract

This paper presents an experimental investigation on the seismic response of medical equipment supported on wheels and/or casters. Two pieces of equipment were tested: a large ultrasound machine and a cart carrying smaller medical equipment. In the first phase, the resistance of the wheels and casters of the equipment was characterized through a controlled-displacement procedure on the shake table. In the second phase, extensive shake table testing was carried out to investigate the seismic response of the equipment. The input signals for the shake table tests included floor motions of a four-story steel braced-frame hospital designed to satisfy seismic requirements of a site in the Los Angeles area. The results of 96 shake table tests reported in this study include the seismic performance of the equipment under both unlocked and locked conditions, located on various floor levels of the building. It was observed that engaging the casters' locking mechanism does not necessarily decrease the relative displacement. The displacement response was sensitive to the excitation intensity and the orientation of the equipment with respect to the input excitation. Based on the experimental observations, appropriate structural engineering demand parameters associated with the relative displacement and relative velocity demands of the equipment are proposed and used to develop conditional probability curves. Finally, in an effort to make possible the extrapolation of the results of this experimental program to similar equipment on wheels/casters, the performance of a simple numerical model in predicting the peak seismic demands is evaluated.

5.1 Introduction

Severe nonstructural damage and loss of functionality in medical facilities during the 1994 Northridge, 1995 Kobe, and 1999 Chi-Chi earthquakes resulted in impaired emergency response operations, demonstrating that the resilience of critical facilities, such as hospitals, is highly correlated to the seismic performance of their nonstructural components [1,2]. Although the *immediate occupancy* performance objective is aimed in the seismic design of hospitals (either directly through a performance-based approach or indirectly through the importance factor in prescriptive codes), this objective is oftentimes not met due to failure of nonstructural components, even when the structural system performs adequately. More recent examples of such disparity between structural and nonstructural performance include hospitals during the 2010 Chile Earthquake [3,4]. The Chilean seismic design codes used in the design of the hospitals were very similar to the recent United States codes. Post-disaster reconnaissance reports noted that, whereas structural damage to the buildings was minimal, there were several cases of damage to unsecured equipment and contents that fell or broke during the earthquake, hindering the emergency response function of the hospitals [3,4]. In many cases, large, unanchored equipment, such as incubators and computers, was reported damaged after falling to the floor [3]. Similarly, in the 2011 Christchurch earthquakes, poor performance of utility networks and damage to nonstructural components were reportedly the major problems affecting the operation of the Canterbury hospital system [5].

The list of nonstructural components in a building is vast. Both the FEMA E-74 [6] and the CSA S832 [7] documents divide nonstructural components into three broad categories: architectural components, equipment (electrical, mechanical and plumbing), and contents. The present study focuses on freestanding items under the *equipment* and *contents* (EC) categories.

The rocking response of freestanding objects has been studied in great length in [8-12]. The problem of sliding objects has been studied at various levels in [13-20]. Recently, notable full-scale shake table test studies which included the performance of nonstructural components were undertaken. Ryan et al. [21] carried out a shake table study of a five-story, steel moment-frame building, in both fixed-base and base-isolated configurations. The building featured an array of nonstructural components, including interior partition walls, ceiling systems, sprinkler piping systems, and loose contents [22]. The recently completed NEES Nonstructural Grand Challenge Project was the largest research effort to date investigating the seismic performance of ceiling-piping-partition systems [23-28]. Retamales et al. [23] carried out an experimental study on the seismic response, failure mechanisms and fragilities of cold-formed steel framed gypsum partitions walls. Tian et al. investigated experimentally the seismic behavior of fire suppression sprinkler piping joints [24] and systems [25], and evaluated various models to simulate the moment-rotation hysteretic behavior of T joints and subsequently to numerically model complete fire sprinkler piping systems [26]. Soroushian et al. developed fragility curves for fire sprinkler piping systems with grooved fit joints [27] and threaded joints [28].

Pantoli et al. [29] conducted shake table tests of a five-story reinforced-concrete building (both fixed base and base isolated) that featured a variety of nonstructural components and systems. Di Sarno et al. [30] and Cosenza et al. [31] investigated the dynamic response of nonstructural components (two freestanding cabinets and a desk) in typical hospital rooms through shake table tests and conducted fragility analysis.

The present study focuses on the seismic performance of wheel-supported and/or caster-supported EC, which are abundant in hospitals. About 30% of the hospital equipment and appliances are on wheels/casters due to mobility requirements [32]. The concern with equipment and appliances on wheels/casters during earthquakes is that they might exhibit large movements. Excessive movements could tear off or disconnect electric plugs and impair the functionality of the equipment. For instance, large movements of an anesthesia machine may not only tear off its electric plug, but also disconnect its connections to piped hospital oxygen, medical air, and nitrous oxide supplies. This would lead to malfunction of the equipment and possible loss of life. Large motion of EC in the operating room is also a big concern for doctors during operation. Moreover, large displacement increases the possibility of collision with other furniture, equipment, and surrounding partitions. Another adverse effect of excessive motion of EC during earthquakes is the possible blockage of safe egress routes. Impact as a result of collision introduces high accelerations that can lead to damage to acceleration-sensitive equipment and components. In the case of heavy equipment on wheels, a collision with people in vicinity of the equipment may result in injury.

A common seismic mitigation strategy for EC in science laboratories and other building types is tethering (using straps, chains, etc.). However, this practice has been shown to sometimes result in significant increase in accelerations, which may, in turn, result in damage to the equipment or even its contents (e.g., acceleration-sensitive biological samples in incubators) [33]. Base isolation is a seismic mitigation strategy that is becoming increasing popular for protecting both the structure and nonstructural components and systems of hospitals [32,34].

To date, there has been only one comprehensive experimental program that examined the performance of hospital equipment on wheels/casters [32,35,34]. It included full-scale shake table experiments of a four-story RC building at E-Defense to evaluate the performance of fixed-base and base-isolated medical facilities. Various rooms at different floor levels of the building were outfitted with hospital equipment and appliances to replicate realistic hospital rooms. The experimental program was aimed at studying various aspects of the facility. Shi et al. [34] focused specifically on the performance of items on casters. It was observed that the equipment with unlocked casters may experience movements as large as three meters. Multiple collisions with other equipment, furniture, and partitions were observed that resulted in accelerations up to 10 g. The experimental results of the base-isolated building showed that most equipment and appliances (including the ones with locked casters) experienced negligible movement except for those with unlocked casters that exhibited very large motions, leading to collisions with other equipment and surrounding partitions [34]. For equipment with locked casters, the response was very small when the building was tested as base-isolated, but when the building was tested as fixed-base, especially under near-fault ground motion, the equipment experienced the largest response and damage [34]. It appears that locking the casters is not one-size-fits-all solution, which calls for further investigation. Although these publications [32,35,34] reported very valuable qualitative observations from the shake table tests on the response of medical appliances, including ones on casters/wheels, the reported quantitative data was limited and did not allow extrapolation to other equipment on casters, e.g., estimation of their peak relative displacement and velocity and generation of fragility curves for this EC group.

In this study, the seismic response of an ultrasound machine and a cart loaded with medical equipment, housed in a conventional braced-frame hospital building, was investigated experimentally. The experimental program consisted of two phases: first, the frictional resistance of the wheels/casters was evaluated; then, shake-table experiments were performed using site-compatible ground and floor motions scaled to three earthquake intensity levels, i.e., maximum considered earthquake (MCE), design based earthquake (DBE), and service level earthquake (SLE)— chosen by the authors to be 50% of DBE, intended to represent events that are more likely to occur over the lifetime of the building. The scaling factor of 0.5 is not intended to represent any particular return period but was chosen to quantify the response of the EC over a wider range of floor shaking intensity. The factor of 0.5 has also been used elsewhere, e.g. [36]. The floor motions at various levels of the building were generated from a series of nonlinear time history analyses. The shake table input excitation was unidirectional, and the equipment was placed in different orientations with respect to the excitation direction, both in locked and unlocked configurations. The motion of the equipment during the experiments was recorded using a combination of a vision-based measurement technique and accelerometers. The paper discusses in detail observations on the seismic response of the equipment under different testing conditions. The experimental data is used to identify the most appropriate *structural* engineering demand parameters (EDPs) associated with the *nonstructural* engineering demand parameters (EDP_N s) of interest, i.e., maximum relative displacement and maximum relative velocity of the EC. Relationships between the EDP_N s and EDPs are established through regression analysis, and a probability analysis is carried out to quantify the conditional probability that the EDP_N s will exceed various thresholds, given the value of the structural EDP.

5.2 Test specimens

Two test specimens (procured from Hamilton Health Sciences) were used in this study: (1) An ultrasound, representing a typical heavy piece of medical equipment, supported on two wheels in the rear and two twin-wheel casters in the front, as shown in Figure 5-1 (left), and (2) A cart loaded with typical light medical equipment, supported on four twin-wheel casters, as shown in Figure 5-1 (right). The ultrasound was composed of three main parts: the main body (or case), the control panel, and the monitor. The main body housed most of the electronics and accounted for the majority of the mass of the equipment. The control panel and monitor were mounted flexibly on the main body, so that they could move and rotate depending on user needs. The dimensions and weight of the specimens are summarized in Figure 5-2. The majority of the mass of the ultrasound was carried by the rear wheels, and the front casters were primarily for turning the machine. The ultrasound featured a brake mechanism acting on the front casters only (Figure 5-3). The brake mechanism was activated through a pedal engaging a positive braking system on the tread surface of both rubber tires of each twin-wheel caster. When the brake was engaged (referred to herein as 'locked' condition) the resistance to motion was significantly increased, but if sufficient force was applied, the wheel started rolling and the equipment moved; once in motion, the resistance dropped significantly (as discussed later). The pedal, however, was not designed to lock the swivel raceway of the caster; hence, the casters were free to rotate about the vertical pivot axis. The wheels in the rear of the ultrasound also featured rubber tires. Note that the rear wheels were always free to roll. The light hospital cart was supported on four twin-wheel casters, the type typically installed on the majority of light-weight office and laboratory items. None of the casters of this particular cart had a brake mechanism, although similar casters with brakes are also common.

5.3 Resistance evaluation tests

The first phase of the experimental program involved evaluation of the lateral resistance of the equipment. Quantitative characterization of the frictional resistance will provide data for the calibration of models to be used in future studies. The lateral resistance tests were conducted using the shake table at the Applied Dynamics Laboratory, McMaster University.

5.3.1 Test setup and procedure

The schematic of the slow cyclic test setup is depicted in Figure 5-4. A mock floor lined with tile typically used in hospitals was constructed on the shake table to simulate realistic conditions. The equipment was secured to two fixed supports on either side through pre-tensioned aircraft cables. Each pre-tensioned cable was equipped with a 220-N (50-lb) load cell (Interface MB-50) to measure the tension in the cables, and with a turnbuckle for adjusting the tension. The sensor data was acquired at 2000 samples per second rate using a NI cDAQ-9174. A minimum of 120 N pre-tensioning force was maintained in each cable in all cyclic tests. A string potentiometer (Celesco SP1-12) was attached to the equipment to record any absolute displacement of the equipment during testing. A string potentiometer (Celesco PT-101-40A) was also attached to the shake table to measure displacement of the shake table. The difference between the readings of the two potentiometers provides the relative displacement between the equipment and the floor. Cyclic tests on the ultrasound were performed for two conditions: (a) with the casters in the 0-degree position, and (b) with the casters in the 180-degree position, as shown in Figure 5-2. Various cyclic motions with low velocities were applied to the shake table. However, only the results of the experiments for three cycles of a sine wave with 0.025 Hz frequency and amplitude of 20 cm (i.e., peak velocity of 0.5 cm/s) are presented in the paper.

5.3.2 Test results

The pre-tensioned cables successfully held the equipment in place, without notable deformation. It is also worth mentioning that the ultrasound did not show any movement in the direction orthogonal to the loading direction, even when the front casters were rotating. Based on the force-displacement plots in Figure 5-5, a force of approximately 40 N was required to start moving the equipment (relative to the floor), but as the wheels and casters started rolling, the resistance dropped. As the table moved further, the resistance again built up and then dropped repeatedly. A closer look at the wheels and casters provided an explanation for this behavior. The tread surface of the caster tires had certain flattened spots, a phenomenon called *flat-spotting*, caused by uneven wear due to brake locking and possibly plastic flow of the tire elastomer under stress. The fluctuation in the force is most likely due to the uneven surface of the caster tires. The fluctuation in the force is most likely due to the uneven surface of the caster tires. Figure 5-5 (left) shows the force-displacement loops for a test with the casters set to the 0-degree position at the start of the test. The peak resistance force reached 60 N during the test. It can be seen that the fluctuation in force is consistent over the three cycles plotted.

The casters did not rotate about the pivot axis during this test. However, when the casters were set at the 180-degree position at the start of the test, they rotated to 90 degrees at maximum travel of the table. Figure 5-5 (right) shows the force-displacement loops corresponding to the 180-degree test, where it can be seen that the peak resistance force increased from about 40N before rotation initiates to 85N at the 90-degree position. In these experiments, the maximum travel of the table was not enough to complete a full rotation of the casters to the 0-degree position. It is noted that these tests were conducted with the casters being unlocked. Resistance evaluation of the locked ultrasound was not performed due to the capacity limit of the load cells used. However, the breakaway and dynamic resistances are estimated from the recorded acceleration (see Figure 5-14) to be equal to 508 N and 221 N, respectively. Figure 5-6 shows the recorded force-displacement loops for the hospital cart. Only one cycle is shown because the signal was noisy, which may be in part due to the measured force being at the lower end of the load cell's recording range. Unlike the ultrasound, which did not exhibit noticeable movement, relative to the table, in the perpendicular direction, the cart exhibited substantial motion in the perpendicular direction. This motion occurred at the time when the casters were rotating about their pivot axes. The figure shows that a force of about 10 N was required to overcome the frictional resistance of the casters, while the maximum recorded force was about 15 N.

5.4 Shake table tests

5.4.1 Shake table test procedure

The shake table at McMaster University, with displacement capacity of ± 25 cm, made it possible to simulate a range of realistic floor motions (up to 50 cm) to investigate the seismic response of the hospital equipment. The floor motions used as input for the shake table tests were generated by nonlinear time history analysis of an elaborate nonlinear structural model in OpenSees [37]. Details of the structural model are presented in the following sections. For the tests, the equipment was placed directly on the simulated hospital floor constructed on the shake table. The methodology makes various assumptions and is constrained by limitations of the experimental facilities, e.g., ignoring the dynamic interaction between the equipment and the building, modeling assumptions in OpenSees, possible collisions between the equipment and its surroundings, the effect of out-of-plane floor excitation, etc. In addition, the vertical component of the floor motion is not considered in this study since the shake table used is bidirectional [although only unidirectional tests were performed]. However, it is noted that according to the results of the full-scale shake table tests at E-Defense [35], which did include vertical excitation, the horizontal movement of the EC on wheels and casters is not affected significantly by vertical floor excitation. This is due to the fact that, unlike in the case of sliding EC, the normal contact force does not contribute to the horizontal resistance of the wheels. Even a very low force would be adequate to overcome the resistance of the wheels and casters to rolling (which arises by friction between the caster's axle and roller or sliding bearings) in the unlocked condition. Even in cases where the casters were locked, the movement of the equipment was due to the sliding at the brake–tire contact points, as shown in Figure 5-3, rather than at the tire–floor contact points. Note that if the brakes are engaged and prevent the wheel from turning, the equipment will slide on the floor surface if the floor acceleration is strong enough to overcome the friction force at the tire–floor interface. In this case, the type of floor finish (e.g., vinyl, linoleum, terrazzo, etc.) and the vertical floor accelerations may influence the seismic response of the EC.

5.4.2 Instrumentation

The motion of the shake table in the horizontal direction was tracked using an accelerometer (MEAS 4002-005) and a displacement sensor (Temposonics® LPRCCU04901). Also, one accelerometer (Entran EGCS-D0-2) was attached to the inside of the ultrasound to measure the accelerations that internal electronic parts may experience during seismic shaking. As the motion of the equipment was expected to be complicated, a vision-based measurement system was used in lieu of conventional contact sensors. A video camera with a 2.7K (2704×1520 pixel) resolution at a 60 frames per second rate was used to track the motion of LED lights attached to the body and monitor of the ultrasound. In the case of the hospital cart, LED lights were attached to the rigid handle of the cart and also to the top of the smaller medical equipment on the cart to track relative displacements. Displacement and velocity response histories were computed from post-processing of the recorded frames. The accuracy of the vision-based measurements is approximately 0.5-mm and 3-cm/s for displacement and velocity, respectively. A detailed evaluation of the accuracy of the vision-based measurements in this study is presented in [38].

5.4.3 Structural design

A hypothetical four-story steel braced-frame hospital building located in Los Angeles, California, with site coordinates (34.02197^{o}N , 118.28587^{o}W) was designed according to the requirements of ASCE 7-05 [39] for Site Class C. The mapped spectral accelerations are $S_S = 1.843$ g and $S_1 = 0.640$ g. The resulting DBE-level design spectrum is shown in Figure 5-7. The Steel Special-Concentrically-Braced-Frame (SCBF) lateral load resisting system for this building with hospital occupancy, i.e., Risk Category IV, and importance factor $I = 1.5$ was designed according to the requirements of IBC2006 [40], AISC360-05 [41], and ASCE 7-05 [39]. The SCBF was designed with a response modification factor, over-strength factor, deflection amplification factor, and drift ratio limit of $R = 6$, $\Omega = 2$, $C_d = 5$ and 1.5% (obtained from static analysis of elastic structure), respectively. The characteristic yield strength of steel was assumed to be 345 MPa for frame members and 318 MPa for brace members. All brace members of the SCBF were checked to ensure they were seismically compact, and limitations were applied on the slenderness ratio of each member. The lateral loads were carried by two braced bays on each side of the building perimeter, as shown in Figure 5-8, which shows the building layout. All other members were designed for gravity loads. Floor slabs consisted of 82.5-mm-thick lightweight concrete over a 50.8-mm-thick steel deck. A dead load of 4.0 kPa was applied on the floor that included the weight of the floor slab and 0.96 kPa for cladding. The self-weight of the structural members was considered separately in the analysis. Assuming 10% for operating rooms with uniform live load of 2.87 kPa, 65% for patient rooms with uniform live load of 1.92 kPa, and 25% for corridors with uniform live load of 3.83 kPa, an average live load of 2.5 kPa was considered on the floor slabs. The structural members were designed for a calculated base shear coefficient of C = 0.307. The steel sections used in the structural members are summarized in Table 5-1.

5.4.4 Structural modeling, ground motions, and structural response

The building was modeled in OpenSees [37]. The beams, columns, and braces in the x-z frame, shown in Figure 5-8, were modeled using force-based beam-column elements. Equivalent loads and masses were calculated and transferred to the 2D frame. The Steel02 material model with 3% strain hardening was considered for all the beam-column elements. Sections were discretized using 4 fibers along the thickness and 16 fibers along the web or flange length of the W and HSS sections. The beam-to-column connections were modeled as pinned-pinned. Columns were fixed at the base. To capture the bucking behavior of braces, the simulation procedure proposed in Hsiao et al. [42] was implemented. Braces were simulated using 6 beam-column elements; of which, 4 were placed in the middle quarter length of the brace, as illustrated in Figure 5-9 (left). Seven Gauss integration points were assumed for nonlinear curvature distribution for each beam-column element. The required imperfection of the braces followed a sine function with the apex at 0.1% of the length of the brace. A rotational nonlinear spring at each end of the brace was introduced to account for the stiffness and energy dissipation of the gusset plate. The initial stiffness of the gusset for each brace is calculated using the relation suggested in [42]:

$$K_\theta = \frac{EW_w t^3}{12L_{ave}} \tag{5.1}$$

where E is Young's modulus of steel, W_w is the Whitmore width of a 45° projection angle, L_{ave} is the average of the L_1, L_2 and L_3 lengths, as shown in Figure 5-9 (right), and t is the thickness of the gusset plate, chosen as 12.5 mm for all the gusset plates in this study. The W_w and L_{ave} values used are provided in Table 5-1. The Steel02 material model with 1% post-yield stiffness was utilized for these rotational springs. The aforementioned assumptions together with the use of corotational transformation for the brace beam-column elements allowed capturing the global buckling of the brace under cyclic loading [43,42], while local buckling was assumed not to occur owing to the use of seismically compact sections. The vibration period in the first two modes was computed to be 0.54 s and 0.23 s, for the elastic structure. 2% Rayleigh damping, including both mass- and stiffness-proportional terms, was considered in the dynamic analysis of the model. The stiffness-proportional term of the damping was based on the last committed stiffness of the elements.

A set of four ground motions were selected from the PEER Strong Motion Database, NGA-West2, for the nonlinear time history analysis. The target design spectrum parameters $S_{DS} = 1.229$ g and $S_{D1} = 0.555$ g were used for spectrum-based ground motion selection. The Mean-Square-Error method with multiple period points from 0.1 s to 3.0 s was utilized in both the selection and the scaling of the ground motions. Only the H2 component of the recorded ground motions was considered in the scaling process. Properties of the selected ground motions and their corresponding scaling factors are listed in Table 5-2. Acceleration response spectra of the scaled ground motions are shown in Figure 5-7. Both the horizontal (H2) and vertical components of ground motions were applied to the structure. Earthquake simulations were performed at the SLE (i.e., 50%

DBE), DBE, and MCE levels. The peak structural demands computed from the analysis are presented in Table 5-3.

The roof-level peak response is included for completeness but was not used in shake table tests. The maximum inter-story drift is less than 2.5% for all the ground motions at the DBE level except for NORTHR at the third story. The mean of peak drift ratios is 2.54% under DBE and 4.09% under MCE levels. The analysis provided floor motions that were used subsequently in the shake table tests. Note that due to the 50-cm peak-to-peak stroke capacity of the shake table, high pass Bessel filters with cutoff frequencies of 0.18 Hz and 0.23 Hz were applied to the NORTHR and MANJIL motions, respectively, before using them in the nonlinear time-history analysis. Figure 5-10 compares the desired and observed 3rd story response spectra reproduced by the shake table under MANJIL-DBE excitation. As can be seen, the shake-table's performance decreases at higher frequencies. The observed response spectrum exceeded the desired spectrum by 35% at frequencies greater than 6 Hz. However, as presented in Table 5-4, for all four ground motions, the shake-table maintained the peak displacement and peak velocity errors in reasonable ranges of 1.6% and 5.3%, respectively.

5.4.5 Test program

The shake table experiments were conducted using the ground, 1st, 2nd, and 3rd story motions as input. The ultrasound was tested under two conditions: with locked and with unlocked casters. The casters of the hospital cart were not lockable; thus, it was tested only in the unlocked condition. Most of the tests were performed with the ultrasound's wheels parallel to the direction of excitation (same position as depicted in Figure 5-4). For some tests, the equipment was rotated 45^{o} (oblique) and 90^{o} (perpendicular) to investigate the effect of equipment orientation. Table 5-5 summarizes the experimental program adopted in this study.

5.4.6 Seismic response of the ultrasound machine

5.4.6.1 Parallel to excitation

The responses of the ultrasound (i.e., body) and the attached monitor component in the horizontal plane *X*-*Y* were recorded using a motion-tracking technique [38]. The excitation for all the tests in this study was in the *X*-direction. Two LEDs were attached to the body and two to the monitor. Tracking the motion of two points (i.e., two LEDs) on the component provided a means to also measure the rotation (i.e., twisting) of that component about the vertical axis *Z*. Figure 5-11 shows the absolute displacement of the ultrasound and its monitor (with respect to the floor) in the *X*-direction, together with the rotation due to the 3rd story motion corresponding to the NORTHR record at DBE level. The relative displacement is obtained by subtracting the position of the floor from the average position of the two LEDs attached on the ultrasound. Figure 5-12 illustrates the *X*-*Y* plane relative displacement and relative velocity orbits (obtained by numerical differentiation) of the ultrasound under unlocked and locked conditions. The ultrasound is positioned parallel to the excitation. A small displacement is observed in the direction perpendicular to the excitation. Interestingly, in this particular example, the ultrasound exhibits larger displacement when the casters are locked than unlocked. Nevertheless, the relative velocity is smaller under the locked condition. The larger displacement under the locked condition is due to the fact that larger inertia forces and consequently larger accelerations can be transmitted to the ultrasound that can result in larger displacement responses. However, this is not always the case. The amplification in displacement due to addition of resistance is highly correlated to the characteristics of the input excitation [44]. For instance, if the floor acceleration cannot overcome the resistance, there will be no relative displacement/velocity whatsoever.

Figure 5-13 shows the absolute acceleration response of the unlocked (top row) and locked (bottom row) ultrasound due to the 3rd story LOMAP-DBE excitation. The equipment experiences peak acceleration of about 0.1 g and 0.2 g under the unlocked and locked conditions, respectively. The figure also compares the acceleration histories recorded using the attached accelerometer (left column) to those derived from vision-based position measurements (right column).Vision-based acceleration results are based on twice-differentiated smoothed displacement using a first order Savitzky-Golay filter with a frequency resolution of 10 Hz. As it is evident in the figure, the high-frequency acceleration spikes recorded by the accelerometer were not captured in the acceleration history derived from displacement response. It should be noted that the accelerometer was attached on internal parts of the ultrasound, while the LEDs were attached on the case (i.e., body). Consequently, the difference between the plotted responses may be in part due to inherent differences in the dynamic response of the two points of the equipment. The vision-based acceleration history compares better with the accelerometer history in the case of the locked ultrasound, for which the equipment experienced larger accelerations. Overall, the vision-based acceleration measurements provide a reasonable quantification of the accelerations experienced by the equipment.

As mentioned earlier, the frictional resistance of the locked ultrasound was not evaluated through cyclic testing. The absolute acceleration response can be used to provide a crude estimate of this resistance. Figure 5-14 plots absolute acceleration and relative displacement response of the locked ultrasound subjected to the 3rd story NORTHR-DBE excitation. The major movement and peak acceleration occur at 7.8 s. Before this time, even though the equipment experiences vibrations with accelerations as large as 0.1 g, the casters' wheels do not actually rotate. An acceleration of 0.19 g is required for causing rigid-body motion (rather than vibration) of the locked ultrasound, evidenced by the subsequent drifting in the relative displacement (Figure 5-14-bottom). This value, i.e., 0.19, can be thought of as breakaway friction coefficient. Thereafter, the ultrasound exhibits accelerations ranging from 0.05 g to 0.09 g. Figure 5-15 shows the absolute acceleration of the monitor component in the *X*-direction, obtained using vision-based measurements from the LEDs attached on the monitor. The monitor experiences a peak acceleration of 0.44 g (vector sum).

5.4.6.2 Oblique to excitation

In order to investigate the effect of the excitation direction on the response, a number of tests were carried out with the ultrasound placed in an oblique orientation: as close as possible (visually but not measured precisely) to 45 degrees relative to the excitation direction (Figure 5-17-right). Figure 5-16 compares the relative displacement and velocity responses for the unlocked and locked ultrasound subjected to the 3rd story

LOMAP-DBE excitation. As can be seen from the displacement plot, the ultrasound has the tendency to move merely in the rolling direction of the wheels. Although the locked ultrasound exhibits significantly smaller relative displacement than the unlocked ultrasound, it experiences slightly greater relative velocity. Figure 5-17 plots the absolute acceleration response in the *X* and *Y* directions for the same experiment. The acceleration responses are comparable in magnitude under locked and unlocked conditions due to the fact that, by rotating the equipment, the resistance increases in the direction of excitation since the wheels do not tend to slide in the direction perpendicular to rolling. The component of excitation in the direction perpendicular to rolling can excite the twist mode of response of the ultrasound. Large amount of rotation was observed in these tests. Figure 5-18 compares the rotation for the unlocked and locked ultrasound. The unlocked ultrasound experiences a rotation as large as 35 degrees. The locked ultrasound rotated 16 degrees due to the fact that casters, even when locked, are free to rotate about their pivot.

5.4.6.3 Perpendicular to excitation

A number of experiments were performed with the ultrasound placed perpendicular to the excitation direction. Despite the slender aspect ratio of the ultrasound on the plane of the excitation, no notable rocking (i.e., uplift of the wheels) was observed under any of the 3rd story DBE-level motions. Similar to the tests carried out in the oblique orientation, the ultrasound tended to move along the rolling direction of the wheels. Although one may normally expect minimal movement in the direction perpendicular to the excitation, Figure 5-19, which presents the response of the equipment in the perpendicular orientation, shows that this is not the case. Twisting of the ultrasound due to rotation of the casters about their pivot axes and lateral movement of the front side places the ultrasound in an oblique position with respect to the excitation; this creates an acceleration component in the direction parallel to the rolling direction of the wheels, causing motion of the equipment in perpendicular direction relative to the excitation. In this particular experiment, as shown in Figure 5-19, the displacement of the unlocked ultrasound exceeded 120 cm, resulting in the ultrasound gently hitting the surrounding barrier built around the edges of the shake table. Figure 5-20 shows the acceleration responses of the ultrasound case and monitor due to the 3rd story LOMAP-DBE excitation. The peak recorded vector-sum acceleration is approximately the same (about 1.2 g) under unlocked and locked conditions. The monitor, however, exhibited considerably larger acceleration (2.7 g) in the unlocked condition than in the locked condition (1.0 g). This significantly larger acceleration is attributed to rotational motion of the body of the ultrasound in the unlocked condition.

5.4.7 Seismic response of the hospital cart

The hospital cart was supported on four identical casters, which were not lockable. No accelerometer was attached to the cart to measure acceleration; instead, accelerations were computed from vision-based displacements. Figure 5-21 presents the relative displacement and velocity response of the cart under the 3rd story LOMAP-DBE excitation. Although the cart moves predominantly in the direction of the excitation (peak displacement of 25.6 cm), the response in the perpendicular direction is appreciable (10.1 cm). From the displacement orbits shown in Figure 5-21 (left), it is evident that each reversal in the direction of motion along the *X*-direction induces an incremental increase in displacement along the *Y*-direction, which occurs as a result of the casters rotating 180^o about their pivot axes. Such motions were also observed during the cyclic resistance experiments. The rotation of the cart under the same excitation is shown in Figure 5-22. The vision-based acceleration is shown in Figure 5-23. The hospital cart experiences a peak acceleration of 0.08 g. Taking the peak resistance of 16 N recorded in the cyclic tests (see Figure 5-6), the peak acceleration can be computed to be $16\,\text{N} \times \text{g}/(23\,\text{kg}) = 0.07\,\text{g}$, which is in good agreement with the cyclic resistance test results. Note that in all the experiments, no relative displacement was observed between the equipment items mounted on the cart and the cart.

5.4.8 Response in different story levels

Figure 5-24 presents the peak relative displacement and velocity of the equipment items when they are placed in different stories of the building under SLE, DBE, and MCE earthquake intensities. In general, the relative displacement and velocity responses increase as the number of stories and input intensity increase; however, in some cases this observation does not hold. In some cases, the response changes very little in going from DBE to MCE, likely due to yielding of the building structure that limits the floor accelerations.

5.5 Regression and probability analysis

In this section the data obtained from the experimental program is analyzed in order to propose the most appropriate EDP. The EDP_Ns considered are peak relative displacement ($u_{\max}$) and peak relative velocity ($v_{\max}$) of the equipment. Figure 5-25 plots the EDP_Ns against three possible EDPs: peak floor absolute acceleration (A_f), peak floor absolute velocity (V_f), and peak floor absolute displacement (D_f). Note that the data from the tests in which the equipment was stopped by the surrounding barrier is not included in the plots. As can be seen, $u_{\max}$ shows the least scatter against D_f. While, in the case of $v_{\max}$, the least scatter is observed for V_f. Hence, D_f and V_f are chosen as the EDPs for $u_{\max}$ and $v_{\max}$, respectively. Considering top-left and bottom-middle figures, the fitted lines to data corresponding to ultrasound-unlocked and ultrasound-locked do not show a distinguishable trend on the advantage of locking the wheels/casters. Therefore, one may draw the conclusion that locking wheels/casters does not necessarily result in reduced seismic demands on EC in fixed-base buildings. A lognormal distribution is fitted to the $u_{\max}$ and $v_{\max}$ demand data. To this end, both EDP_N s are first transformed to log space, where linear regression is performed, as shown in Figure 5-26. Assuming a lognormal distribution means that the transformed data follows a normal distribution. The associated standard deviation of the relative displacement and relative velocity in log scale is obtained using the maximum likelihood theorem, leading to 0.439 and 0.162, respectively. Given the standard deviation for the lognormal distribution, corresponding conditional probability curves were generated, as presented in Figure 5-27. Unlike the fragility curves presented in [16], [17], and [19] for sliding equipment, the conditional probability curves presented herein are independent of the equipment resistance and floor absolute acceleration. Therefore, their applicability is limited to equipment items with low resistance, e.g., equipment on wheels/casters, in conventional buildings. Applicability of such probability curves can be questionable when the floor undergoes large absolute displacement but with acceleration lower than the value to overcome the resistance of the wheels. This might be the case for the equipment and contents of base-isolated buildings, which calls for further investigation. The proposed displacement and velocity probability functions can be used to predict the occurrence probability of a certain damage limit state. For instance, the peak displacement probability curves can be used to predict the probability that a certain displacement disconnect or tear off electric plugs and cause serious disruption in operation of the equipment.

The conditional probability curves presented in Figure 5-27 can be used to estimate the probability that a medical EC item on wheels/casters will experience: a maximum relative displacement that exceeds a displacement threshold u_c, given the value of the peak floor absolute displacement (left); a maximum relative velocity that exceeds a velocity threshold v_c, given the value of the peak floor absolute velocity (right). The values of the displacement and velocity capacities, u_c and v_c respectively, used in this study were chosen arbitrarily. Further research is required to establish the values of u_c and v_c, and their associated uncertainties, that correspond to the onset of various damage states, e.g., an EC item becoming disconnected from a medical gas supply line or electrical outlet, or colliding with a hospital occupant with enough momentum to cause injury.

5.6 Evaluation of a simple model for numerical simulations

A simple model that could be used by practicing engineers and researchers would be beneficial to extend the results of this study to similar EC on wheels/casters which are very common not only in hospitals but also other critical facilities. This section evaluates the performance of Newmark's sliding block model in estimating the maximum displacement and velocity of the EC supported on wheels/casters. The numerical procedure used is discussed in [45]. Note that Newmark's model is based on two simplifying assumptions: (a) the block is rigid, and (b) the surface friction obeys a rigid-plastic behavior defined by a constant kinetic friction coefficient, μ. These assumptions undermine the dynamic contributions due to any flexibility in the equipment, the fluctuations evident in the friction force as shown in Figures 5 and 6, as well as the tendency of the EC to move out of plane due to rotation of the casters. The equivalent friction coefficient was obtained by equating the area under the force-displacement loops presented in Figures 5 and 6 with the area of the rectangles representing the Coulomb model. Based on Figure 5-5 (left) and Figure 5-6, the unlocked ultrasound and medical cart experience equivalent friction coefficient values of 0.0071 and 0.0288, respectively. Using these values, the response of unlocked ultrasound and medical cart was computed.

Figure 5-28 shows the displacement response of the EC when subjected to 3rd story MCE-level motions. As can be seen, the performance of the model varies from one experiment to another. It provides a reasonable estimate of the peak and residual displacements of the medical cart under LOMAP-MCE and CHICHI-MCE. It also performs relatively well in the case of the ultrasound subjected to MANJIL-MCE. In other cases, however, it performs poorly, and its predictions can be considered rough estimates at best.

Table 5-6 presents the mean error associated with the peak displacement response for a set of 16 floor excitations. Note that, based on Figure 5-5 (right), the equivalent friction coefficient of the ultrasound increased to 0.0104 when tested with the casters positioned at 180 degrees. Predictions of the model using this value of μ are also included in the table. Furthermore, the equivalent μ of the locked ultrasound was estimated to be 0.05 using the acceleration records. Simulations using the model underestimated both the peak relative displacement and velocity response of the EC. While the errors are relatively large for peak displacement, the model gives reasonable estimates of the peak relative velocity. The simulations resulted in mean errors of -31.2%, -15.5%, and -15.2% when predicting the peak displacement responses and -2.2%, -7.5%, and -5.6% when predicting the peak velocity responses of the unlocked-ultrasound, locked-ultrasound and medical cart, respectively.

It is clear that that this simple model can only provide a very rough estimate of the response of EC supported on casters. An advanced model that takes into account the fluctuation in resistance force, flexibility of the equipment, and rotation of the casters is necessary to obtain accurate estimates of the response. However, the development of such an advanced model is beyond the scope of this paper and is left for future investigation.

5.7 Conclusion

This study investigated the seismic response of hospital equipment supported on wheels and casters. In the first phase, the frictional resistance of the wheels and casters was determined through cyclic tests using a shake table. In the second phase, the seismic response of equipment located on various floor levels of a hypothetical four-story steel braced-frame hospital was evaluated. The absolute acceleration response of the different floors of the building, computed using nonlinear time-history analysis of the building model in OpenSees, was used as input for the shake table tests. In addition to conventional accelerometers, a vision-based measurement system was utilized to quantify the complex motion of the equipment during the shake table tests. The performance of the equipment was evaluated at three intensity levels and for both unlocked and locked casters. Although the electronic functionality of the equipment was not assessed before/after the shake table test, there was no physical damage to the equipment (detachment of components or failure of any sort) as a result of the shaking. Furthermore, there was no notable rocking, and the main mode of response was rolling of the wheels and casters. It was observed that locking the casters can in some cases result in amplified response, depending on the input excitation intensity and orientation of the equipment with respect to the input excitation direction. While the general trend follows an increase in relative displacement and velocity at higher stories and input intensity, quite a few exceptions were observed. An interesting observation made was that, when equipment with casters and wheels was placed with the wheels perpendicular or at an oblique angle to the excitation direction, significant motion was observed in the direction the wheels were pointing towards.

The last part of the paper involves an attempt to find the most appropriate *structural* engineering demand parameters (EDPs) associated with the relative displacement and relative velocity demands of the equipment on wheels/casters. It was observed that these *nonstructural* engineering demand parameters (EDP_N s) exhibit the least scatter when expressed as a function of an EDPs with the same physical dimension; i.e., the peak relative displacement of the equipment was best correlated with the peak floor displacement, whereas the peak relative velocity of the equipment with the peak floor velocity. The regression analysis showed that locking wheels/casters does not necessarily result in reduced seismic demands on EC in fixed-base buildings. Considering the proposed EDPs, a lognormal distribution model was fitted to the data, and conditional probability curves were developed for various capacity levels. It should be noted that the results of this study are applicable to unlocked equipment or locked equipment with relatively low kinetic resistance. In the case of locked equipment with high resistance, the reader is referred to studies on fragility of sliding equipment (e.g. [14,16,17,19] and references reported therein). Finally, in order to extrapolation the results of this experimental program to similar equipment on wheels/casters, the performance of Newmark's rigid sliding block model in predicting the peak seismic demands was evaluated. It was observed that this simplified model underestimates the peak displacement demands by about 30% and peak velocity demands by about 6%.

5.8 References

1. Cimellaro GP, Reinhorn AM, Bruneau M. Seismic resilience of a hospital system. *Structure and Infrastructure Engineering* 2010; **6**(1-2):127-144.
2. Filiatrault A, Sullivan T. Performance-based seismic design of nonstructural building components: The next frontier of earthquake engineering. *Earthquake Engineering and Engineering Vibration* 2014; **13**(1):17-46.
3. Mitrani-Reiser J, Mahoney M, Holmes WT, de la Llera JC, Bissell R, Kirsch T. A functional loss assessment of a hospital system in the Bío-Bío province. *Earthquake Spectra* 2012; **28**(S1):S473-S502.
4. Miranda E, Mosqueda G, Retamales R, Pekcan G. Performance of nonstructural

components during the 27 February 2010 Chile earthquake. *Earthquake Spectra*. 2012; **28**(S1):S453-S471.

5. Jacques CC, McIntosh J, Giovinazzi S, Kirsch TD, Wilson T, Mitrani-Reiser J. Resilience of the canterbury hospital system to the 2011 Christchurch earthquake. *Earthquake Spectra* 2014; **30**(1):533-554.
6. FEMA E-74. *Reducing the risks of nonstructural earthquake damage – a practical guide*. United States Federal Emergency Management Agency: Washington, DC, 2011.
7. *CSA S832-06 (R2011): Seismic risk reduction of operational and funcional components (OFCs) of buildings*. Canadian Standards Association: Mississauga, ON, 2011.
8. Housner GW. The behavior of inverted pendulum structures during earthquakes. *Bulletin of the Seismological Society of America* 1963; **53**(2):404–417.
9. Yim CK, Chopra AK, Penzien J. Rocking response of rigid blocks to earthquakes. *Earthquake Engineering and Structural Dynamics* 1980; **8**(6):565–587.
10. Makris N, Konstantinidis D. The rocking spectrum and the limitations of practical design methodologies. *Earthquake Engineering and Structural Dynamics* 2003; **32**(2):265–289.
11. Makris N, Vassiliou MF. Sizing the slenderness of free-standing rocking columns to withstand earthquake shaking. *Archive of Applied Mechanics* 2012; **82**(10-11):1497-1511.
12. Chatzis MN, Smyth AW. Modeling of the 3D rocking problem. *International Journal of Non-Linear Mechanics* 2012; **47**(4):85-98.
13. Choi B, Tung CCD. Estimating sliding displacement of an unanchrored Body subjected to earthquake. *Earthquake Spectra* 2002; **18**(4):601–613.
14. Lopez Garcia D, Soong TT. Sliding fragility of block-type non-structural components. Part 1: unrestrained components. *Earthquake Engineering and Structural Dynamics* 2003; **32**(1):111–129.
15. Hutchinson TC, Chaudhuri SR. Bench-shelf system dynamic characteristics and their

effects on equipment and contents. *Earthquake Engineering and Structural Dynamics* 2006; **35**(13):1631–1651.

16. Konstantinidis D, Makris N. Experimental and analytical studies on the response of freestanding laboratory equipment to earthquake shaking. *Earthquake Engineering and Structural Dynamics* 2009; **38**(6):827–848.
17. Konstantinidis D, Makris N. Experimental and analytical studies on the response of 1/4-scale models of freestanding laboratory equipment subjected to strong earthquake shaking. *Bulletin of Earthquake Engineering* 2010; **8**(6):1457–1477.
18. Nikfar F, Konstantinidis D. Sliding response analysis of operational and functional components (OFC) in seismically isolated buildings. Proc. *3rd Specialty Conference on Disaster Prevention and Mitigation, Canadian Society of Civil Engineering (CSCE)*, Montreal, QC, 2013.
19. Konstantinidis D, Nikfar F. Seismic response of equipment and contents in base-isolated buildings subjected to broad-band ground motions. *Earthquake Engineering and Structural Dynamic* 2015; **44**(6):865–887.
20. Lin SL, MacRaeb GA, Dhakalb RP, Yeowb TZ. Building contents sliding demands in elastically responding structures. *Engineering Structures* 2015; **86**(1):182–191.
21. Ryan K, Soroushian S, Maragakis E, Sato E, Sasaki T, Okazaki T. Seismic simulation of an integrated ceiling-partition wall-piping system at E-Defense. I: Three-dimensional structural response and base isolation. *Journal of Structural Engineering (ASCE)* 2015; **142**(2).
22. Soroushian S, Maragakis EM, Ryan KL, Sato E, Sasaki T, Okazaki T, Mosqueda G. Seismic simulation of an integrated ceiling-partition wall-piping system at E-Defense. II: Evaluation of nonstructural damage and fragilities. *Journal of Structural Engineering (ASCE)* 2015; **142**(2).
23. Retamales R, Davies R, Mosqueda G, Filiatrault A. Experimental Seismic Fragility of Cold-Formed Steel Framed Gypsum Partition Walls. *Journal of Structural Engineering (ASCE)* 2013; **139**(8):1286–1293.
24. Tian Y, Filiatrault A, Mosqueda G. Experimental seismic fragility of pressurized fire

suppression sprinkler piping joints. *Earthquake Spectra* 2014; **30**(4):1733–1748.

25. Tian Y, Filiatrault A, Mosqueda G. Seismic response of pressurized fire sprinkler piping systems I: Experimental study. *Journal of Earthquake Engineering* 2015; **19**(4):649–673.
26. Tian Y, Filiatrault A, Mosqueda G. Seismic response of pressurized fire sprinkler piping systems II: Numerical study. *Journal of Earthquake Engineering* 2015; **19**(4):674–699.
27. Soroushian S,ZAE, Maragakis EM, Echevarria A, Tian Y, Filiatrault A. Seismic fragility study of fire sprinkler piping systems with grooved fit joints. *Journal of Structural Engineering (ASCE)* 2015; **141**(6).
28. Soroushian S, Zaghi AE, Maragakis EM, Echevarria A, Tian Y, Filiatrault A. Analytical seismic fragility of fire sprinkler piping systems with threaded joints. *Earthquake Spectra* 2015; **31**(2):1125–1155.
29. Pantoli E, Chen MC, Hutchinson TC, Astroza R, Conte JP, Ebrahimian H, Restrepo JI, Wang X. Landmark Dataset from the Building Nonstructural Components and Systems (BNCS) Project. *Earthquake Spectra* 2015 [In-Press].
30. Di Sarno L, Petrone C, Magliulo G, Manfredi G. Dynamic properties of typical consultation room medical components. *Engineering Structures* 2015; **100**:442-454.
31. Cosenza E, Di Sarno L, Maddaloni G, Magliulo G, Petrone C, Prota A. Shake table tests for the seismic fragility evaluation of hospital rooms. *Earthquake Engineering and Structural Dynamics* 2015; **44**(1):23-40.
32. Sato E, Furukawa S, Kakehi A, Nakashima M. Full-scale shaking table test for examination of safety and functionality of base-isolated medical facilities. *Earthquake Engineering and Structural Dynamics* 2011; **40**(13):1435–1453.
33. Comerio MC, Stallmeyer JC. Laboratory equipment: estimating losses and mitigation costs. *Earthquake Spectra* 2003; **19**(4):779–797.
34. Shi Y, Kurata M, Nakashima M. Disorder and damage of base-isolated medical facilities when subjected to near-fault and long-period ground motions. *Earthquake Engineering and Structural Dynamics* 2014; **43**(11):1683–1701.

35. Furukawa S, Sato E, Shi Y, Becker T, Nakashima M. Full-scale shaking table test of a base-isolated medical facility subjected to vertical motions. *Earthquake Engineering and Structural Dynamics* 2013; **42**(13):1931–1949.
36. Yang T, Konstantinidis D, Kelly J. The influence of isolator hysteresis on equipment performance in seismic isolated buildings. *Earthquake Spectra* 2010; **26**(1):275–293.
37. McKenna F, Fenves GL, Scott MH. Open system for earthquake engineering simulation (OpenSees) 2000 [Internet]. http://opensees.berkeley.edu.
38. Nikfar F, Konstantinidis D. Evaluation of vision-based measurements for shake-table testing of nonstructural components. *Journal of Computing in Civil Engineering (ASCE)* 2015 [under review].
39. ASCE/SEI 7-05. *Minimum design loads for buildings and other structures*. American Society of Civil Engineers: Reston , Virginia, 2006.
40. IBC2006-05. *International Building Code (IBC)*. Falls Church 2005.
41. ANSI/AISC 360-05. *Specifications for structural steel buildings*. Chicago: American Institute of Steel Construction; 2005.
42. Hsiao PC, Lehman DE, Roeder CW. Improved analytical model for special concentrically braced frames. *Journal of Constructional Steel Research* 2012; **73**:80–94.
43. Uriz P, Filippou FC, Mahin SA. Model for cyclic inelastic buckling of steel braces. *Journal of Structural Engineering* 2008; **134**(4):619–628.
44. Nikfar F, Konstantinidis D. Effect of the stick-slip phenomenon on the sliding response of objects subjected to pulse excitations. *Journal of Engineering Mechanics (ASCE)* 2015 [under review].
45. Nikfar F, Konstantinidis D. Solving dynamical systems with path-dependent nonlinearities using MATLAB ODE solvers. *Proc. 10th National Conference in Earthquake Engineering*, Earthquake Engineering Research Institute; 2014; Anchorage, AK.

Table 5-1. Steel sections used in the structure of the building

Story	Gravity Columns	Braced Columns	Girders	Braces	L_{ave} (m)	W_w (m)
1	W14×68	W14×233	W14×68	HSS 12×12×6/8	0.50	1.5
2	W14×68	W14×145	W14×68	HSS 10×10×6/8	0.45	1.3
3	W14×48	W14×68	W14×68	HSS 9×9×5/8	0.40	1.1
4	W14×38	W14×38	W14×68	HSS 7×7×5/8	0.35	0.9

Table 5-2. Ground motions used in this study, together with their scaling factors

ID	**Scale Factor**	**Earthquake Name**	**Year**	**Station Name**	**Magnitude**	**V_{s30} (m/s)**
LOMAP	1.34	Loma Prieta	1989	WAHO	6.93	388.33
NORTHR	1.06	Northridge-01	1994	Castaic - Old Ridge Route	6.69	450.28
MANJIL	0.91	Manjil	1990	Abbar	7.37	723.95
CHICHI	1.38	Chi-Chi Taiwan-03	1999	TCU129	6.2	511.18

Table 5-3. Peak structural response quantities obtained from the nonlinear time history analysis

Ground Motion	Level	Absolute Displacement (cm)			Absolute Velocity (cm/s)			Absolute Acceleration (g)			Peak Inter-story Drift (%)		
		SLE	DBE	MCE	SLE	DBE	MCE	SLE	DBE	MCE	SLE	DBE	MCE
LOMAP	Gnd	4.0	7.9	11.9	25.6	51.1	76.7	0.44	0.88	1.32	-	-	-
	1st	4.5	8.2	11.9	40.6	70.0	89.8	0.91	2.35	3.69	0.30	0.46	0.69
	2nd	5.6	9.5	13.1	50.6	98.5	98.4	1.23	3.00	3.05	0.34	0.52	1.37
	3rd	6.8	17.0	21.5	48.5	79.1	81.5	0.96	1.42	1.57	0.37	2.46	3.33
	Roof	7.6	18.0	22.5	66.8	98.3	101.4	1.03	1.36	1.13	0.35	0.45	0.50
NORTHR	Gnd	5.3	10.6	15.9	27.5	54.9	82.4	0.25	0.51	0.76	-	-	-
	1st	7.0	11.3	17.6	41.4	89.8	98.2	1.08	2.00	2.45	0.38	0.43	0.83
	2nd	8.8	9.7	18.3	62.2	69.2	124.3	1.32	1.36	2.48	0.42	1.19	0.51
	3rd	10.6	17.5	25.3	71.8	86.4	90.6	0.97	1.32	1.52	1.00	**3.54**	**6.78**
	Roof	11.9	18.3	26.2	83.0	95.1	100.4	1.23	1.02	1.31	0.40	0.39	0.47
MANJIL	Gnd	4.6	9.3	14.0	19.1	38.1	57.2	0.25	0.51	0.76	-	-	-
	1st	4.8	9.4	14.5	27.9	63.0	77.2	0.56	1.59	1.83	0.32	0.39	0.52
	2nd	6.0	9.7	14.9	49.6	82.6	111.8	0.66	2.34	2.12	0.39	0.48	0.46
	3rd	7.4	11.1	23.7	62.6	65.1	90.4	0.93	1.28	1.23	0.35	2.06	3.95
	Roof	8.9	11.0	24.3	72.2	80.2	115.6	1.05	1.09	1.18	0.38	0.42	0.53
CHICHI	Gnd	9.1	18.2	27.3	25.3	50.6	75.9	0.65	1.31	1.96	-	-	-
	1st	9.8	18.7	27.8	34.5	84.7	120.8	0.85	2.37	3.03	0.36	0.34	0.38
	2nd	10.7	20.0	29.1	56.5	74.0	109.2	1.52	1.60	2.69	0.43	1.07	1.06
	3rd	11.5	22.7	30.5	62.5	65.0	94.6	1.23	1.56	1.50	1.17	2.08	2.28
	Roof	12.2	23.1	30.6	73.4	66.1	96.6	1.10	1.39	1.10	0.40	0.44	0.38

Table 5-4. Performance of shake-table in reproducing simulated floor displacement and velocity.

3rd Story Under	Peak Table Displacement (m)			Peak Table Velocity (m/s)		
	Desired	Observed	Error (%)	Desired	Observed	Error (%)
LOMAP-DBE	0.170	0.171	0.59	0.791	0.824	4.17
LOMAP-MCE	0.215	0.217	0.93	0.815	0.868	6.50
NORTHR-DBE	0.175	0.176	0.57	0.864	0.895	3.59
NORTHR-MCE	0.253	0.244	-3.56	0.906	0.906	0.00
MANJIL-DBE	0.111	0.111	0.00	0.651	0.675	3.69
CHICHI-DBE	0.227	0.227	0.00	0.650	0.684	5.23

Table 5-5. Shake table test matrix including the orientation of the equipment with respect to the shaking direction

Motion	Level	Ultrasound-unlocked (degree)			Ultrasound-locked (degree)			Hospital Cart (degree)		
		SLE	DBE	MCE	SLE	DBE	MCE	SLE	DBE	MCE
LOMAP	Gnd	0	0,45,90	0	0	0,45,90	0	0	0,90	0,90
	1st	0	0	0	0	0	0	-	-	-
	2nd	0	0	0	0	0	0	-	-	-
	3rd	0	0,45,90	0	0	0,45,90	0	0	0,90	0,90
NORTHR	Gnd	0	0,45,90	0	0	0,45,90	0	0	0,90	0,90
	1st	0	0	0	0	0	0	-	-	-
	2nd	0	0	0	0	0	0	-	-	-
	3rd	0	0,45,90	0	0	0,45,90	0	0	0,90	0,90
MANJIL	Gnd	-	0	-	-	0	-	-	0	-
	3rd	-	0	-	-	0	-	-	0	-
CHICHI	Gnd	-	0	-	-	0	-	-	0	-
	3rd	-	0	-	-	0	-	-	0	-

Note: the orientation angles are approximate

Table 5-6. Error in the predictions of the model

	Peak Displacement Error (%)		Peak Velocity Error (%)	
	Mean	σ	Mean	σ
Unlocked-Ultrasound ($\mu = 0.0079$)	-31.2	27.2	-2.2	4.6
Unlocked-Ultrasound ($\mu = 0.0104$)	-33.3	25	-2.3	4.8
Locked-Ultrasound ($\mu = 0.050$)	-15.5	37.1	-7.5	10.4
Medical Cart ($\mu = 0.0288$)	-15.2	28.2	-5.6	5.5

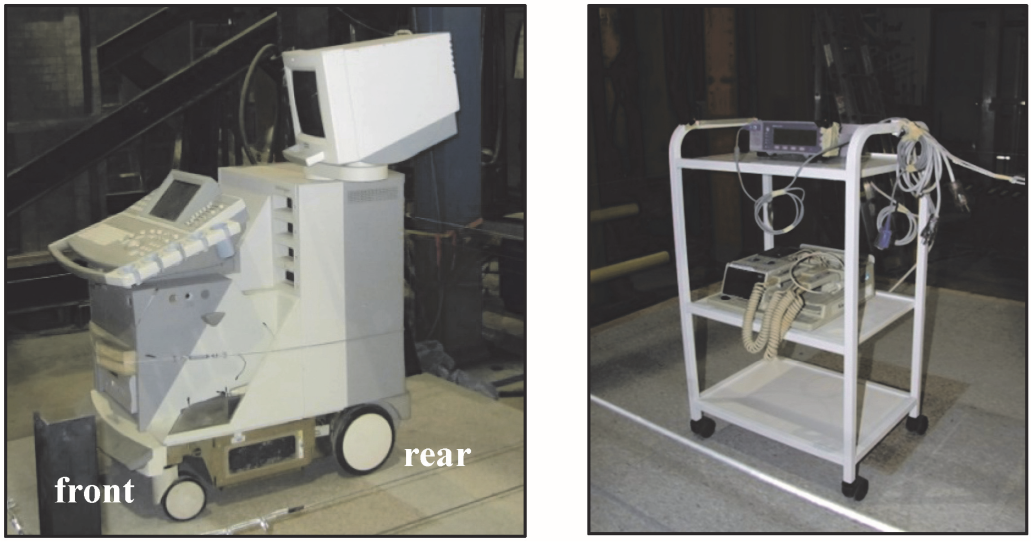

Figure 5-1. Hospital equipment used in this study. Left: Heavy ultrasound supported on wheels (rear) and twin-wheel casters (front). Right: Light hospital cart supported on 4 twin-wheel casters; the cart is carrying a pulse oximeter on the top tray and defibrillator on the middle tray.

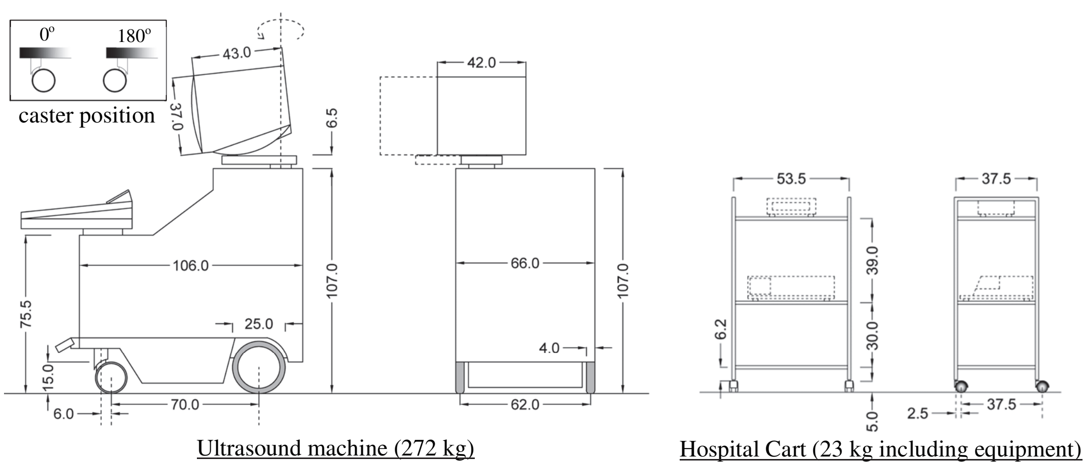

Figure 5-2. Schematics of the tested equipment (dimensions in cm).

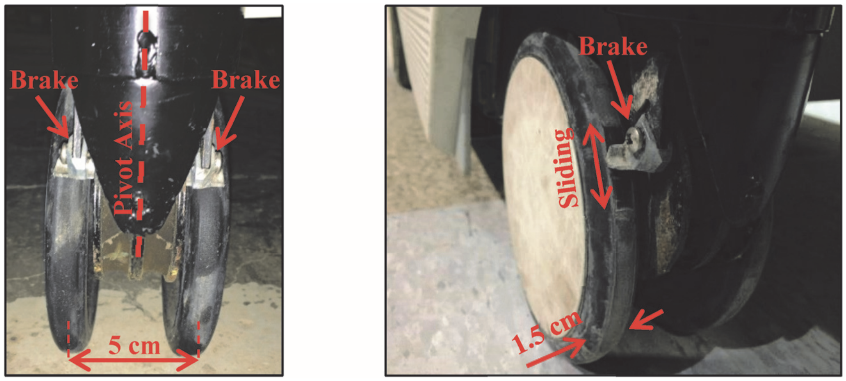

Figure 5-3. Positive brake mechanism of the ultrasound's twin-wheel casters. The dark streak on the tire, where the brake engages, indicates that the brakes do not completely lock the wheels.

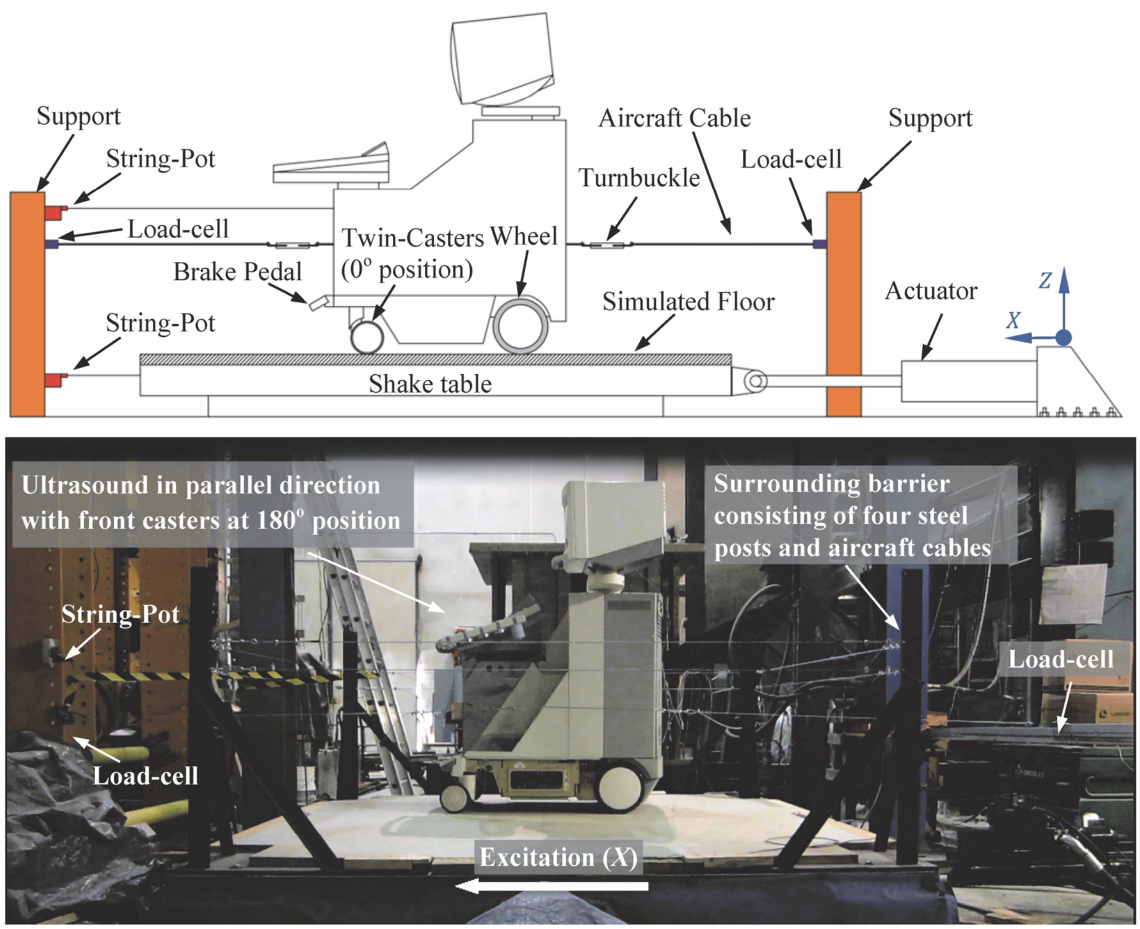

Figure 5-4. Top: Schematic of the resistance test setup (surrounding barrier not shown). Bottom: Photograph of the test setup.

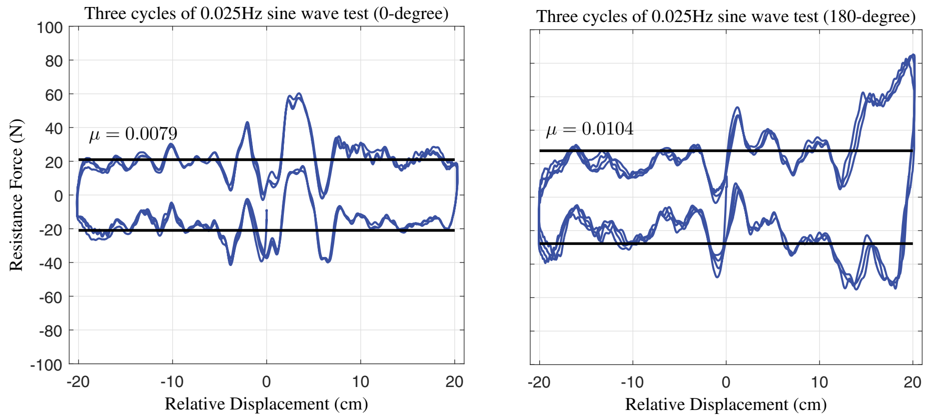

Figure 5-5. Force-displacement loops for the unlocked ultrasound. Left: with casters initially set at the 0-degree position. Right: with casters initially set at the 180-degree position.

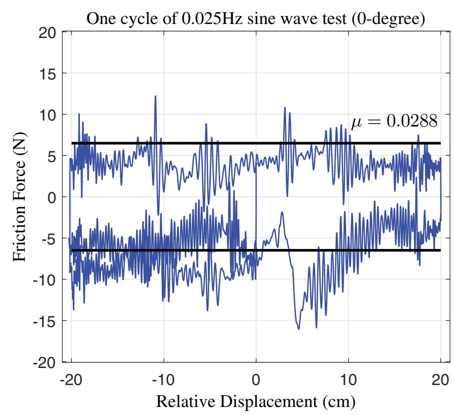

Figure 5-6. Force-displacement loops for the hospital cart (casters initially at 0-degree position).

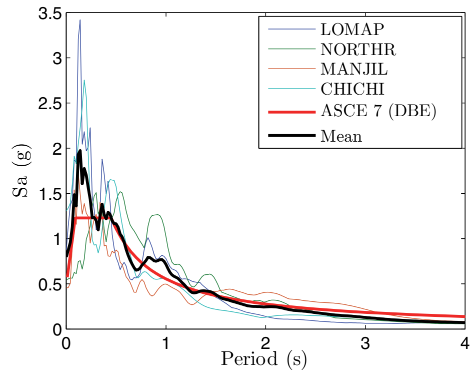

Figure 5-7. Acceleration response spectra for the scaled ground motions.

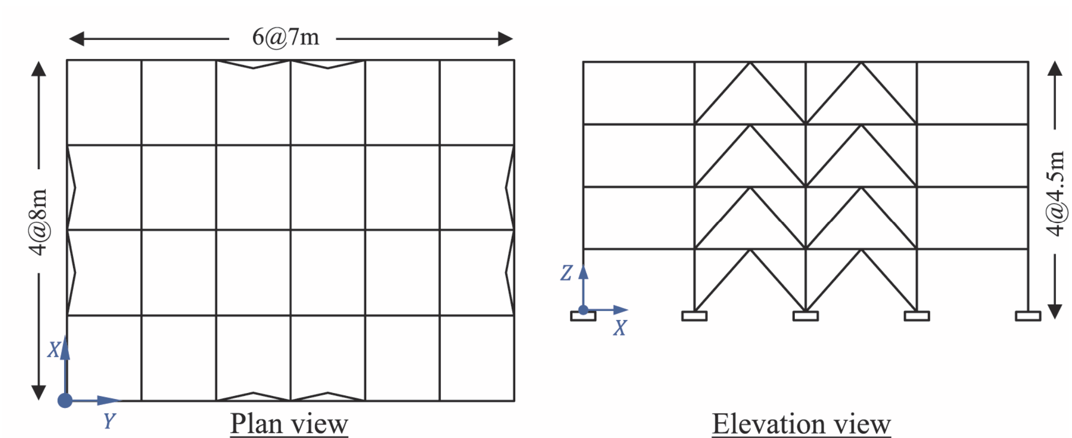

Figure 5-8. Plan and elevation views of the building.

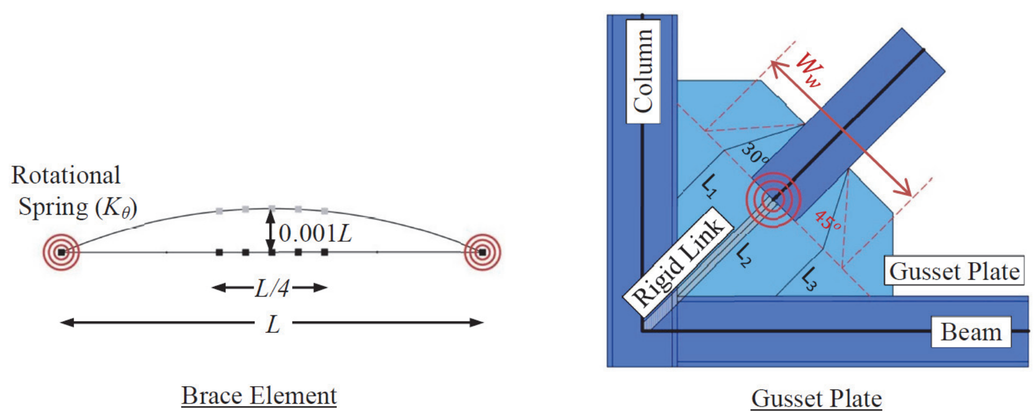

Figure 5-9. Brace and gusset plate elements.

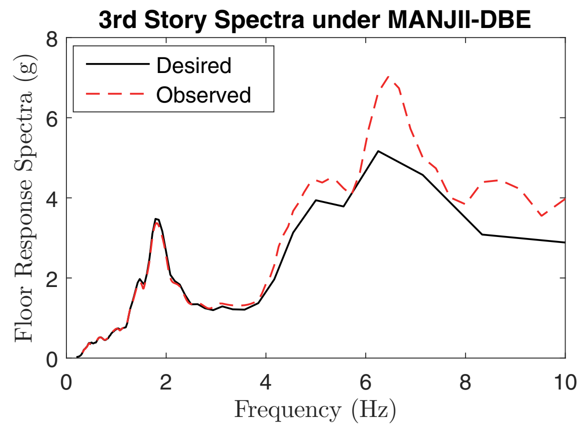

Figure 5-10. Comparison of desired and observed simulated floor spectra

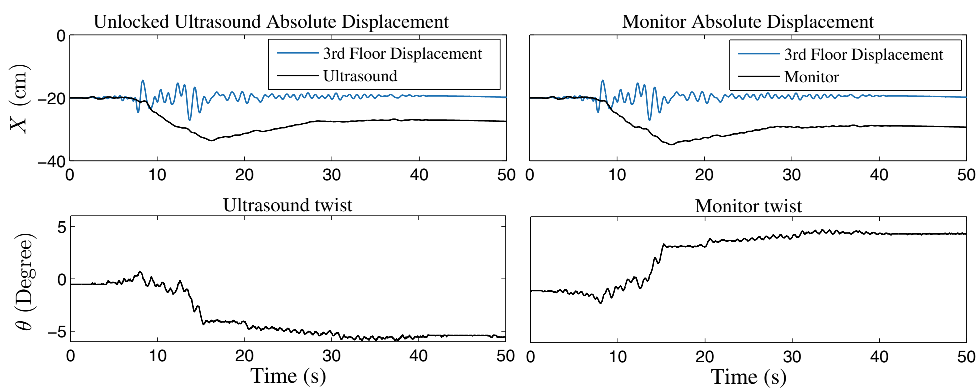

Figure 5-11. Absolute X-direction displacement and rotation of the unlocked ultrasound (left) and its monitor (right) under the 3rd story NORTHR-DBE excitation.

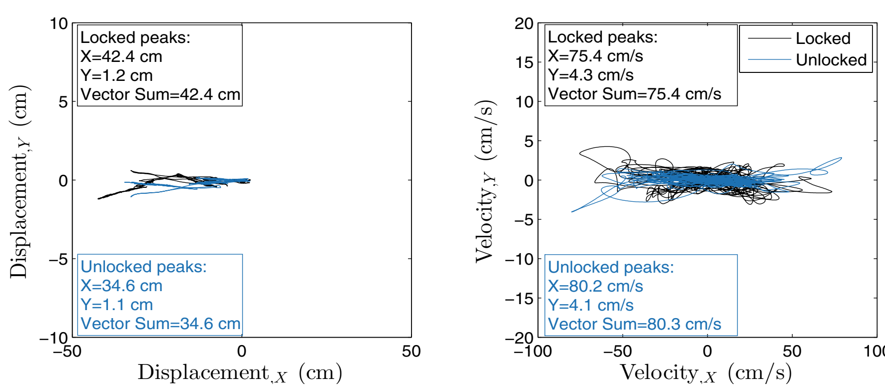

Figure 5-12. Relative displacement and velocity orbits of the locked and unlocked ultrasound under the 3rd story NORTHR-DBE excitation.

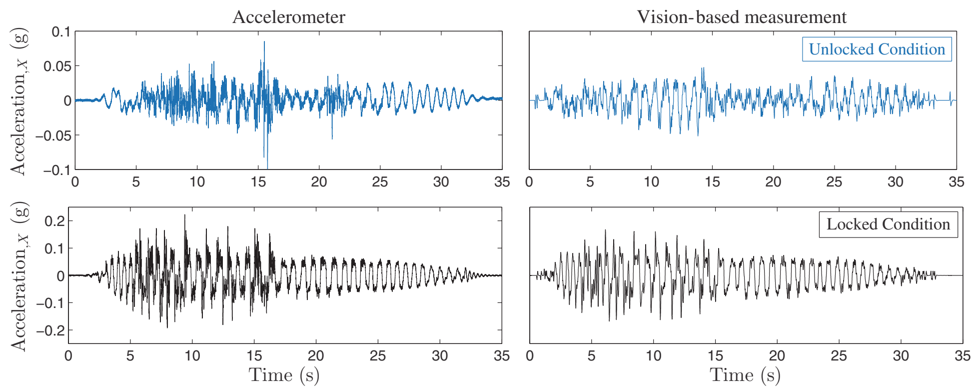

Figure 5-13. Absolute acceleration response of the ultrasound due to the 3rd story LOMAP-DBE excitation under locked (top) and unlocked conditions (bottom). Left: from accelerometer measurements. Right: from twice-differentiating the vision-based displacement measurements.

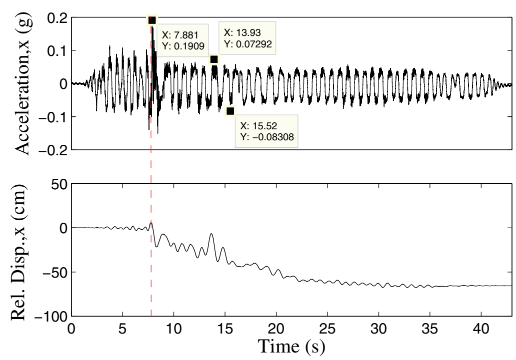

Figure 5-14. Estimation of the breakaway acceleration of the locked ultrasound, tested at 0-degree orientation under the 3rd story NORTHR-DBE excitation.

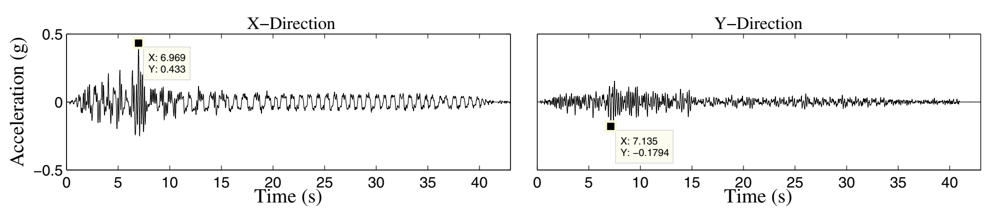

Figure 5-15. Absolute acceleration of the monitor of the locked ultrasound subjected to the 3rd story NORTHR-DBE motion. The vector sum of the acceleration in the X-Y plane is 0.44 g.

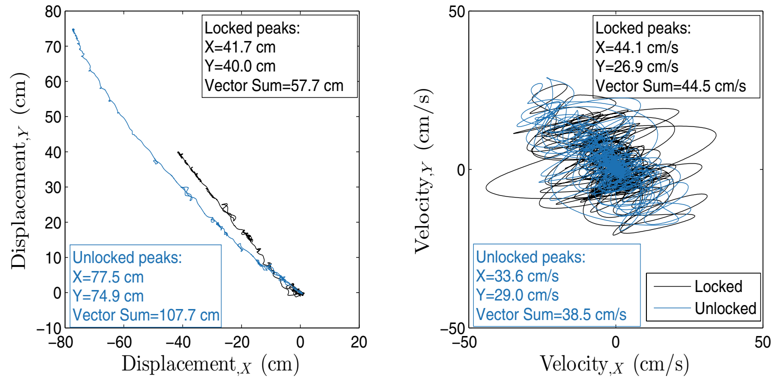

Figure 5-16. Relative displacement and velocity orbits of the locked and unlocked ultrasound tested in the 45-degree orientation relative to the input excitation: 3rd story LOMAP-DBE.

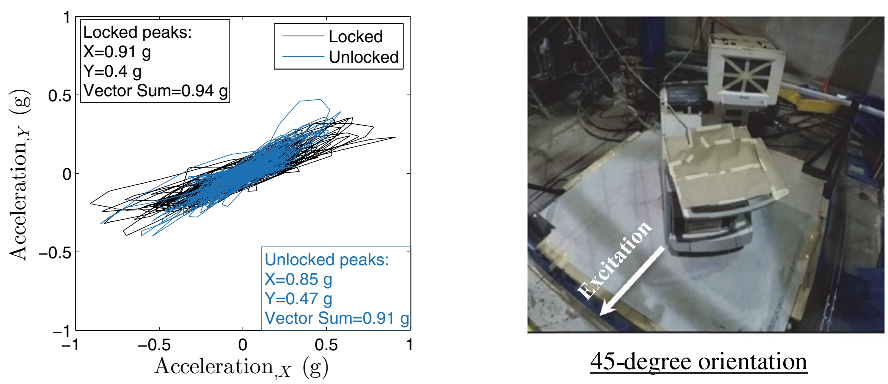

Figure 5-17. Absolute acceleration orbits of the locked and unlocked ultrasound tested in the 45-degree orientation relative to the input excitation: 3rd story LOMAP-DBE.

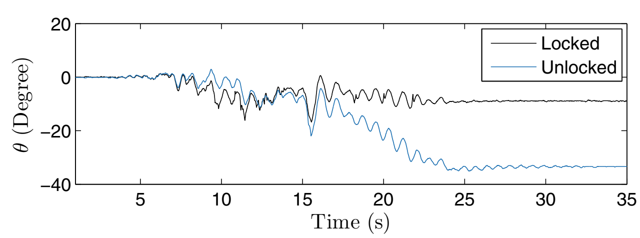

Figure 5-18. Rotation of the locked and unlocked ultrasound tested in the 45-degree orientation relative to the input excitation: 3rd story LOMAP-DBE.

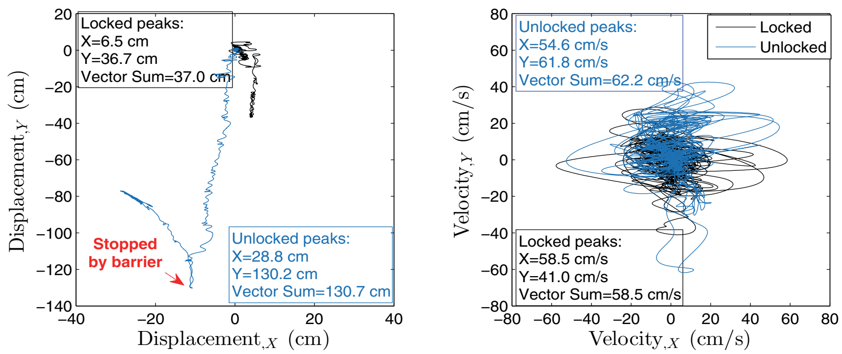

Figure 5-19. Relative displacement and velocity orbits of the locked and unlocked ultrasound tested in the perpendicular orientation relative to the input excitation: 3rd story LOMAP-DBE.

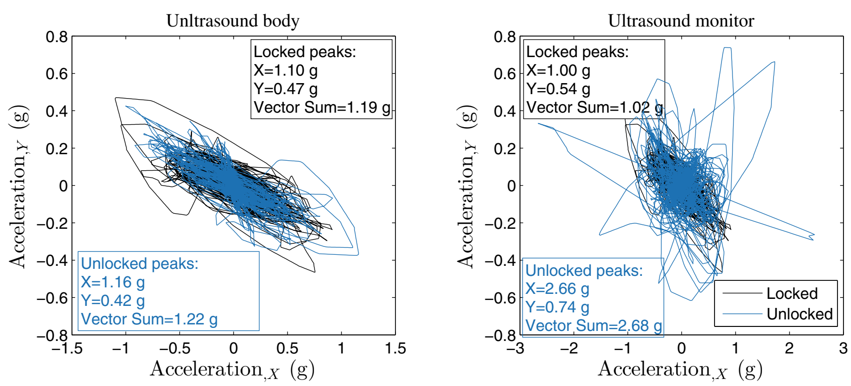

Figure 5-20. Absolute acceleration of the case and monitor of the locked and unlocked ultrasound tested in the perpendicular orientation relative to the input excitation: 3rd story LOMAP-DBE.

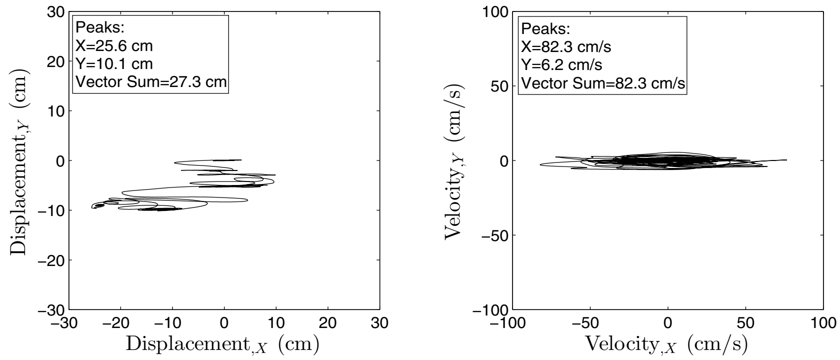

Figure 5-21. Relative displacement and velocity orbits of the hospital cart subjected to the 3rd story

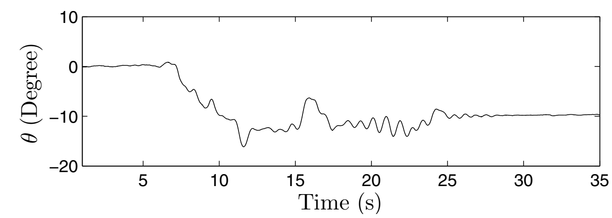

Figure 5-22. Rotation of the hospital cart under the 3rd story LOMAP-DBE excitation.

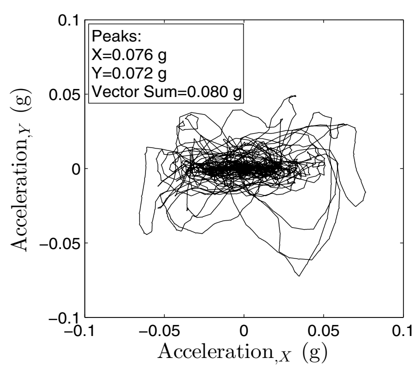

Figure 5-23. Absolute acceleration orbits of the hospital cart under the 3rd story LOMAP-DBE excitation.

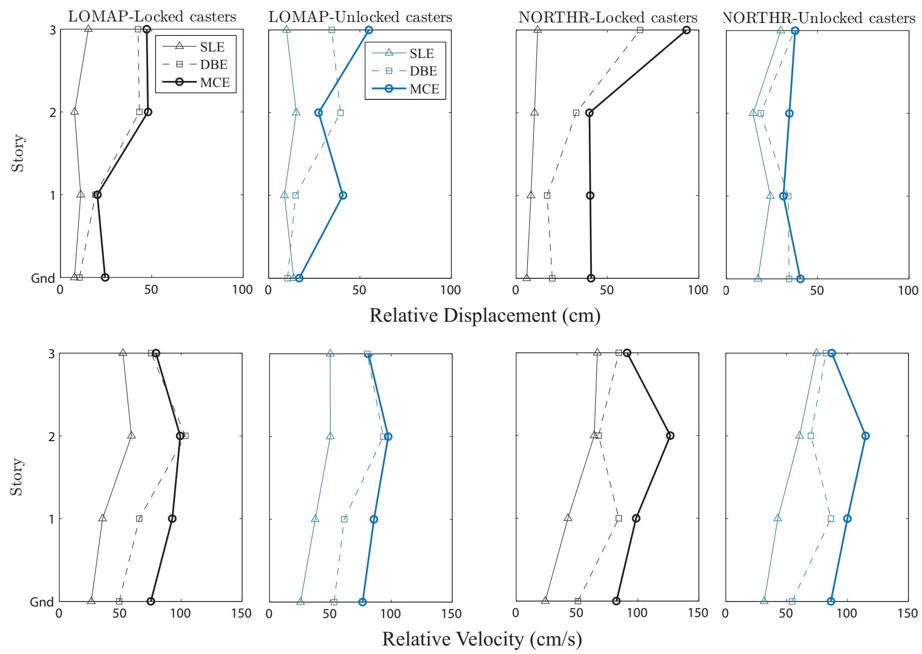

Figure 5-24. Peak demands on the ultrasound on different stories for the three hazard levels.

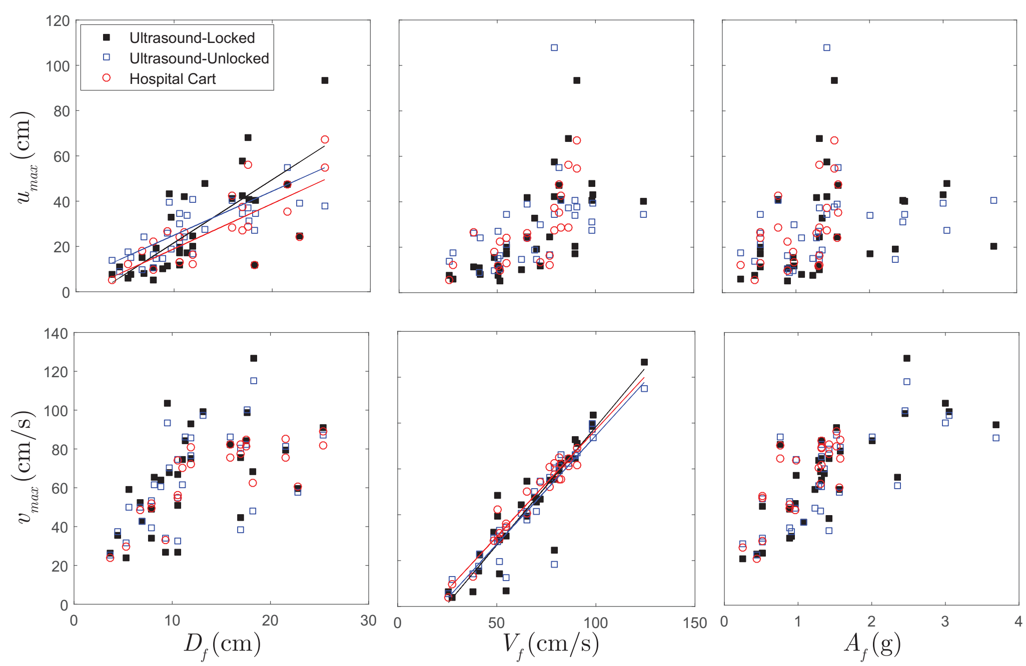

Figure 5-25. Peak relative displacement and relative velocity responses of ultrasound and hospital cart as a function of peak floor absolute acceleration, velocity, and displacement.

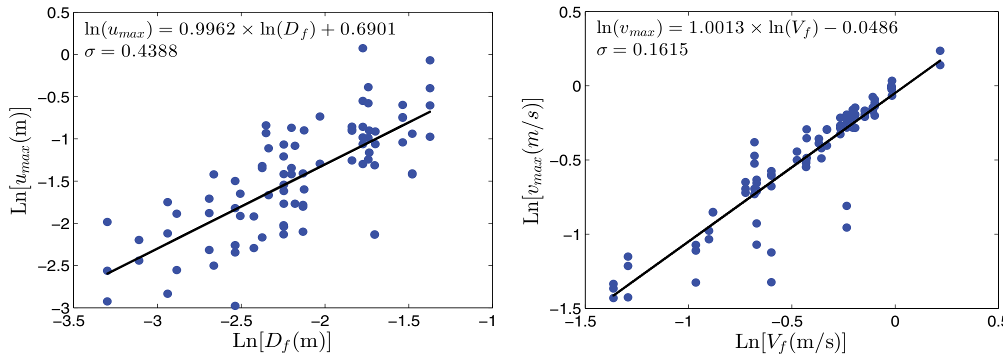

Figure 5-26. Regression analysis of the displacement and velocity demands data.

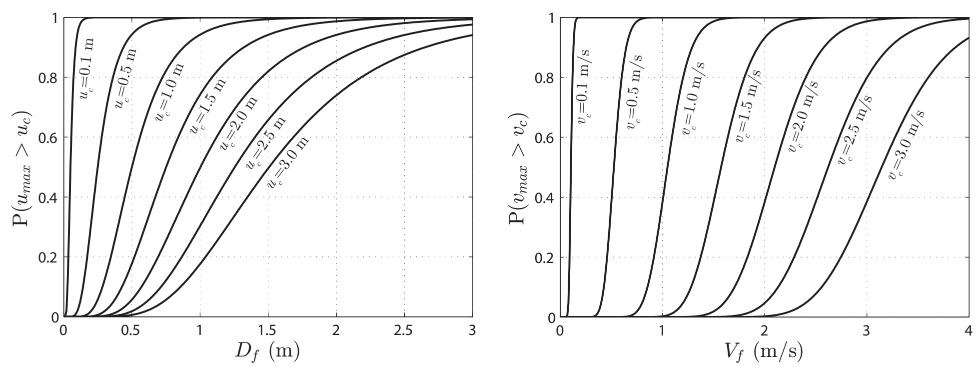

Figure 5-27. Conditional probability curves for medical equipment supported on wheels/casters. Left: Peak relative displacement. Right: Peak relative velocity.

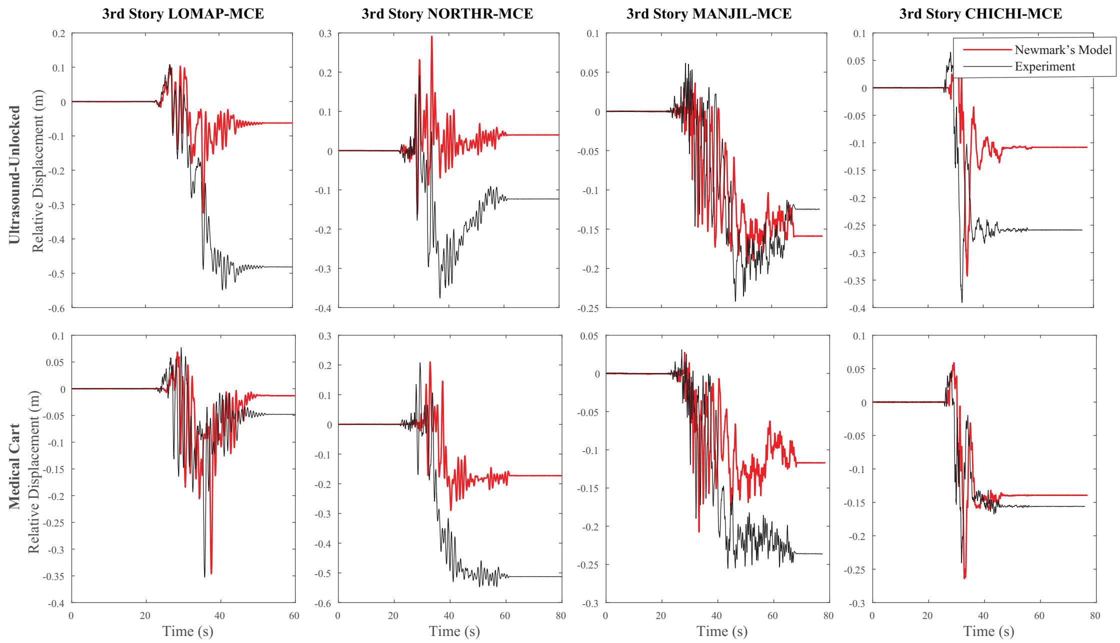

Figure 5-28. Comparison between the Newmark's sliding model and experimental results.

Chapter 6: Experimental Study on the Seismic Response of Equipment on Wheels/Casters in Base-Isolated Hospitals

Nikfar F., Konstantinidis D., 2016, Experimental Study on The Seismic Response of Equipment on Wheels/Casters in Base-Isolated Hospitals, to be submitted to *Earthquake Engineering and Structural Dynamics*.

Abstract

Seismic isolation is proven to be an effective technique for protecting building structures from damaging earthquakes. It has been the method of choice for critical facilities including hospitals in Japan and the United States in recent years. However, there have been only a few studies that investigated the performance of building equipment and contents, and particularly those supported on wheels/casters, in such buildings. About one-third of equipment and contents in a typical hospital are supported on wheels/casters. This study investigates the seismic response of this type of equipment and contents in base-isolated buildings through shake table tests of two pieces of hospital equipment on wheels/casters. This paper adopts a comparative approach to examine the performance of bilinear (LRB) and triple-friction-pendulum (TFP) isolation systems against a conventional fixed-base hospital. It was observed that, on average, base isolation reduces the relative displacement demands on equipment. However, in some cases, it amplified the relative displacement demands comparing to the fixed-base buildings. Furthermore, reduction in relative velocity demands on equipment was evident in all the cases. It is concluded that, in a base-isolated building, locking the wheels/casters is preferable for reducing the maximum displacement demands on equipment supported on wheels/casters. Finally, the paper provides probability functions that can be used by practicing engineers to estimate the peak relative displacement and relative velocity of equipment of this type in base-isolated buildings.

6.1 Introduction

Immediate occupancy and functionality of critical facilities including hospitals are of utmost importance immediately after a damaging earthquake, as they must continue to provide emergency health services in the aftermath of an extreme event. Although recent earthquakes have proven an acceptable performance of structural elements of code-compliant hospitals, in many cases the nonstructural component damages were the main causes of disruption of their functionality [1-6]. Recent examples of poor nonstructural performance in structurally code-compliant hospital buildings include hospitals during the 2010 Chile Earthquake [7]. The hospital buildings were designed based on Chilean seismic design codes, which are very similar to recent United States codes. Nevertheless, reconnaissance missions reported that there were several cases of damage to unsecured equipment and contents (EC) that fell or broke during the earthquake, hindering the emergency response function of the hospitals [7]. In many cases, large, unanchored equipment, such as incubators and computers, was reported damaged after falling to the floor [7]. Similarly, in the 2011 Christchurch earthquakes, poor performance of utility networks and damage to nonstructural components were reportedly the major problems affecting the operation of the Canterbury hospital system [8].

Although severe nonstructural damage and loss of functionality in medical facilities were observed during the 1994 Northridge, 1995 Kobe, and 1999 Chi-Chi earthquakes [9,10], only a handful of studies have been conducted since then to investigate the seismic performance of typical medical equipment and hospital components. A notable full-scale shake-table test study, which included the performance of structural and nonstructural components in fixed-base and base-isolated hospitals, was carried out at the E-Defence facility [11-13]. Pantoli et al. [14] conducted shake table tests of a five-story reinforced-concrete building (both fixed-base and base-isolated) that featured a variety of nonstructural components and systems. Di Sarno et al. [15] and Cosenza et al. [16] investigated the dynamic response and fragility of components in typical hospital rooms through shake table tests.

This study focuses on the seismic performance of wheel-supported and/or caster-supported EC, which are abundant in hospitals. About one-third of the hospital equipment and appliances are on wheels and casters due to their mobility requirements [11]. The concern with equipment and appliances on wheels and casters during earthquakes is that they might exhibit large movements. Excessive movements could tear off or disconnect the electric plugs and impair the functionality of the equipment. For instance, large movements of an anesthesia machine may not only tear off its electric plug, but also disconnect its connections to piped hospital oxygen, medical air, and nitrous oxide. This would lead to malfunction of the equipment and possible loss of life. Large motion of EC in an operating room is also a big concern for medical room personnel. Moreover, large displacement increases the possibility of collision with other furniture, equipment and surrounding partitions. Impact as a result of collision introduces high accelerations that can lead to damage to acceleration-sensitive equipment and components. In the case of heavy equipment on wheels, a collision with people in the vicinity of the equipment may result in injury.

The hazard associated with these items can stem from any or a combination of the following: (a) excessive displacement that can increase the potential of impact with adjacent EC as well as other nonstructural components, including partition walls; (b) large relative velocity, which, if coincident with large relative displacement, may result in damaging impact that can put the safety of the people working in the vicinity of the equipment or the functionality of the equipment at risk; (c) large accelerations, particularly in the high frequency range, that can cause resonance and damage to the electronic parts and attached components of the equipment. Therefore, desirable characteristics of earthquake protection systems for building equipment include the ability to decrease floor acceleration, relative displacement, and relative velocity together with shifting the floor vibration frequency to frequencies lower than the equipment resonance frequency.

Seismic isolation appears to be an ideal solution for protecting a building's EC since it aims to control all of the aforementioned demand parameters. While this claim was made more than three decades ago [17], the supporting research for unanchored EC is limited. Nikfar and Konstantinidis [18] studied the performance of sliding EC in isolated buildings under broadband and pulse-like ground motions. Sliding fragility curves for broadband ground motions are presented in [19]. To date, there has been only one comprehensive experimental program that examined the performance of hospital equipment on wheels/casters in a base-isolated hospital [11-13]. It included full-scale shake table experiments of a four-story RC building at E-Defense to evaluate the performance of fixed-base and base-isolated medical facilities. Various rooms at different floor levels of the building were outfitted with hospital equipment and appliances to replicate realistic hospital rooms. The experimental program was aimed at studying various aspects of the facility. Shi et al. [13] focused specifically on the performance of items on casters. It was observed that the equipment with unlocked casters may experience movements as large as three meters. Multiple collisions with other equipment, furniture, and partitions were observed that resulted in accelerations up to 10 g [13]. The experimental results of the base-isolated building showed that most equipment and appliances (including the ones with locked casters) experienced negligible movement except for those with unlocked casters that exhibited very large motions, leading to collisions with other equipment and surrounding partitions [13]. For equipment with locked casters, the response was very small when the building was tested as base-isolated, but when the building was tested as fixed-base, especially under near-fault ground motion, the equipment experienced the largest response and damage [13].

This paper presents the findings of a shake table study investigating the seismic response of an ultrasound machine and a cart loaded with medical equipment, housed in (a) a conventional braced-frame hospital building, (b) a hospital building isolated by Lead Rubber Bearings (LRB), and (c) a hospital building isolated by a Triple Friction Pendulum (TFP) system. The ultrasound machine is an example of a common heavy piece of equipment, and the hospital cart is typical representation of light items on wheels/casters. The floor motions used as input in the shake table experiments were generated from a series of nonlinear time history analyses of the building models using site-compatible ground motions scaled to three earthquake intensity levels, i.e., maximum considered earthquake (MCE), design based earthquake (DBE) and service level earthquake (SLE) (chosen to be 50% of DBE in this study). The shake table excitation was unidirectional, and the equipment was tested in both locked and unlocked configurations. The response of the equipment during the experiments was recorded using a motion capture technique and accelerometers. The response of the equipment under fixed-base and base-isolated conditions (using both LRB and TFP systems) is discussed. It is shown that, on average, base isolation considerably reduces the relative displacement and relative velocity of EC supported on wheels/casters. However, depending on the kinematics of the input motion, there were cases where the EC may experience larger displacement in base-isolated buildings. Furthermore, it is observed that locking the wheels/casters is effective in reducing the relative displacement and relative velocity responses of EC in base-isolated buildings; although, there were few cases where locking resulted in larger response. The experimental data was also used to produce conditional probability functions to estimate the peak relative displacement and relative velocity of unlocked equipment in base-isolated buildings.

6.2 Test specimens

Two test specimens were used in this study: an ultrasound machine weighting 272 kg which represents a typical heavy piece of medical equipment, supported on two wheels (rear) and two casters (front), and a cart loaded with typical light medical equipment (all together 23 kg), supported on four casters, as shown in Figure 6-1 (right). The ultrasound was composed of three main parts: the main body (or case), the control panel, and the monitor. The main body housed most of the electronics and accounted for the majority of the equipment’s mass, and the control panel and monitor were mounted flexibly on the main body, so that they could move and rotate depending on user needs. The tested ultrasound featured a brake mechanism acting on the front casters only. The light hospital cart was supported on four twin wheel casters, the type typically installed on the majority of light-weight office and laboratory items. None of the casters of this particular cart had a brake mechanism, although similar casters with brake are also common. More details about the dimensions, brake mechanism, and resistance of the wheels/caster of the equipment are presented by in [20].

6.3 Shake table test program

6.3.1 Test procedure and instrumentation

The shake table facility at the Applied Dynamics Laboratory, McMaster University, was utilized for simulating the horizontal floor motions of a fixed-base and two base-isolated buildings to investigate the seismic response of the hospital equipment. The floor motions used as input for the shake table tests were generated by nonlinear time history analysis of an elaborate nonlinear structural model in OpenSees [21]. The structural model and detailed modeling assumptions are presented in the following sections. For the tests, the equipment was placed directly on a simulated hospital floor constructed on the shake table. The vertical component of the floor motion is not considered in this study since the shake table used is bidirectional—although only unidirectional tests were performed. However, it is noted that according to the results of the full-scale shake table tests conducted at E-Defense [12] which did include vertical excitation, the horizontal movement of the EC on wheels and casters is not affected significantly by vertical floor responses. This is due to the fact that, unlike in the case of sliding EC, the normal contact force does not contribute to the horizontal resistance of the wheels. Even a very low force would be adequate to overcome the resistance of the wheels and casters to rolling in unlocked condition. Moreover, in cases where the casters were locked, the brake mechanism did not fully lock the wheels, and the movement of the equipment was in fact due to slipping between the brake pads and the caster wheel, rather than sliding between the caster wheel and floor surface.

The motion of the shake table in the horizontal direction was tracked using an accelerometer (MEAS 4002-005) and a displacement sensor (Temposonics® LPRCCU04901). Also, one accelerometer (Entran EGCS-D0-2) was attached to the inside of the ultrasound to measure the accelerations that internal electronic parts may experience during seismic shaking. As the motion of the equipment was expected to be complicated, a vision-based measurement system was used in lieu of conventional contact sensors. A video camera with a 2.7K (2704×1520 pixel) resolution at a 60 frame per second rate was used to track the motion of LED lights attached to the body and monitor of the ultrasound. In the case of the hospital cart, LED lights were attached to the rigid handle of the cart and also to the top of the smaller medical equipment on the cart to track relative displacements. Displacement and velocity response histories were computed from post-processing of the recorded frames. The accuracy of the vision-based measurement is estimated to be about 1-mm and 7-cm/s for displacement and velocity, respectively. The detailed evaluation of the accuracy of the vision-based measurements in this study is presented in [22].

6.3.2 Structural Design

6.3.2.1 Site specific design criteria

A hypothetical four-story hospital building located in Los Angeles, California with site coordinates (34.02197°N , 118.28587°W) was designed according to the loading requirements of ASCE 7-05 [23] for Site Class C. According to ASCE 7-05, the soil condition of the site is classified as Site Class C. The mapped spectral accelerations are $S_S = 1.843\,\mathrm{g}$ and $S_1 = 0.640\,\mathrm{g}$. The resulting DBE-level design spectrum is shown in Figure 6-2.

6.3.2.2 Fixed-base hospital

The Steel Special-Concentrically-Braced-Frame (SCBF) lateral load resisting system for the fixed-base building with hospital occupancy, i.e., Risk Category IV, and importance factor $I = 1.5$ was designed according to the requirements of IBC2006 [24], AISC360-05 [25], and ASCE 7-05 [23]. The SCBF was designed with a response modification factor, over-strength factor, and drift ratio limit of $R = 6$, $\Omega = 2$, and 1.5% (obtained from static analysis of elastic structure), respectively. The characteristic yield strength of steel was assumed to be 345 MPa for frame members and 318 MPa for brace members. Assuming a SCBF as lateral load resisting system, all brace members were checked to ensure being seismically compact and limitations were applied on the slenderness ratio of each member. The lateral loads are carried by two braced bays on each side of the building perimeter, as shown in Figure 6-3. All other members were designed for gravity loads. Floor slabs consisted of 82.5-mm-thick lightweight concrete over a 50.8-mm-thick steel deck. A super dead load of 4.0 kPa was applied on the floor that included the weight of the floor slab and 0.96 kPa for cladding. The self-weight of the structural members was considered separately in the analysis. Assuming 10% for operation-rooms with uniform live load of 2.87 kPa, 65% for patient rooms with uniform live load of 1.92 kPa, and 25% for corridors with uniform live load of 3.83 kPa, an average live load of 2.5 kPa was considered on the floor slabs. The structural members were designed for a calculated base shear coefficient $C = 0.307$. Geometry of the building is schematically shown in Figure 6-3.Steel sections used in the structural members are summarized in Table 6-1.

6.3.2.3 Base-isolated hospital

The design and maximum displacement values of the isolation system were obtained from [23]

$$D_D = \frac{gS_{D1}T_D}{4\pi^2 B_D}\ ,\ D_M = \frac{gS_{M1}T_M}{4\pi^2 B_M} \tag{6.1}$$

where T_D, T_M are the effective isolation period values at DBE and MCE levels; B_D, B_M are the damping modification factors for the 5% damped response spectrum at DBE and MCE levels; and S_{D1}, S_{M1} are the 1-s spectral acceleration values for DBE and MCE events. Both LRB and TFP isolation systems are designed to exhibit effective period and damping of $T_M = 2.5$ s and $\zeta_M = 15$ % at the MCE level. The design and maximum effective isolation stiffness values are obtained from

$$K_D = \left(\frac{2\pi}{T_D}\right)^2 m_{BI}\ ,\ K_M = \left(\frac{2\pi}{T_M}\right)^2 m_{BI} \tag{6.2}$$

where m_{BI} is the total mass of the building, including the base mat. Depending on the isolation hysteretic model, the design displacement and stiffness can be obtained through iteration. The superstructure was designed for the base shear of $V_s = K_D D_D$, which in this case leads to a base shear coefficient of $C_{BI} = 0.157$ for the LRB system. Comparing the base shear coefficient of the base-isolated hospital to the inelastic base shear coefficient of the fixed-base hospital, $C_{FB} = 0.307$, the assumed base-isolation is expected to contribute to 49% reduction in the design base-shear. According to ASCE 7 code, the superstructure of seismically isolated buildings should be designed using a response modification factor R_I to be in the range $1 \leq 3R/8 \leq 2$. A low response factor like this limits the nonlinear deformations and consequently the damage to the superstructure. Because of the same reason, use of lateral systems with low ductility (small R factor) is favorable which also compensates the cost associated with base-isolating. A Steel Ordinary-Concentrically-Braced-Frame (OCBF) lateral load resisting system ($R = 3\frac{1}{4}$) is used as the lateral system for the superstructure. Even though the superstructure could be designed for a response factor of $R = \frac{3}{8} \times 3\frac{1}{4} = 1.21$, the full base shear force ($V_s = K_D D_D$) is used for designing the OCBF system ($R = 1.0$). Using an OCBF system, the brace slenderness ratio limitation no longer dictates the maximum length of the brace; therefore, instead of double braces, a single brace is used for each braced bay. The designed OCBF satisfies the 1.5% drift limit at DBE level. Figure 6-3(right) shows the brace configuration of the superstructure.

6.3.3 Modeling

6.3.3.1 Structural model

The buildings including the structure and isolation system were modeled in OpenSees [21]. The beams, columns, and braces were modeled using force-based beam-column elements. Equivalent loads and masses were calculated and transferred to the 2D frame (X-Z frame shown in Figure 6-3). The Steel02 material model with 3% strain hardening was considered for all the beam-column elements. Sections were discretized using 4 fibers along the thickness and 16 fibers along the web or flange length of the W and HSS sections. The beam-to-column connections were modeled as pinned-pinned. Columns were fixed at the base in the fixed-base hospital. To capture the bucking behavior of the braces, the simulation procedure proposed in Hsiao et al. [27] was implemented. Braces were simulated using 6 beam-column elements; of which, 4 elements were placed in the middle quarter length of the brace. Seven Gauss integration points were assumed for nonlinear curvature distribution for each beam-column element. The required imperfection of the braces followed a sine function with the apex at 0.1% of the length of the brace. A rotational nonlinear spring at each end of the brace was introduced to account for the stiffness and energy dissipation of the gusset plate. The initial stiffness of the gusset for each brace is calculated using the relation suggested in [27]. The Steel02 material model with 1% post-yield stiffness was utilized for these rotational springs. The aforementioned assumptions together with the use of corotational transformation for the brace beam-column elements allowed capturing the global buckling of the brace under cyclic loading [28,27], while local buckling was assumed not to occur owing to the use of seismically compact sections. The fundamental vibration period of the fixed-base and the superstructure of the base-isolated buildings in X-Direction (used later in the shake table study) were computed to be 0.54 s and 0.62 s, respectively. 2% Rayleigh damping, including both mass- and stiffness-proportional terms, was considered in the dynamic time-history analysis of the fixed-base model. The stiffness-proportional term of the damping was based on the last committed stiffness of the elements. However, a stiffness proportional damping is considered in the dynamic time-history analysis of the base-isolated buildings. The mass-proportional term of the Rayleigh damping model would apply an excessive artificial damping at frequencies lower than the superstructure fundamental frequency leading to undesirable suppression of the first mode response of the base-isolated structure [29].

6.3.3.2 LRB and TFP models

An assembly of an elastic column, an elastic-perfectly-plastic horizontal spring, and a nonlinear elastic vertical spring (Figure 6-4-a) is used to model the LRB system with a bilinear lateral load-displacement behavior in horizontal direction (Figure 6-4-b), fllowing the approach proposed in [26]. The vertical spring element allowed the consideration of geometric stiffness due to $P-\Delta$ effect. The elastic column has a lateral stiffness equivalent to the second stiffness of the isolation system (K_b). Parameters of the elastic-perfectly-plastic spring that acts in parallel with the elastic column in the horizontal direction are based on an initial stiffness of $K_1 - K_b$ and yielding displacement of u_y. The LRB is considered to have a vertical stiffness of $1000K_b$ in compression. The *double stiffness model* with 3% tensile yield strain and overstrain ratio of 0.06 is used to capture the compression and tensile behavior of the LRB [30]. The combination of the column vertical stiffness and a nonlinear elastic spring in vertical direction produced the double stiffness behavior shown in Figure 6-4 (c). The LRB isolators were modeled separately, one beneath each column. Assuming a yield displacement of $u_y = 0.01\text{ m}$, the characteristic strength of the bilinear model can be computed from [26]

$$Q = \frac{\pi K_M \zeta_M D_M^2}{2\left(D_M - u_y\right)} \tag{6.3}$$

Given Q and u_y, the second stiffness, $K_b = \left(K_M D_M - Q\right)/D_M$, yield strength, $F_y = Q + K_b u_y$, and consequently initial stiffness, $K_1 = F_y/u_y$, of the isolators was obtained. Once the bilinear model was defined, the corresponding design period and damping were determined through iteration ($T_D = 2.26\text{ s}$, $\zeta_D = 23\%$). Using Equation (6.1) the peak isolation displacement at MCE and DBE levels were computed as $D_M = 0.38\text{ m}$ and $D_D = 0.20\text{ m}$, respectively.

The design of the TFP system considered in this study is motivated by the actual TFP system used in the full-scale shake table study of a five-story base-isolated building at E-Defense facility [31]. This TFP system consists of four concave surfaces as shown in Figure 6-5. In practice, the curvature and friction of the surfaces are adjusted to form three independent pendulum mechanisms each activated depending on the intensity of excitation. The first pendulum mechanism is formed due to the sliding of inner slider and the two articulated sliders. The low friction coefficient $\mu_1 = \mu_2$ between the inner slider and both top and bottom articulated sliders allows the first pendulum mechanism to form under small earthquakes. However, the small spherical radius $R_1 = R_2$ of the inner slider leads to a relatively large stiffness that is favorable for maintaining the serviceability of the building under small earthquakes. Sliding between the lower articulated slider and the bottom concave plate forms the second pendulum mechanism, which is activated when the acceleration exceeds the friction coefficient μ_3 between the surfaces. The large spherical radius R_3 of the concave surface leads to a small stiffness for the pendulum. The third pendulum mechanism is formed by sliding between the upper articulated slider and top concave plate. The friction coefficient μ_4 between these surfaces is usually higher than μ_3 leading to its activation at large earthquakes. Displacement limits of sliders d_i and surface friction coefficients μ_i can be chosen in a way that the bearing exhibits stiffening regimes at large displacement to control the peak isolation displacement at extreme events. More details on the TFP parameters and its possible hysteretic regimes can be found in [32,33,34,31]. The effective pendulum lengths of the sliding surfaces $L_i = R_i - h_i$ together with the displacement limits of the sliders d_i, and friction coefficients μ_i, determine the hysteresis of TFP bearings. The design parameters of the TFP system used in this study are $\mu_1 = \mu_2 = 0.02$, $\mu_3 = \mu_4 = 0.08$, $L_1 = L_2$, $L_3 = L_4$, and $d_2 = d_3$ leading to a three-stage hysteresis backbone, as shown in Figure 6-5.

To obtain a TFP system equivalent to the LRB system, the effective stiffness K_{eff} and effective viscous damping ratio $\zeta_{eff} = E_{loop} / (2\pi K_{eff} D^2)$ of the two isolation systems are equated at a target displacement *D*. Such an approach based on linear isolation theory is also suggested in ASCE 7 [23]. The MCE event isolation displacement D_M is targeted in this study to obtain an equivalent TFP system. This requires satisfying the effective stiffness condition:

$$K_{M,\,\mathrm{LRB}} = K_{M,\,\mathrm{TFP}} \tag{6.4}$$

where

$$K_{M,\,\mathrm{LRB}} = \frac{Q + K_b D_M}{D_M} \tag{6.5}$$

and [35]

$$K_{M,\,\mathrm{TFP}} = \frac{\mu_4 + \dfrac{1}{L_3 + L_4} K_b \left(D_M - u_3 \right)}{D_M} W \tag{6.6}$$

in which $u_3 = u_2 + \left(\mu_4 - \mu_3 \right)\left(L_3 + L_2 \right)$, $u_2 = \left(\mu_3 - \mu_1 \right) L_1 + \left(\mu_3 - \mu_2 \right) L_2$, and W is the weight above the isolation layer. Furthermore, the effective damping condition (at D_M) should also be satisfied

$$E_{\mathrm{loop,\ LRB}} = E_{\mathrm{loop,\ TFP}} \tag{6.7}$$

where

$$E_{\mathrm{loop,\ LRB}} = 4Q\left(D_M - u_y \right) \tag{6.8}$$

and [35]

$$\begin{aligned} E_{\mathrm{loop,\ LRB}} = \Bigg[& 4\left(\mu_4 - \frac{1}{L_3 + L_4} u_3 \right) D_M - 4\left(\frac{1}{L_2 + L_3} - \frac{1}{L_3 + L_4} \right) u_3^2 \\ & -4\left(\frac{1}{L_1 + L_2} - \frac{1}{L_2 + L_3} \right) u_2^2 - 4\left(\frac{\mu_1}{D_y} - \frac{1}{L_1 + L_2} \right) D_y^2 \Bigg] \times W \end{aligned} \tag{6.9}$$

where D_y is the displacement associated with initiation of sliding which is assumed to be 0.0005 m in this paper. $L_1 = 0.3080\ \mathrm{m}$ and $L_3 = 1.0385\ \mathrm{m}$ are obtained through solving the system of equations consisting of Equation (6.4) and Equation (6.7). Subsequently, $R_1 = L_1 + h_1 = 0.346$, $R_2 = L_2 + h_2 = 1.1525$, and $R_3 = R_2$. The final step to fully describe the TFP system is specifying the displacement limits, d_i. For the three-stage hysteretic TFP considered in this study, the displacement limits affect only the displacement at which stiffening takes place, i.e., u_5 which is equal to u_4. The peak isolation displacement at MCE level, D_M, multiplied by the accidental eccentricity (i.e., $1.24D_M$ for this building) prescribed in ASCE 7 code can be assumed as the stiffening point to obtain d_3 and d_4. However, such amplification was not considered in this study since the shake table tests were uniaxial and subsequently the structural models were analyzed under one horizontal excitation together with the vertical component. Therefore, the D_M was taken as the stiffening point leading to $d_3 = d_4 = 0.192$ m . As it is evident from the equations provided in Figure 6-5, d_1 and d_2 merely control the extent isolator can displace within the stiffening regime until it reaches its limit. These parameters are considered sufficiently large not to let the isolators use up their displacement limits under all the excitations. Figure 6-6 compares the hysteresis loops of the equivalent LRB and TFP systems at SLE, DBE, and MCE Levels. The effective period and damping of both isolation systems are presented at three levels. As can be seen, both systems have very similar characteristics in terms of effective damping and period at DBE level. Nevertheless, at SLE level, TFP system is stiffer and less damped comparing to the LRB system assumed.

6.3.4 Structural responses

A set of four ground motions were selected from the PEER Strong Motion Database, NGA-West2, for the nonlinear time history analysis. The target design spectrum parameters $S_{DS} = 1.229$ g and $S_{D1} = 0.555$ g were used for spectrum-based ground motion selection. The Mean-Square-Error method with multiple period points from 0.1 s to 3.0 s was utilized in both the selection and the scaling of the ground motions. Only the H2 component of the recorded ground motions was considered in the process of scaling. Properties of the selected ground motions and the corresponding scaling factors are listed in Table 6-2. Acceleration response spectra of the scaled ground motions are shown in Figure 6-2. Both horizontal (i.e., H2) and vertical components of ground motions were applied to the structure and the resultant floor absolute accelerations were computed. Earthquake simulations were performed at SLE (i.e., 50% DBE), DBE, and MCE levels.

Figure 6-7 presents the floor absolute displacement under four ground motions. The first row plots are associated with the SLE level for which the absolute floor displacements are very close for the fixed-base (FB), LRB, and TFP systems. The plots corresponding to DBE level in the second row of the figure show that although larger floor displacement is expected for the base-isolated buildings, the fixed-base building might exhibit larger displacement at the floors undergoing large yielding deformations.

Similarly at MCE level, the third and fourth levels of the fixed-base building experienced a larger floor displacement under the LOMAP and NORTHR records compared to the base-isolated buildings. However, the base-isolated buildings exhibit larger displacement under MANJIL and CHICHI excitations. Comparing LRB and TFP systems, except for the CHICHI at SLE level, the floor displacements were slightly larger for the building isolated with TFP system. Figure 6-8 shows the peak floor absolute velocity responses. As can be seen, in all the cases the base-isolated buildings had considerably smaller floor absolute velocity than the fixed-base building. This tends to result in smaller relative velocity response of the contents, reducing potential damage due to impact. The effectiveness of base isolation in reducing the contents' relative velocity was examined later in this paper. Similar to the displacement response, on average, the TFP system exhibited slightly larger floor relative velocity than LRB system.

The floor absolute acceleration is an important input parameter controlling the initiation of movement or sliding (sliding equipment or equipment with locked wheels/casters) of unanchored EC. It is expected that base-isolating the building greatly reduces the accelerations and can potentially prevent the initiation of sliding of EC. In the case of attached equipment, reduction in floor accelerations will considerably reduce the accelerations transmitted to the equipment. Figure 6-9 illustrates the peak floor absolute acceleration responses. Considerable reduction in floor absolute acceleration is evident for base-isolated building comparing to the fixed-base building. The peak floor accelerations of base-isolated buildings were 0.26g, 0.54g, and 0.80g at SLE, DBE, and MCE levels, occurring under the MANJIL motion. The equivalent frictional resistance of the wheels and casters were approximately 0.01, 0.19, and 0.02 for the Unlocked-Ultrasound, Locked-Ultrasound, and Hospital Cart, respectively, as presented by the authors in [20]. Note that in almost all the cases the peak floor acceleration exceeded the resistance of the wheels resulting in a relative displacement between the equipment and the floor.

Figure 6-10 demonstrates the peak interstory drift ratios of the fixed-base (SCBF) and superstructure (OCBF) of the base-isolated buildings. The SCBF drift ratio is less than 2.5% for all the ground motions at DBE level except for NORTHR with 3.5%. The mean of the peak drift ratios of SCBF is 2.54% under DBE and 4.09% under MCE earthquakes. The base-isolated superstructure exhibits a minimal drift with peaks less than 0.41% (occurred under MANJIL-MCE level). Note that both LRB and TFE isolation systems resulted in very close peak drift ratios of their superstructures.

Figure 6-11 compares the floor acceleration spectra at the 3rd floor of the fixed-base and base-isolated buildings under the NORTHR and MANJIL motions at three intensity levels. Floor spectra provide information about the response of the attached EC as well as frequency content of the floor response. Comparing the plots of fixed-base to base-isolated buildings, base isolation considerably reduced the floor spectra in for all the frequencies. In the fixed-base building, location and number of peaks are different at different intensities, while the shape of spectra is preserved in buildings equipped with LRB and TFP systems. The peak isolation displacements computed at different input intensities are summarized in Table 6-3. In most of the cases, TFP exhibits slightly larger deformations than LRB. The peak isolation deformations are 0.099 m, 0.175 m, and 0.264 m under SLE, DBE, and MCE level excitations.

6.4 Shake table tests results

The seismic response of the equipment placed at the 3rd floor, evaluated through shake-table tests, was reported in this paper. The experimental data corresponding to the ground and other floor responses were reported in [20]. The ultrasound was tested under two conditions: with locked and with unlocked casters. The casters of the hospital cart were not lockable; thus, it was tested only in the unlocked condition. Tests were performed with the ultrasound's wheels parallel to the direction of excitation (more details on the behavior of equipment in oblique position can be found in [20]. Table 6-4 summarizes the experimental program adopted in this study.

The motion of the shake table in the horizontal direction was tracked using an accelerometer and a displacement transducer. One accelerometer was attached to the inside of the ultrasound to measure the accelerations that internal electronic parts may experience during seismic shaking. As the motion of the equipment was expected to be complicated, a vision-based measurement system was used in lieu of conventional contact sensors. A video camera with a 2.7K (2704×1520 pixel) resolution at a 60 frames per second rate was used to track the motion of LED lights attached to the body and monitor of the ultrasound. In the case of the hospital cart, LED lights were attached to the rigid handle of the cart and also to the top of the smaller medical equipment on the cart to track relative displacements. Displacement and velocity response histories were computed from post-processing of the recorded frames. The accuracy of the vision-based measurements is approximately 0.5-mm and 3-cm/s for displacement and velocity, respectively. A detailed evaluation of the accuracy of the vision-based measurements in this study is presented in [22]. Peak relative displacement orbits of the equipment in the 3rd floor of the fixed-base and base-isolated hospitals under NORTHR are potted in Figure 6-12. Note that the peak values shown are the magnitude of the relative displacement vector. Under DBE and MCE level excitations the locked-ultrasound experiences considerably larger displacement in fixed-base than base-isolated building. The unlocked-ultrasound shows larger displacement in building with LRB than fixed-base and TFP system. Except at SLE level where Hospital Cart shows larger displacement in the building with LRB system, base-isolating reduced the response comparing to the fixed-base building. Comparing the LRB and TFP, all the equipment items experience relatively smaller displacements in the building isolated with TFP system. The relative velocity responses of the equipment under the same input are depicted in Figure 6-13. As it is evident in the figure, base-isolating has greatly reduced the relative velocity response of the equipment and consequently decreased the potential impact forces. No general conclusion can be drawn on the effectiveness of locking in reducing or increasing the displacement and velocity responses of equipment based on the last two figures as its effects vary depending on the structural system and intensity of excitation.

Figure 6-14 compares the peak responses under NORTHR and LOMAP earthquakes. The left two columns plot the relative displacement and the right two columns show the relative velocity responses. It appears that base isolation does not necessarily reduce the displacement response of the hospital cart and unlocked-ultrasound, as in many cases the equipment experienced larger displacements in the base-isolated condition than the fixed-base condition. In contrast, the reduction in the displacement response of the locked-ultrasound is evident in base-isolated building. Based on the figure, the TFP system, on average, resulted in slightly smaller relative displacement response of the contents. Considering the relative velocity plots, in all the cases base isolation greatly reduced the response of all the equipment items. The velocity responses of equipment are very close for the LRB and TFP isolation systems.

6.5 Regression and probability study

In order to obtain a better representation of how different structural systems, i.e., fixed-base, LRB, and TFP, affect the displacement and velocity responses of the equipment with unlocked wheels/casters, the experimental data is presented in a probabilistic framework. Figure 6-15 shows the fragility curves associated with different systems for relative displacement and relative velocity demands of equipment. Peak Ground Acceleration (PGA) adopted for scaling the ground motions is considered as the intensity measure in generating the fragility curves. The first row plots correspond to the curves for 0.25 m, 0.5 m, and 1.0 m relative displacement thresholds. Based on these plots, base-isolating resulted in smaller probability to exceed the thresholds, indicating a superior performance of TFE system in reducing this demands. Considering the relative velocity curves on the second row plots, again, base isolation effectively reduced the probability of exceeding the velocity thresholds. In this case, the curves are very close for both isolation systems with a slightly better performance for the LRB system.

It has been shown by the authors [20] that parameters with the same dimension as the demand are better representatives of the input intensity. Hence, the experimental data associated with the peak relative displacement ($u_{\max}$) and relative velocity ($v_{\max}$) of the equipment in base-isolated buildings (i.e., both LRB and TFP systems) was re-plotted in Figure 6-16 as a function of peak floor absolute displacement (D_f) and peak floor absolute velocity (V_f), respectively. A linear regression was performed on the base-isolated data for ultrasound-locked, ultrasound-unlocked, and hospital cart. Comparing the lines associated with locked and unlocked ultrasound, it can be seen that, on average, locking the wheels/caster results in lower relative displacement and relative velocity demands on the equipment in base-isolated buildings. Therefore, locking the wheels/casters is preferable for equipment in base-isolated buildings. Consequently, the wheels/casters with automatic locking system would be a good choice for EC in base-isolated buildings. Nevertheless, as the authors have shown in their previous work [20], locking the wheels/casters does not necessarily lead to reduced demands. Note that in all the experiments the floor absolute accelerations exceeded the resistance capacity of the locked wheels. Increase in resistance to values greater than the floor absolute accelerations results in no relative displacement and velocity.

Taking the introduced intensity parameters, a lognormal distribution was fitted to relative displacement and relative velocity demand data corresponding to hospital cart and ultrasound-unlocked. To this end, both demand parameters ($u_{\max}$ and $v_{\max}$) were first transformed into log space, where linear regression was performed, as shown in Figure 6-17. The associated standard deviation of the relative displacement and relative velocity in log scale was obtained using maximum likelihood theorem, leading to 0.4036 and 0.0808, respectively.

Given the standard deviation for the lognormal distribution, corresponding conditional probability curves were generated, as presented in Figure 6-18. It is worth mentioning that these curves were generated merely for the equipment with unlocked wheels/casters and are independent of the equipment resistance and floor absolute acceleration. The inclusion of equipment with locked-wheels/casters would result in un-conservative estimate of probability. Moreover, determination of the resistance would be problematic as it would vary depending on the brake mechanism of the equipment as well as frictional resistance of the wheels and floor surfaces. Assuming a relatively rigid sliding equipment, the conditional probability curves suggested by the authors in [19] for sliding EC could be used provided that the resistance of the locked wheels/casters is evaluated. Furthermore, only the data of base-isolated buildings (LRB and TFP systems) are used since similar curves for a conventional building (fixed-base SCBF) were presented by the author in [20]. Therefore, the applicability of these curves is limited to equipment items with low resistance, e.g., equipment with unlocked wheels/casters, in base-isolated buildings.

6.6 Conclusion

This paper presented results of an experimental investigation on the seismic response of medical equipment supported on wheels/casters in fixed-base and base-isolated hospitals. The study included extensive shake table testing of two pieces of medical equipment on wheels/casters. The shake table simulated the floor absolute acceleration response of three prototype buildings: (1) a fixed-base hospital building featuring steel special-concentric-braced-frames, (2) a hospital building isolated using lead-rubber-bearing system, and (3) a hospital building isolated using triple-friction-pendulum system. The paper adopted a comparative approach to examine the performance of lead-rubber-bearing and triple-friction-pendulum isolation systems against the conventional fixed-base hospital. The floor absolute acceleration response of the buildings were computed using nonlinear time-history analysis of the building models in OpenSees under four ground motions for three intensity levels: SLE (defined as 50% DBE), DBE, and MCE. The performance of one of the two pieces of equipment was evaluated for both unlocked and locked casters. Although the electronic functionality of the equipment was not assessed before/after the shake table test, there was no physical damage to the equipment (detachment of components or failure of any sort) as a result of the shaking. Furthermore, there was no notable rocking, and the main mode of response was rolling of the wheels and casters.

It was shown that, overall, base-isolation is effective in reducing the relative displacement demand on the equipment on wheels and casters, although there were some cases where isolation resulted in amplified displacement responses. In all the cases, isolation resulted in considerably lower relative velocity demands, leading to reduced potential of damage due to impact. Comparing the LRB system with the TFP system, it is observed that the TFP system performs slightly better in reducing the peak displacement demand on the equipment, while the performance is almost the same as the LRB system when it comes to peak relative velocity demand. Furthermore, linear regression of the data corresponding to the base-isolated buildings demonstrated that the peak relative displacement and relative velocity were reduced under the locked condition. Therefore, locking the casters is recommended for equipment and contents in base-isolated buildings. Finally, the paper developed fragility functions that can be used to estimate the peak relative displacement and relative velocity of equipment on wheels and casters in base-isolated buildings.

6.7 References

1. Filiatrault A, Uang CM, Folz B, Christopulos C, Gatto K. *Reconnaissance report of the February 28, 2001 Nisqually (Seattle-Olympia) Earthquake*. La Jolla, CA: Department of Structural Engineering, University California, San Diego; 2001. Structural Systems Research Project Report N SSRP-2000/15.
2. Boroschek RL. Seismic vulnerability of the healthcare system in El Salvador and recovery after the 2001 earthquakes. *Special Papers-Geological Society of America*. 2004;375.
3. Myrtle R, Masri S, Nigbor R, Caffrey J. Classification and prioritization of essential systems in hospitals under extreme events. *Earthquake Spectra*. 2005;21(3):779–802.
4. Mosqueda G, Retamales R, Filiatrault A, Reinhorn A. Testing facility for experimental evaluation of non-structural components under full-scale floor motions. *The Structural Design of Tall and Special Buildings*. 2008;18(4):387–404.
5. Fierro EA, Miranda E, Perry,CL, Lynn AC, Reitherman R. Behavior of nonstructural components in recent earthquakes. In: *Proc. 2011 Architectural Engineering National Conference*; 2011; Oakland, CA.
6. Miranda E, Mosqueda G, Retamales R, Pekcan G. Performance of nonstructural components during the 27 February 2010 Chile earthquake. *Earthquake Spectra*. 2012;28(S1): S453-S471.
7. Mitrani-Reiser J, Mahoney M, Holmes WT, de la Llera JC, Bissell R, Kirsch T. A

functional loss assessment of a hospital system in the Bío-Bío province. *Earthquake Spectra*. 2012;28(S1):473-502.

8. Jacques CC, McIntosh J, Giovinazzi S, Kirsch TD, Wilson T, Mitrani-Reiser J. Resilience of the canterbury hospital system to the 2011 Christchurch earthquake. *Earthquake Spectra*. 2014;30(1):533-554.
9. Cimellaro GP, Reinhorn AM, Bruneau M. Seismic resilience of a hospital system. *Structure and Infrastructure Engineering*. 2010;6(1-2):127-144.
10. Filiatrault A, Sullivan T. Performance-based seismic design of nonstructural building components: The next frontier of earthquake engineering. *Earthquake Engineering and Engineering Vibration*. 2014;13(1):17-46.
11. Sato E, Furukawa S, Kakehi A, Nakashima M. Full-scale shaking table test for examination of safety and functionality of base-isolated medical facilities. *Earthquake Engineering and Structural Dynamics*. 2011;40(13):1435–1453.
12. Furukawa S, Sato E, Shi Y, Becker T, Nakashima M. Full-scale shaking table test of a base-isolated medical facility subjected to vertical motions. *Earthquake Engineering and Structural Dynamics*. 2013;42(13):1931–1949.
13. Shi Y, Kurata M, Nakashima M. Disorder and damage of base-isolated medical facilities when subjected to near-fault and long-period ground motions. *Earthquake Engineering and Structural Dynamics*. 2014;43(11):1683–1701.
14. Pantoli E, Chen MC, Hutchinson TC, Astroza R, Conte JP, Ebrahimian H, Restrepo JI, Wang X. Landmark Dataset from the Building Nonstructural Components and Systems (BNCS) Project. *Earthquake Spectra*. 2015;(In-Press).
15. Di Sarno L, Petrone C, Magliulo G, Manfredi G. Dynamic properties of typical consultation room medical components. Engineering Structures. 2015;100:442-454.
16. Cosenza E, Di Sarno L, Maddaloni G, Magliulo G, Petrone C, Prota A. Shake table tests for the seismic fragility evaluation of hospital rooms. *Earthquake Engineering and Structural Dynamics*. 2015;44(1):23-40.
17. Kelly JM, Tsai HC. Seismic response of light internal equipment in base-isolated

structures. *Earthquake Engineering and Structural Dynamics*. 1985;13(6):711–732.

18. Nikfar F, Konstantinidis D. Sliding response analysis of operational and functional components (OFC) in seismically isolated buildings. In: *3rd Specialty Conference on Disaster Prevention and Mitigation, Canadian Society of Civil Engineering (CSCE)*; 2013; Montreal.
19. Konstantinidis D, Nikfar F. Seismic response of equipment and contents in base-isolated buildings subjected to broad-band ground motions. *Earthquake Engineering and Structural Dynamics*. 2015;44(6):865–887.
20. Nikfar F, Konstantinidis D. Shake table investigation on the seismic performance of hospital equipment supported on wheels/casters. *Earthquake Engineering and Structural Dynamics*. 2016;[submitted].
21. McKenna F, Fenves GL, Scott MH, Fenves GL. Open system for earthquake engineering simulation (OpenSees) [Internet]. 2000 [cited 2012]. Available from: http://opensees.berkeley.edu.
22. Nikfar F, Konstantinidis D. Evaluation of vision-based measurements for shake-table testing of nonstructural components. *Journal of Computing in Civil Engineering (ASCE)*[Submitted]. 2015.
23. ASCE/SEI 7-05. *Minimum design loads for buildings and other structures*. Reston (Virginia): American Society of Civil Engineers; 2006.
24. IBC2006-05. International Building Code (IBC). Falls Church 2005.
25. ANSI/AISC 360-05. *Specifications for structural steel buildings*. Chicago: American Institute of Steel Construction; 2005.
26. Erduran E, Dao ND, Ryan KL. Comparative response assessment of minimally compliant low-rise conventional and base-isolated steel frames. *Earthquake Engineering and Structural Dynamics*. 2011;40(10):1123--1141.
27. Hsiao PC, Lehman DE, Roeder CW. Improved analytical model for special concentrically braced frames. *Journal of Constructional Steel Research*. 2012;73:80–94.

28. Uriz P, Filippou FC, Mahin SA. Model for cyclic inelastic buckling of steel braces. *Journal of Structural Engineering*. 2008;134(4):619–628.
29. Ryan K, Polanco J. Problems with Rayleigh damping in base-isolated buildings. *Journal of Structural Engineering (ASCE)*. 2008;134(11):1780-1784.
30. Yang QR, Liu WG, He WF, Feng DM. Tensile stiffness and deformation model of rubber isolators in tension and tension-shear states. *Journal of Engineering Mechanics (ASCE)*. 2010;136(4):429-437.
31. Dao ND, Ryan KL, Sato E, Sasaki T. Predicting the displacement of triple pendulum™ bearings in a full-scale shaking experiment using a three-dimensional element. *Earthquake Engineering and Structural Dynamics*. 2013;42(11):1677–1695.
32. Fenz DM, Constantinou MC. Spherical sliding isolation bearings with adaptive behavior: Theory. *Earthquake Engineering and Structural Dynamics*. 2008;37(2):163-183.
33. Morgan TA, Mahin SA. Achieving reliable seismic performance enhancement using multi-stage friction pendulum isolators. *Earthquake Engineering and Structural Dynamics*. 2010;39(13):1443-1461.
34. Becker TC, Mahin SA. Experimental and analytical study of the bi-directional behavior of the triple friction pendulum isolator. *Earthquake Engineering and Structural Dynamics*. 2012;41(3):355-373.
35. Becker TC, Mahin SA. Approximating peak responses in seismically isolated buildings using generalized modal analysis. *Earthquake Engineering and Structural Dynamics*. 2013 (early view).

Table 6-1. Steel sections used in the fixed-base (SCBF) and base-isolated (OCBF) structures

Story	Gravity Columns	Girders	SCBF		OCBF	
			Braced Columns	Braces	Braced Columns	Braces
1	W14×68	W14×68	W14×233	HSS 12×12×6/8	W14×145	HSS 10×10×5/8
2	W14×68	W14×68	W14×145	HSS 10×10×6/8	W14×145	HSS 10×10×6/8
3	W14×48	W14×68	W14×68	HSS 9×9×5/8	W14×68	HSS 9×9×5/8
4	W14×38	W14×68	W14×38	HSS 7×7×5/8	W14×38	HSS 8×8×5/8

Table 6-2. Ground motions used in this study, together with their scaling factors

ID	Scale Factor	Earthquake Name	Year	Station Name	Magnitude	V_{s30} (m/s)
LOMAP	1.34	Loma Prieta	1989	WAHO	6.93	388.33
NORTHR	1.06	Northridge-01	1994	Castaic - Old Ridge Route	6.69	450.28
MANJIL	0.91	Manjil	1990	Abbar	7.37	723.95
CHICHI	1.38	Chi-Chi Taiwan-03	1999	TCU129	6.2	511.18

Table 6-3. Peak isolation displacement (in meters)

Level	LOMAP		NORTHR		MANJIL		CHICHI	
	LRB	TFP	LRB	TFP	LRB	TFP	LRB	TFP
SLE	0.059	0.069	0.096	**0.099**	0.042	0.062	0.054	0.051
DBE	0.112	0.116	0.125	**0.175**	0.094	0.132	0.090	0.102
MCE	0.149	0.162	0.211	0.220	0.201	**0.264**	0.125	0.136

Table 6-4. Shake table test program

No.	Cases	System	Floor Level	Earthquake	Hazard Level	No.	Cases	System	Floor Level	Earthquake	Hazard Level
1	U-U, U-L , C*	FB	3	LOMAP	SLE	13	U-U, U-L , C	TFP	3	LOMAP	SLE
2	U-U, U-L , C	FB	3	LOMAP	DBE	14	U-U, U-L , C	TFP	3	LOMAP	DBE
3	U-U, U-L , C	FB	3	LOMAP	MCE	15	U-U, U-L , C	TFP	3	LOMAP	MCE
4	U-U, U-L , C	FB	3	NORTHR	SLE	16	U-U, U-L , C	TFP	3	NORTHR	SLE
5	U-U, U-L , C	FB	3	NORTHR	DBE	17	U-U, U-L , C	TFP	3	NORTHR	DBE
6	U-U, U-L , C	FB	3	NORTHR	MCE	18	U-U, U-L , C	TFP	3	NORTHR	MCE
7	U-U, U-L , C	LRB	3	LOMAP	SLE	19	U-U, U-L , C	FB	3	MANJIL	DBE
8	U-U, U-L , C	LRB	3	LOMAP	DBE	20	U-U, U-L , C	LRB	3	MANJIL	DBE
9	U-U, U-L , C	LRB	3	LOMAP	MCE	21	U-U, U-L , C	TFP	3	MANJIL	DBE
10	U-U, U-L , C	LRB	3	NORTHR	SLE	22	U-U, U-L , C	FB	3	CHICHI	DBE
11	U-U, U-L , C	LRB	3	NORTHR	DBE	23	U-U, U-L , C	LRB	3	CHICHI	DBE
12	U-U, U-L , C	LRB	3	NORTHR	MCE	24	U-U, U-L , C	TFP	3	CHICHI	DBE

**U-U: Ultrasound-unlocked, U-L: Ultrasound-Locked, C: Hospital Cart*

Figure 6-1. Medical equipment used in this study. Left: An ultrasound machine supported on wheels (rear) and casters (front). Right: A light hospital cart carrying a pulse oximeter on the top tray and defibrillator on the middle tray.

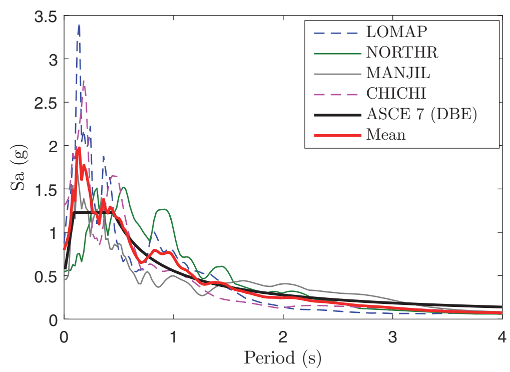

Figure 6-2. Design spectrum and 5% damped acceleration spectra for scaled ground motions.

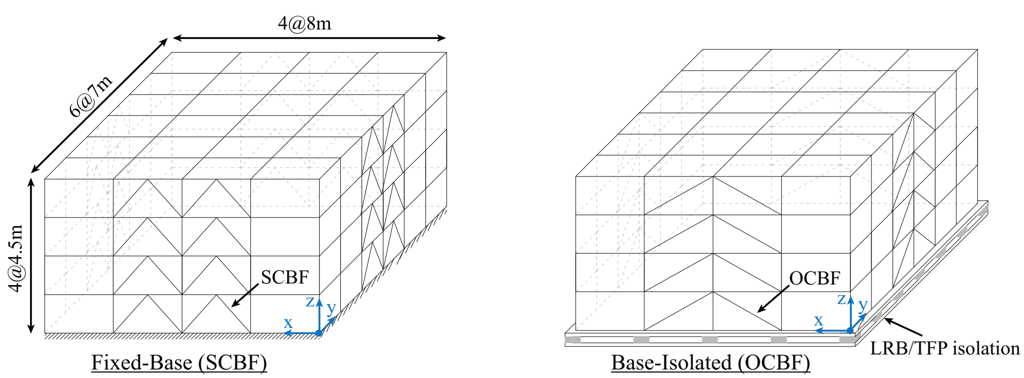

Figure 6-3. Schematics of the fixed-base and base-isolated buildings.

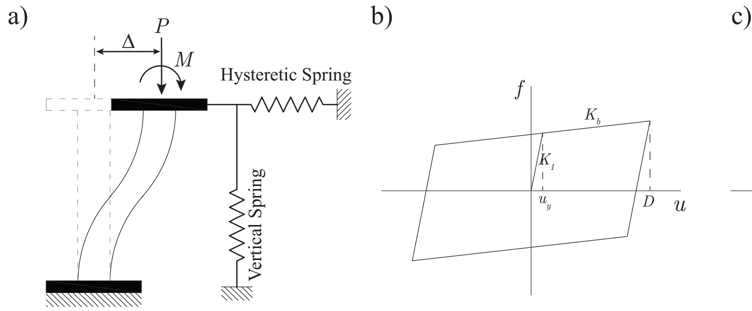

Figure 6-4. a) LRB hysteretic model consisting of an elastic column element in parallel with a lateral hysteretic and vertical elastic nonlinear spring. b) Resultant lateral force-displacement hysteresis of the model. c) Resultant vertical force-displacement of the isolator.

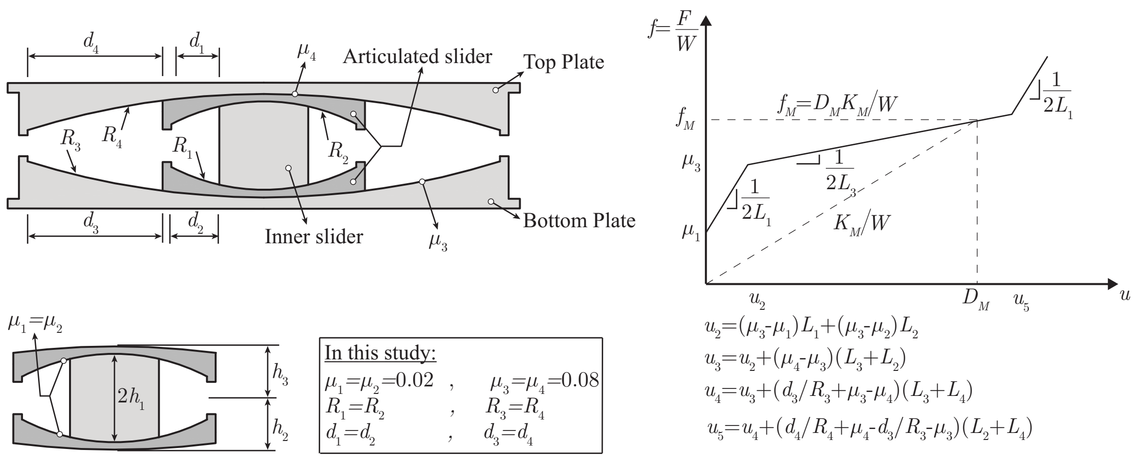

Figure 6-5. TFP system considered in this study.

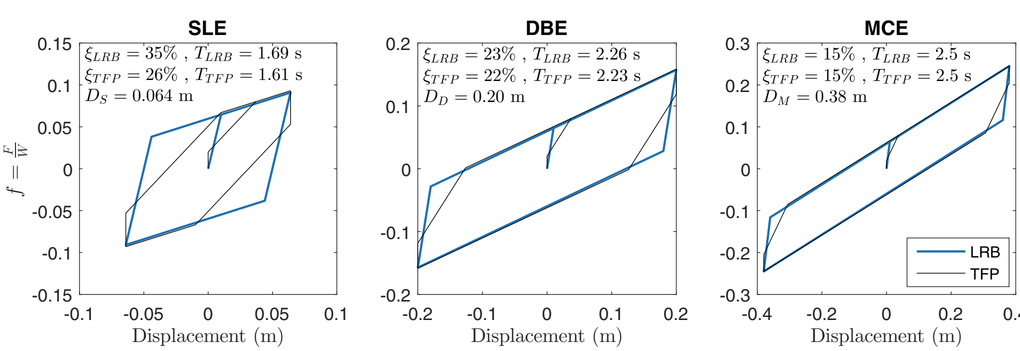

Figure 6-6. Normalized hysteresis loops of equivalent LRB and TFP systems.

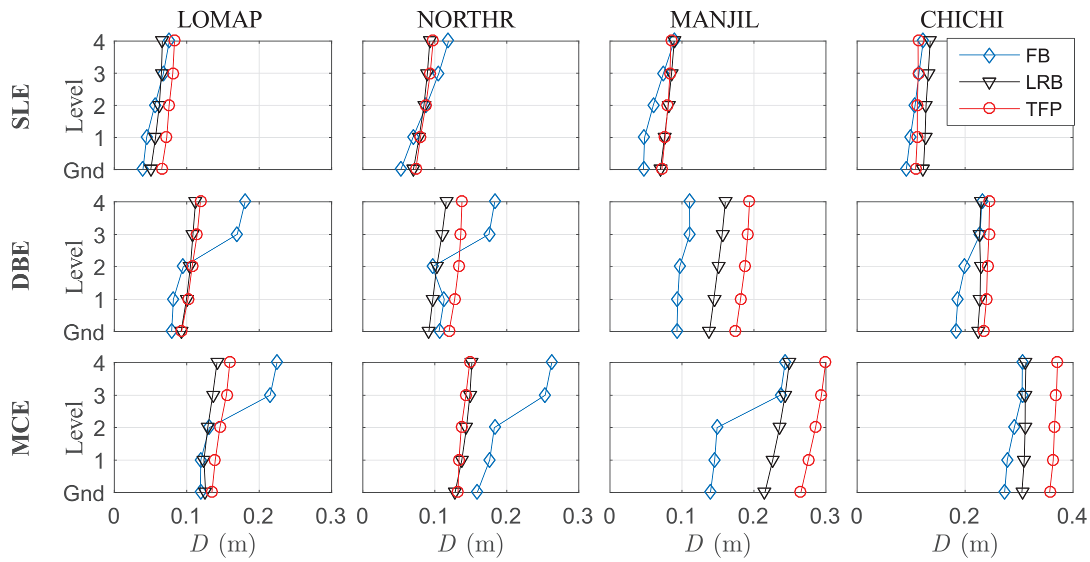

Figure 6-7. Peak absolute floor displacement.

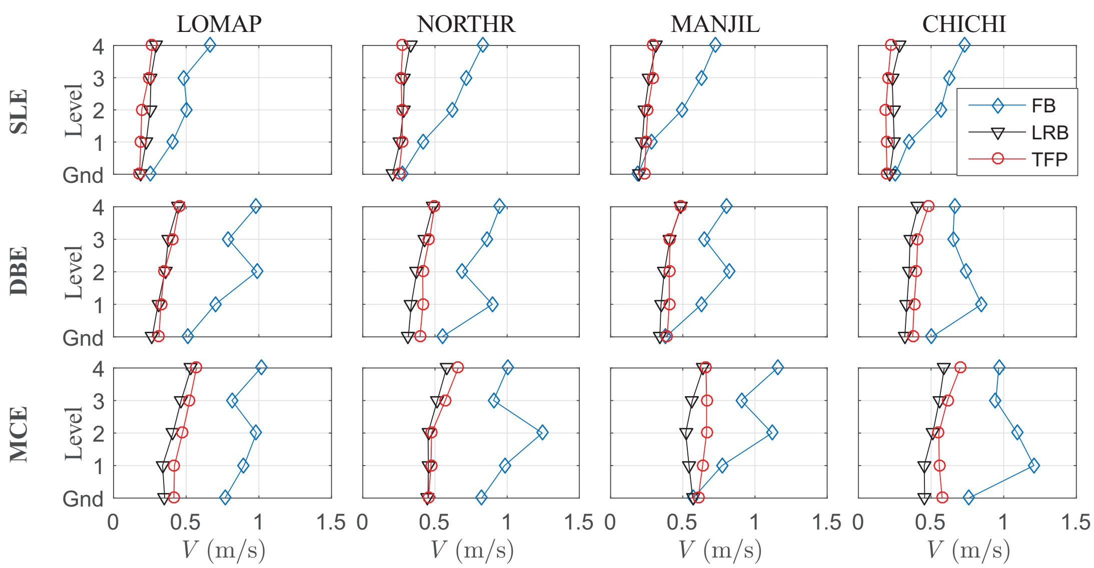

Figure 6-8. Peak absolute floor velocity.

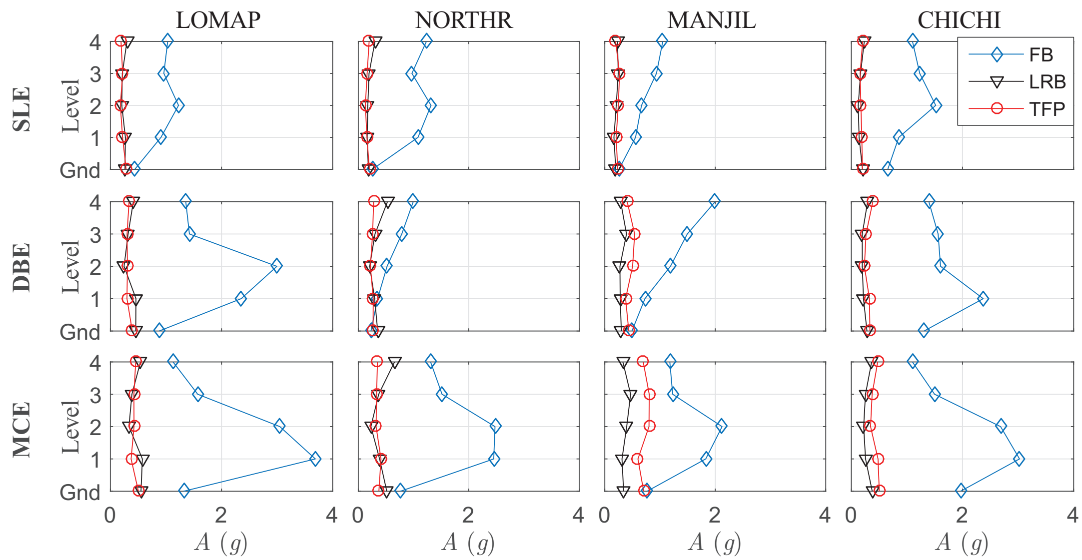

Figure 6-9. Peak absolute floor acceleration.

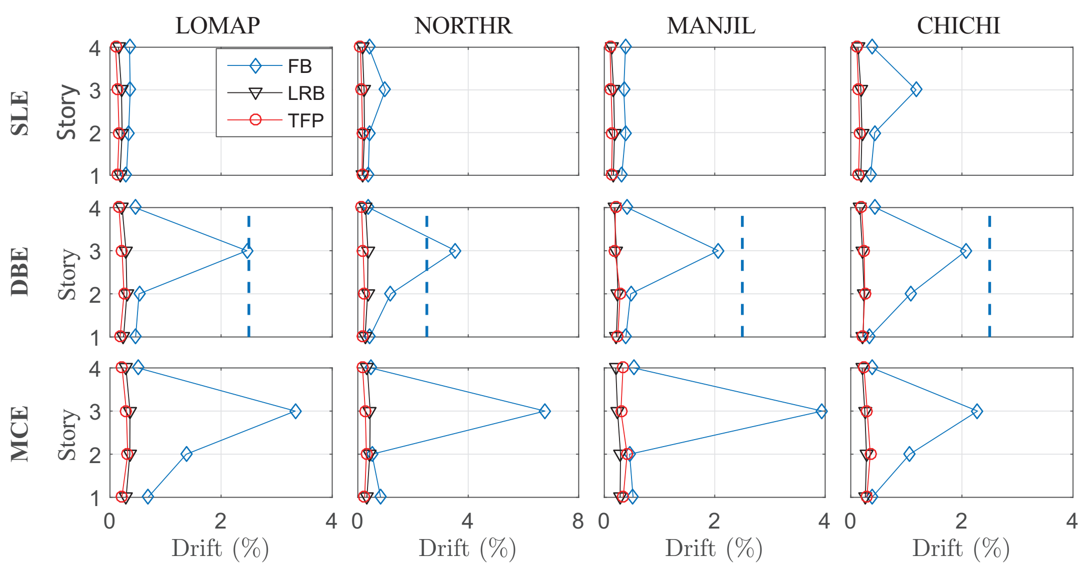

Figure 6-10. Interstory drift ratio.

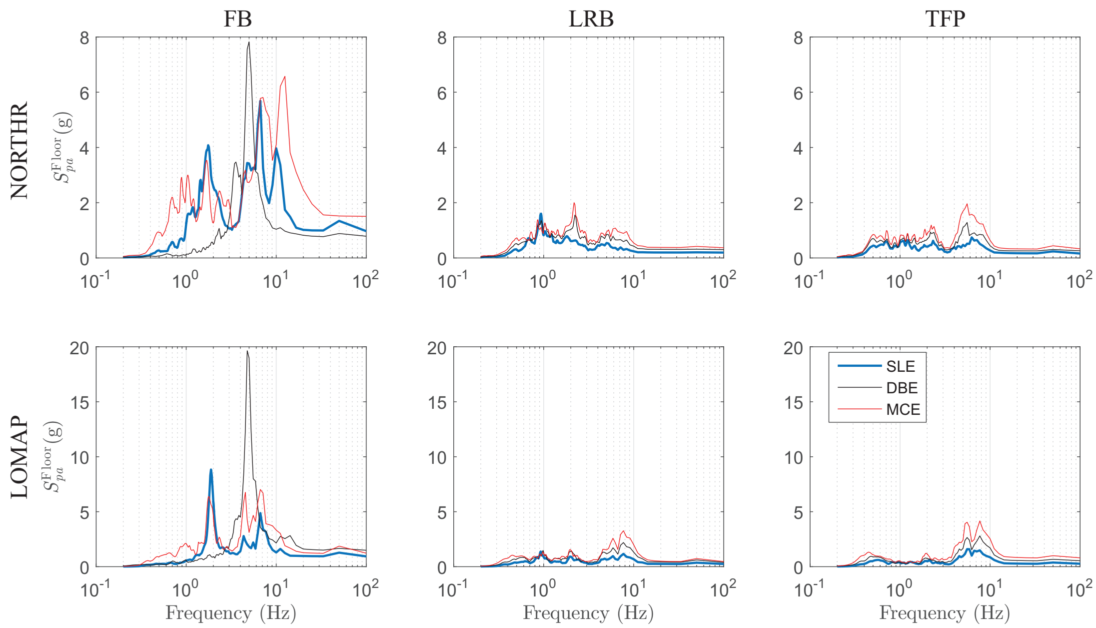

Figure 6-11. 2% damped 3rd floor acceleration spectra.

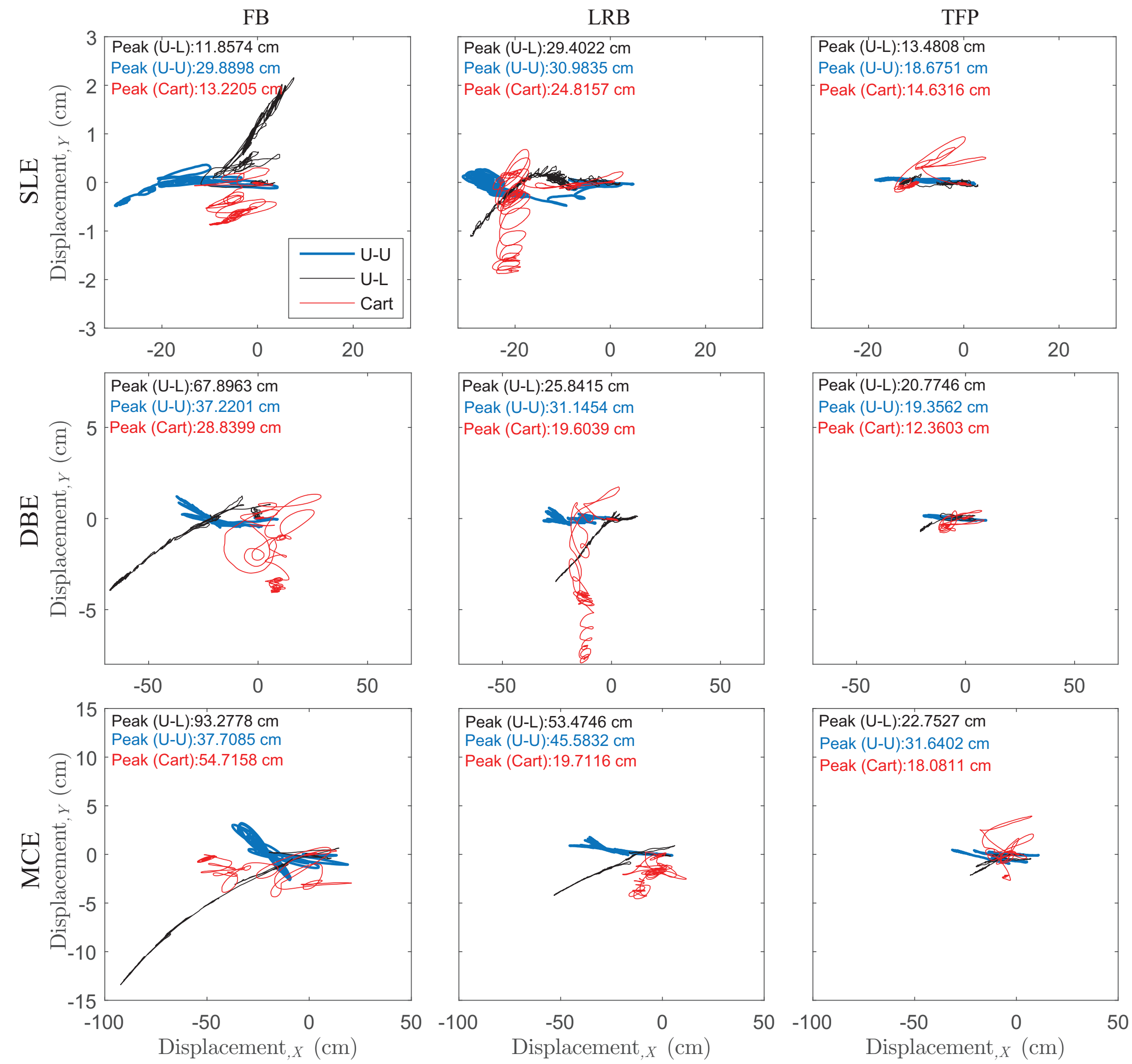

Figure 6-12. Relative displacement orbits of the hospital cart, ultrasound-locked (U-L), and ultrasound-unlocked (U-U) under the 3rd floor NORTHR-DBE excitation.

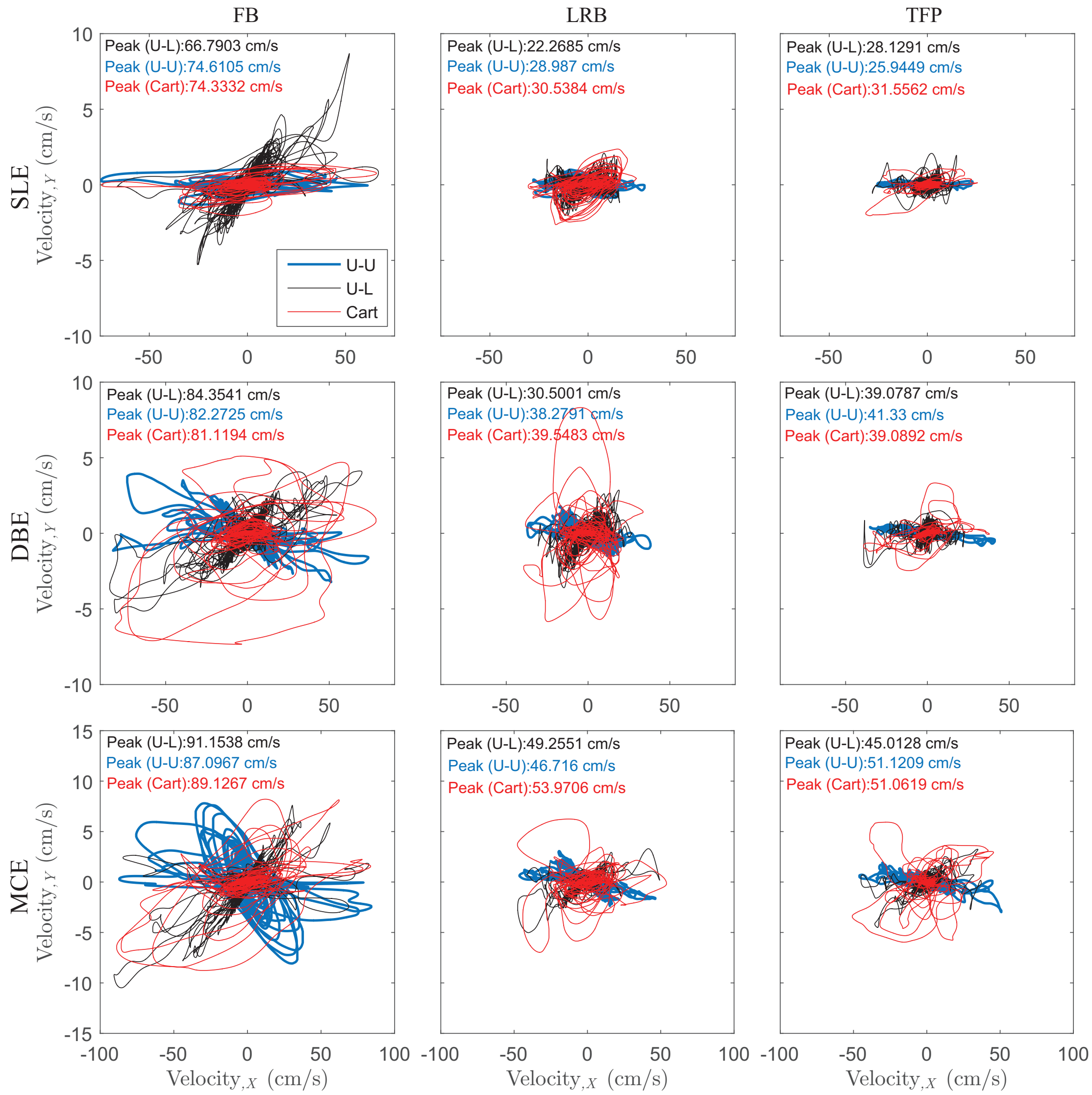

Figure 6-13. Relative velocity orbits of the hospital cart, ultrasound-locked (U-L), and ultrasound-unlocked (U-U) under the 3rd floor NORTHR-DBE excitation.

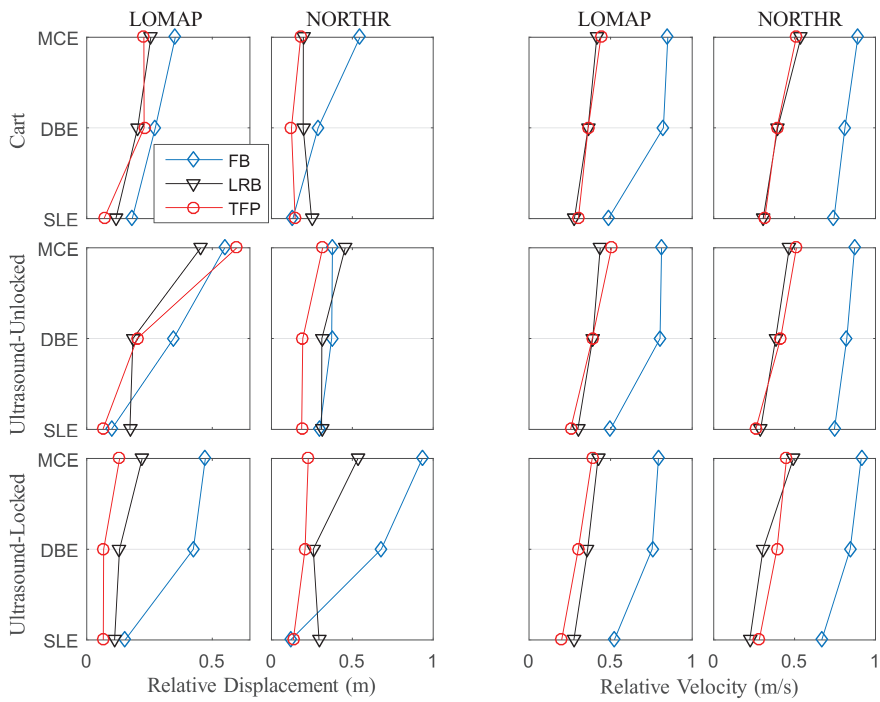

Figure 6-14. Comparison of peak displacement and velocity responses for Cart, Ultrasound-Unlocked, and Ultrasound-Locked placed on the 3rd floor.

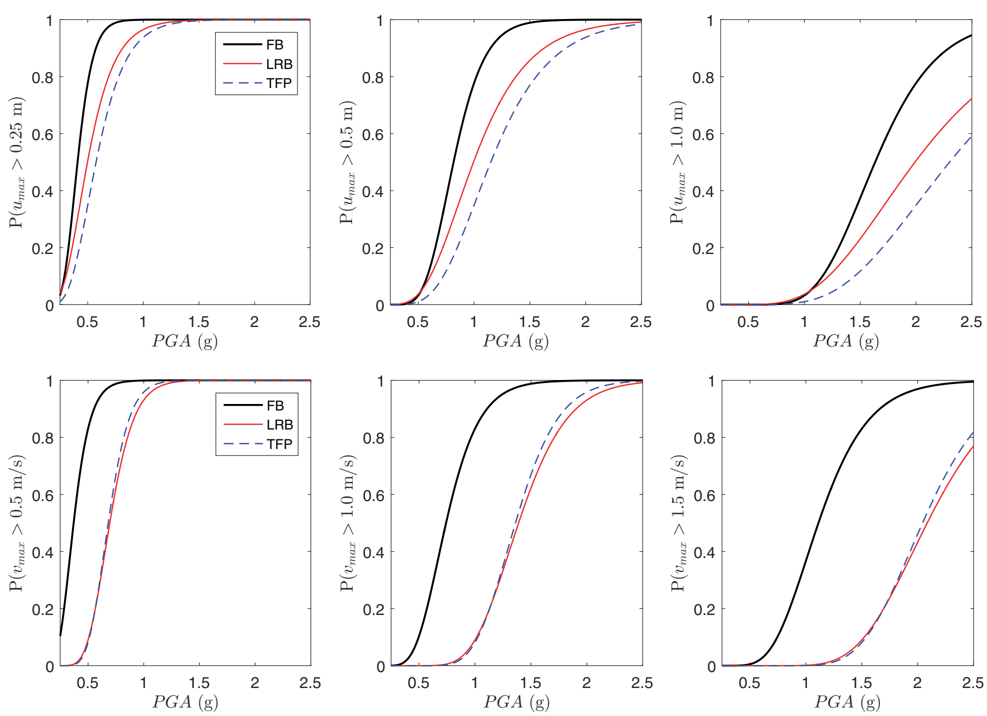

Figure 6-15. Fragility curves comparing the different systems.

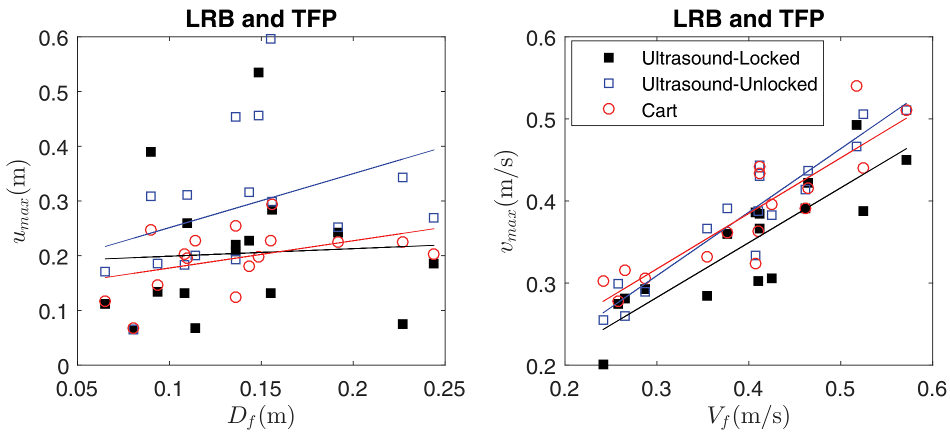

Figure 6-16. Demand parameter vs intensity measure for equipment in base isolated hospitals (LRB and TFP data).

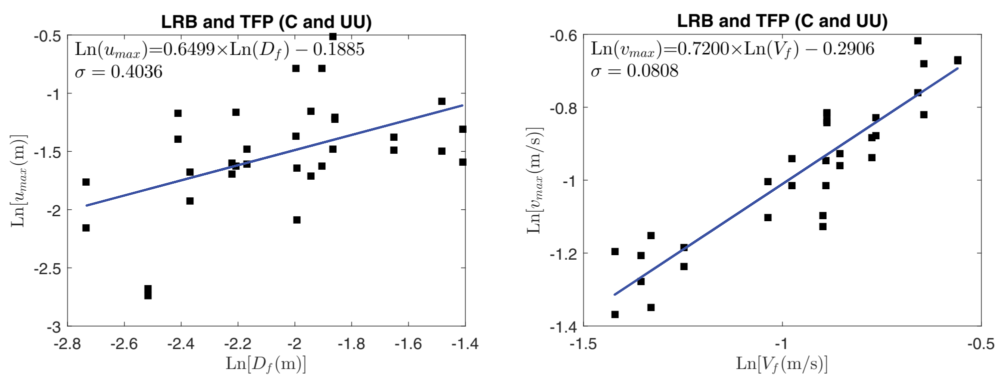

Figure 6-17. Regression analysis of the displacement and velocity demand data of equipment with unlocked wheels/casters (C and UU) in base-isolated building for LRB and TFP systems.

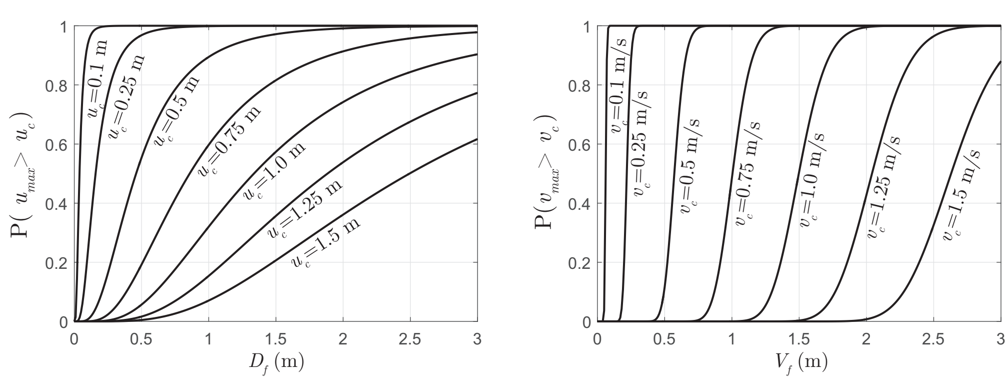

Figure 6-18. Conditional probability curves. Left: Peak relative displacement (unlocked wheels/casters). Right: Peak relative velocity (unlocked wheels/casters).

Chapter 7: Evaluation of Vision-Based Measurements for Shake Table Testing of Nonstructural Components

Nikfar F., Konstantinidis D., 2016, Evaluation of Vision-Based Measurements for Shake Table Testing of Nonstructural Components, submitted to the *Journal of Computing in Civil Engineering (ASCE)*.

Abstract

Freestanding building equipment and contents may experience large displacements during earthquake shaking. A non-uniform mass distribution and a complicated supporting system mechanism (e.g., equipment on wheels and casters) may cause freestanding contents to exhibit complex motions, such as twisting, when subjected to base excitation. Measuring such motion by traditional, contact-type displacement sensors is challenging. Owing to recent advances in video capture sensors and image processing techniques, vision-based motion tracking and measurement have been introduced as a practical, economical, and fairly accurate measuring method. This paper presents a procedure utilized to evaluate the accuracy of a consumer-grade camera for the purpose of measuring the displacement of a piece of medical equipment during shake table testing. The camera considered in this study has fixed focal length, and it can capture video recordings with different resolution and frame rates. The camera was positioned at a distance from the target, as it would be in a real application, during the test to track the motion of four LED lights attached to the shake table. The capabilities of the camera were evaluated using as input a signal with varying frequency and amplitude. A wavelet approach was proposed and utilized in order to synchronize the vision-based displacement measurement with the output of the displacement transducer installed on the shake table to be used later in accuracy assessments. Absolute and relative error curves

are presented to demonstrate the errors in the frequency range of interest of the actual experiment. Finally, contour plots specifying the displacement, velocity, and acceleration accuracy of vision-based measurements that can be used in future applications are proposed.

7.1 Introduction

In the last two decades, the application of vision-based motion tracking and measurement has become widespread in various engineering fields, including biomechanics, mechanics, robotics, and aerospace. This emerging technology is also increasingly becoming of interest for structural and earthquake engineering applications. Although conventional measuring devices are accurate, they have a number of limitations. Displacement, velocity, and acceleration measurements require sensors (e.g., DCDTs, LVDTs, string potentiometers, velocity sensors, accelerometers, etc.) that are usually costly, time-consuming to calibrate and install, limited in number in any laboratory, prone to damage in the case when their capacity is exceeded, and limited to single-point measurement. In some cases (e.g. measuring the response of lightweight nonstructural components), the added mass and stiffness of contact sensors may influence the response they are trying to measure (Hutchinson et al. 2005). In applications that involve quantification of the complex 3D motion of unanchored nonstructural equipment and contents, which may include large sliding, uplift rotations and twisting (Konstantinidis and Makris 2005, 2007, 2009; Chatzis and Smyth 2012; Di Egidio et al. 2014) under seismic excitation, the use of contact sensors is often impractical, if not impossible. In addition, conventional sensors require a data acquisition system, which, in the case of dynamic testing applications, can be very costly. In contrast, vision-based tracking methods do not have the aforementioned limitations. Vision-based measurement has the potential of tracking the motion of multiple points captured within a scene. Cameras are easy to install and motion tracking usually does not require direct links eliminating the interaction concerns. Moreover, unanticipated demands such as excessive displacements will not damage the device. Of course, depending on the measurement resolution requirements of a given experiment, sometimes an acceptable accuracy is achievable only when very expensive high-resolution and -speed cameras are utilized.

Kanda et al. (2005) evaluated the performance of a vision-based motion capture method for estimating the earthquake induced displacement, acceleration, and damage to building structures. Fukuda et al. (2010) suggested the use of vision-based displacement measurement for real-time monitoring of dynamic responses of large civil engineering structures such as bridges and buildings. This technique was utilized for measuring the frictional characteristics and 3D motion capturing of unattached building equipment and contents under seismic excitations (Hutchinson et al. 2005; Chaudhuri & Hutchinson 2005; Nastase et al. 2008; Doerr et al. 2008). CCD (Charge Coupled Device) cameras were used to capture the motion of some of the hospital equipment items in an experimental program performed at the E-Defense shake table facility (Sato et al. 2011; Shi et al. 2014). Shi et al. (2014) evaluated the accuracy of a motion capture system used for measuring the displacement and velocity responses of medical appliances in a full-scale shake table study. A 30 fps camera with 1920×1080 pixel resolution aiming at an approximate angle of 45^{o} with respect to the horizontal plane was used. Since the camera's axis was not perpendicular to horizontal plane, the image scale ratio (i.e., the ratio representing the physical distance corresponding to one pixel of image) was not constant, but it ranged from 3 to 4 mm. It was shown that the motion capture system used had a maximum absolute error of 10 mm and 0.09 m/s for peak displacement and peak velocity of 3150 mm and 2.2 m/s, respectively. Note that the accuracy evaluations were performed for input motion frequencies as low as 0.6 Hz for displacement and 1 Hz for velocity measurements. The behavior of rolling isolation systems was evaluated in a shake table study using video recordings (Harvey et al. 2014; Harvey & Gavin 2014). A combination of conventional sensors (including accelerometers and string potentiometers) and video cameras was utilized to measure the 3D motion of freestanding stiff asymmetric structures (Wittich & Hutchinson 2015). Yokota et al. (2012) investigated how surveillance cameras could be used to estimate the earthquake motions from image analysis of sliding objects in different floors of a building. Recently, a monocular computer vision method is proposed for measuring three-dimensional rocking motion of objects (Greenbaum et al. 2015). Feng and Feng (2015) investigated the performance of two template-matching techniques for tracking the displacement of multiple points.

The application of vision-based measurement is not limited to measuring displacement. It can be also utilized to obtain acceleration of moving objects. Even though inexpensive accelerometers are available in the market, still vision-based acceleration measurement has some advantages over some conventional accelerometers, as discussed in (Leifer et al. 2011), including superior ability to measure accelerations due to low-frequency or rigid-body motions of objects, as it would be inapplicable for most lightweight accelerometers due to their poor response at low frequencies (Leifer et al. 2011). Leifer et al. (2011) assessed the accuracy of vision-based acceleration measurements using twice-differentiated video tracking data. They demonstrated how applying a smoothing filter such as Savitzky-Golay (Savitzky & Golay 1964) to the video data can remove the noise, while still preserving features of the signal, and improve the acceleration measurements. Previous research to evaluate the accuracy of vision-based measurements was performed only for distinct frequencies and fixed amplitudes (Chang & Ji 2007; Fukuda et al. 2010). Harvey and Gavin (2014) explored the frequency-dependent degradation of vision-based acceleration measurements using a tracking signal with time-dependent frequency and amplitude. They presented the results of their accuracy evaluations as contour plots correlating the error to the frequency and amplitude of the tracking signal. However, the application of the presented contour plots is limited to that specific experimental program with a specific frame rate and pixel-to-physical coordinate scale ratio.

Nikfar and Konstantinidis (2015) carried out a shake table investigation on the seismic performance of medical equipment supported on wheels and casters. The shake table at the Applied Dynamics Laboratory, McMaster University, was used to simulate the floor response of fixed-base and base-isolated hospital buildings. The schematic of the experimental setup used in that study is depicted in Fig. 7-1(a). A displacement transducer and an accelerometer were used to track the motion of the shake table. On the other hand, the complexity and magnitude of the motion of the hospital equipment made the use of contact position sensors for tracking the motion of the equipment very challenging and time-consuming. Instead, a cost-effective vision-based measurement approach was explored. As shown in Fig. 7-1, LED lights were attached to the body and monitor of the specimen (an ultrasound machine). The position of the LED lights were detected in each frame and tracked from one frame to the next. Fig. 7-1(b) shows one frame of a video recording. As can be seen, two LED lights were attached on the body and two on the monitor component. In each set, the LEDs were attached at a *physical distance* of 24 cm.

The present paper discusses a separate experimental program designed and conducted to evaluate the accuracy of a low-cost vision-based system for measuring displacement, velocity, and acceleration. The experimental program contains a series of controlled shake table experiments performed to evaluate the accuracy of the low-cost vision-based system. This study preceded the one presented in Nikfar and Konstantinidis (2015). The confidence gained upon completion of this study on the accuracy of the vision-based measurement system facilitated the use of this approach in the experimental study by Nikfar and Konstantinidis (2015).

The vision-based measurement system utilized a consumer-grade camera (*GoPro® Hero4 Black action camera*) that featured a fixed focal length, while allowing considerable flexibility in terms of resolution, frame rate, and angle-of-view (AOV). The combination of frame-rate and resolution options of the camera are such that the video is stored in the camera's internal memory and does not require costly equipment (e.g., digital video recorders or frame grabbers and solid-state storage modules) that are usually integral components of vision-based measurement systems. The processing of video streams recorded by the camera to extract measurements is conducted using tools that are readily available to researchers (such as MATLAB), eliminating the cost of commercial digital image correlation packages.

The contribution of this study is threefold: (1) proposing a wavelet-based approach for synchronization of video and conventional sensor recordings that makes the accuracy evaluation as well as measurements with a combination of video and conventional sensors possible; (2) evaluation of the accuracy of displacement, velocity, and acceleration measurements of a low-cost vision-based system; and (3) proposing easy-to-use contour plots that can be utilized to determine accuracy of vision-based systems, based on camera frame-rate and resolution (image scale ratio).

7.2 Experimental program

7.2.1 Test setup for accuracy measurement

The experimental test setup for evaluating the accuracy of the vision-based measurements is illustrated in Fig. 7-2. The camera was placed 160 cm above four LED lights that were attached to surface of a simulated hospital floor built on the shake table. Note that this distance was the same as the distance between the camera and the LEDs attached on the body of equipment in the shake table program that followed the accuracy evaluation. A round bubble level was used to make sure that the camera's axis is perpendicular to the plane of motion. The camera recordings were used to track the four LED lights attached on the shake table. Fig. 7-4(a) shows one frame of a video recording. The shake table's displacement and acceleration responses were recorded using a displacement sensor (Temposonics® LPRCCU04901) and an accelerometer (MEAS 4002-005). The sensor data was acquired at 2000 samples per second rate using a NI cDAQ-9174.

7.2.2 Sine sweep signal for shake-table tests

Motivated by the procedure used by Harvey and Gavin (Harvey & Gavin 2014), a geometric up-chirp signal with decaying amplitude was used as the shake-table displacement input, defined by

$$D(t) = \bar{D}_0 \exp\left[-\alpha (t - t_0)^q\right] \sin\phi(t), \; t_0 \le t \le t_f \tag{7.1}$$

where $\bar{D}_0 = \bar{D}(t_0)$ [with $\bar{D}(t)$ being a function that modulates the amplitude of $D(t)$], q controls the shape of $D(t)$, and α is defined such that $\bar{D}_f = \bar{D}(t_f)$:

$$\alpha = \ln\left(\frac{\bar{D}_0}{\bar{D}_f}\right) t_f^{-q} \tag{7.2}$$

In Eq. (7.1), $\phi(t)$ is phase of the signal, described by

$$\phi(t) = 2\pi \frac{f_0 t + \left(f_f - f_0\right) t^{p+1}}{\left(p+1\right) t_f^p} \tag{7.3}$$

in which $f_0 = f(t_0) = \left.\frac{d\phi}{dt}\right|_{t=t_0}$ and $f_f = f(t_f) = \left.\frac{d\phi}{dt}\right|_{t=t_f}$ are the instantaneous signal frequencies at t_0 and t_f, respectively. In this study, a 40-s signal, i.e., $t_0 = 0$ s and $t_f = 40$ s, with $p = 3$, $q = 2$, $\bar{D}_0 = 15$ cm, $\bar{D}_f = 0.375$ cm, $f_0 = 0.05$ Hz, and $f_f = 10$ Hz is considered. The displacement, velocity, and acceleration time histories of the input signal are presented in Fig. 7-3. The red dashed line in Fig. 7-3(left) plots the variation in signal frequency. Table 7-1 tabulates time corresponded frequencies of the driving input excitation. Such a signal provides a continuous spectrum of frequencies for experimental testing, thereby reducing the number of experiments required for evaluating the frequency capability of the vision-based measurement system. Moreover, the decaying amplitude of the signal allows testing under high frequency excitations, while keeping the acceleration demands on the shake table below the rated capacity.

7.3 Vision-based measurement procedure

The vision-based measurement procedure is done in five steps: (a) camera calibration, (b) feature detection, (c) tracking, (d) transformation, and (e) computation of velocity and acceleration.

7.3.1 Camera calibration (image correction)

Due to the perspective characteristics of the camera lens, the captured images usually exhibit distortion. The calibration process involves finding a transformation matrix to correct this distortion. In this study, the camera calibration was performed using the calibration software (GoPro Studio 2.5.6) provided with the camera. Details on calibration procedure employed for GoPro action cameras can be found in (Balletti et al.

2014). Fig. 7-4 shows a frame from a video recording before and after calibration, illustrating the transformation of curvy edges into straight lines.

7.3.2 Feature detection

Feature detection is the process of recognizing the object in the frames (i.e., images) of a video recording. It is common to subtract the background image (i.e., the portion of the image containing the non-moving objects) from all the frames of a video recording in order to obtain images containing only the moving objects with high luminosity. However, utilization of LED lights in the experiments eliminates the necessity of this step since pixels corresponding to the LED lights area exhibit very high luminosity compared to the other pixels of the image. In this study, first, a Blob filter was applied to the images for smoothing the image, then, the background was eliminated directly through the application of a threshold (not subtracting the background image), and in the last phase, the pixel coordinates of the centers of the LEDs, i.e., pixels with the highest luminosity, were detected by finding extrema in the image.

7.3.3 Tracking

Tracking involves finding the correlation between the detections from one frame to the next. A linear Kalman filter was implemented using MATLAB (MathWorks 2002) to track the position of LEDs in all the frames of the video recording. The filter's algorithm consists of two steps: (1) prediction of the future location of the moving object based on previous detections. Note that a constant acceleration scheme is assumed herein; and (2) correction (refinement) of the estimated location using the actual detections in the next frame. This procedure assists the estimation of the target object's expected position in some of the frames where feature detection is unsuccessful due to lighting problems or when the target object is obscured by other objects. Moreover, it helps tracking multiple point detections. Note that in the shake-table experiments, there were instances where LED lights were instantaneously obscured by safety ropes or sensor wires for few frames. The Kalman filter helped in estimating the position of the LEDs in those frames. Since safety restrictions in the laboratory prevented testing in dark environment, there were situations where unwanted reflections from overhead light sources resulted in additional high-luminosity points detected in the image. Implementation of the Kalman filter facilitated the tracking of multiple points and eliminating the unwanted detections. However, depending on the choice of parameters, the Kalman filter can result in very smooth estimates of the actual detections, suppressing some of the frequencies in the results. In order to avoid such frequency filtering, a secondary routine was developed in this study. This simple routine gets the Kalman filter estimates and finds the corresponding actual detections in all the frames. For a given frame, the routine searches for the closest detection within a small radius from the position estimated by the Kalman filter. Therefore, the motion tracking used in this study is the result of the actual detections without filtering.

7.3.4 Transformation

Each pixel in the image represents a distance in physical domain. As mentioned earlier, LED lights were attached at a distance of 24 cm from each other. Determining the number of pixels between two LED lights, the transformation scale from pixel to physical coordinate can be obtained:

$$S = \frac{\text{physical distance between LEDs}}{\text{number of pixels between LEDs on image}} \tag{7.4}$$

Multiplying the pixel coordinates (x, y) of an LED point on the image by S gives the physical position coordinates (X, Y) of the LED.

7.3.5 Computation of velocity and acceleration

Camera sensors, similar to other sensors, exhibit noise. The noise in measurement is associated with the discretization uncertainty (Robbe et al. 2014). Fig. 7-5 illustrates how discretization can introduce noise in vision-based measurements. As shown in the figure, in the case where the center of the LED is located at mid-distance between two pixels, small changes in environmental conditions such as LED brightness fluctuations, scene illumination, and small vibration of the camera or specimen can affect the position in pixel domain. Therefore, such noise can be present even when the LED is in still conditions. In general, any change in position of the LED from one pixel to another occurs within a duration of $1/FR$ s, where FR is the frame rate (or sampling frequency).

Thus, the magnitude of the noise in physical domain will be equal to the scale ratio, *S*, and can occur within 1/*FR* s.

Since differentiation is a noisy process, noise embedded in the displacement signal produces larger noise in the computed velocity and acceleration signals. The maximum velocity noise resulting from point-by-point differentiation will be equal to $S \times FR$; while the maximum acceleration noise will be $2S \times FR^2$. The factor 2 refers to the possibility of the change in velocity from $-S \times FR$ to $+S \times FR$ within 1/*FR* s. For instance, for an experiment with $S = 0.001\ \mathrm{m}$ and $FR = 60\ \mathrm{Hz}$, the maximum displacement, velocity and acceleration noise values will be 0.001 m, 0.06 m/s, and $7.2\ \mathrm{m/s^2}$, respectively. Even though the displacement noise appears to be small, the consequent maximum velocity and acceleration noises can be considerably large. A number of smoothing/filtering methods were suggested in previous works (Kienle et al. 2008; Leifer et al. 2011; Harvey & Gavin 2014) to suppress noise. However, special attention should be paid in selecting the method of filtering so that the coherent displacement path captured by the camera is not attenuated by the filtering. For seismic applications, where motions usually contain a broad range of frequency content, it has been suggested that low-pass filters are not suitable (Leifer et al. 2011). In contrast, windowing methods that preserve the fundamental path of the high-frequency components of the motion, while reducing the noise, are considered to be more appropriate (Leifer et al. 2011). Still, filters applying simple moving-average methods are not deemed appropriate in seismic applications with non-zero accelerations because they result in reduction in acceleration peaks (Leifer et al. 2011). Since this study focuses on seismic applications of camera measurements with non-zero acceleration, the Savitzky-Golay filter (Savitzky & Golay 1964) is utilized for pre-filtering the displacement data. The Savitzky-Golay filter is based on the least square approach that can effectively suppress the noise while preserving the features of the data. In order to choose a Savitzky-Golay filter that preserves frequencies up to a certain value, the effective window length must correspond to the length of the shortest feature that should be preserved (Leifer et al. 2011). Thus, an appropriate filter for this study to preserve frequencies up to 10 Hz will have a length equal to the length of the corresponding half-cycle harmonic, i.e., $0.5 \times (1/10\ \text{Hz}) = 0.05\ \text{s}$. The effect of filter-window length on velocity and acceleration results will be discussed later.

7.4 Video signal synchronization using wavelet transform

The data acquisition system, collecting data from conventional sensors, and the low-cost camera used in the experimental program did not feature trigger synchronization. As video recording was started manually, synchronization between the camera video stream and the signal from the displacement sensor attached to the shake table was necessary for evaluating the accuracy of the vision-based measurements. In this study, a wavelet transform procedure is proposed and utilized for this purpose.

For a given signal $f(t)$ and a given wavelet $\psi(s,\delta)$, the wavelet transform is described by

$$C(s,\delta) = \frac{1}{\sqrt{s}} \int_{-\infty}^{\infty} f(t)\psi\left(\frac{t-\delta}{s}\right) dt \tag{7.5}$$

where $C(s,\delta)$ is the value of the wavelet transform for scale s and translation δ. Scale is responsible for dilation or contraction of the wavelet, and δ translates (moves) the wavelet in time. The combination of s and δ that maximizes *C*, i.e., $s \to S$ and $\delta \to \Delta$, corresponds to the wavelet, $\psi_{S,\Delta}(t)$, that is the best match for the given signal.

Assuming $f(t)$ to be the signal from a displacement transducer tracking the position of the shake table and $\psi(s,\delta)$ to be the position computed from camera video, the translation, Δ, that can produce the maximum value of *C* can be obtained from Eq. (7.5). Note that $s = 1$ is used in the process of wavelet transform since the camera recording used is already transformed from pixel domain to physical domain using the transformation scale from Eq. (7.4). It is worth mentioning that if the camera recording in pixel domain was used as the wavelet ψ, the scale corresponding to the maximum wavelet transform coefficient, i.e., s=S ,would be in fact identical to the transformation scale from pixel coordinate to physical coordinate as described by Eq. (7.4). This method can also be used to determine scales of multiple points at different depths. In this case, the signal associated with each point can be matched to the shake table reference signal (in physical domain) to find the scale corresponding to the maximum wavelet transform coefficient, *S*.

To facilitate the synchronization during the accuracy evaluation portion of the study, a cosine signal with period of 20 s and amplitude of 10 cm (i.e., very low-amplitude acceleration signal) was introduced to the shake table command signal before the simulated ground motion. Synchronization was performed based on this cosine signal. Note that the choice of signal period and amplitude depends on the test application at hand. These quantities should be chosen so that they do not excite the test specimen to a level that results in any damage. Furthermore, if the specimen is at all excited dynamically by the one-cosine cycle, sufficient time should be allotted between the expiration of the one-cosine cycle and the onset of the actual earthquake excitation to allow the specimen to come to a rest. In addition, the amplitude and period of this one-cycle cosine signal should be sufficiently large to reduce the contribution of pixel discretization and frame rate related errors as much as possible. Thus, larger amplitude and period would result in more accurate synchronization. Note that the amplitude is limited to the shake-table's displacement capacity and camera AOV. The same procedure was performed on the video recordings and shake-table sensor data collected during the shake table test of the medical equipment to obtain the relative displacement of the equipment with respect to the shake table. The relative displacement was computed by subtracting the position of the shake table from the position of the equipment. If the position of both the equipment and the shake table were obtained from the camera video, the resultant relative displacement would exhibit a noise level twice as large as the camera measurement noise. Use of the shake-table transducer readings, instead of the camera, would help avoid the doubled error. However, this requires synchronized shake-table- and camera measurements. To achieve this, the aforementioned wavelet approach was used. It should be noted that the long-period, low-amplitude acceleration cycle appended before the actual signal was so weak in acceleration amplitude that it could not result in any relative displacement of the equipment with respect to the shake table. Therefore, during this cycle, the shake table and equipment moved in unison. Fig. 7-6 shows an example of synchronized shake table and camera recording signals. The black line shows the absolute position of the ultrasound equipment as measured using the camera, while the red line shows the absolute position of the shake table as measured using the displacement transducer attached on the shake table. It can be seen that both signals are synced according to the initial one-cycle cosine wave.

7.5 Characteristics of camera recordings

A *GoPro®* *Hero4 Black* action camera was used for the experiments. The camera offers a number of combinations for resolution, frame rate (*FR*), and angle of view (AOV). However, due to the camera limitations, the resolution has to be reduced when higher *FR* videos are to be captured. Table 7-2 summarizes the camera sensor modes and transformation scale values used in the experimental program. The *FR* value in these tests ranged from 30 fps to 240 fps.

7.6 Accuracy assessment

A series of thirteen shake-table experiments, summarized in Table 7-2, were performed using as input the waveform shown in Fig. 7-3. The displacement measured using the displacement sensor (Temposonics® LPRCCU04901), $d(t)$, and the acceleration measured using the accelerometer (MEAS 4002-005), $a(t)$, are assumed as 'true' displacement and acceleration responses. The velocity resulting from numerical integration of $a(t)$ is considered to be the 'true' velocity.

The accuracy assessment presented in this section follows the procedure proposed by Harvey and Gavin (Harvey & Gavin, 2014). The absolute errors are described by

$$\begin{aligned} &E_d(t) = C_d(t) - d(t), && \text{Displacement Absolute Error} \\ &E_v(t) = \dot{C}_d(t) - \int a(t)dt, && \text{Velocity Absolute Error} \\ &E_a(t) = \ddot{C}_d(t) - a(t), && \text{Acceleration Absolute Error} \end{aligned} \tag{7.6}$$

where $C_d(t)$ is the *unfiltered* camera displacement measurement, and $\dot{C}_d(t)$ and $\ddot{C}_d(t)$ are first and second derivatives of the *filtered* camera displacement measurement. One may wonder whether filtering the displacement would result in a more accurate displacement measurement. A case study performed by the authors showed that filtering the displacement signal using a Savitzky-Golay filter, which is used to obtain velocity and acceleration, would underestimate the displacement peaks at high frequencies. Thus, the unfiltered data was used for displacement measurements in this study.

7.6.1 Displacement measurement

To compute the absolute displacement error, first the local peaks of the shake-table displacement were obtained. These are the moduli of the Hilbert transform of the shake-table displacement time history (performed in MATLAB). Then, the local peaks of the true shake-table displacement were compared to the corresponding local peaks of the displacement from camera measurements. A similar procedure was performed to compute the velocity and acceleration errors, discussed in the subsequent sections. Fig. 7-7 shows the comparison between the true and camera-measured displacement peaks for Test 3. Fig. 7-8 presents the absolute displacement error $E_d(t)$ for four experiments with relatively similar *S* but different *FR* values. The displacement noise level, $E_d = \pm S$, is shown with dashed lines. The error greater than the displacement noise is attributed to insufficient camera *FR,* demonstrating the frequency capability of the camera. As can be seen, in Test 3 with $FR = 30$ fps, the error exceeds the noise level at $t = 24.1$ s, which corresponds to the driving frequency of 2.2 Hz. Increasing the *FR* to 60 fps in Test 4, there is only a small error at $t = 33.7$ s, which corresponds to $\overline{f} = 6$ Hz. Considering Test 7 recorded with $FR = 90$ fps, the error does not exceed the noise level throughout the experiment. Considering the figure corresponding to Test 9 with $FR = 120$ fps, it would be expected that the noise level is not exceeded. However, the error slightly exceeds the noise level at $\overline{f} = 5.5$ Hz. This small inconsistency might have to do with artifacts introduced to the image by the camera's video compression algorithm. Since the camera used in this study is a consumer-grade action camera, intended to capture quality videos for nonprofessionals rather than for precision applications, the compression algorithms used at higher FR values may be more aggressive in an effort to reduce file size. Kellner et al. (2010) noted that the aggressive video compression methods used during processing of high frame rate video streams in an effort to maintain reasonable requirements for transfer and storage of the data sometimes result in degradation in quality. Considering the first three plots, it appears that to minimize frequency related errors in displacement measurements, the camera should be capable of capturing videos with FR of at least 9 times the highest frequency of the input.

7.6.2 Velocity measurement

As mentioned earlier, the displacement response measurement is filtered before differentiation to obtain velocity. Filtering is performed to reduce the noise level in the measurement. Even though the Savitzky-Golay filter performs very well in smoothing the noise, and it is known as a filter that minimizes the reduction of peak values (Leifer et al. 2011), some level of reduction in peaks is still introduced, depending on the window length. Fig. 7-9 demonstrates a comparison for velocity and velocity absolute error when a first-order Savitzky-Golay filter with 0.025 s (1/4-cycle with 10 Hz frequency), 0.037 s (3/8-cycle cycle with 10 Hz frequency), and 0.05 s (1/2-cycle with 10 Hz frequency) window lengths is used. It can be seen that an increase in the window length results in a reduction in local peak values. This reduction increases with the driving frequency. However, comparing the E_v plots, shows that increase in window length effectively reduces the level of noise in velocity measurements, resulting in a better estimation of velocity at lower frequencies. Thus, there is a compromise between the level of error in low and high frequencies—reduction in one results in increase in the other.

Fig. 7-10 illustrates the frequency capability of the camera in measuring velocity. Camera measurements from Test 3, captured using $FR = 30$ fps, show the highest error in high frequencies compared to 60 fps (Test 4) and 90 fps (Test 7) videos. E_v exhibits a large decrease when increasing the FR from 30 fps in Test 3 to 60 fps in Test 4. However, as the figure shows, there is only a slight improvement from 60 fps to 90 fps. This is because, after a frequency, filtering becomes the main source of error.

7.6.3 Acceleration measurement

The effect of filter window length on acceleration is presented in Fig. 7-11. The top row of the figure compares the true and camera-measured values of local peaks for acceleration. It can be seen that the acceleration noise effectively decreases as the window length increases. Similar to velocity measurements, increase in window length improves the measurement error at low frequencies. Considering the bottom row, in contrast to velocity measurement, the maximum acceleration absolute error E_a is not affected much by the increase in window length. Therefore, use of longer window length appears to be preferable.

Fig. 7-12 illustrates the frequency capability of the camera in measuring acceleration. The figure shows that increasing the frame rate improves the acceleration measurement capability at high frequencies. Although it is not shown in the figure, comparing the measurements from the other three LED lights shows that higher frame rate leads to greater noise and larger error at low frequencies. In order to improve the error at low frequencies, while maintaining the same level of error at high frequency, video capturing should be performed with a smaller scale ratio, *S*, value.

7.6.4 Experimental results summary

The frequency capability of the camera in measuring displacement, velocity, and acceleration is presented through contour plots in Fig. 7-13. In these plots, the horizontal axis represents the driving frequency of the shake table and the vertical axis the *FR* of the camera. The left plot shows the displacement absolute error E_d normalized by the displacement noise *S*. The middle plot presents the velocity absolute error E_v normalized by the velocity noise $S \times FR$. The right plot shows the ratio of acceleration absolute error E_a normalized by the acceleration noise $2S \times FR^2$. These contour plots are generated using the entire set of experimental results. The maximum of the error ratio is used for multiple tests with the same *FR*. It can be seen that a $FR = 60 \sim 80$ fps is the minimum frame rate that could be used to make the best use of the resolution capacity of the camera to capture frequencies up to 10 Hz. This means that the error ratio is not affected by the driving frequency for frame rates greater than 80 fps. Once the required *FR* is known for an experiment, the accuracy can be improved by reducing the scale ratio, S. Reduction in the scale ratio is achievable either through using cameras with higher resolution sensors, reducing the distance between the camera and object, or decreasing the AOV. However, the resolution is limited to the number of pixels representing the targeted field of view. Considering the absolute displacement error contours, the maximum error ratio is bounded by 3.5 at a frequency of about 7.5 Hz. Note that the displacement amplitude of the shake table controls the maximum displacement error ratio at the time the frequency reaches 7.5 Hz. From that point to the end of excitation, the amplitude decreases further and consequently the maximum error ratio decreases.

7.6.5 Example: vision-based measurement accuracy for shake table tests of ultrasound machine

This section presents an example that illustrates the use of the contour plots presented in the previous section. We are interested in assessing the accuracy of the vision-based measurements made with the same camera during the shake-table testing of medical equipment on wheels and casters (Nikfar & Konstantinidis 2015). To do so, the following properties are needed: (a) The frame rate, FR, of the video recording, (b) The transformation scale from pixel to physical coordinate, S, and (c) The maximum frequency of interest ($\bar{f}$), which in our case is the maximum expected frequency experienced by the ultrasound machine. The video recording was captured at 60 fps. As presented in Fig. 7-1(b), 307 pixels corresponded to a 24 cm distance between the LED lights attached on the body (case) of the Ultrasound. Therefore, the image has the transformation scale of $S = 24/307 = 0.0782$ cm/pixel. In order to obtain the range of frequency of the measurement, we take the Fourier transform of the displacement signal, as shown in Fig. 7-14. It can be seen that frequencies higher than 3 Hz have nearly zero Fourier amplitude (or energy). Thus, with FR = 60, and assuming $\bar{f} = 3\,\text{Hz}$ as the peak frequency, the expected peak displacement, velocity, and acceleration absolute errors can be obtained using the contour plots presented in Fig. 7-13 (dashed lines). Based on the contour plots, the normalized absolute errors are: $E_D / S < 0.5$, $E_v / (S \times FR) < 0.5$, and

$E_a/(2S \times FR^2) < 0.25$. Consequently, the measurement is expected to have peak absolute errors of:

$$E_d < 0.5 \times 0.0782 = 0.039\,\text{cm}$$

$$E_v < 0.5 \times (0.0782 \times 60) = 2.35\,\text{cm/s}$$

$$E_a < (2S \times FR^2) < 0.25 \times (2 \times 0.07802 \times 60^2)/(980) = 0.14\,\text{g}.$$

In this example, the assessment of the vision-based measurements is conducted after completion of the experimental program. The procedure could also be implemented in the design phase of an experiment to determine what combination of camera settings or positioning needs to be used to achieve the desired levels of measurement accuracy.

7.6.6 Some applications of contour plots in measuring the response of nonstructural components

The contour plots presented can be used for evaluating the vision-based accuracy in a variety of applications related to nonstructural components provided that the scale ratio, *S*, of the recorded image can be determined. There are scenarios in which *S* may change depending on the position of the target in the plane of motion, and consequently the accuracy may change during measurement. One example is when the camera is aimed at an angle to the targeted object, e.g., in (Sato et al. 2011; Shi et al. 2014). In this case, the planar motion of the object would change the depth and the scale of the image since the motion has a component in the direction parallel the camera's axis. Given the distance, focal length, and aiming angle of the camera with respect to the shake table, the scale ratio can be obtained by generating a map from physical to pixel coordinates. In this case, the scale will be a function of the position of the pixel in the image, as will be the measurement accuracy. The position-dependent scale ratio can also be obtained experimentally by measuring the pixel distance between two fixed points on every frame. A conservative estimate of the maximum error of such an experiment would correspond to the largest scale ratio captured during the experiment.

Another practical application that requires the determination of *S* for different points is a testing scenario where multiple points would need to be tracked at multiple depths. For instance, measuring the response of the monitor and the body of the ultrasound machine requires tracking of LED lights located at different depths relative to the camera (as shown in Fig. 7-1). The scale ratio for LED points attached to each component would be equal to the distance of the camera lens to the plane of motion of each point, *d*, divided by the focal length of camera, *f*, ($S = d/f$). *S* can also be determined using Equation 7.4. However, it requires consideration of two fixed points with known physical distance on different components or objects, similar to Fig. 7-1, and measurement of the corresponding pixel distance. Since *S* increases for points farther from the camera, the accuracy would be reduced when measuring points at farther distance. The wavelet approach, presented in this paper, could be utilized to determine the scale ratio of each LED light. In this case, Equation 7.5 can be utilized to scale the tracked signal in pixel coordinates to the shake table signal (i.e., the initial cosine signal). Although this approach does not require tracking of two LEDs for each component, a wavelet analysis should be performed for each tracked point to find the scale corresponding to the maximum wavelet transform coefficient.

In some applications, advanced filtering and edge detection techniques allow tracking a large number of points on an object. Knowing that higher accuracy can be achieved if points with smaller scale ratios are used for measurement, one can track the points with the smallest scale ratio throughout the experiment and use contour plots to estimate the measurement accuracy.

Moreover, there might be a need to determine the accuracy when out-of-plane motion of an object is to be measured. Multiple cameras could be used for this purpose. As the distance of the object may change with respect to the camera's axis, *S* may change. Again, *S* can be obtained by considering two fixed points with known distance on the object and keeping track of the pixel distance to obtain *S* in every frame. Another way to do so is to use a measurement from one camera to find the distance of the object with respect to the other camera and find the corresponding scale ratio in every frame (i.e., $S = d/f$). Once *S* is obtained for each tracked point and in every frame, one may use the maximum *S* observed during detection to find the most conservative estimate of the measurement accuracy using the contour plots. Applicability of this procedure through experimental verification is left for future investigations.

Note that *S* is only one of the parameters influencing the measurement accuracy. Based on the contour plots, *FR* also affects the accuracy of the measurement, especially when high-frequency vibrations are to be measured. The trade-off between *FR* and resolution, in conjunction with the fact that increase in either *FR* or resolution tends to improve [with rare exceptions, such as Test 9 with $FR = 120$ fps, discussed in the *Displacement Measurement* section] the accuracy of vision-based measurements, poses an optimization challenge. For instance, for the problem at hand with maximum driving frequency of $\overline{f} = 10$ Hz, the range for which an optimization could be performed is for *FR values* between 30 fps (i.e., smallest *FR* used) and $FR = 90$ fps (beyond which there is no appreciable improvement in error reduction—see the contour plots). In this range, increase in frequency and resolution (i.e., reduction in scale ratio) may improve the vision-based measurement accuracy. It should be noted that the normalized velocity and acceleration errors are proportional to the camera *FR*, meaning that, for a constant normalized error, the velocity and acceleration errors would increase if a higher *FR* camera was used. Another parameter that complicates the problem is that for a constant $E_v / S \times FR$, E_v scales linearly with *FR*, while for $E_a / S \times FR^2$, E_a scales with the square of *FR*. Thus, the optimum *S* and *FR* configurations might be different for velocity and acceleration measurements, as it might be for displacement. The investigation of this optimization problem for available consumer-grade cameras with different *FR*–Resolution capabilities is another area to extend the application of this study.

Future applications of this study may benefit from an investigation into the performance of filtering schemes other than the Savitzky-Golay filter, potentially improving the accuracy of vision-based measurements for shake table testing of nonstructural components.

7.7 Conclusion

This study investigated the accuracy of vision-based displacement, velocity, and acceleration measurements of a consumer-grade action camera intended for use in shake-table testing of nonstructural components. The accuracy of the vision-based measurements was evaluated through shake-table experiments using as input a signal with time-dependent frequency and amplitude. Camera recordings with various frame rates and resolutions were utilized to evaluate the camera measurement capabilities. The displacement, velocity, and acceleration absolute errors were evaluated by comparing the vision-based measurements with the 'true' response, as recorded using displacement and acceleration sensors. A wavelet transform method was proposed and utilized to synchronize camera and conventional sensor recordings. Such synchronization is necessary, and is often a challenge, in experimental setups where a combination of camera and conventional sensors are used to collect data. Moreover, the study examined the application of the Savitzky-Golay filter and the effect of filter window length for smoothing the displacement measurements and reducing the noise in the computed velocity and acceleration responses. It was shown that the maximum recommended window length is very effective in reducing the noise, but can cause reduction in velocity and acceleration peaks in high frequencies. Finally, utilizing all the experimental data collected in this study, contour plots demonstrating the frequency capability of the camera were generated. The contour plots can be used to determine the maximum displacement, velocity, and acceleration errors for a wide combination of camera resolution and frame rate values.

7.8 References

Balletti, C., Guerra, F., Tsioukas, V. & Vernier, P., 2014. Calibration of action cameras for photogrammetric purposes. *Sensors*, 14(9), pp.17471-90.

Chang, C.C. & Ji, Y.F., 2007. Flexible videogrammetric technique for three-dimensional structural vibration measurement. *Journal of Engineering Mechanics (ASCE)*, 133(6), p.656–664.

Chatzis, M.N. & Smyth, A.W., 2012. Modeling of the 3D rocking problem. *International Journal of Non-Linear Mechanics*, 47(4), pp.85-98.

Chaudhuri, S.R. & Hutchinson, T.C., 2005. Characterizing frictional behavior for use in predicting the seismic response of unattached equipment. *Soil Dynamics and Earthquake Engineering*, 25, p.591–604.

Di Egidio, A., Zulli, D. & Contento, A., 2014. Comparison between the seismic response of 2D and 3D models of rigid blocks. *Earthquake Engineering and Engineering Vibration*, 13(1), pp.151-62.

Doerr, K.-U., Kuester, F., Nastase, D. & Hutchinson, T.C., 2008. Development and evaluation of a seismic monitoring system for building interiors—Part II: Image data analysis and results. *IEEE Transactions on Instrumentation and Measurement*, 57(2), pp.345-54.

Feng, D. & Feng, M.Q., 2015. Vision-based multipoint displacement measurement for structural health monitoring. *Structural Control and Health Monitoring*, (In-Press).

Fukuda, Y., Fengy, M.Q. & Shinozuka, M., 2010. Cost-effective vision-based system for monitoring dynamic response of civil engineering structures. *Structural Control and Health Monitoring*, 17, p.918–936.

Greenbaum, R., Smyth, A. & Chatzis, M., 2015. Monocular computer vision method for the experimental study of three-dimensional rocking motion. *Journal of Engineering Mechanics (ASCE)*.

Harvey, P.S. & Gavin, H.P., 2014. Assessing the accuracy of vision-based accelerometry. *Experimental Mechanics*, 54(2), p.273–277.

Harvey, P.S. & Gavin, H.P., 2014. Double rolling isolation systems: A mathematical model and experimental validation. *International Journal of Non-Linear Mechanics*, 61, p.80–92.

Harvey, P.S., Zéhil, G.-P. & Gavin, H.P., 2014. Experimental validation of a simplified model for rolling isolation systems. *Earthquake Engineering & Structural Dynamics*, 43(7), p.1067–1088.

Hutchinson, T.C., Chaudhuri, S.R., Kuester, F. & Auduong, S., 2005. Light-based motion tracking of equipment subjected to earthquake motions. *Journal of Computing in Civil Engineering (ASCE)*, 19(3), p.292–303.

Kanda, K., Miyamoto, Y., Kondo, A. & Oshio, M., 2005. Monitoring of earthquake induced motions and damage with optical motion tracking. *Smart Materials and Structures*, 14(3), p.S32–S38.

Kellner, C.R., Sanders, W.R., and Davis, D.R. (2010). Systems and methods for managing frame rates during multimedia playback. *U.S. Patent No. 7,660,512.* Washington, DC: U.S. Patent and Trademark Office. Issued: February 9, 2010.

Kienle, S.C., Sims, A.M. & Leifer, J., 2008. Full-field transient acceleration measurement using videogrammetry. In *Conference: 2008 IMAC-XXVI: Conference & Exposition on Structural Dynamics*. Orlando, FL, 2008.

Konstantinidis, D. & Makris, N., 2005. Report No. 2005/07 *Experimental and analytical studies on the seismic response of freestanding and anchored laboratory equipment*. CA: Pacific Earthquake Engineering Research Center (PEER) University of California, Berkeley. Report No. PEER 2005-07.

Konstantinidis, D. & Makris, N., 2007. The dynamics of a rocking block in three dimensions. In *Proc. 8th HSTAM (Hellenic Society for Theoretical and Applied Mechanics) International Congress on Mechanics*. Patras, Greece, 2007.

Konstantinidis, D. & Makris, N., 2009. Experimental and analytical studies on the response of freestanding laboratory equipment to earthquake shaking. *Earthquake Engineering and Structural Dynamics*, 38(6), p.827–848.

Leifer, J., Weems, B.J., Kienle, S.C. & Sims, A.M., 2011. Three-dimensional acceleration measurement using videogrammetry tracking data. *Experimental Mechanics*, 51(2), p.199–217.

MATLAB, 2002. *High-performance language software for technical computing. The MathWorks, Inc.: Natick, MA*.

Nastase, D. et al., 2008. Development and evaluation of a seismic monitoring system for building interiors—Part I: Experiment design and results. *IEEE Transactions on Instrumentation and Measurement*, 57(2), pp.332-44.

Nikfar, F. & Konstantinidis, F., 2015. Shake table tests of hospital equipment supported on wheels/casters. *Earthquake Engineering and Structural Dynamics*, (Submitted).

Robbe, C., Nsiampa, N., Oukara, A. & Papy, A., 2014. Quantification of the uncertainties of high-speed camera measurements. *International Journal of Metrology and Quality Engineering*, 5(2).

Sato, E., Furukawa, S., Kakehi, A. & Nakashima , M., 2011. Full-scale shaking table test for examination of safety and functionality of base-isolated medical facilities. *Earthquake Engineering and Structural Dynamics*, 40(13), p.1435–1453.

Savitzky, A. & Golay, M.J.E., 1964. Smoothing and differentiation of data by simplified least square procedures. *Analytical Chemistry*, 36(8), p.1627–1639.

Shi, Y., Kurata, M. & Nakashima, M., 2014. Disorder and damage of base-isolated medical facilities when subjected to near-fault and long-period ground motions. *Earthquake Engineering and Structural Dynamics*, 43(11), p.1683–1701.

Wittich, C.E. & Hutchinson, T.C., 2015. Shake table tests of stiff, unattached, asymmetric structures. *Earthquake Engineering and Structural Dynamics*, 44(14), pp.2425-43.

Yokota, A., Hamamoto, T., Koga, H. & Watanabe, T., 2012. Estimation of earthquake ground motion by image aalysis of sliding objects taken with a fixed camera.

Tsukuba, Japan, 2012. 21st International Conference on Pattern Recognition (ICPR 2012).

Table 7-1: Driving frequency of the decaying up-chirp displacement signal at various times

Time (s)	0	5	10	15	20	25	30	35	40
$\bar{f}$ (Hz)	0	0.02	0.15	0.52	1.24	2.43	4.2	6.67	9.95

Table 7-2: Camera settings and image characteristics used in the experiments

Test #	Image Size (pixel)	*FR* (fps)	AOV	*S* (mm)
1	3840×2160	30	Wide	1.013
2	2704×1520	30	Wide	1.425
3	2704×1520	30	Medium	0.952
4	2704×1520	60	Medium	0.952
5	1920×1440	80	Wide	2.311
6	1920×1080	60	Narrow	0.963
7	1920×1080	90	Narrow	0.926
8	1920×1080	120	Narrow	0.922
9	1280×960	120	Wide	0.975
10	1280×720	60	Medium	2.224
11	1280×720	120	Medium	2.224
12	1280×720	120	Narrow	1.383
13	1280×720	240	Narrow	0.898

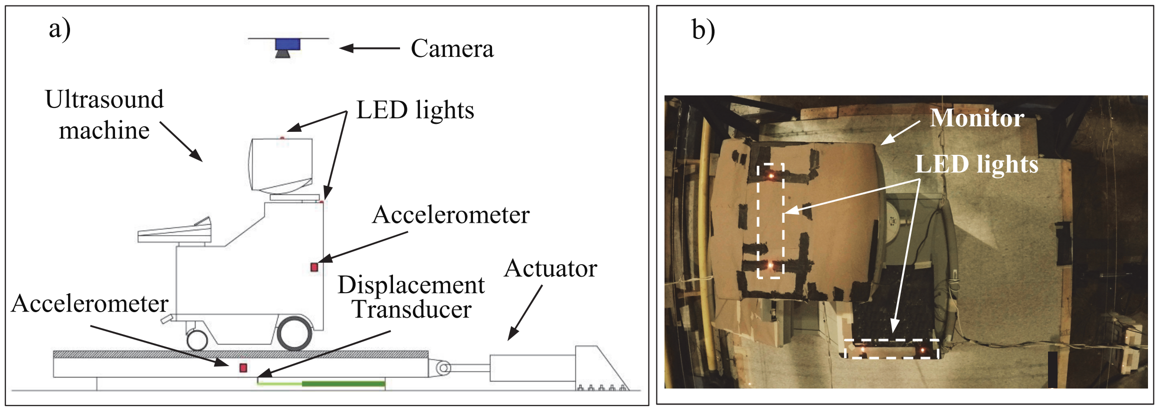

Fig. 7-1. (a) Schematic of the experimental setup. (b) Camera view from top. The distance between two LEDs attached on the monitor is 458 pixels; the corresponding distance for the LEDs attached on the ultrasound body is 307 pixels.

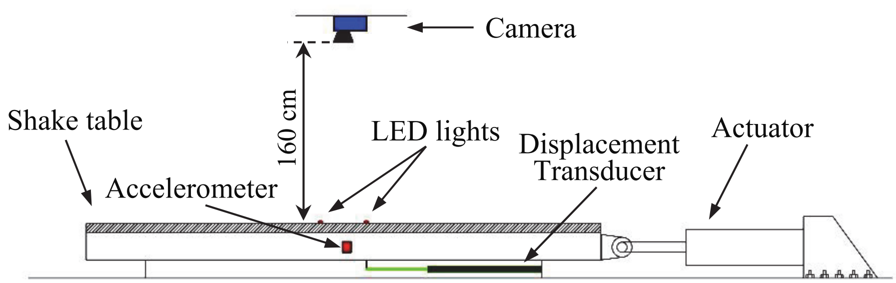

Fig. 7-2. Schematic of the experimental setup for assessing the accuracy of the vision-based measurements.

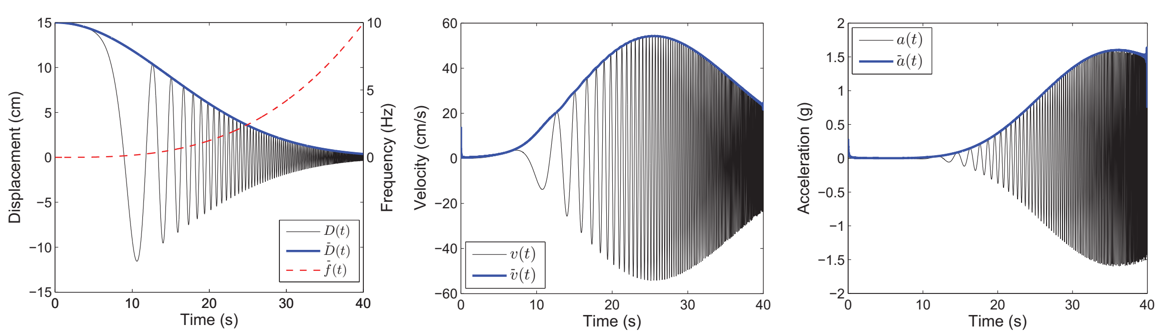

Fig. 7-3. Displacement, velocity, and acceleration time histories of the decaying up-chirp signal used as shake-table input.

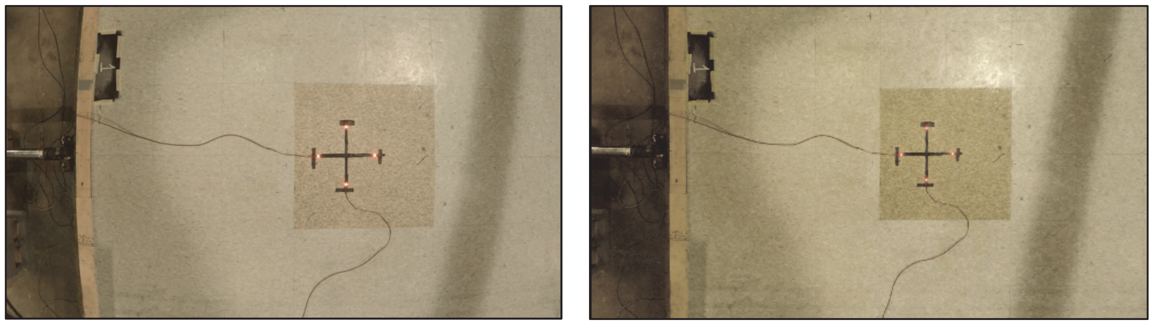

Fig. 7-4. Example of image calibration/correction. Left: distorted/uncorrected image. Right: undistorted/corrected image.

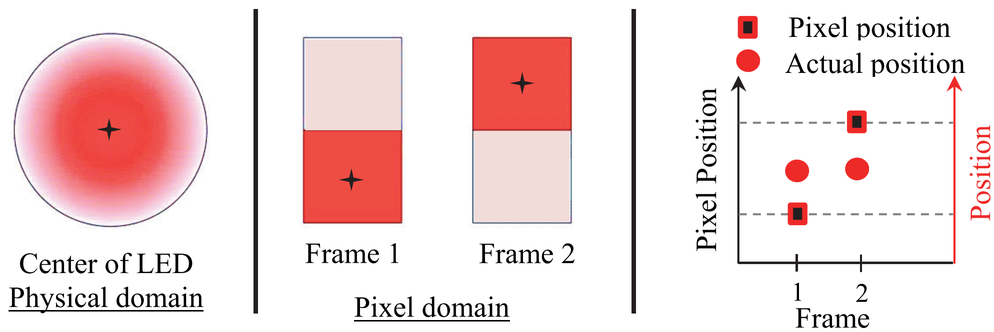

Fig. 7-5. Illustration of camera sensor noise.

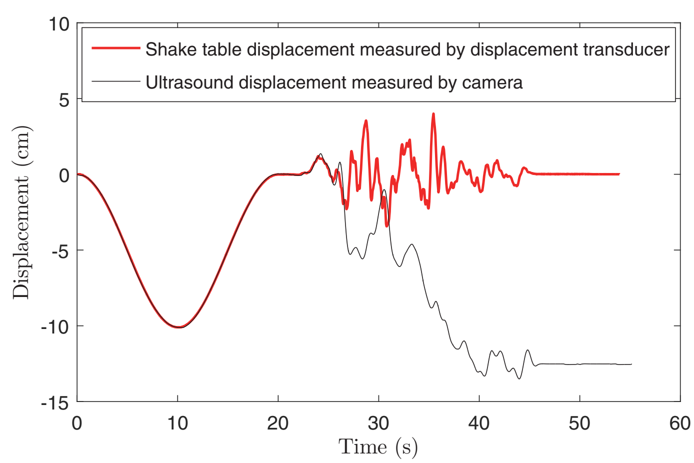

Fig. 7-6. Synchronized signals for absolute position of the ultrasound (using camera recordings) and of the shake table (using the displacement transducer) under 70% of the 1989 Loma Prieta earthquake excitation.

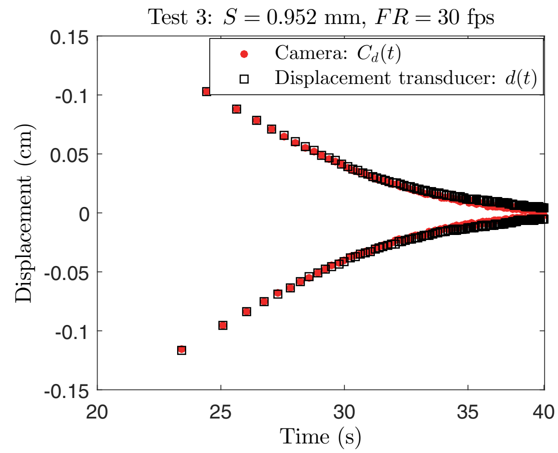

Fig. 7-7. Comparison of the local displacement peaks obtained using the camera and the displacement transducer.

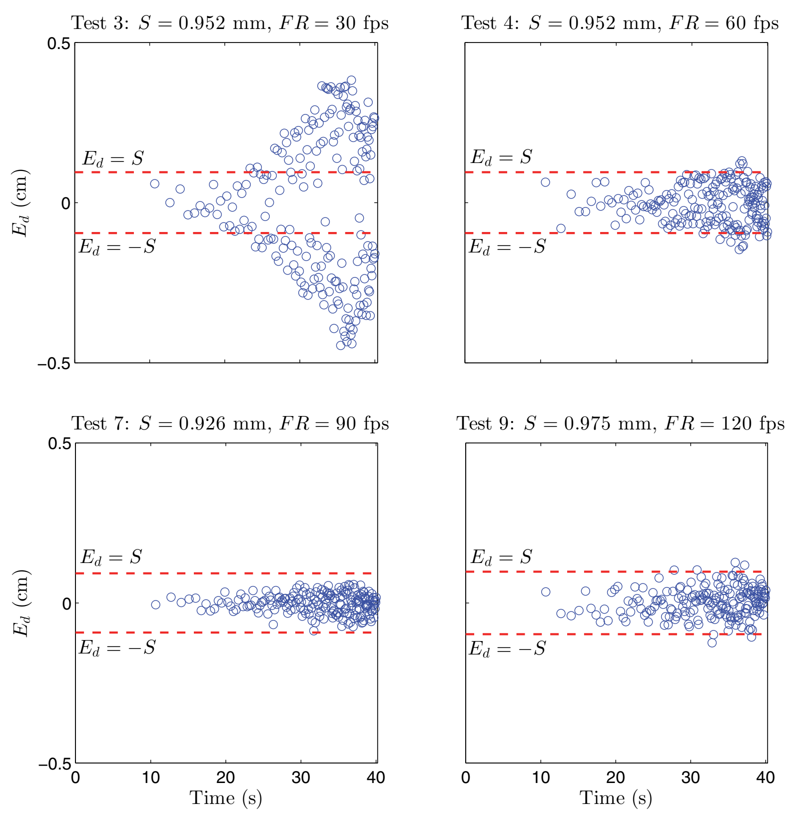

Fig. 7-8. Frequency capability of the camera for measuring displacement.

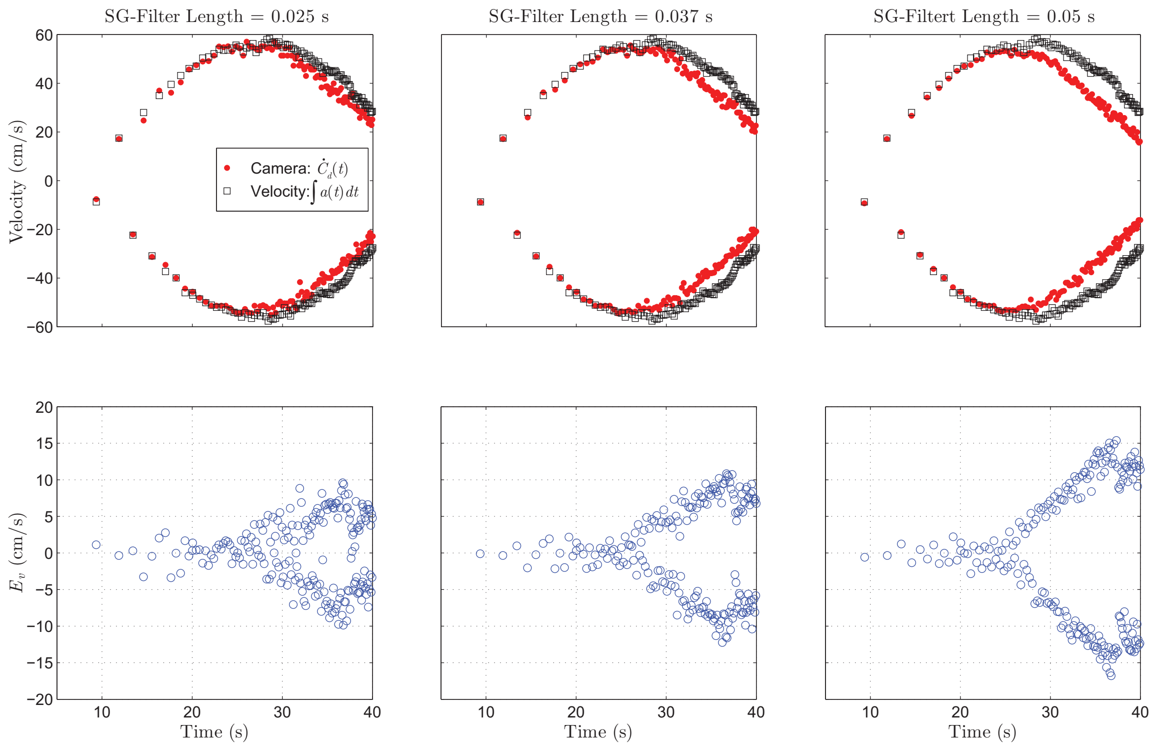

Fig. 7-9. Effect of filter window length on velocity measurements for Test 4.

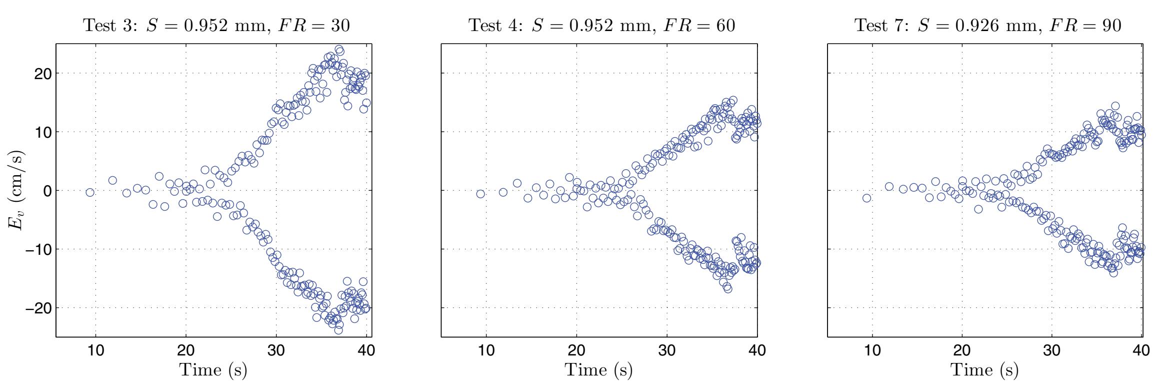

Fig. 7-10. Frequency capability of the camera in measuring velocity (for SG filter with 0.05 s window length).

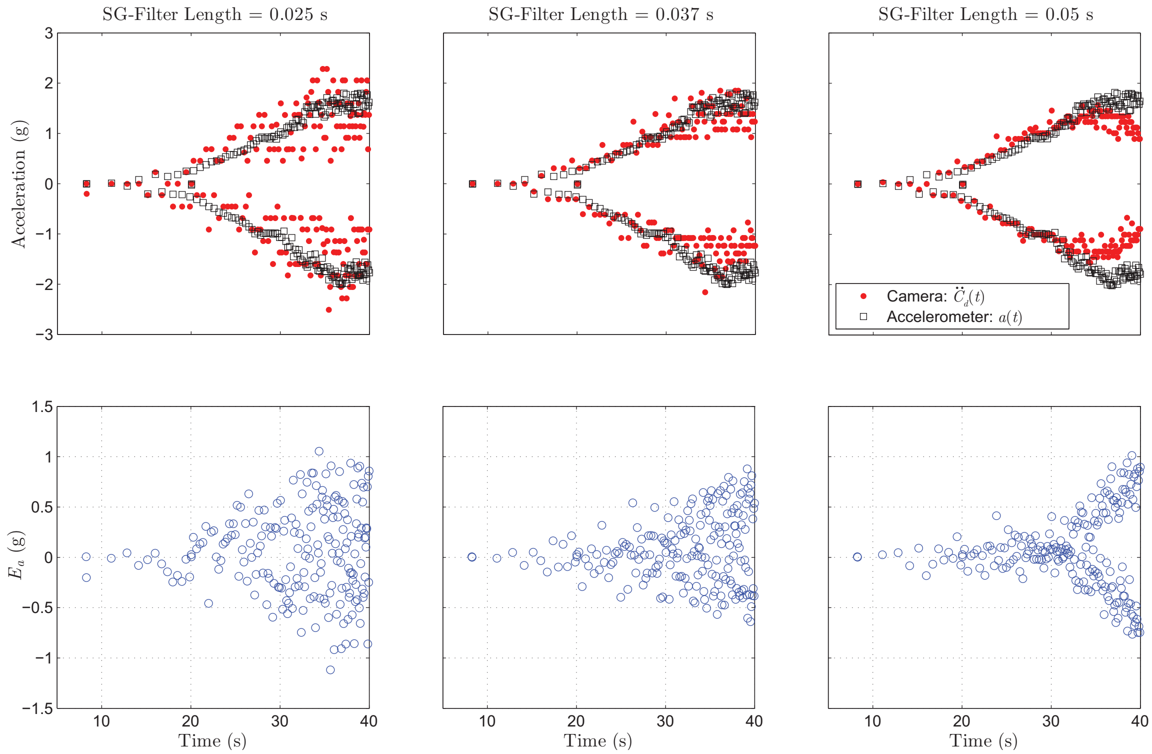

Fig. 7-11. Effect of filter window length on acceleration measurements for Test 4.

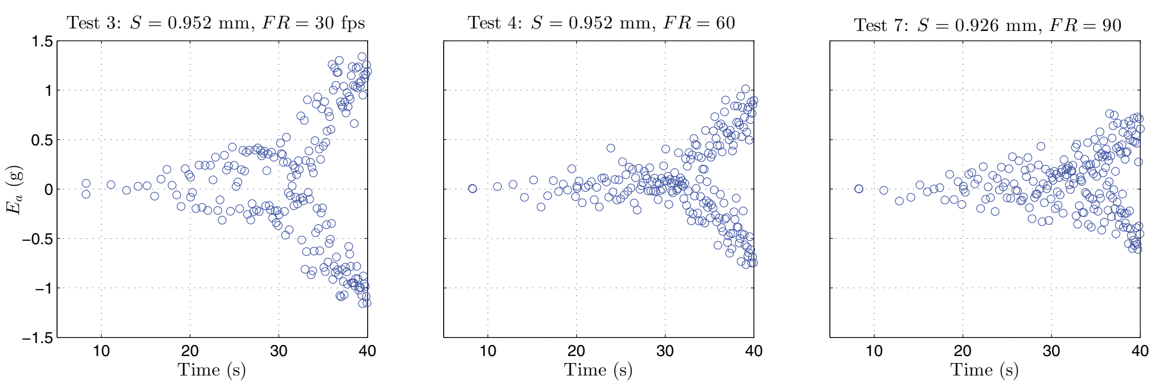

Fig. 7-12. Frequency capability of the camera in measuring acceleration (for SG filter with 0.05 s window length).

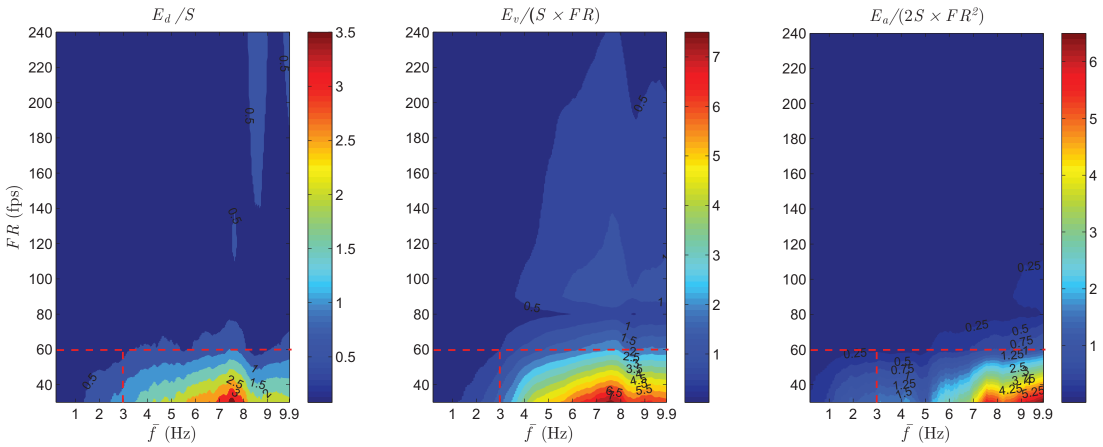

Fig. 7-13. Frequency capability of the camera (for SG filter with window length of 0.05 s).

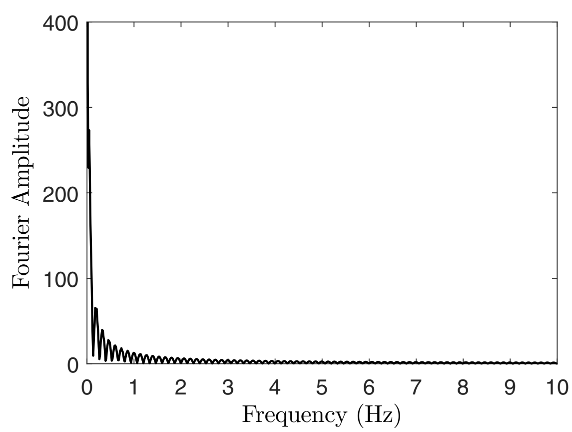

Fig. 7-14. Frequency content of the displacement response of the ultrasound machine shown in Fig. 7-6 measured at a frame rate of 60 fps.

Chapter 8: Conclusions and Recommendations

8.1 Summary

Continued functionality of critical facilities, including hospitals, power plants, emergency response centers, and key government facilities, is highly correlated to the performance of nonstructural components, including equipment and contents (EC), which are the focus of this study. Anchoring EC is the first solution that comes to mind and has been implemented in many facilities. However, it is often not an ideal method since it can be very costly and in some cases not possible to implement. Seismic isolation of building was proposed more than three decades ago as an alternative method to protect both buildings and their EC. It has become the method of choice for critical facilities, particularly hospitals in Japan and the United States. However, the supporting research on its effectiveness for unanchored EC is rather limited. This study generated knowledge on the seismic behaviour of two types of freestanding EC that tend to exhibit large motion: (1) EC that slide on their support surface, and (2) EC that move due to rolling of the wheels/casters on which they are supported. The effectiveness of base isolation as a earthquake hazard mitigation for reducing the seismic demands on these types of EC was investigated. Chapter 1 presented an introduction on the importance of nonstructural components and some examples where nonstructural damage resulted in disruption in functionality of buildings. Chapter 2 and Chapter 3 investigated the seismic response of sliding EC in base-isolated buildings under broad-band and pulse-like ground motions, respectively. Chapter 4 compared various numerical models for simulating the sliding response of structures/objects, and, by including the flexibility of the EC and the velocity-dependence of the friction force, presented an advanced model capable of capturing the stick-slip phenomenon during sliding. Chapter 5 evaluated the frictional resistance of two pieces of hospital equipment on wheels/casters. It presented the results of an extensive shake table testing program to evaluate the seismic response of equipment on wheels/casters in a steel special-concentric-braced-frame hospital. Chapter 6 investigated the seismic response of equipment supported on wheels/casters in base-isolated hospitals and compared the seismic demands on the equipment with the steel special-concentric-braced-frame hospital. Chapter 7 described the experimental setup designed for carrying out the shake table testing program on hospital equipment on wheels/casters. Particularly, it elaborated on the hybrid use of conventional sensors and a low-cost vision-based measurement system developed to measure the seismic responses of the equipment during the shake table tests. Major conclusions for these chapters are summarized in the subsequent sections.

8.2 PART I: Seismic response of sliding equipment and contents

8.2.1 Sliding response under broad band-ground motions

The effectiveness of seismic isolation on reducing the seismic demands on sliding EC was assessed by comparing the response of EC inside base-isolated buildings to the response of the same EC inside corresponding fixed-base buildings. Two types of base isolation systems were considered: viscously damped linear elastic, and bilinear. The results of the parametric investigation under broad-band ground motions suggest that seismic isolation is in general an excellent earthquake protection technology for reducing seismic demands (sliding displacement and absolute acceleration) on sliding equipment and contents in buildings. There are, however, cases for which seismic isolation results in amplification of sliding displacement response, more notably for low friction coefficients and high earthquake intensities. The study showed that providing a minimum amount of damping at the isolation level works effectively to decrease the sliding displacements of EC. However, the use of very large amounts of isolation damping is not warranted, since it was observed that damping ratios larger than about 20% did not provide any additional benefit. For a viscously damped linear elastic isolation system, larger isolation damping results in lower EC absolute accelerations, while for a bilinear isolation system, hysteretic damping has an adverse effect on absolute accelerations. An appropriated engineering demand parameter was suggested for sliding EC which used in probability analysis leading to design fragility curves to estimate peak sliding demand.

8.2.2 Sliding response under pulse-like ground motions

A comprehensive parametric investigation on the sliding response of EC in seismically isolated buildings subjected to pulse type excitations was conducted through the use of dimensional analysis. Viscoelastic and bilinear isolation systems were assumed. Under pulse excitations, amplification occurred in the peak sliding displacement of EC with increasing isolation-to-pulse period ratio, specifically for low friction coefficient values or large acceleration pulse amplitudes. The highest amplification was associated with the resonance condition, where the isolation period is very close to the pulse period. An increase in the isolation nominal period to values greater than the pulse period resulted in reduced sliding displacement and consequently more effective isolation. Even a relatively small amount of isolation damping, say 10%, proved to be very effective in reducing the sliding displacements under resonance condition, while large damping ratios, say over 20%, provided little additional benefit in controlling the maximum sliding displacement for non-resonance cases. It was demonstrated that neglecting the static phase of friction is not always conservative when estimating the maximum sliding displacement of EC with low friction. However, in the range of kinetic-to-static friction coefficient ratio of sliding equipment tested previously (ratios between 0.7 to 1.0), the maximum sliding response exhibits similarity, meaning that the response is governed by the kinetic friction value. It was illustrated that the dynamic interaction between the EC and the base-isolated building is negligible when the building is subjected to very long-period pulses (i.e., pulses with periods longer than isolation nominal period). Even under the resonance condition, the interaction between EC with $m_{EC} / M_b < 0.2$ and base-isolated building results in less than 10% increase in the peak normalized sliding response. However, the interaction becomes considerable under pulses with periods shorter than the isolation period, indicating the importance of considering the short-period acceleration pulses overriding the coherent long-period pulse in certain pulse-like ground motions. In the case of a bilinear isolation system, the dimensional analysis revealed the existence of complete similarity in the sliding response of contents with respect to the yield displacement of the isolation layer. In other words, the peak sliding displacement is insensitive to the exact value of isolation yield displacement. The study showed that the peak sliding displacement of EC is not affected appreciably by the lateral flexibility of the superstructure when the superstructure-to-isolation period ratio is less than 0.3.

8.2.3 Effect of the Stick-Slip Phenomenon on the sliding of EC

A classification for friction and sliding models was proposed to clearly distinguish the sliding problems. The mathematical formulation of the stick-slip sliding problem was derived. It was shown that the presence of elasticity (equivalently, the flexibility of the structure above the sliding surface) and unstable friction force (considering the static friction phase through the Stribeck friction model) change the nature of sliding problem considerably and may introduce stick-slip oscillations in the sliding process. The effects of the kinetic-to-static friction ratio, transition sharpness from static to kinetic friction, viscous damping at the contact surface, and elasticity of contact (or the flexibility of the structure above the slide surface) were investigated through dimensional analysis. The results of conventional sliding models, including Newmark's sliding model and coupled sliding models with Coulomb or Static+Coulomb friction, were compared with the results of the stick-slip model. It was demonstrated that simplified sliding models may underestimate the sliding response. It was also shown that the sliding response is influenced by the sequence of pulses in the input excitation; therefore, the study suggested the consideration of minor pulses in pulse-like ground motions together with the coherent pulse in order to obtain more reliable approximations. Furthermore, it was demonstrated that the previous finding regarding the dominant role of kinetic friction in sliding of rigid EC cannot be extended to flexible EC.

8.3 PART II: Seismic response of equipment and contents supported on wheels/casters

A series of experimental tests was conducted to evaluate the seismic response of two pieces of medical EC supported on wheels/casters. The experimental program consisted of two phases: (a) resistance evaluation through controlled displacement experiments using shake table, and (b) shake table experiments to evaluate the seismic response of the equipment. The controlled displacement experiments resulted in force-displacement loops from which the equivalent frictions were approximated to be 0.01, 0.19, 0.02 for Unlocked-Ultrasound, Locked-Ultrasound, and Hospital Cart, respectively.

The shake table simulated the floor responses of a steel special-concentric-braced-frame hospital, a hospital isolated with LRB isolation system, and a hospital isolated using TFP bearings under earthquake excitations. A combination of conventional and camera sensors was developed in order to measure the seismic response of the equipment during the shake table tests. A non-uniform mass distribution within the equipment and complicated supporting system mechanism (equipment on casters) could cause complex motions of freestanding contents such as twisting when subjected to base excitations. Measuring such motions would be challenging by traditional, contact-type displacement sensors. It was shown that the accuracy of the vision-based measurements is approximately 0.5 mm and 3 cm/s for displacement and velocity, respectively.

It was observed that locking the casters can, in some cases, result in amplified response depending on the input excitation intensity and orientation of the equipment with respect to the input excitation direction. The regression analysis of the experimental data showed that locking does not necessarily decrease the seismic demands on the EC in fixed-base building, while it is very effective in base-isolated buildings. Therefore, the study suggested the use of wheels/casters with automatic locking mechanism for EC in base-isolated buildings.

It was shown that, overall, base isolation was effective in reducing the relative displacement demand on the equipment on wheels/casters although there were some cases where base isolation resulted in amplified displacement responses. In all the cases, isolation resulted in considerable lower relative velocity demands leading to reduced potential of damage due to impact. Comparing the bilinear (LRB) system with TFP system, it was observed that TFP system performed slightly better in reducing the peak displacement demands on the equipment, while the peak relative velocity demand was almost the same for the two systems.

Lastly, the experimental data was presented within a probabilistic framework leading to fragility functions that can be used to estimate the peak relative displacement and relative velocity demands on wheel/caster-supported EC in fixed-base and base-isolated buildings.

8.4 Recommendation and future study

Though this study tried to narrow down the gap in knowledge regarding the seismic behaviour of freestanding EC and the effectiveness of base isolation in reducing the demands on this class of EC, there are still areas that call for further investigations. The following provides some recommendations for future research:

- In Chapter 2 and Chapter 3, a simplified shear building was considered for the superstructure in the parametric study. Such a model neglects the flexibility and vibration of the superstructure in the vertical direction (including the vibration of the floor slabs, beams, and columns), the possible coupling in the horizontal and vertical response of the superstructure that can be influential in the case of moment resisting frames, and coupling in the horizontal and vertical behaviour of isolation system. The investigation of the effects of the neglected parameters through more advanced analytical models would be the next step of this research.
- In Chapter 3, the pulse-like ground motions were approximated by their coherent pulse. It was shown that the sequence of minor pulses in a given pulse-like ground motion is important and can affect the peak sliding response of EC. Therefore, the author suggests investigating the contribution of minor pulses as well as high frequency residual of pulse-like ground motions on the peak sliding demand.
- Chapter 4 formulated the sliding of flexible EC. More experimental investigations seem to be necessary to understand the behaviour of flexible sliding EC and perform verification of the stick-slip sliding model developed in this study.
- This study did not include a numerical investigation of the seismic response of EC on wheels/casters. Evaluating the performance of simplified models, including Newmark's rigid sliding block model, in estimating the response of EC on

wheel/casters would be beneficial for engineers who need to estimate the seismic demands of EC on wheels/casters. Detailed modeling of hospital equipment using a three-dimensional mathematical model capable of capturing all possible modes of response of EC on wheels/casters, including rolling of wheels/casters, sliding of wheels/casters, and rocking, would be very beneficial in better understanding the behaviour of this class of EC.

- It is observed during shake table tests that the EC on wheels/casters tend to accumulate displacement in one direction. More investigations would be necessary to identify the sources of this behaviour and incorporate them in future numerical simulations.
- The experimental program conducted in this study contained uniaxial shake table tests. The next step to this study would be performing 2- and 3-dimensional shake table testing. Moreover, the results of the 2D or 3D shake table tests will be necessary for validating the more advanced analytical models of EC on wheels/casters.
- The current codes lack in providing practical damage limit states for freestanding EC (for both sliding EC and EC on wheels/casters) to be used in future risk assessments. For instance, the author suggests categorizing various types of buildings (e.g., hospitals, power plants, science laboratories, office buildings, etc.), determining the important freestanding EC in terms of functionality of the building or cost, and quantifying the damage limit states corresponding to each building category and specified EC (e.g., the percentage of laptops in office buildings that may fall off the desk if they slide more than a threshold or the percentage of hospital EC that may hit partition walls or neighbouring equipment if they move more than a threshold).